Sticking with droplets: Mathematical models of capillary adhesion

Matthew Butler

Corpus Christi College

University of Oxford

A thesis submitted for the degree of

Doctor of Philosophy

Trinity 2020

Acknowledgements

There are many people who deserve thanks for helping me to produce this thesis. First and foremost, I would like to thank my supervisor, Dominic, whose support, insight and guidance has been indispensable over the last four years. All of my work has been greatly improved due to his excellent advice and many helpful suggestions. In addition, the work contained within this thesis is not entirely my own, and I owe great thanks to Finn, Lucie and Thomas for the experiments they performed; this thesis would not be the same without their efforts.

Many others within the department have supported me along the way, and I'd particularly like to thank my officemates, Alex and Michael, for being available and willing to talk about all kinds of problems, both research-related and not. I am also grateful to Ousmane for the patience he showed in teaching me new ways to solve problems, and to the members of Journal Club and Lab Lunch for introducing me to lots of new ideas and making Oxford such a great place to work.

I did not get through this DPhil by staying within the confines of the Mathematical Institute, and so I would also like to thank all the friends I have made along the way. I am particularly grateful to those involved in ultimate in Oxford, who always made me feel so welcome and have left me with some great memories of my time in Oxford.

Finally I'd like to thank my family: my parents for their support over many years, my brother for his advice and willingness to proofread, and my partner, Fiona, who inspired me to join the dark (blue) side and has continued to make my life all the better for it.

Statement of Originality

The research presented in this thesis was performed in the Mathematical Institute at the University of Oxford between October 2016 and August 2020 and was supervised by Professor Dominic Vella.

This thesis describes my own work, except for the experiments in Chapter 3, which were performed by Lucie Domino, and those in Chapter 4, which were performed by Finn Box and Thomas Robert. Their contributions have been appropriately credited in the text of this thesis.

The results of this thesis are original, apart from those in Chapter 1, which constitutes review material, and where reference is made to the work of others. In particular, §2.2.3 and §3.2 reproduce previously known results, although the derivations in both cases are new. No part of the thesis has been submitted previously for a degree of the University or elsewhere.

Two papers based on the work presented in this thesis have been published. One paper, based on the elasto-capillary adhesion presented in Chapter 4, has been published in *Physical Review Fluids* [Butler et al., 2019]. The second, published in the *IMA Journal of Applied Mathematics* [Butler and Vella, 2020], focuses on the capillary detachment of Chapter 5. In both publications, I performed the theoretical analysis and D. Vella supervised the research; in the former paper (as with Chapter 4), the experiments were performed by F. Box and T. Robert.

Abstract

A small amount of liquid trapped between two solid surfaces can pull them together because of the effects of surface tension. This effect is called capillary adhesion, and is thought to be important in many small-scale scenarios, including helping insects to adhere. In this thesis, we study aspects of capillary adhesion using mathematical modelling.

We begin by considering whether the forces generated through capillary adhesion with a fixed volume of liquid can be enhanced by splitting a liquid bridge into many smaller bridges. By carefully calculating the bridge shape (and when bridges can span a given gap), capillary adhesion of rough surfaces is shown to be significantly enhanced compared to smooth surfaces. It is also shown that roughness may lead to a steady-state resistance to shear, which is compared quantitatively to experiments in insects.

Next, we turn to study solid-solid contact in the presence of capillary adhesion. Equilibria are found for impermeable and permeable elastic spheres in contact with a flat, rigid substrate. When saturated, a porous sphere can naturally secrete its own adhering liquid as its pore space is compressed by deformation. Numerical results and scaling laws are found to describe the equilibria with and without an applied force; results without a force are compared to experiments on hydrogel beads in contact.

We then investigate in more detail the effect of surface deformation on capillary adhesion through a model of a thin membrane under tension. Calculating the equilibrium adhesion forces shows that an increase in adhesion of more than an order of magnitude can be achieved compared to a comparable undeformable system; this is supported by experimental results. The dynamics of adhesion are investigated via a lubrication model. The slow drainage of a liquid-filled dimple explains why adhesion may not always be achieved in practice unless sufficient time is allowed to adhere. We also investigate how the deformability may be exploited to detach in a controllable manner.

Finally, we study how detachment occurs using a dynamic two-dimensional model of a loaded plate attached to a rigid substrate by a liquid bridge. Using a linear stability analysis, the motion of the plate is shown to decouple into two modes — separation and tilting — with the tilting mode growing fastest. As the plate tilts it may contact the substrate, depending on the width of the plate. We characterize how plate width and initial condition may determine whether a plate ultimately detaches or adheres and show that tilting may lead to anomalous detachment: plates that should stick, detach.

Contents

List of Figures

Chapter 1

Introduction

1.1 Background and motivation

Insect adhesion

The ability of some animals to climb vertical surfaces and walk upside-down has been an area of scientific interest for hundreds of years [Hooke, 1665, Power, 1664, Stork, 1983, Ishii, 1987, Hanna et al., 1991, Autumn et al., 2002]. One particularly diverse group of climbing animals are insects, which are capable of extraordinary feats of adhesion: they are able to climb apparently smooth vertical surfaces, such as glass, and have been observed supporting loads exceeding 100 times their body weight whilst upside-down and remaining adhered [Dirks and Federle, 2011a] (see fig. 1.1a). This adhesion occurs reliably on surfaces with various surface chemistries and roughnesses [England et al., 2016, Drechsler and Federle, 2006], across a wide range of scales [Labonte and Federle, 2015, Labonte et al., 2016], and the insects are able to adhere and detach continuously during locomotion.

The current biological understanding is that in many insect species this adhesion is mediated by a secreted fluid underneath the insect's feet [Dirks, 2014, Dirks and Federle, 2011b]. It is believed that the surface tension of this oily secretion acts to adhere their feet to the substrate [Dirks and Federle, 2011a] — insects adhere, at least in part, due to capillary effects. The various ways in which capillary effects cause adhesion (discussed more in §1.3) are collectively referred to as capillary adhesion.

Insects' adhesive organs can largely be divided into two types: hairy and smooth [Bullock et al., 2008]. Loosely speaking, the insects with hairy footpads (such as flies and beetles) adhere due to a large number of small adhesive contacts on each foot, while insects with smooth footpads (including ants, cockroaches and stick insects) have a small number of larger contacts. In some recent studies, the adhesion of hairy-footed insects has

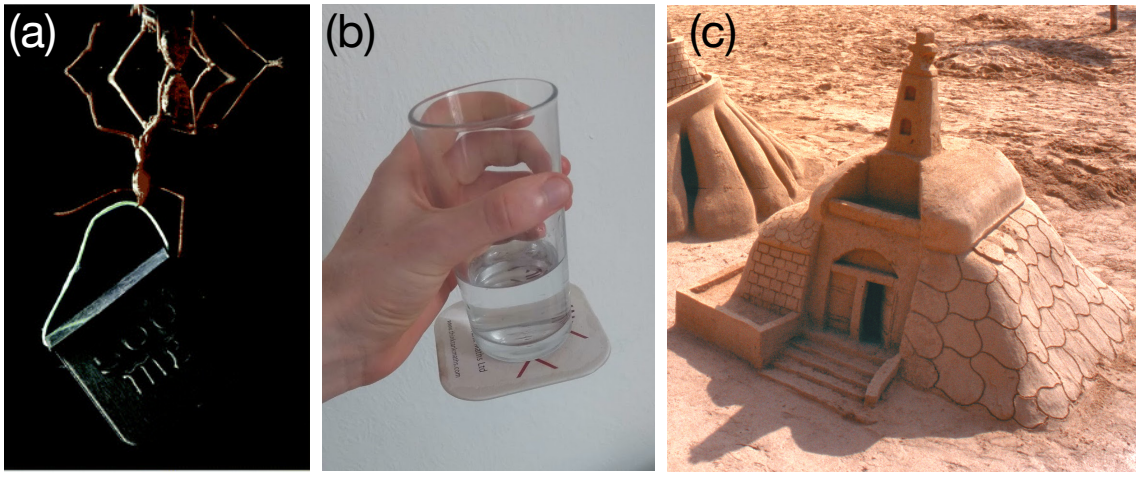

Figure 1.1: Examples of capillary adhesion. (a) An Asian weaver ant holds onto a 500mg mass while remaining adhered to a glass substrate. The mass is over 100 times the ant's bodyweight. Reproduced from Dirks and Federle [2011a] with permission from The Royal Society of Chemistry. (b) A coaster may remain attached to the base of a glass as it is lifted up due to condensation or spillage wetting the base. (c) A sandcastle can remain standing because the grains are adhered by small amounts of intervening water. Photo courtesy of Jim Jamieson.

been mathematically modelled: Slater et al. [2014] considered the stability and rupture of an array of adhesive bridges when a beetle is under attack by a group of ants, while Gernay et al. [2016] and Gilet et al. [2018] have considered the effect of bending of the hairs on the capillary adhesion of beetles.

Modelling of the capillary adhesion of smooth-padded insects, however, still remains fairly basic, often focusing on static configurations of fluid bridges between rigid surfaces such as spheres or planes [Dirks, 2014, Butt and Kappl, 2009]. Quantifying this underlying mechanism gives plausible values of the observed normal adhesive strength, but adhesion also persists when walking up a vertical wall and hence capillary adhesion must resist shear. Moreover, detachment requires the bridging fluid to be de-stabilized [Lowry and Steen, 1995, Macner and Steen, 2014] and, if performed dynamically, can lead to large resistive viscous forces [Bikerman, 1968].

While it is believed that many insects use the surface tension of a liquid to achieve their adhesion [Dirks, 2014], many questions remain: why do some insects have deformable footpads [Gorb et al., 2000]? Why does the fluid secretion appear to be a water-in-oil emulsion [Dirks et al., 2010]? How are the insects able to withstand such strong shear forces [Federle et al., 2004, Clemente et al., 2009]? And how do insects control capillary adhesion [Federle and Labonte, 2019]?

Further examples of capillary adhesion

Beyond insects, there are many other instances in nature of organisms using surface tension for some form of adhesion. One such example is tree frogs, which are believed to use a similar mechanism to insects when adhering to (and moving about on) surfaces in a range of climatic conditions [Persson, 2007, Barnes et al., 2011, Tulchinsky and Gat, 2015]. Other organisms need to adhere for much longer times, such as the underwater adhesion of mussels and some types of bacteria [Nyarko et al., 2016]. The sticky projectile tongue of a chameleon [Kreitschitz et al., 2015], and the glue-like droplets on some spiders' webs [Guo et al., 2019], help these predators to catch — and hold onto — their passing prey. Fluid-based adhesion is also used by plants and insects to transport important materials: flax plants are able to spread their seeds when they become stuck to passing animal hides due to a viscous seed coating [Brau et al., 2016] and bees use a sugary secretion to collect pollen to bring back to their hives [Shin et al., 2019]. In many of these examples, capillary adhesion can be assisted by the viscosity of the adhering fluid that resists dynamic separation of two surfaces.

Traditional methods of adhesion include glues, welds and claws, but recent scientific study has opened up new avenues for man-made adhesives based on those observed in nature; these are called bio-inspired adhesives. There has been much interest in the adhesive abilities of geckos, which are believed to adhere using van der Waals forces [Autumn et al., 2002]. Examples of new gecko-inspired devices include: a soft pressure-controlled pad that can deform to grasp complex surfaces [Song et al., 2017], a robotic gripper for use in capturing space-debris [Jiang et al., 2017], and 'Gecko tape' [Geim et al., 2003, Gorb et al., 2007]. Other organisms have been studied as a means to develop new bio-inspired adhesives, for example an octopus-inspired patch that uses suction to adhere underwater [Baik et al., 2017] and a snail-inspired hydrogel adhesive [Cho et al., 2019]. One example of an adhesive design inspired by insects is the switchable rigid capillary adhesive device of Vogel and Steen [2010], but there is still significant potential for further development in the area of bio-inspired capillary adhesion.

The ability to attach two surfaces (and subsequently detach them) under an applied load is also important in many commonplace and industrial situations, and capillary adhesion is prevalent in these settings as well. In everyday life, the condensation on the outside of a glass of a cold drink may cause a coaster to remain attached to the bottom of the glass as it is lifted (see fig. 1.1b), while the grains in a sandcastle (such as the one pictured in fig. 1.1c) stick together best at a particular volume fraction of liquid [Halsey and Levine, 1998, Pakpour et al., 2012]. Similar processes are important in understanding the cohesion of soil [Haines, 1925, Fisher, 1926, Middleton and Wilcock, 1994]. The

presence of capillary bridges can be problematic in technological applications, such as in the stiction of magnetic storage discs [Mate, 1992, Gao and Bhushan, 1995] and also during the production of micro-electro-mechanical devices (MEMS) [Tanaka et al., 1993, Mastrangelo and Hsu, 1993]. However, it can also be beneficial, helping to form nano-scale structured assemblies during the drying of pre-wetted nanotube forests [Chakrapani et al., 2004, Pokroy et al., 2009, de Volder and Hart, 2013].

The wide range of scenarios in which surface tension plays a key role in adhesion highlights its importance; the focus of this thesis is to use mathematical modelling to investigate capillary adhesion, inspired in part by the innate climbing abilities of insects. A particular focus of this work is to understand how modifications of existing basic models affect predictions of the adhesion force. The hope is that this modelling approach helps to improve the current understanding of capillary adhesion, inspire new adhesive technologies and answer some of the unresolved questions already mentioned in this introduction.

First, however, we begin with an overview of the physics and mathematics of surface tension that will be used throughout this thesis; we will present some basic models of capillary adhesion that will be useful for comparison with the later results.

1.2 Surface tension

A recurring theme throughout this thesis is the action of surface tension, or capillary effects. In this section, the key concepts are explained and we consider some basic scenarios in which surface tension applies an attractive, or adhesive, force between two solid surfaces. Throughout the rest of the thesis we will compare our results to these basic cases, and so they are presented in some detail here.

Surface tension occurs at the interface between two immiscible fluids, and many of its physical properties have been well understood since at least the early 19th century [Young, 1805, Laplace, 1806]. At a molecular scale, the molecules of one fluid have a preference for being next to other molecules of the same kind because there is a higher energetic cost to having differing neighbouring molecules. The overall effect is that, at the interface between the two substances, the molecular-scale attraction between same-fluid molecules causes a macroscopic tension, γ, along the interface. Alternatively, there is an energetic cost per unit area, γ, to increasing the area of the interface. The property γ is called the surface tension, and its value depends on the chemistry of the two fluids (as well as environmental conditions such as temperature). In general, surface tension can vary spatially — for example if a surfactant, such as soap, is present — but in this thesis it will always be uniform along the interface.

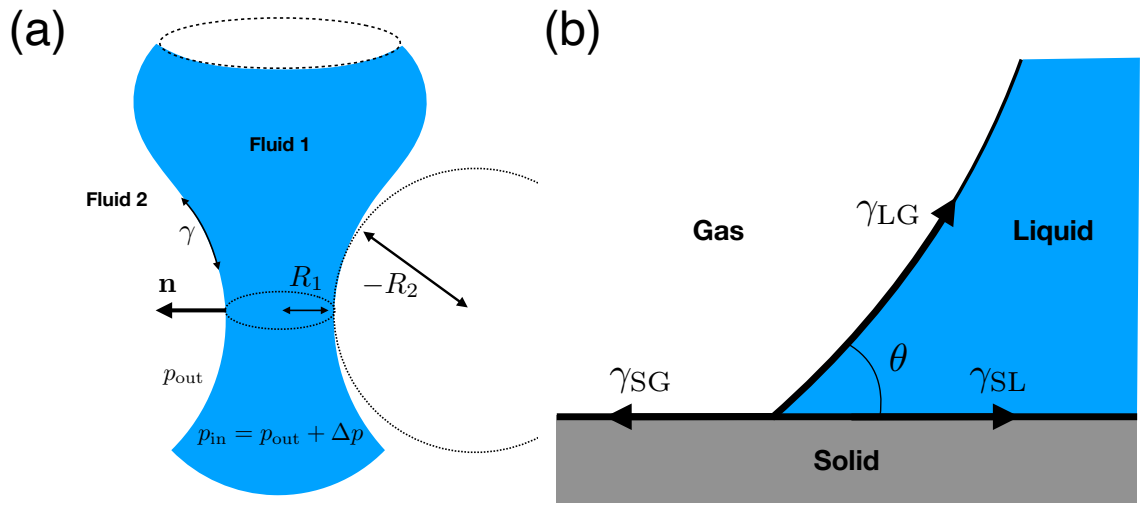

Figure 1.2: (a) An interface between two fluids with normal $\mathbf{n}$ has a surface tension γ. The radii of curvature $R_{1,2}$ are defined to be positive if the normal $\mathbf{n}$ to the interface points out of the circle. (b) An interface meets a solid surface at a contact angle θ that is given by the Young-Dupré equation (1.3). This equation can be viewed as a force balance (parallel to the solid surface) between the surface tensions $\gamma_{\text{SG}}, \gamma_{\text{SL}}, \gamma_{\text{LG}}$ of each interface.

At an interface between two immiscible fluids, a force balance on the interface shows that, in the presence of surface tension, there is a jump in the normal component of the fluid stress that is proportional to the curvature of the interface, with proportionality constant γ [see, for example, Bush, 2011], i.e.

$$[\sigma \cdot \mathbf{n}]^{+}_{-} = \gamma \kappa \mathbf{n}. \tag{1.1}$$

Here $\sigma = -p\mathbb{I} + \mu[\nabla \mathbf{u} + (\nabla \mathbf{u})^{\top}]$ is the stress tensor for a Newtonian fluid with pressure p, velocity $\mathbf{u}$ and dynamic viscosity μ; $\mathbf{n}$ is the normal to the interface (pointing into the $+$ fluid) and $\kappa = \nabla \cdot \mathbf{n}$ is the (mean) curvature of the interface.

1.2.1 Capillary statics

For a static fluid, the surface tension simply causes a jump in the pressure across the interface

$$\Delta p = \gamma \kappa = \gamma \left(\frac{1}{R_1} + \frac{1}{R_2} \right), \tag{1.2}$$

where $\Delta p = p_{\text{in}} - p_{\text{out}}$ is the pressure jump and $R_{1,2}$ are the (signed) principal radii of curvature of the interface (see fig. 1.2a). This equation for the pressure jump due to surface tension is called the Young-Laplace equation [Young, 1805, Laplace, 1806]. Note that the pressure is higher on the side that the surface curves towards — spherical bubbles and droplets are at a higher pressure than their surroundings.

In these static scenarios, there is no fluid flow and hence no pressure gradient within each fluid. Provided that the external pressure is constant, the interface must then be a surface of constant curvature, such as a section of a sphere, catenoid or nodoid.

When a fluid-fluid interface in equilibrium meets a rigid and solid surface, it intersects the surface at an angle θ, which is called the contact angle. An example of this is shown in fig. 1.2b. The contact angle indicates which of the two fluids prefers to wet the solid surface (and to what degree): the fluid on the side with a smaller angle preferably coats the solid. If $\theta < \pi/2$ then the fluid is called wetting, and if $\theta > \pi/2$ then it is called non-wetting.

The equilibrium contact angle θ depends on the chemistries of the three media. In energetic terms, the surface energy γ_{12} is the energetic cost to increase the area of an interface between substance 1 and substance 2 by a unit area. An energy minimisation near the contact line between a solid, liquid and gas (denoted by S, L and G respectively) then gives the Young-Dupré equation [de Gennes et al., 2004]

$$\cos\theta = \frac{\gamma_{\mathsf{SG}} - \gamma_{\mathsf{SL}}}{\gamma_{\mathsf{LG}}}. \tag{1.3}$$

Since the γ_i can also be considered as tension forces acting at the interface (with $\gamma_{\mathsf{LG}} = \gamma$), with units of a force per unit length, the Young-Dupré equation can be interpreted as a horizontal force balance of the three tensions acting at the contact line. In general, static contact angles can vary between advancing and receding angles due to contact angle hysteresis, but throughout this thesis we ignore this effect and suppose that the static contact angle is always given by the value in (1.3).

In this thesis, we will be particularly interested in scenarios involving a droplet joining two solid surfaces (such as that illustrated in fig. 1.4 between two plates) — a capillary bridge. This bridge applies adhesive capillary forces on the two surfaces, pulling the solids towards each other. For simplicity, the fluid in the capillary bridge will be referred to as a liquid and the bridge is a 'liquid bridge', whilst the surrounding ambient fluid will often be called a gas. In general, however, the same models hold for a more general liquid–fluid system (e.g. if the external fluid is also a liquid), although often the properties of the ambient surrounding fluid will be neglected.

1.2.2 Capillary dynamics

For flows involving surface tension, the interfacial condition (1.1) couples the internal stresses of each fluid through the shape of the interface that separates them. In general this is more complicated than the Young-Laplace equation (1.2) for the fluid pressure

because it also includes terms to account for viscous stresses. However, even though the Young-Laplace equation is primarily a static condition, it is valid in some dynamic scenarios as well; for this thesis, it is important to consider the case when there is fluid flow in a thin film between solid surfaces, such as a short and wide liquid bridge. Then (provided that the liquid is sufficiently viscous that the reduced Reynolds number is small) the lubrication approximation may be used, which means that the fluid pressure does not vary significantly between the solids, only along them. For capillary bridges, the liquid-gas interface spans the narrow gap and the normal stress is dominated by the pressure; the condition (1.1) reduces to a simple (local) pressure jump and the Young-Laplace equation (1.2) holds at each point on the interface (even though the liquid pressure is not uniform).

Additionally, how a contact line behaves dynamically is still an active area of research [e.g. Shi et al., 2018, Barrio-Zhang et al., 2020]; in the dynamic models that follow we shall take one of the simplest models for the dynamics of a contact line and assume that the bridge contact line is mobile so that bridge motion occurs at constant contact angle without pinning. Since contact angle hysteresis is neglected, this dynamic contact angle shall be considered to be the static angle given by the Young-Dupré equation (1.3). This constant contact angle motion is reasonable provided that the liquid motion is relatively slow [see eqn. 7 of Snoeijer and Andreotti, 2013, for example].

Another dynamical capillary effect that will be important throughout this thesis is the spontaneous migration of liquid bridges in a sloping geometry. We turn to consider this now, before moving on to the main focus of the thesis: capillary adhesion.

Capillary migration of liquid bridges

Surface tension is well-known to induce fluid motion in a range of different scenarios. In some situations, this capillary motion may be due to gradients in the surface tension itself, which are called Marangoni flows [Scriven and Sternling, 1960]. However, flow can also be generated without surface tension gradients because of gradients in the surrounding environment, for example the motion of droplets on a surface due to gradients in the softness of the substrates, called durotaxis [Style et al., 2013], or the spontaneous motion of droplets on cones due to gradients in substrate curvature [Lv et al., 2014, McCarthy et al., 2019, Chan et al., 2020, 2021].

Perhaps the simplest way to generate spontaneous motion in a liquid bridge is to place it in a tapered channel (a similar mechanism will be important at various points throughout this thesis). Consider a liquid bridge confined between two solid surfaces that are *not* parallel, but instead slope towards one another in some direction, as shown in fig. 1.3. Note that the bridge's free surface is more curved at the narrower end since it

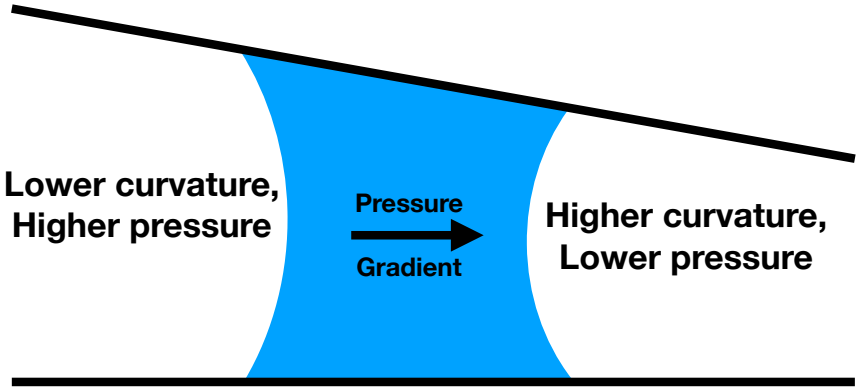

Figure 1.3: A wetting liquid bridge between non-parallel plates will migrate towards the narrower end due to differences in capillary pressure at each edge. (Note that the pressure here refers to the pressure just inside the liquid bridge).

has to approach the solids at the same contact angle as the other end, whilst in a narrower gap. If the liquid is wetting, $\theta < \pi/2$, then this curvature is more negative: the pressure inside the bridge is lower at the narrower end, generating a flow of liquid towards the narrow gap. For non-wetting liquids, the pressure is higher at the narrower end and the flow is out of the gap[1]. (This can also be understood energetically: wetting liquids seek to cover as much of the surfaces as possible and must migrate to the narrower region to do so; the converse is true for non-wetting liquids, which seek to minimize their contact with the surfaces.)

This geometry-induced capillary flow was first observed by Hauksbee [1710], and has been studied quantitatively recently via simulations [Concus and Finn, 1998, Ruiz-Gutiérrez et al., 2018, Ruiz-Gutiérrez and Ledesma-Aguilar, 2020] and experimentally [Renvoisé et al., 2009, Reyssat, 2014, Bradley et al., 2019].

This mechanism for motion of a liquid bridge is entirely generated by the combination of surface tension and local geometry, and can result in the bridge moving to local extrema in the gap separation. As we shall see later, this can be an important factor in increasing the capillary adhesion force: as the bridges become more confined they have a higher capillary pressure jump (since they are in a narrower gap) that acts over a larger area.

[1]Equilibria of liquid bridges *are* possible between sloping surfaces, provided they are sufficiently non-wetting and dependent on the wedge angle [Concus and Finn, 1998, Concus et al., 2001, Ruiz-Gutiérrez et al., 2018].

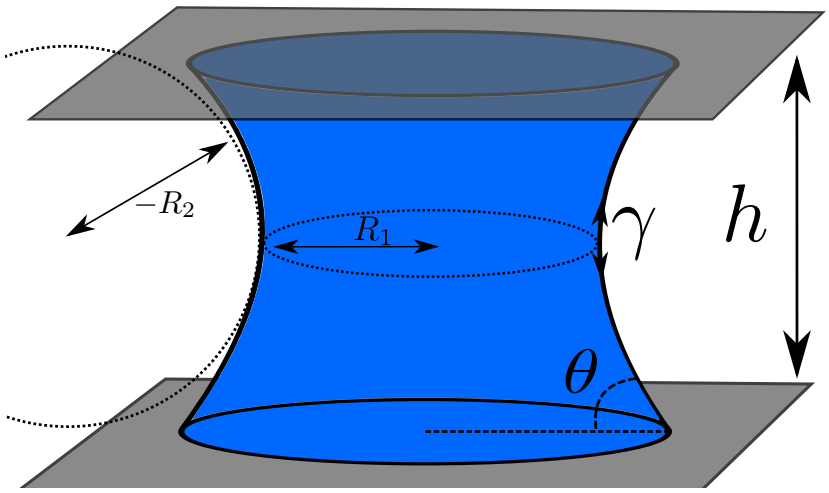

Figure 1.4: A liquid bridge of volume V and surface tension γ sits between two parallel, rigid plates that are separated by a distance h. In equilibrium the free surface has a constant curvature $\kappa = 1/R_1 + 1/R_2$ (note that $R_2 < 0$) and intersects the solid surfaces at a contact angle θ.

1.3 Basic capillary adhesion

The main focus of this thesis is to investigate the forces, particularly the adhesion forces, that can be generated by surface tension when a liquid droplet is confined between two surfaces to form a liquid bridge. These capillary forces can be substantial, particularly at microscopic scales [Lambert, 2013] where surface tension forces (which scale with length) dominate volume forces (which scale with length cubed) such as gravity. We shall focus on cases where gravity is negligible, which corresponds to small enough lengthscales; in particular, the gap width h between the solids must be much smaller than the capillary length $l_c = \sqrt{\gamma/\rho g}$ (ρ being the liquid density and g the acceleration due to gravity), so that the Bond number $\mathrm{Bo} = \rho g h^2/\gamma \ll 1$.

The surface tension of a liquid–gas interface acts in two distinct ways to apply an adhesion force. Firstly, there is a contribution from the capillary pressure difference, Δp, between the liquid and surrounding gas. If the pressure in the gas is uniform then the resulting force on the solid surface (often called the Laplace pressure force) is $\int \Delta p\, \mathbf{n}\, \mathrm{d}A$, where the integral is taken over the wetted surface area of the solid and $\mathbf{n}$ is the outward normal to the solid. For a planar surface and a liquid bridge in equilibrium (i.e. $\Delta p =$ constant), the normal component of the force simplifies to $F_P = \Delta p \times A$ for a wetted area A.

The second component of the capillary adhesion force is caused by the surface tension

pulling parallel to the interface along the contact line: $\int \gamma \mathbf{t}\ \mathrm{d}s$, where the integral is around the curve along which the liquid–gas interface meets the solid and $\mathbf{t}$ is the tangent to the interface there. The component of this force acting normal to a planar surface is $F_T = \gamma \sin\theta \times l$ where l is the length, or perimeter, of the contact line.

These forces are straightforward to determine once the shape of a bridge is known. However, the details of capillary bridge shape are quite involved for general bridge sizes and depend sensitively on the geometry of the confining surfaces — the bridge shapes (and hence the adhesion forces) between two plates and between two spheres differ. We will now consider previous results for the adhesion force in some specific geometries, and examine the commonly made approximations in calculating the adhesion force.

1.3.1 Plate-plate adhesion

To understand the capillary force in the various systems considered in this thesis, it will be helpful to have a basic case for comparison: consider two parallel, rigid plates that are separated by a distance h, as shown in fig. 1.4. Between these two plates is a liquid bridge of volume V. The liquid–gas interface (sometimes referred to as the meniscus) has a surface tension γ and meets each of the solid surfaces at a contact angle θ.

When a liquid bridge is confined between two planar surfaces and has a circular wetting footprint, the total capillary force pulling on one of these plates is the sum of the contributions from the Laplace pressure and tension

$$F = F_P + F_T = -\gamma\kappa\pi r^2 + 2\pi r\gamma \sin\theta, \tag{1.4}$$

where r is the radius of the wetted area and κ the curvature of the free surface (for a normal pointing outwards from the liquid). Note that the sign of the force has been chosen so that a positive force corresponds to an attractive, or adhesive, force. This sign convention for the normal, adhesion force shall be taken throughout the rest of this thesis.

Wide, short bridges — the pancake solution

If the plates are brought very close together, so that the bridge radius r is large compared to its height, $r \gg h$, then the radius of curvature of the interface in the direction between the plates ($R_1 \sim h$) is much smaller than that around the bridge ($R_2 \sim r$) and the shape of the interface can be approximated as an arc of a circle [Fisher, 1926, Meurisse and Querry, 2006, Cai and Bhushan, 2008]. The curvature of the free surface is then approximately inversely proportional to the plate separation

$$\kappa \approx -\frac{2\cos\theta}{h}. \tag{1.5}$$

Note that if the contact angles differ on each surface, then the $\cos\theta$ term can be replaced by the average of the cosines: $\overline{\cos\theta} = (\cos\theta_1 + \cos\theta_2)/2$. Additionally, because the variation in bridge radius due to the curvature of the meniscus is small compared to the bridge radius itself, the bridge volume can be approximated by assuming it is cylindrical, i.e. $V \approx \pi r^2 h$.

In this limit, the tension force applied around the wetted perimeter ($\propto r \times \gamma \sin\theta$) is negligible compared to the Laplace pressure force ($\propto r^2 \times \gamma\cos\theta/h$) provided that the liquid is sufficiently wetting that $\tan\theta \ll r/h$. Combining these simplifications, when the bridge is sufficiently wide and short, the leading order expression for the adhesion force is

$$F_{\text{pancake}} = \frac{2\bar{\gamma}V}{h^2}, \tag{1.6}$$

where $\bar{\gamma} = \gamma\cos\theta$ (or, when the contact angles on each plate differ, $\bar{\gamma} = \gamma\overline{\cos\theta}$).

When the plates are close together, we discover a simple relation for adhesion: the force obeys an inverse square law with the plate separation when $r/h \gg 1$ (or alternatively $V/h^3 \gg 1$). In this limit, a simple method to increase the adhesion force is to bring the surfaces closer together. In addition, note that the force is proportional to the liquid volume so that bridges with a larger volume have a larger adhesion force. Equation (1.6) is referred to as the 'pancake solution' since it is valid when the bridge is wide and thin, reminiscent of the shape of a pancake.

An exact solution

An exact analytical solution for the bridge shape and its capillary adhesion force when a liquid bridge is confined between two rigid, parallel plates was found by Carter [1988]. This solution is parametric with parameter $m \in [-\sec\theta, 0]$ and, for given m and contact angle θ, gives the constant curvature of the interface $\kappa(m,\theta)$ and the plate separation $h(m,\theta)$ by

$$V\kappa^3 = -2\pi\left[4\left(\cos\theta - \frac{\cos^3\theta}{3}\right) + \frac{1-m^2}{m^2}\cos\theta + 4mQ + \frac{3(1-m^2)}{m}S\right], \tag{1.7}$$

$$\frac{h}{V^{1/3}} = \frac{-2(\cos\theta + mS)}{V^{1/3}\kappa}, \tag{1.8}$$

where the functions $Q(m,\theta), S(m,\theta)$ are defined by the integrals

$$Q = \int_\theta^{\frac{\pi}{2}} \frac{\sin^4 x}{\sqrt{1-m^2\cos^2 x}}\,\mathrm{d}x, \quad S = \int_\theta^{\frac{\pi}{2}} \frac{\sin^2 x}{\sqrt{1-m^2\cos^2 x}}\,\mathrm{d}x. \tag{1.9}$$

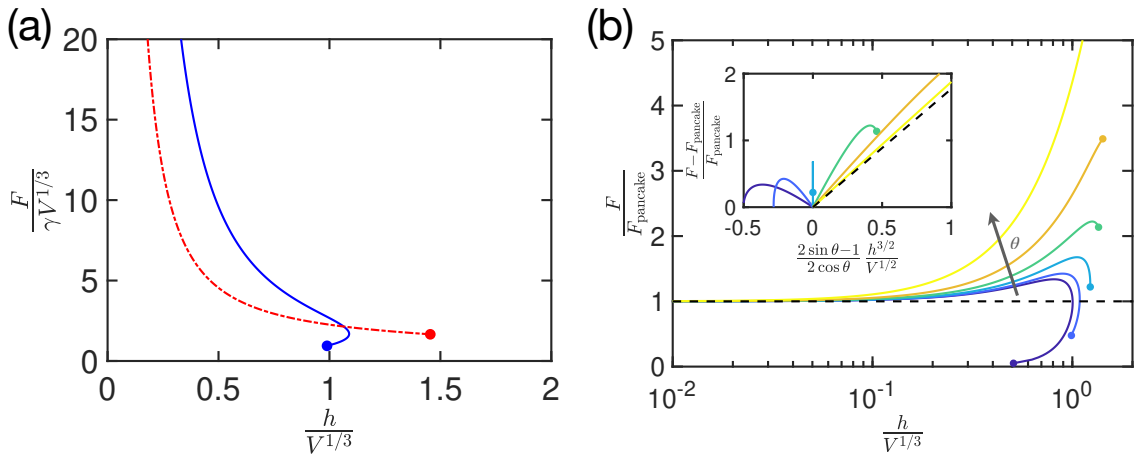

Figure 1.5: (a) Examples of the adhesion force, F, as a function of the plate separation h, calculated using the solution of Carter [1988], eqns. (1.7)–(1.10), for contact angles $\theta = 15°$(blue solid curve) and $\theta = 75°$ (red dot-dashed curve). (b) A comparison of the exact solution for the adhesion force, F, to the approximate solution when the liquid bridge is short and wide, F_{pancake} given by (1.6) for contact angles $\theta = \{0°, 15°, 30°, 45°, 60°, 75°\}$ (arrow denotes increasing θ). Inset: The correction to the adhesion force does not appear to be well-approximated by (1.11) (black dashed line). Note that in all cases the curves end abruptly at some finite plate separation (denoted by solid circles); the solutions cease to exist at these points.

The adhesion force applied by the capillary bridge to the plates (including both the pressure and tension components) is calculated to be

$$F(m,\theta) = \frac{\pi\gamma}{\kappa(m,\theta)}(1 - m^{-2}). \tag{1.10}$$

Fixing the contact angle θ and varying m in the interval $[-\sec\theta, 0]$ sweeps out the force–displacement curve for any given contact angle. Solutions for contact angles $\theta = 15°, 75°$ are shown in fig. 1.5a. Note that the force-displacement curves terminate when $m = -\sec\theta$, which occurs at a finite plate separation, $h/V^{1/3}$, illustrated by filled circles.

Comparison between asymptotic and exact solutions

From the asymptotic solution for a wetting pancake bridge, (1.6), the adhesion force is expected to follow an inverse square law with the plate separation h as $h/V^{1/3} \to 0$. To verify this, fig. 1.5b shows the adhesion force calculated from the integral solutions (1.7)–(1.10) derived by Carter [1988] compared to the pancake solution (1.6) for various different wetting contact angles (i.e. $\theta < \pi/2$).

As expected, the adhesion force does indeed agree well with the asymptotic theory when the plate separation is small: $F \approx F_{\text{pancake}}$ for $h/V^{1/3} \ll 1$. In particular, when $h/V^{1/3} < 0.1$, the more wetting liquids ($\theta \leq 60^\circ$) have an adhesion force that is within 10% of the prediction of (1.6). At larger plate separations than this, the adhesion force is generally underestimated by (1.6), which gives better predictions for more wetting liquids. When the separation becomes too large — for $h/V^{1/3} \gtrsim 1$ — there is no longer any equilibrium solution; this cannot be predicted by the pancake approximation (1.6).

In deriving (1.6), the force applied by surface tension at the contact line was ignored, as was the azimuthal curvature of the bridge. The tension force, $F_T = 2\pi\gamma r \sin\theta$, and the azimuthal correction to the pressure force, are both approximately one bridge aspect ratio smaller in magnitude than the leading order pressure force, and so should become more important as the plates are separated and the bridge becomes taller and narrower. In addition, the tension force is expected to have a stronger effect on liquids with contact angles closer to $\theta = \pi/2$ due to the factor $\sin\theta$. These effects are both consistent with the discrepancy between the analytical and asymptotic results observed in fig. 1.5b. A naive correction to the pancake solution may therefore be to approximate the pressure jump by $\Delta p \approx \gamma(-2\cos\theta/h + 1/r)$ and add the tension force around the perimeter, giving $F \approx F_{\text{pancake}} - \gamma\pi r + F_T$. This can be rearranged (again, using $V \approx \pi r^2 h$) to give

$$\frac{F}{F_{\text{pancake}}} \approx 1 + \sqrt{\pi}\,\frac{2\sin\theta - 1}{2\cos\theta}\left(\frac{h}{V^{1/3}}\right)^{3/2}. \tag{1.11}$$

Approximations like this that simply add the tension force and approximate the second component of the curvature by $1/r$ are used in the adhesion literature [e.g. Dirks, 2014, Labonte and Federle, 2015]. However, plotting the error in F/F_{pancake} as a function of $\sqrt{h^3/V}$ (see the inset to fig. 1.5b) shows that the predictions of eqn. (1.11) are not borne out by the analytical solution. In particular, (1.11) would suggest that the difference between the exact and asymptotic solutions should follow the dashed line in the inset of fig. 1.5b, but this is only observed as $\theta \to \pi/2$, and (1.11) even gets the wrong sign of the correction for $\theta < \pi/6$. The curves in this inset do appear to initially behave linearly but with the wrong slope, suggesting that the correction is of order $\sqrt{h^3/V}$ but that the θ dependence in (1.11) is not correct. At the order of the correction, the details of the bridge shape are more complex than suggested by (1.11) — the principle radii of curvature of the free surface are not in fact $h/(2\cos\theta)$ and r [see Reyssat, 2015, for example]. As a result, care must be taken when calculating solutions for bridges that are not wide and thin, with $h/V^{1/3} \gtrsim 0.1$ being a rule of thumb for when more detailed analysis is required.

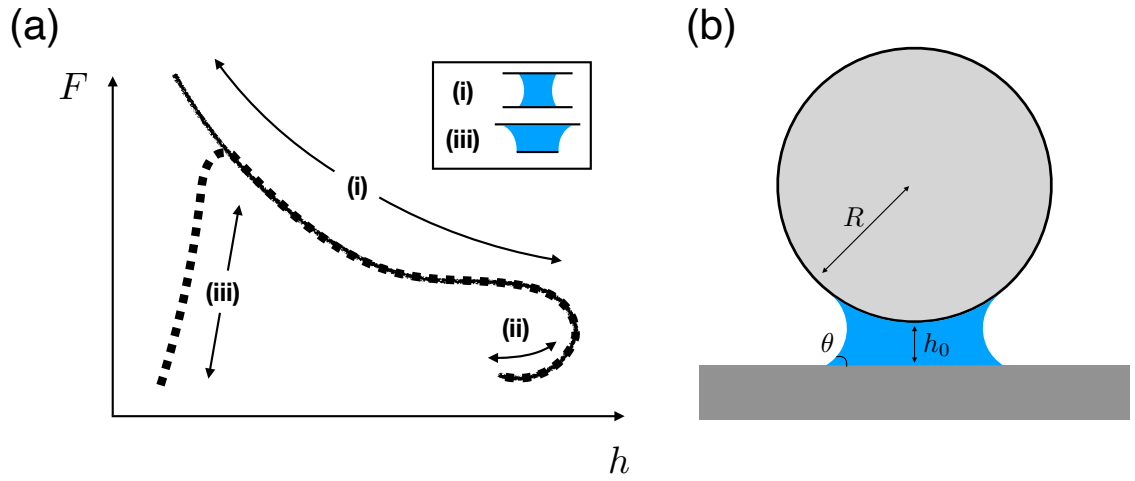

Figure 1.6: (a) A schematic force-displacement diagram that may become pinned to the plate edges. The solid curve shows the behaviour with fixed contact angle, as described in §1.3.1. The dashed curve shows the behaviour for a pinned contact line [see e.g. Slater et al., 2014]. Along these solutions, the branch (i) is stable to height-controlled perturbations but unstable to force-controlled perturbations (see §1.3.3), (ii) is unstable to both, and (iii) is stable to both. Inset: an illustration of the bridge shapes on branches (i) and (iii). (b) A rigid sphere of radius R is adhered to a planar substrate by the surface tension of a liquid bridge. The plane and sphere are separated by a minimum separation h_0.

1.3.2 Other geometries

So far in this introduction to capillary adhesion, we have focused on the adhesion of two infinite plates (or, at least, plates that are much wider than the bridge). However, the adhesion of plates of finite length, or surfaces that are not perfectly flat is also of interest. Here, we will highlight some of the differences that arise in such situations.

When considering the adhesion of finite parallel plates, it is important to know whether the bridge has reached the edge of the plate or not. If the triple contact line between the solid, liquid and gas reaches the edge of a plate, then it is no longer possible to use the Young-Dupré equation (1.3) for the contact angle. Instead, the meniscus may be pinned at the corner, so that the radius of the wetted region is fixed, with the contact angle varying to accommodate any further changes (see inset (iii) of fig. 1.6a)[2]. A similar effect may be observed before the edge is reached, if the contact line becomes pinned due to small-scale roughness or impurities.

When pinning has occurred (on one or both plates), the adhesion force does not follow the inverse square law (1.6) as the plate separation is further reduced. When bringing

[2]Although the macroscopic contact angle may appear to vary, at a microscopic scale the contact angle can still satisfy the Young-Dupré equation [see, for example, fig. 3 in Mansfield et al., 1997].

the plates closer together, the Laplace pressure force decreases, becoming repulsive and eventually exceeding the adhering tension force; at very small separations the total capillary force is repulsive as the liquid bridge bulges out [Macner and Steen, 2014, Slater et al., 2014]. A maximum adhesion force is obtained when the meniscus just begins to unpin from the plate edge (after which it behaves like the fixed contact angle case). The typical behaviour is illustrated in fig. 1.6a, alongside the fixed contact angle case for comparison. Note that in an experiment that experiences some degree of pinning before the bridge reaches the plate edge, a composite of these results may be obtained as the contact line changes between being fixed and mobile.

In addition to solutions for bridges between parallel plates, there are many studies that have considered adhering bridges in more complex geometries [e.g. Butt and Kappl, 2009]. One commonly studied geometry is the adhesion of spheres [Mason and Clark, 1965, Heady and Cahn, 1970, Pitois et al., 2000, Willett et al., 2000, Wang et al., 2017] because capillary forces are believed to play an important role in adhering grains such as sand and soil [Haines, 1925, Fisher, 1926, Halsey and Levine, 1998]. Similar to the Carter [1988] solution for two plates outlined in §1.3.1, there are known analytic solutions for the bridge shape in sphere-plate [Orr et al., 1975] and sphere-sphere geometries [Melrose, 1966].

For a simple solution to the capillary adhesion of a sphere to a plate in the same spirit as the pancake approximation, consider a sphere of radius R adhered to a plane by a liquid bridge, as shown in fig. 1.6b. Suppose that the bridge is small compared to the size of the sphere, so that locally the separation appears parabolic, $h(r) \approx h_0 + r^2/2R$, with r the radial coordinate in the plane of the plate and h_0 the minimum distance between the sphere and plate. If the meniscus of the bridge is at $r = r_M \gg h(r_M)$ then the curvature of the meniscus will be $\kappa \approx -2\cos\theta/h(r_M)$, where the effect of the slope of the sphere on the contact angle has been ignored since $r_M/R \ll 1$. The force, when dominated by the Laplace pressure $F = -\Delta p \times A = -\gamma\kappa \times \pi r_M^2$, can then be approximated by [Fisher and Israelachvili, 1981, Cai and Bhushan, 2008]

$$F_{\text{sphere}} \approx 4\pi\bar{\gamma}R\frac{r_M^2}{r_M^2 + 2Rh_0}, \tag{1.12}$$

where the meniscus position, r_M can be determined from the fixed volume constraint, $V \approx \pi r_M^2(h_0 + r_M^2/4R)$. Note that when the sphere and plate are in contact ($h_0 = 0$) this reduces to

$$F_{\text{sphere}} \approx 4\pi\bar{\gamma}R \tag{1.13}$$

which also holds whenever the sphere is very close to contact, $r_M/\sqrt{h_0 R} \gg 1$. Surprisingly, in this case the adhesion force is independent of the bridge volume, depending

only on the interfacial properties γ, θ (recalling $\bar{\gamma} = \gamma\overline{\cos\theta}$) and the sphere radius R. Similar expressions are found when two spheres of radius R_1 and R_2 are adhered, with the sphere radius in (1.13) replaced using $1/R = 1/R_1 + 1/R_2$ [see Butt and Kappl, 2009, for example].

1.3.3 Stability, and the difference between force- and height-control

Having obtained equilibrium solutions for the shape of a liquid bridge between two solid surfaces, it is not clear whether these solutions will be observed in reality — it is also important to consider the stability of the different solutions. Here, we consider an overview of some important stability results that will be useful for the rest of the thesis; more detail can be found in the review article of Bostwick and Steen [2015], for example.

There are two main physically-distinct situations when considering deviations from equilibrium of a liquid bridge. In the first scenario, the position of the surfaces may be controlled and the shape of the bridge evolves appropriately within the given geometry. This shall be referred to as 'height-control', as often this problem reduces to simply controlling the separation between the two solid surfaces and studying perturbations in a fixed geometry. Alternatively, the load applied to the solids is controlled and the positions of the solid surfaces adjust according to the forces exerted on them. This is 'force-control', with perturbations conducted with fixed applied load. In this thesis the focus will often be on height-control, which may be appropriate in certain adhesion scenarios, such as during the initial stages of approach in adhesion or perhaps when solid-solid contact occurs far from the liquid which is left to bridge a gap of fixed height. Force-control is appropriate in many other scenarios. It will be useful to keep the difference between these two types of adhesion control in mind in the rest of this thesis [see Slater et al., 2014, for an example of the differences].

Consider the equilibrium solutions for a bridge between the two parallel plates from §1.3.1. These solutions show some interesting behaviour (see fig. 1.5, or the sketch in fig. 1.6a): in particular, folds (saddle-node bifurcations) are present in the solution space, particularly when the contact angles are small and the liquid wets the plates.

One might therefore expect that a subset of these branches are stable, with stability being lost or gained through these folds; the stability may also be dependent on whether the system is height- or force-controlled. The force-control case will be investigated in more detail in Chapter 5, but the important distinction shall be outlined here with reference to the branches shown in fig. 1.6a. When controlling the plate separation (height-control), the branch of solutions — labelled (i) — in which the behaviour of the force is close to

the inverse square law (1.6) is (linearly) stable to small perturbations, while the branch beyond the fold (ii) is unstable. Starting from a stable equilibrium solution with small separation h, we can consider increasing the separation and following the curve of stable solutions. For small contact angles, as the separation is increased, a fold is reached; beyond this there is no longer an equilibrium solution and any bridge would rupture. For larger contact angles (see fig. 1.5) — above approximately 30° [Carter, 1988] — there is no fold, but again there is eventually no longer any equilibrium solution; once past the maximal separation the bridge must rupture, for example via the Rayleigh-Plateau instability [Rayleigh, 1878].

Conversely, in the force-control scenario, there is *no* stable solution for any finite separation h and any perturbation will result in the plates either being pulled together into contact or moving apart from one another and ultimately detaching [Ward, 2011]. This instability in the force-controlled case can be understood by considering what happens to a small perturbation of the plates together or apart. If the plates are perturbed towards each other from an equilibrium solution with a given load, then the separation at the meniscus is reduced, increasing the magnitude of the capillary pressure (since it is approximately $\Delta p \sim 1/h$) and spreading the bridge footprint over a larger area as it is compressed. This results in an increase in the capillary force; the adhesive capillary force is now stronger than the applied load and pulls the plates together. In the opposite scenario, where the plates are perturbed apart, the capillary force decreases and so it can no longer support the applied load as the curvature and wetting area decrease, and so the plates separate.

These stability results are similar in other situations and geometries, perhaps with small differences. For example, the curves will vary as the Bond number is increased and gravity becomes more important [see Lowry and Steen, 1995, for example], and in the pinned contact line scenario, the solution at small separations is stable under perturbations in both height- and force-control [Slater et al., 2014] — this branch of solutions is labelled (iii) in fig. 1.6a. More detailed analyses of the stability of pinned bridges between discs can be found in Meseguer [1984] or Lowry and Steen [1995], for example.

1.4 Thesis overview

In this thesis, a variety of mathematical models of aspects of capillary adhesion are presented. In Chapter 2, we investigate how the capillary adhesion force is affected by dividing a given volume of liquid into many bridges. The focus is on quantifying whether the total adhesion force increases as the liquid is split into many smaller bridges when one of the

solid surfaces is rough. We also consider the effect of roughness on the resistance to shear.

The contact adhesion of an elastic sphere with a rigid plate is the focus of Chapter 3, particularly when the contact is accompanied by an intervening liquid that provides capillary adhesion. If the sphere is saturated and poroelastic, then it can secrete its own adhering liquid upon contact with the plate. We compare theoretical predictions for a loaded poroelastic sphere to classic contact adhesion results and experiments involving unloaded hydrogel beads.

Chapter 4 explores the effect of elastic deformation on capillary adhesion. A model is presented involving a thin membrane under tension adhering to a rigid substrate due to the surface tension of a liquid bridge. The equilibria of the system are found as a function of two key dimensionless parameters, and the adhesion force is calculated and compared to experimental data. The dynamic evolution is studied numerically and asymptotically, and strategies for how to control adhesion are developed to adhere strongly and detach efficiently. (Note that this work has recently been published in *Physical Review Fluids* [Butler et al., 2019].)

The detachment of a capillary load is considered in Chapter 5 using a two-dimensional dynamic model of a loaded plate attached to a substrate by a liquid bridge. Linear stability analyses and numerical simulations are used to investigate the initial motion away from an unstable equilibria and the importance of plate tilting in determining whether the load ultimately adheres or detaches from the substrate. (The work contained in this chapter has been recently published in the *IMA Journal of Applied Mathematics* [Butler and Vella, 2020].)

Finally, in Chapter 6 we summarize the results of this thesis and consider potential avenues for future work.

Chapter 2

Splitting capillary bridges on rough surfaces

In this chapter, the effect of 'bridge splitting' is considered in the case of capillary adhesion: for a fixed total volume of liquid, does having more capillary bridges increase the total adhesion force? Previous studies have shown that the capillary-induced adhesion force between two planar surfaces is only substantially enhanced by bridge splitting in specific circumstances. Here this previous result is reconsidered, and it is shown that bridge splitting may significantly increase the adhesion forces when one of the surfaces is rough. The resistance to shear is also examined, and it is shown that bridge splitting on a rough surface can lead to a steady capillary-induced shear force that scales linearly with translation velocity, even in the absence of contact-line pinning.

2.1 Introduction

Simple analytical models of a liquid bridge between between smooth planar surfaces, such as that of eqn. (1.6), show that the capillary adhesion force is proportional to the total volume of liquid in the bridge. However, many observational studies show that some insects (including flies and beetles) have hairy footpads, which give many points of adhesive contact [Gorb, 1998, Eisner and Aneshansley, 2000], whilst others (including some species of ants and stick insects) have an adhesive consisting of a water-in-oil emulsion: many small water droplets are dispersed in an oil [Federle et al., 2002, Dirks et al., 2010]. It is possible that these emulsion droplets may themselves form bridges. The ubiquity of some form of 'bridge splitting' in natural occurrences of capillary adhesion suggests that it must be somehow beneficial to insects [Dirks and Federle, 2011a]; one possibility is that such an emulsion somehow enhances capillary adhesion, which is apparently at odds with the conclusion from the simple models that the capillary adhesion force is simply

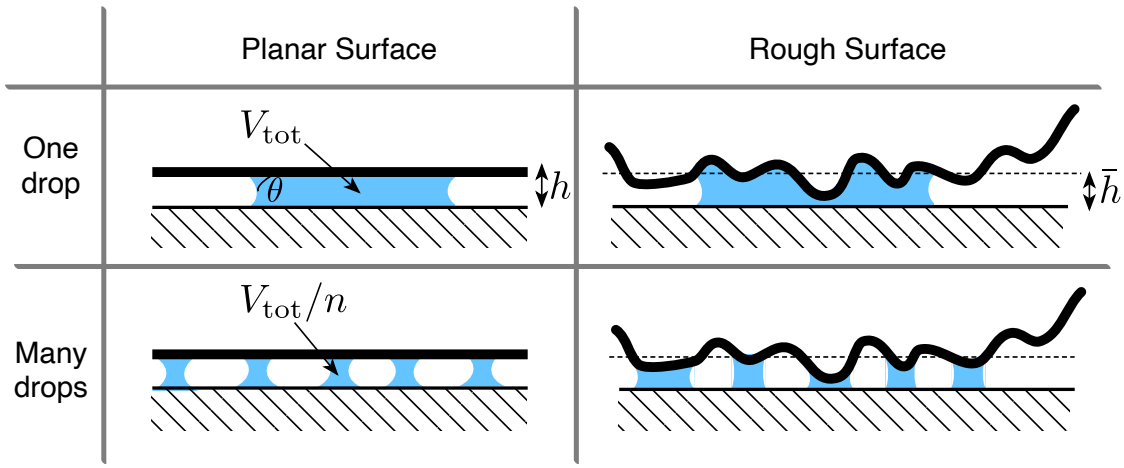

Figure 2.1: Capillary adhesion between planar (left) and rough (right) surfaces, as mediated by a single bridge (top) and many, smaller, bridges (bottom). In each case, the total volume of liquid is V_{tot}, which may be enclosed within a single bridge, or within many. The contact angle of the liquid is shown as the angle θ and the separation of the surfaces is h in the smooth case, while for rough surfaces an equivalent parameter is the mean separation, $\bar{h}$.

proportional to liquid volume (suggesting that adhesion is not enhanced by splitting into a large number of bridges with the same total volume).

As previously discussed in Chapter 1, the simple pancake solution (1.6) with $F \propto V$ is not quite the whole story — could the details of bridge shape away from the pancake case make a significant difference? A detailed study of the effect of dividing a fixed volume of liquid into many bridges between flat plates (as illustrated on the left hand side of fig. 2.1) was presented by De Souza et al. [2008]. They found that, with a fixed liquid volume, it is indeed possible to increase the adhesion force by having many bridges, but that this enhancement is modest (giving less than a two-fold increase in adhesion, as we shall quantify later) when the surface is well-wetted by the liquid (as is believed to be the case in many physiologically relevant cases). If the bridge splitting observed in insect adhesion does not lead to a sizeable increase in the adhesion force on smooth surfaces then the question becomes: what is its purpose?

One key piece of physics that was omitted in the splitting study of De Souza et al. [2008] is surface roughness, which is known to play an important role in adhesion. For 'dry' adhesives on rough surfaces, there can be a trade-off between adhesive attraction due to, for example, van der Waals forces, and repulsion from deformation of the adhering solid: if the surface is sufficiently rough, or the adhering solid sufficiently stiff, then the surfaces

may not be able to conform to one another, resulting in only partial adhesion [Zilberman and Persson, 2002, Persson and Gorb, 2003]. Perhaps to combat this, many climbing organisms have a large number of small contacts [Federle, 2006]. For dry adhesion, the theory of Johnson et al. [1971] (often called JKR adhesion) suggests that there is a finite pull-off force that scales linearly with the radius of spherical contacts (see Chapter 3 for more details). When dividing a single large pad into many smaller pads, it may then be expected that there is an increase in the total adhesion force for a similar contact area [Arzt et al., 2003], but this may be limited by other physical constraints [Spolenak et al., 2005]. Having many smaller contacts may be additionally beneficial by allowing the adhesive organ to conform more closely to a rough substrate [Beutel and Gorb, 2001].

In this chapter, the question of whether bridge splitting is similarly beneficial for capillary adhesion on a rough surface will be addressed. One important feature of capillary adhesion that is qualitatively different to the dry case is that neither the number nor the position of capillary bridges are fixed. Indeed, when surfaces are in close contact in a humid environment, condensation can form new capillary bridges between them, and the roughness of these surfaces can play a significant role in the resulting adhesion [Wang et al., 2009, DelRio et al., 2007, Persson, 2008, Rabinovich et al., 2002].

The possibility of capillary condensation is well-studied, but is unlikely to have a direct impact in cases where controlled adhesion is required, such as the adhesion of insects, since adhesion must occur regardless of external humidity. However, the significance of capillary bridge mobility seems not to have been appreciated in capillary adhesion previously. In particular, mobile wetting liquid bridges will naturally migrate to local minima in the separation between two surfaces because of a geometry-induced capillary pressure gradient (see §1.2.2 and fig. 1.3). This motion has two important effects on the capillary adhesion force: firstly, the liquid bridge is more confined vertically when it reaches the minimum, and so spreads further laterally, increasing the area over which the suction pressure operates. Secondly, the gap separation at the bridge's edge is smaller when at the minimum, and hence the suction pressure is larger (in magnitude). Both of these effects can be seen by comparing the two panels in the lower half of fig. 2.1. Since both effects are expected to increase the force of capillary adhesion on rough surfaces, they suggest that capillary adhesion may be enhanced on rough surfaces by splitting a single capillary bridge into many smaller bridges, each of which may move to a local minimum of separation between the two surfaces.

In this chapter, we consider how to maximize the adhesion force of bridges in the presence of roughness for a given volume of liquid: is it significantly better to have many smaller bridges rather than one large bridge? Results derived from a model of many

capillary bridges between a rough surface and a plate will be compared to the usual simple model of 'pancake' capillary adhesion between two planar surfaces. The behaviour of splitting bridges on rough surfaces will also be compared with the detailed study by De Souza et al. [2008] of many bridges between parallel, planar surfaces. Finally, when there are many capillary bridges beneath a rough surface, the geometry–capillary-induced migration of bridges also gives a mechanism to generate a resistance to steady shear; the magnitude of this resistive force shall be investigated and compared to measurements of the steady shear force generated by insect feet [Federle et al., 2004].

2.2 Adhesion force when splitting bridges

2.2.1 Simple capillary adhesion

A simple model of capillary adhesion is a single, stationary liquid bridge of a given volume V_1, that is confined between two parallel, rigid plates. As explained in Chapter 1, if the bridge is wetting and much wider than it is tall then an approximation to the adhesion force is the pancake solution, eqn. (1.6). This is rewritten here in a dimensionless form that will be useful for comparison with the results in the rest of the chapter:

$$\frac{F_{\text{flat}}}{\gamma V_1/h^2} \approx 2\overline{\cos\theta}. \tag{2.1}$$

Crucially, in this approximation, the adhesion force scales linearly with the volume of the bridge $F_1 \propto V_1$. If this is always a good approximation, then it may be expected that there is never a benefit to splitting a given volume of liquid V_{tot} into n identical bridges because the total force is independent of the number of bridges: $F_{\text{tot}} = nF_1 \propto nV_1 = V_{\text{tot}}$. Note that, because of this invariance when splitting, if the volume V_1 is replaced by V_{tot} in (2.1) then F_{flat} could instead be considered as the total adhesion force due to n bridges.

However, as the liquid is divided into smaller bridges, other effects that are neglected when making the approximation (2.1) may become more important — for example the tension force at the contact line, or the second radius of curvature. In fact, adhesion may be expected to increase with the number of bridges when accounting for the tension force. If each bridge volume can be well approximated by a cylinder, $V_1 \approx \pi r^2 h$, then the tension force per bridge $F_T = 2\pi r \times \gamma \sin\theta \propto \sqrt{V_1}$; the total contribution to the adhesion force by the tension of n bridges of volume $V_1 = V_{\text{tot}}/n$ grows like $\sqrt{n}$ for a fixed total volume V_{tot}. It may therefore be expected that the total adhesion force increases with splitting, as was found by Cai and Bhushan [2008].

As previously mentioned in Chapter 1, however, simply adding the contributions of the tension force and extra curvature does not accurately portray the behaviour of the

adhesion force for a single bridge as the bridge volume decreases. In particular, these approximations do not take account of when stable bridges can no longer be formed and will rupture. It is therefore necessary to make a more detailed calculation of the bridge shape to determine whether dividing into many bridges results in an increase in the adhesion force.

2.2.2 Modelling capillary adhesion

A liquid bridge in equilibrium cannot include flow and hence has no pressure gradient. It therefore has a constant capillary pressure as given by the Young-Laplace equation, (1.2), and so, since the pressure is proportional to the curvature, the bridge must be a constant curvature surface. To find the capillary adhesion force provided by such a bridge, the shape of the bridge must be found first before determining the corresponding force as the sum of Laplace pressure forces and capillary line tension forces.

The exact shape of a single capillary bridge can be determined by solving a set of ordinary differential equations (ODEs) that describe a surface of constant curvature, subject to boundary conditions that impose that the bridge meets the given solid surfaces, does so at contact angle(s) θ and has a bridge volume V_1. While this problem shall be solved numerically from ODEs here, note that in Chapter 1, an analytical solution for two smooth, parallel plates due to Carter [1988] was presented; here, we approach the problem by solving a series of ODEs because this method does not constrain the geometry to planar surfaces, allowing more versatility to describe other topographies.

The shape of an axisymmetric bridge can be described by a single curve that gives the free surface when it is rotated about the central axis. This curve can be entirely determined by the function $\varphi(s)$, where φ is the angle between the tangent to the curve and the horizontal, which is parametrized by the arc length, s, as illustrated in fig. 2.2. The vertical and radial coordinates of this curve $r = \rho(s)$ and $z = \zeta(s)$ are determined from the angle by elementary geometry: $\mathrm{d}\rho/\mathrm{d}s = \cos\varphi$, $\mathrm{d}\zeta/\mathrm{d}s = \sin\varphi$. The function $\varphi(s)$ for the constant curvature surface satisfies the ODE [see, for example, de Gennes et al., 2004, Qian and Gao, 2006, Slater et al., 2014, Macner and Steen, 2014]

$$\frac{\mathrm{d}\varphi}{\mathrm{d}s} + \frac{\sin\varphi}{\rho} = \kappa = \frac{\Delta p}{\gamma}, \tag{2.2}$$

where κ is the (unknown) constant surface curvature, and the arc length $s \in [0, s_{\mathsf{max}}]$ for some (unknown) total arc length s_{max}.

This system is subject to boundary conditions that enforce that the bridge meets the given solids at a specific contact angle, θ, as well as an integral constraint imposing the

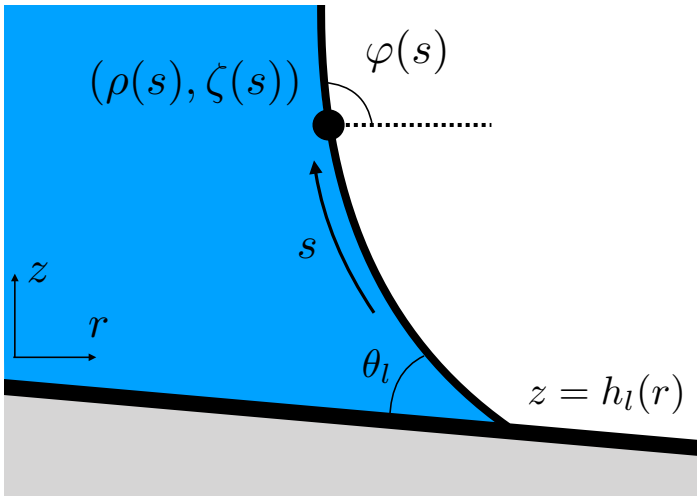

Figure 2.2: The surface of a liquid bridge $(r, z) = [\rho(s), \zeta(s)]$ is parametrized by the arc length, s, (measured from one contact line) and is defined in terms of the angle, $\varphi(s)$, between its tangent and the horizontal. (In this diagram, the liquid bridge is to the left of the curve defining the free surface.) The liquid bridge interface meets the lower surface $z = h_l(r)$ at the static contact angle θ_l (and similarly for the upper surface which is not depicted).

total bridge volume

$$V_1 = \pi \int_0^{s_{\mathsf{max}}} \rho(s)^2 \sin\varphi \, \mathrm{d}s - 2\pi \int_0^{\rho(s_{\mathsf{max}})} x[h_u(\rho(s_{\mathsf{max}})) - h_u(x)] \, \mathrm{d}x \\ - 2\pi \int_0^{\rho(0)} y[h_l(y) - h_l(\rho(0))] \, \mathrm{d}y, \quad (2.3)$$

where $z = h_l(r)$ and $z = h_u(r)$ define the surfaces of the lower and upper solid, respectively. Note that the latter two integrals here account for the volume excluded due to the presence of the solid surfaces within the bridge perimeter.

This system is simplified by eliminating the unknown constant curvature κ by differentiating (2.2) with respect to s. For numerical convenience, the integral constraint (2.3) is also converted into an additional ODE by introducing a function for the cumulative volume $\int_0^s \pi\rho(\eta)^2 \sin\varphi(\eta) \, \mathrm{d}\eta$. For given solid surfaces separated by a typical lengthscale L (that shall be defined concretely for each specific problem), the problem is non-dimensionalized by scaling all extrinsic lengths by L, while the meniscus arc length is scaled by the total arc length, s_{max}. These different lengthscales introduce a dimensionless parameter $\varsigma = s_{\mathsf{max}}/L$. The problem of finding the shape of a constant curvature liquid bridge then

becomes that of solving

$$\begin{aligned}
&\frac{\mathrm{d}^2\varphi}{\mathrm{d}S^2} + \varsigma\frac{\cos\varphi}{\varrho}\frac{\mathrm{d}\varphi}{\mathrm{d}S} - \varsigma^2\frac{\sin\varphi\cos\varphi}{\varrho^2} = 0,\\
&\frac{\mathrm{d}\varrho}{\mathrm{d}S} = \varsigma\cos\varphi, \qquad \frac{\mathrm{d}\xi}{\mathrm{d}S} = \varsigma\sin\varphi,\\
&\frac{\mathrm{d}v}{\mathrm{d}S} = \varsigma\pi\varrho^2\sin\varphi, \qquad \frac{\mathrm{d}\varsigma}{\mathrm{d}S} = 0,
\end{aligned} \tag{2.4}$$

where $S = s/s_{\mathsf{max}} \in [0,1]$ is the (scaled) arc length; $\varrho(S) = \rho(s)/L$ and $\xi(S) = \zeta(s)/L$ are the dimensionless radial and vertical coordinates of the meniscus; φ is the inclination angle as defined previously; $v(S) = \int_0^S \varsigma\pi\varrho(x)^2\sin[\varphi(x)]\ \mathrm{d}x$ is the dimensionless cumulative volume and $\varsigma = s_{\mathsf{max}}/L$ is the dimensionless total arc length. The positions of the solid surfaces are now given by $\tilde{z} = H_l(\tilde{r}), H_u(\tilde{r})$ where $H_{u,l} = h_{u,l}/L$ and the dimensionless cylindrical coordinates are $(\tilde{r},\tilde{z}) = (r/L, z/L)$.

This is a sixth order system of ODEs and so six boundary conditions are required. Two of the required boundary conditions are simply that the bridge interface meets each solid surface

$$\xi(0) = H_l[\varrho(0)], \qquad \xi(1) = H_u[\varrho(1)]. \tag{2.5}$$

Two further conditions are given by the contact angles at each end, carefully accounting for the slope of each of the solids

$$\varphi(0) = \pi - \theta_l + \tan^{-1}\left\{H_l'[\varrho(0)]\right\}, \qquad \varphi(1) = \theta_u + \tan^{-1}\left\{H_u'[\varrho(1)]\right\}, \tag{2.6}$$

where the dash notation denotes differentiation with respect to $\tilde{r}$, and θ_l and θ_u are the contact angles at each of the solids.

The final two boundary conditions enforce the fixed volume condition (2.3)

$$\begin{aligned}
v(0) &= 0,\\
v(1) &= v_1 + 2\pi\int_0^{\varrho(1)} x[H_u(\varrho(1)) - H_u(x)]\ \mathrm{d}x + 2\pi\int_0^{\varrho(0)} y[H_l(y) - H_l(\varrho(0))]\ \mathrm{d}y,
\end{aligned} \tag{2.7}$$

where $v_1 = V_1/L^3$.

In principle, solving the coupled ODEs (2.4) subject to the boundary conditions (2.5)–(2.7) gives the shape of the bridge (ϱ,φ,ξ) for given boundaries H_l, H_u, contact angles θ_l, θ_u and bridge volume v_1.

Once the shape of the bridge is known, the force $\mathbf{F}_1$ applied by this bridge on one of the solid surfaces can be calculated as the sum of the contributions from the capillary pressure and tension terms

$$\mathbf{F}_1 = \int_D -\Delta p\ \mathbf{n}\ \mathrm{d}A + \int_{\partial D}\gamma\mathbf{t}\ \mathrm{d}s, \tag{2.8}$$

where $\mathbf{n}$ is the normal to the solid surface, $\mathbf{t}$ is the tangent to the liquid interface, D is the wetted area and ∂D its perimeter. Note that the capillary pressure jump, Δp, is determined from the shape of the bridge through the (constant) meniscus curvature, κ, due to the Young-Laplace equation (1.2), $\Delta p = \gamma\kappa$; the dimensionless curvature $K = \kappa L$ is given by

$$K = \frac{1}{\varsigma}\frac{\mathrm{d}\varphi}{\mathrm{d}S} + \frac{\sin\varphi}{\varrho}. \tag{2.9}$$

After finding the adhesion force due to the surface tension of one bridge, F_1, the total adhesion force, $F_{\text{tot}} = nF_1$, for n identical bridges with a fixed total volume $V_{\text{tot}} = nV_1$ can be calculated.

2.2.3 Bridge splitting on flat surfaces

Let us return to the problem of splitting bridges between two parallel plates, as shown in the left side of fig. 2.1. We would like to know whether having many bridges gives stronger adhesion and, if so, how to maximize the adhesion force by dividing the liquid into many bridges. This problem has been previously studied by De Souza et al. [2008] using an energy minimization approach. Here the work of De Souza et al. [2008] is reproduced by solving the set of ODEs above; we shall move to consider the effect of surface roughness in §2.2.4.

Consider two identical parallel, rigid plates that are a fixed distance h apart. A volume V_{tot} of liquid of surface tension γ is divided into n identical bridges of equal volume $V_1 = V_{\text{tot}}/n$ that meet each plate at a contact angle θ. This scenario is illustrated in the bottom left panel of fig. 2.1. The total adhesion force, F_{tot}, due to these n bridges is found by solving the ODEs (2.4) for the shape of a single bridge of volume V_1, subject to the boundary conditions (2.5)–(2.7) with flat surfaces $H_l = 0$, $H_u = 1$ (using the lengthscale $L = h$). From the bridge shape, the adhesion force from this single bridge, F_1, is calculated as the sum of the contributions from the suction pressure within the bridge and the tension force around the bridge meniscus, just like eqn. (1.4); the total adhesion force is then $F_{\text{tot}} = nF_1$.

Results for the adhesion force when splitting bridges between parallel plates are presented in fig. 2.3. These results can be compared quantitatively with those presented by De Souza et al. [2008] or Carter [1988], confirming the accuracy of the numerical approach. These benchmark results will also be useful for comparison with the results for rough surfaces later.

Figure 2.3 shows the effect of bridge splitting on the adhesion force obtained for bridges between two identical flat surfaces with contact angles $\theta = 0, 30^\circ, 45^\circ, 60^\circ, 70^\circ$ and 80°.

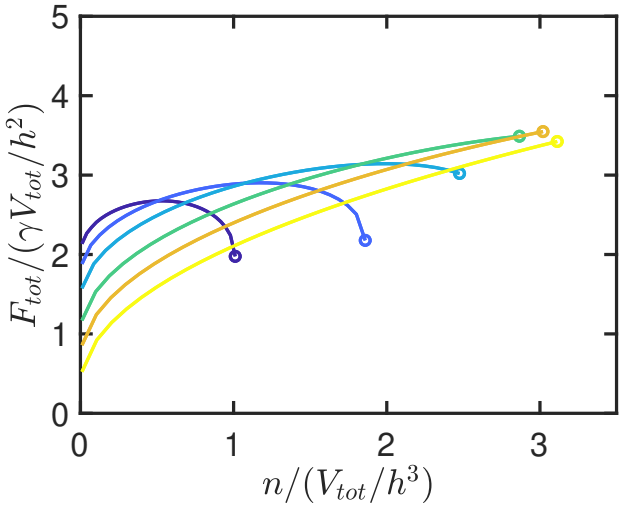

Figure 2.3: The total capillary adhesion force, F_{tot}, obtained when a liquid volume V_{tot} with surface tension γ is split into n bridges that are confined between two parallel plates, separated by a distance h. Results are shown for various different values of the contact angle: $\theta = 0°, 30°, 45°, 60°, 70°, 80°$ (coloured dark blue to yellow). Open circles denote the furthest level of bridge splitting possible before the bridges can no longer exist in equilibrium and must rupture.

For small contact angles, a maximum adhesion force is attained at an intermediate number of bridges, well before the solutions cease to exist and the bridges must break. With larger contact angles, however, the maximum adhesion force is attained when the bridges are only just able to stably bridge the gap: any further splitting would result in breaking of the bridges and no adhesion. The point at which there ceases to be a stable solution shall be referred to as 'rupture'.

In general, as the fixed liquid volume is divided into more bridges, the (positive) azimuthal curvature around each bridge increases, which will act to reduce the suction pressure force F_P; meanwhile, the total contact perimeter increases, resulting in an increase in the tension force F_T. The enhanced importance of the tension force leads to the increase in adhesion force as the bridges are further split for larger contact angles; for highly wetting liquids (smaller θ) the tension contribution is smaller, and eventually is less important than the curvature changes.[1]

De Souza et al. [2008] found that, over all contact angles θ and number of bridges n, the maximum adhesion force is $F_{\text{tot}} \approx 3.6 \times (\gamma V_{\text{tot}}/h^2)$ which is obtained when $\theta \approx 70°$ and the bridges are just at the point of rupture (i.e. there are no solutions with smaller bridge

[1] This is not quite true for perfectly wetting liquids, $\theta = 0$, which have no tension force — see Appendix 2.A for an overview of this case.

size). For perfectly wetting liquids, $\theta = 0$, the increase due to splitting is approximately one third larger than expected on the basis of the simple estimate given by eqn. (2.1): the numerical solutions suggest that a maximum force $F_{\text{tot}} \approx 2.68 \times (\gamma V_{\text{tot}}/h^2)$ does exist, so that there is still a small benefit to bridge splitting, even in the perfectly wetting case where there is no contribution from the capillary tension force. Across all contact angles studied, it is found that dividing the liquid into many bridges only leads to a mild improvement in the adhesion force (i.e. not orders of magnitude larger). A key question is then: is the enhancement from bridge splitting more significant with a rough surface?

2.2.4 Bridge splitting on a rough surface

Capillary adhesion between rough surfaces has previously been considered by Cai and Bhushan [2008], although they assume a circular shape for each bridge meniscus — an assumption that is no longer valid when the bridge is not very wide compared to its height (as will eventually be the case when splitting bridges). Similar to the flat case, we shall find that the details of the bridge shape and when rupture occurs are crucial in determining whether splitting has a beneficial effect. We therefore turn to investigate the bridge shape and adhesion force in this rough scenario in some detail now.

Problem set-up

A given volume of liquid, V_{tot}, is split into n identical bridges, each of volume $V_1 = V_{\text{tot}}/n$. These bridges are sandwiched between two rigid surfaces, and are expected to be located at local minima in the separation between the surfaces (because of geometry-induced capillary pressure gradients, as explained in §1.2.2). For simplicity, one surface is considered to be planar and the other rough; the most important detail is how the distance between the two surfaces varies (which cannot distinguish between two rough surfaces and a rough-smooth pair). However, the geometry of the surfaces does matter somewhat; the contact angle conditions at the triple contact line (2.6) differ depending on which of rough-rough and rough-smooth is taken[2]. As is the case throughout this thesis, the liquid has a surface tension γ and makes a contact angle θ with each of the solid surfaces.

We now need to choose a model for the surface roughness. Consider a rough surface separated from a plane by an average distance $\bar{h}$, as shown in fig. 2.4. Zooming in on a single asperity, if it is locally sufficiently smooth and regular, as well as being close to

[2]In addition, if two rough surfaces mesh well together (i.e. the separation between them varies little compared to the roughness of each surface) then the separation may not be the dominant feature and more detailed calculation may be needed. For two arbitrary surfaces it is expected to be unlikely that they mesh well, but understanding this scenario may be important and is left as future work.

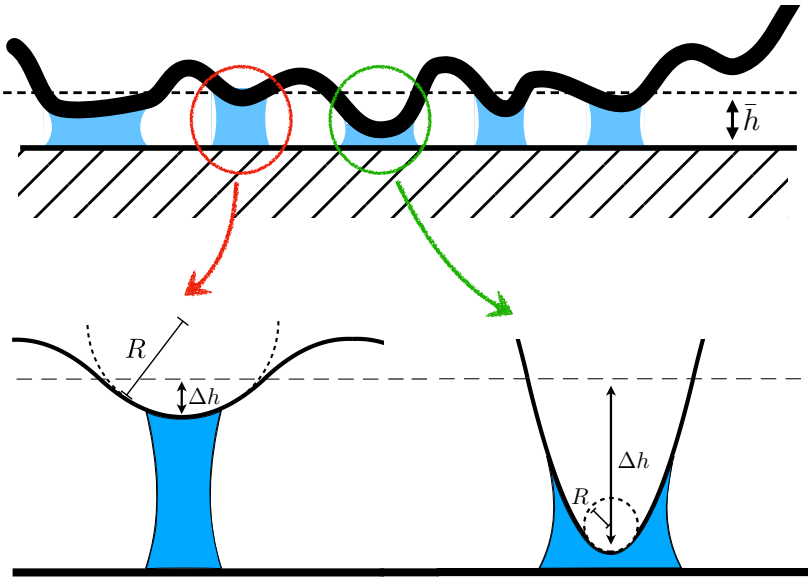

Figure 2.4: A schematic showing the roughness parameters for two different asperities that are approximated locally as parabolas. The left asperity has $\Delta h/\bar{h} = 0.2$, whilst the right one has $\Delta h/\bar{h} = 0.9$. Both asperities shown have the same aspect ratio α defined by eqn. (2.10). (Bridge shape and volumes are not to scale.)

axisymmetric, then the shape of the asperity close to its tip can be approximated by a parabola: $h(r) = h_0 + r^2/2R$, for some $h_0 < \bar{h}$ and R. (Analogous calculations with a linear cone-like roughness are given in Appendix 2.B for comparison.) The n bridges are each confined between a plane and one of these parabolas. In reality, a solid's roughness would be expected to have a variety of roughness amplitudes and wavelengths, as shown in fig. 2.4 — real surfaces are randomly rough. A simpler model shall be considered here, where each asperity is assumed to have the same curvature and amplitude. Surfaces with the same mean separation, $\bar{h}$, are compared and the amplitude of the roughness, $\Delta h = \bar{h} - h_0$, varied at a fixed aspect ratio

$$\alpha = \frac{R\Delta h}{\bar{h}^2}. \tag{2.10}$$

The aspect ratio α gives the relative size of the width of the roughness $\sqrt{2R\Delta h}$ to its average height $\bar{h}$. Examples of two asperities with the same aspect ratio α and different roughness amplitudes Δh are shown in the lower half of fig. 2.4 (for an example of different aspect ratios, see the inset to fig. 2.12 in Appendix 2.B).

For given parameters, the boundary value problem (BVP) defined in §2.2.2 is solved using a non-dimensionalization with the lengthscale $L = \bar{h}$. More specifically, the ODEs (2.4) are solved for the shape of a single bridge of volume V_1, subject to the boundary

conditions (2.5)–(2.7) when one surface is flat, $H_l = 0$, and the other has parabolic shape, $H_u(\tilde{r}) = h_0/\bar{h} + \tilde{r}^2/2(R/\bar{h})$. These boundary conditions can be written as

$$\begin{aligned} \xi(0) = 0, \quad \xi(1) &= \frac{h_0}{\bar{h}} + \frac{[\varrho(1)]^2}{2(R/\bar{h})}, \\ \varphi(0) = \pi - \theta, \quad \varphi(1) &= \theta + \tan^{-1}\left[\frac{\varrho(1)}{(R/\bar{h})}\right], \\ v(0) = 0, \quad v(1) &= \frac{V_1}{\bar{h}^3} + \frac{\pi}{4}\frac{[\varrho(1)]^4}{(R/\bar{h})}. \end{aligned} \tag{2.11}$$

Once the aspect ratio, $\alpha = R\Delta h/\bar{h}^2$, the dimensionless roughness amplitude, $\Delta h/\bar{h}$, and the dimensionless bridge volume, $V_1/\bar{h}^3$, are specified, the values of $h_0/\bar{h}$ and $R/\bar{h}$ to be used in these boundary condition are determined by the relations

$$\frac{h_0}{\bar{h}} = 1 - \frac{\Delta h}{\bar{h}}, \tag{2.12}$$

$$\frac{R}{\bar{h}} = \frac{\alpha}{\Delta h/\bar{h}}. \tag{2.13}$$

For each choice of parameters, the system of ODEs (2.4) is solved subject to the boundary conditions (2.11) using MATLAB's in-built BVP solver `bvp4c`. The adhesion force provided by a single bridge on the planar surface can then be calculated by

$$\frac{F_1}{\gamma V_1/\bar{h}^2} = \frac{-\pi K \varrho(0)^2 + 2\pi\varrho(0)\sin\theta}{V_1/\bar{h}^3}, \tag{2.14}$$

where the dimensionless curvature K is defined in (2.9). (Recall that a positive adhesion force corresponds to the plate being pulled towards the rough surface — adhesion.)

In fact, the dimensionless adhesion force for a single bridge is precisely the dimensionless total adhesion force, $F_{\text{tot}} = nF_1$, from n such bridges with combined volume $V_{\text{tot}} = nV_1$, since

$$\frac{F_{\text{tot}}}{\gamma V_{\text{tot}}/\bar{h}^2} = \frac{F_1}{\gamma V_1/\bar{h}^2}. \tag{2.15}$$

This dimensionless force can be expressed as a function of the scaled number of bridges

$$\frac{\bar{h}^3}{V_{\text{tot}}} n = \left(\frac{V_1}{\bar{h}^3}\right)^{-1}. \tag{2.16}$$

If the two surfaces are sufficiently separated from one another, or equivalently if the bridge volume is sufficiently small, then a stable liquid bridge cannot be formed between the two solid surfaces (just as in §1.3). Particular care must be taken to calculate when rupture occurs, i.e. the maximum number of bridges n, or equivalently the minimum bridge volume $V_1 = V_{\text{tot}}/n$, (as a function of Δh) for which a stable bridge shape exists.

The determination of when rupture occurs is achieved using AUTO-07P, a computational tool for finding bifurcations by arc-length continuation of solutions in multiple parameters [Doedel et al., 2007]. Starting from a numerical solution to the BVP — given by the ODEs (2.4) and boundary conditions (2.11) — for the flat case, $\Delta h = 0$, the number of bridges n is increased until a bifurcation is detected before following this bifurcation as Δh is increased. This gives the locus of the rupture bifurcation $n_{\mathsf{rup}}(\Delta h)$.

Attention is restricted only to those solutions where the bridge is shorter than the average roughness, $\xi(1) < 1$; beyond this limit, the bridges take up a significant portion of each roughness asperity and so approximating the shape as a parabola may no longer be applicable. Additionally, it may reasonably be expected that optimal adhesion through splitting should be achieved when bridges are relatively close to rupture (as was found for flat plates in §2.2.3). Therefore, the adhesion force is calculated as a function of the roughness amplitude Δh and the number of bridges n between the upper limit on n where rupture occurs and the lower limit where the meniscus height is equal to the mean roughness height, $\xi(1) = 1$.

Results for the adhesion force

In the results presented here, we focus on the case of liquid that perfectly wets both surfaces, $\theta = 0$, and an aspect ratio $\alpha = 10$. In Appendix 2.B it is shown that the effects of varying the contact angle and aspect ratio are largely quantitative rather than qualitative with a relatively minor impact on the results (this is particularly the case for the effect of the aspect ratio α).

The total adhesion force, F_{tot}, from n bridges at fixed roughness amplitude, $\Delta h/\bar{h}$, is shown in dimensionless form in fig. 2.5a. It can be seen that (provided that splitting is actually feasible, i.e. the total liquid volume V_{tot} is not too small compared to $\bar{h}^3$) splitting can result in a significant increase in adhesion force. The maximum adhesion force at fixed $\Delta h/\bar{h}$ can be several times larger than the respective simplified flat case, given in eqn. (2.1); moreover, the maximum occurs far from the end-point of splitting, where bridges rupture — for a given roughness amplitude, there is an optimal level of bridge splitting, achieved without those bridges rupturing. Finally, the curves of F_{tot} as a function of $n/(V_{\mathsf{tot}}/\bar{h}^3)$ are relatively wide and flat, meaning that even levels of splitting that are far from optimal are still able to achieve close-to-optimal adhesion forces.

Figure 2.5a also suggests that the total adhesion force increases with increasing roughness, and so it is important to also consider varying the roughness amplitude $\Delta h/\bar{h}$ at fixed number of bridges n, with the results shown in fig. 2.5b as a function of the minimum gap width $h_0 = \bar{h} - \Delta h$. Here, it is apparent that the adhesion force increases as

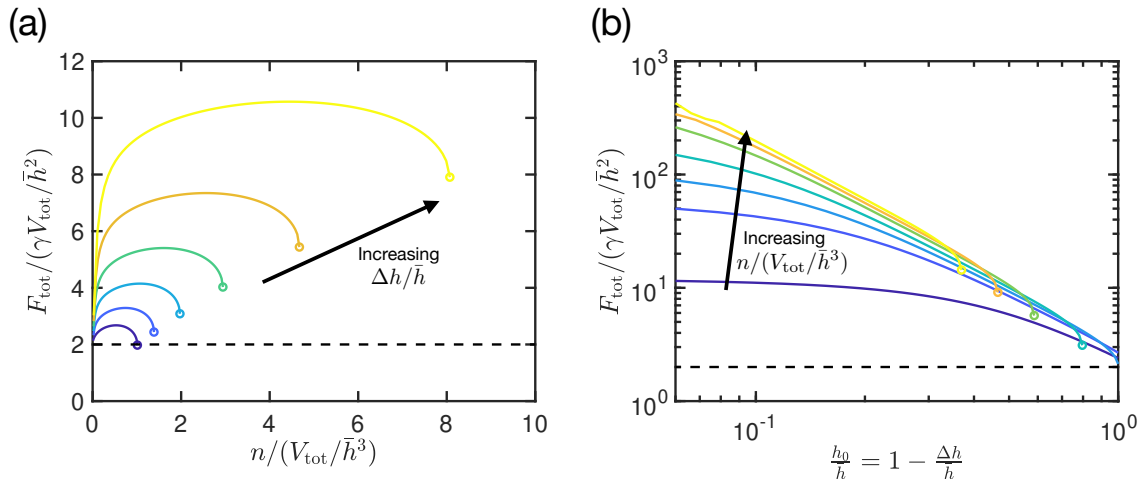

Figure 2.5: The total adhesion force as a function of (a) the number of bridges, n, at fixed roughness amplitudes $\Delta h/\bar{h} = \{0, 0.1, 0.2, 0.3, 0.4, 0.5\}$ (plotted up to rupture, which is indicated by circles), and (b) the minimum gap width, $h_0/\bar{h} = 1 - \Delta h/\bar{h}$, with fixed number of bridges $n/(V_{\rm tot}/\bar{h}^3) = \{0.1, 0.5, 1, 2, 5, 10, 20\}$. In both cases here $\theta = 0$ and $\alpha = 10$, and results are compared to a dashed line denoting eqn. (2.1). Note that in (a), the case $\Delta h = 0$ corresponds to the flat plates studied by De Souza et al. [2008].

the roughness amplitude increases (h_0 decreases). In most of the cases shown, the force increases by several orders of magnitude as the roughness is increased.

The results for the adhesion force as a function of the splitting and roughness are summarized in fig. 2.6a. The colour denotes the (logarithm of the) ratio of the force obtained with a particular surface roughness to that obtained in the simplified flat case described by eqn. (2.1). From this it can clearly be seen that the force generally increases with splitting (although with an intermediate maximum) and with roughness. Importantly, it is possible to get an increase in the adhesion force of over an order of magnitude compared to the flat case.

Plotting the maximum force achieved by splitting as a function of the roughness amplitude (i.e. the envelope of curves in fig. 2.5b), fig. 2.6b is obtained. The maximum force increases with the relative roughness of the surface, appearing to diverge as h_0 decreases like $F_{\rm max} \sim h_0^{-2}$ (recall that h_0 is the minimal gap width). Indeed, the maximum force is greater than that obtained by the simple flat scaling of eqn. (2.1) with $h = h_0$, but is actually less than the maximum force possible if n bridges adhere flat plates separated by h_0, i.e. $F_{\rm max} < 2.68 \times (\gamma V_{\rm tot}/h_0^2)$ (see fig. 2.3); however, note that the difference is almost indistinguishable at the scale of the inset to fig. 2.6b.

We have seen that bridge splitting may give a large increase in the capillary adhesion force between rough surfaces. The mechanism for this enhanced effect was the migration

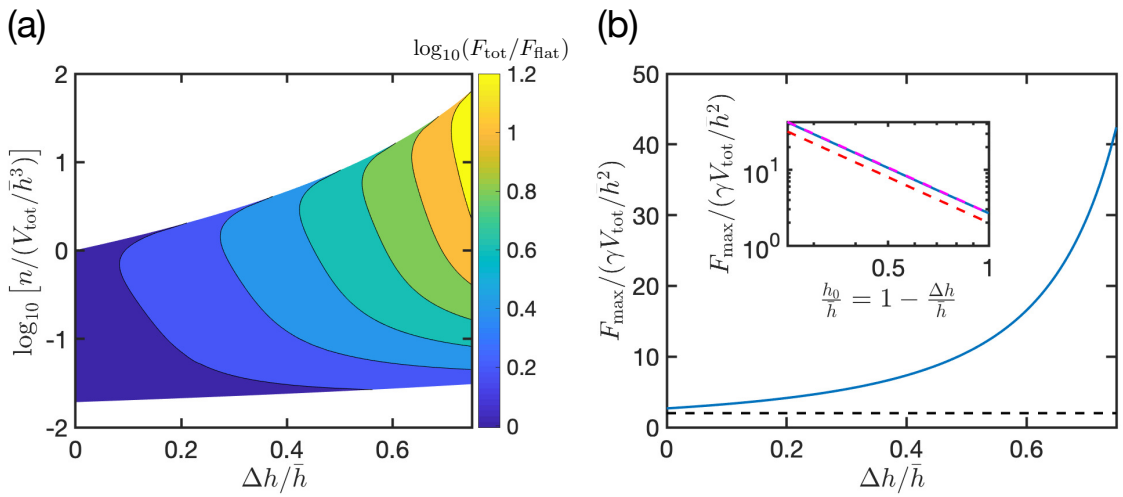

Figure 2.6: (a) The relative increase in the total adhesion force, $F_{\rm tot}$, for n bridges under a rough surface compared to the simplified force calculation for a single bridge between flat surfaces, $F_{\rm flat}$ from eqn. (2.1). Here $F_{\rm tot}/F_{\rm flat}$ is represented by colour (see colour bar), while $\Delta h/\bar{h}$ represents the amplitude of the roughness and $n/(V_{\rm tot}/\bar{h}^3)$ the (scaled) number of bridges. No solutions exist in the upper white region (rupture), whilst solutions where the bridge spreads further than one asperity are ignored (lower white region, $\xi(1) > 1$). (b) The maximum total adhesion force, $F_{\rm max}$, at each roughness amplitude $\Delta h/\bar{h}$ (solid blue curve) compared to the benchmark scaling of eqn. (2.1), shown by the black dashed line. Inset: a log-log plot showing the maximum force (solid curve) as a function of $h_0 = \bar{h} - \Delta h$. The red (lower) dashed line in the inset denotes $y = 2/x^2$, whilst the magenta (upper) dashed line is $y = 2.68/x^2$; these respectively correspond to the simple relation (2.1) and to optimal adhesion, both when splitting between flat plates with a separation h_0. In both (a) and (b), the contact angle and aspect ratio are $\theta = 0$ and $\alpha = 10$, respectively.

of bridges to the local minima in the surface separation, which simultaneously increases the capillary suction pressure and the wetted area over which this suction pressure acts. However, this migration of liquid bridges also gives a mechanism through which tangential motion between two rough surfaces can be resisted — a capillary-induced resistance to shear. We therefore turn now to quantify this.

2.3 Resistance to shear

When insects adhere to a surface they are able to withstand large normal loads relative to their body weight, but also comparatively large shear forces [Dirks, 2014, Dirks and Federle, 2011a]; a long-standing problem in insect adhesion is to understand the origins of this resistance to shear. Experiments on Asian Weaver ants suggest that the shear force increases linearly with the velocity of shearing [Federle et al., 2004], with only a relatively small threshold at $U = 0$ (see fig. 2.7). This linear relationship between force and velocity is evocative of the relationship between rate of shearing and shear stress acting on two parallel plates separated by a Newtonian liquid [Batchelor, 1967, Worster, 2009].

A common means of plotting such data is via a Stribeck curve [Hamrock et al., 2004] showing friction coefficient as a function of dimensionless speed — this clearly distinguishes between boundary lubrication (that is independent of speed) and hydrodynamic lubrication (that increases linearly with speed). The inset of fig. 2.7 shows an estimated Stribeck curve (based on an assumed load $W = 40\ \mu\mathrm{N}$, contact length $L = 0.1\ \mathrm{mm}$ and dynamic viscosity $\mu = 0.1\ \mathrm{Pa\,s}$), where friction coefficients are plotted as a function of the Hersey number ($\mu UL/W$, which is a dimensionless lubrication parameter but for our purposes can be thought of as a dimensionless speed). Again, this shows an approximately linear trend, suggesting the origin of this shear force is hydrodynamic. However, a simple model of a Newtonian liquid bridge between plates does not appear to provide a large enough resistance to shear to explain the observed forces [Federle et al., 2002]; further, a steady state cannot exist in the case of a finite liquid bridge, which would be smeared over the plate by the shearing.

One possible clue as to insects' strong resistance to shear is the presence of emulsion droplets in their oily secretion. As well as the potential benefit of enhancing capillary adhesion, it has also been suggested that these emulsion droplets could endow the liquid with non-Newtonian properties, such as a yield stress, thereby also allowing for resistance to shear [Dirks et al., 2010, Drechsler and Federle, 2006]. Another possibility is that contact angle hysteresis and contact line pinning may oppose shearing as the pull of the contact line contributes a horizontal component [Dirks, 2014]. However, both of these

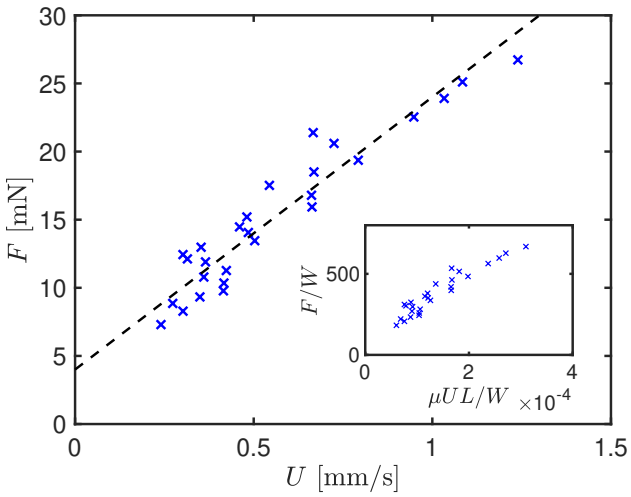

Figure 2.7: An Asian Weaver ant on a rotating turntable experiences a shear force F due to centrifugal forces, whilst sliding at a radial speed U. Experimental data from Federle et al. [2004] are digitally captured and plotted in the main figure. The data appear to be well-approximated by a linear relationship $F = 20U + 4$ (black dashed line) with F measured in mN and U in mm/s. Inset: An approximation for the data as would be seen on a Stribeck curve. For this inset, the load was estimated as $W = 40$ μN, the length of contact $L = 0.1$ mm [both from data in Federle et al., 2004] and the dynamic viscosity $\mu = 0.1$ Pa s [Federle et al., 2002].

mechanisms predominantly generate a static resistance to shear and cannot explain the simple linear relationship between the resistance to shear and the imposed shear velocity.

Here, we shall explore an alternative mechanism for generating resistance to shear. Similar to the motion that aided the enhanced equilibrium capillary adhesion already studied, this mechanism is based on the motion of liquid bridges on a rough surface towards local minima. In shear, however, a liquid bridge trapped beneath a parabolic asperity (see fig. 2.8) is dragged by the imposed shear away from the minimum below a particular asperity; as explained in §1.2.2, the resulting geometric asymmetry introduces a pressure difference that leads to an opposing flow within the liquid bridge. Ultimately, the bridge may be expected to reach a steady state in which this capillary-driven flow precisely balances the dragging caused by imposed shear. The bridge thus remains beneath the asperity (without being smeared out); at the same time, the capillary-induced back-flow applies a force that resists the imposed shear.

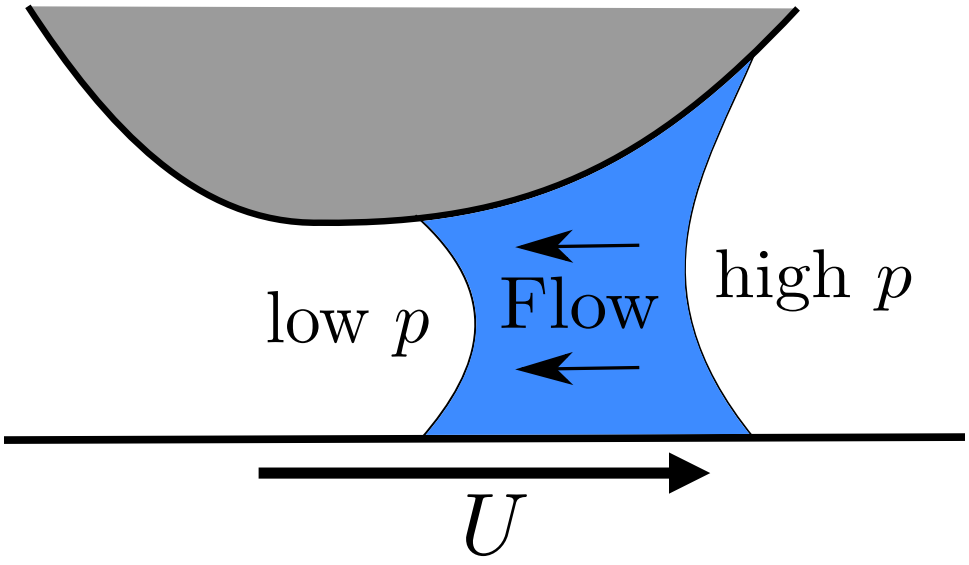

Figure 2.8: Capillary migration of wetting bridges can resist shear: when shearing of the plate displaces a liquid bridge from an asperity, the resulting capillary pressure gradient causes back-flow that can resist the shearing motion.

2.3.1 Model of the shearing motion

Consider a wetting liquid bridge confined between a flat plate and a rough surface with a parabolic profile $h(r) = h_0 + r^2/2R$ (as in §2.2.4). The flat plate is sheared at a constant speed U in the positive x-direction, with the fluid flow modelled by thin-film lubrication equations [see Chapter 5 of Leal, 2007]. (Note that in this section, unlike earlier in this chapter, the bridge must be wide and short.) The horizontal velocity in the liquid is then

$$\mathbf{u} = -\frac{\nabla p}{2\mu} z(h - z) + \mathbf{U}\left(1 - \frac{z}{h}\right), \tag{2.17}$$

where $\nabla = (\partial_x, \partial_y)$ is the gradient operator in the horizontal plane, $\mathbf{U} = (U, 0)$ is the applied shear velocity in the x-direction and μ is the dynamic viscosity of the liquid. Integrating this in z gives the depth-integrated volumetric flux

$$\mathbf{q} = -\frac{h^3}{12\mu}\nabla p + \frac{h}{2}\mathbf{U}. \tag{2.18}$$

Focusing on steady states, for simplicity, conservation of mass [Leal, 2007] then shows that the volumetric flux $\mathbf{q}$ must obey the steady-state Reynolds' equation:

$$\nabla \cdot \mathbf{q} = 0 \quad \Longrightarrow \quad U\frac{\partial h}{\partial x} = \frac{1}{6\mu}\nabla \cdot (h^3 \nabla p), \tag{2.19}$$

which is reminiscent of the governing equations for coating problems [for example, Levich and Landau, 1942, Wilson, 1982].

Consistent with the use of lubrication theory, it is also assumed that the bridge has a much larger radius than the gap width at the meniscus. (Again, note that this differs to the calculations of the adhesion force earlier in the chapter, which could have comparable radius and gap width.) In equilibrium with no shear, $U = 0$, the bridge has its meniscus at $r = a_0$, and its volume is approximately given by $V \approx 2\pi \int_0^{a_0} r(h_0 + r^2/2R)\ \mathrm{d}r = \pi(h_0 a_0^2 + a_0^4/4R)$. Note that when the bridge volume is small, $V/(h_0^2 R) \ll 1$, then the bridge width is small compared to the curvature and the bridge experiences a relatively flat surface with approximately constant gap width, so that $V \approx \pi h_0 a_0^2$; when the bridge is much wider, $V/(h_0^2 R) \gg 1$, then it mostly experiences the curvature of the surface and $V \approx \pi a_0^4/4R$.

At the meniscus, the action of surface tension causes a jump in the normal stress proportional to the curvature of the interface. As discussed previously in §1.2.2, when using the lubrication approximation this simplifies to a jump in the fluid pressure only, which satisfies the Young-Laplace equation locally

$$p|_{\text{meniscus}} = -\frac{2\bar{\gamma}}{h}\bigg|_{\text{meniscus}}, \tag{2.20}$$

where the external atmospheric pressure is taken as the pressure datum, $p = 0$, and the curvature has been approximated by a circular arc between the surfaces — see eqn. (1.5).

Non-dimensionalization

The problem is non-dimensionalized using the height scale $[h] = h_0$, the radial scale $[r] = \sqrt{Rh_0}$ and the pressure scale $[p] = \bar{\gamma}/h_0$. The new dimensionless coordinates are written with hats, so that, for example, the dimensionless separation of the two surfaces is now $\hat{h}(\hat{r}) = 1 + \hat{r}^2/2$.

The dimensionless version of (2.19) gives that the dimensionless liquid pressure $\hat{p}(\hat{r}, \phi)$ — where $(\hat{r}, \phi)$ are the usual (dimensionless) polar coordinates in the plane of the flat surface — must obey the partial differential equation (PDE)

$$\mathsf{Ca}\frac{\partial \hat{h}}{\partial \hat{x}} = \frac{1}{6}\nabla \cdot (\hat{h}^3 \nabla \hat{p}), \tag{2.21}$$

where the (modified) capillary number

$$\mathsf{Ca} = \frac{\mu U}{\bar{\gamma}}\sqrt{\frac{R}{h_0}}. \tag{2.22}$$

The capillary number measures the relative size of the shear (Couette) contribution to the liquid flux compared to the capillary pressure-driven (Poiseuille) flux. Note that this

differs from the usual capillary number [Leal, 2007], $\mu U/\gamma$, since the typical vertical and radial length scales are different here, namely h_0 for Couette flow and $\sqrt{h_0 R}$ for the capillary-driven Poiseuille flow. The system is then controlled by two parameters, the capillary number Ca and the dimensionless bridge volume $\hat{V}$.

We now assume that Ca $\ll 1$ — an assumption that is reasonable for the insect experiments of Federle et al. [2004] (see later) — allowing us to treat the shear as a small perturbation to the bridge equilibrium.

Small Ca perturbation expansion

To find solutions in the small shear limit, Ca $\ll 1$, a perturbation expansion is conducted in Ca about the equilibrium solution to determine the pressure field and bridge position. In particular, the position of the meniscus, $\hat{r}_M$, and the pressure, $\hat{p}$, are expanded in terms of the capillary number

$$\begin{aligned} \hat{r}_M(\phi) &= \hat{a}_0 + A\,\mathsf{Ca}\, f(\phi) \\ \hat{p}(\hat{r},\phi) &= -\frac{2}{\hat{h}(\hat{a}_0)} + \mathsf{Ca}\ \delta p(\hat{r},\phi). \end{aligned} \tag{2.23}$$

We wish to determine the corrections to the radius and pressure, i.e. find the constant A and functions $\delta p(\hat{r},\phi)$ and $f(\phi)$.

Note that the surfaces are flat in the azimuthal angular direction, $h_\phi = 0$, because of the assumption of axisymmetry, so that the gradient of h in the $\hat{x}$-direction in the PDE (2.21) is $\hat{h}_{\hat{x}} = \hat{h}_{\hat{r}} \cos\phi$. It is then natural to seek a separable solution of the form $\delta p(\hat{r},\phi) = P(\hat{r})\cos\phi$ with a similar angular dependence for the meniscus position, $f(\phi) = \cos\phi$. From (2.21), the equation for the radial dependence of the first-order correction to the pressure is

$$P'' + \frac{\hat{h} + 3\hat{r}\hat{h}'}{\hat{r}\hat{h}} P' - \frac{P}{\hat{r}^2} = \frac{6\hat{h}'}{\hat{h}^3}, \tag{2.24}$$

where we recall that $\hat{h}(\hat{r}) = 1 + \hat{r}^2/2$. This is subject to two boundary conditions at $\hat{r} = \hat{a}_0$, where the pressure is set by the curvature through the Young-Laplace equation (2.20) and there is no fluid flux, i.e.

$$P(\hat{a}_0) = \frac{2\hat{h}'(\hat{a}_0)}{[\hat{h}(\hat{a}_0)]^2} A, \tag{2.25}$$

$$P'(\hat{a}_0) = \frac{6}{[\hat{h}(\hat{a}_0)]^2}. \tag{2.26}$$

The magnitude of the meniscus perturbation A is unknown, and so an extra boundary condition is required: the pressure must be non-singular at the origin, and considering (2.24) at small values of $\hat{r}$ gives that

$$P \sim C\hat{r} + \frac{3}{8}(2-C)\hat{r}^3 \quad \text{as} \quad \hat{r} \to 0 \tag{2.27}$$

for some constant C. Note that (2.27) is in fact two conditions with an extra unknown C: when calculating P, (2.27) is imposed a small distance from the origin in both P and its derivative (so that the unknown C can be determined/cancelled). The problem (2.24)–(2.27) is therefore fully specified, when given an equilibrium radius $\hat{a}_0$.

For a given $\hat{a}_0$, the ODE (2.24) is solved for $P(\hat{r})$ subject to the boundary conditions (2.26) & (2.27) using MATLAB's in-built BVP solver `bvp4c`; the relevant radial perturbation A is then calculated from (2.25).

To close the problem requires the determination of $\hat{a}_0$, which comes indirectly from the dimensionless bridge volume constraint. In practice, it is easier to pick $\hat{a}_0$ and find the appropriate dimensionless volume $\hat{V}$ from

$$\hat{V} = \pi\left(\hat{a}_0^2 + \frac{\hat{a}_0^4}{4}\right). \tag{2.28}$$

At leading order in Ca, the pressure is constant and equal to the value in the static case. The change in pressure occurs at $O(\mathrm{Ca})$; two illustrative examples of the first order correction to the pressure field inside the bridge are shown in fig. 2.9 for different dimensionless bridge volumes. In fig. 2.9a, the dimensionless bridge volume is relatively small and the pressure gradient is approximately uniform and aligned with the direction of the imposed shear. For bridges with larger dimensionless volume, as in fig. 2.9b, a recirculating flow is found; this recirculation leads to a much stronger resistive pressure gradient near the origin and a weaker recirculation around it. A natural question to ask is then: how does this affect the resistance to shear?

2.3.2 Resistance to shear during steady motion

For shearing to be maintained in a steady state, a tangential force must be applied to each solid surface. The dimensional shear force that the liquid applies on the flat plate is $\mathbf{F}_{\mathsf{shear}} = \iint \mu \frac{\partial \mathbf{u}}{\partial z}|_{z=0}\, \mathrm{d}A$, which can be expanded in terms of the perturbation solution and rearranged to give the leading order dimensionless shear force in the x-direction

$$\frac{F}{\mu U R} = -2\pi \log[\hat{h}(\hat{a}_0)] - \frac{\pi}{2}\int_0^{\hat{a}_0} \hat{r}\hat{h}P' + \hat{h}P \,\mathrm{d}\hat{r}. \tag{2.29}$$

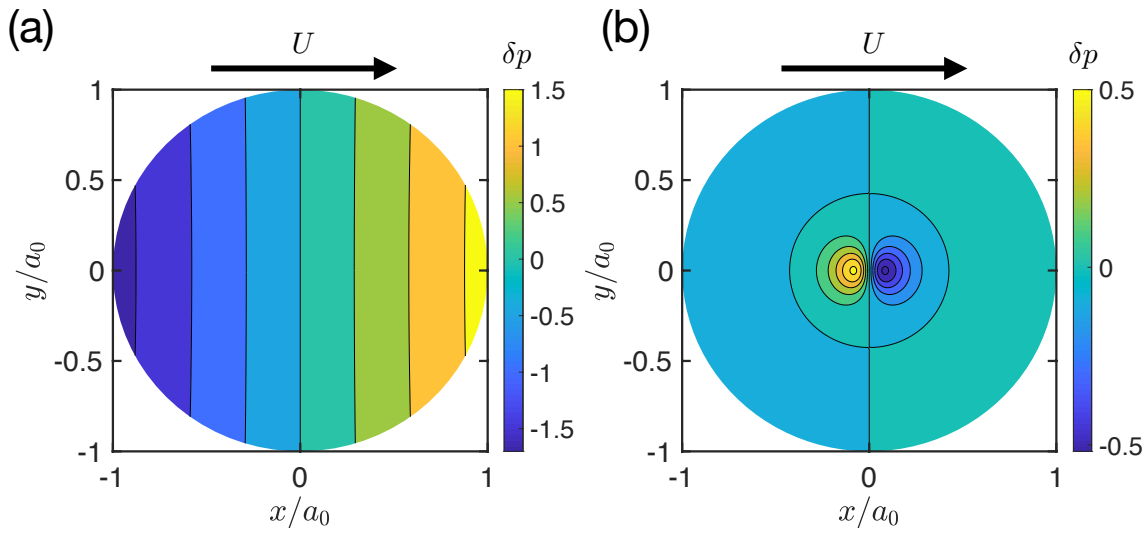

Figure 2.9: The first order correction to the (dimensionless) pressure field inside the bridge, $\delta p(x, y) = (p - p_0)/(\text{Ca}\ \gamma \cos\theta/h_0)$ as it is sheared in steady state for (a) $V/(Rh_0^2) = 1$ and (b) $V/(Rh_0^2) = 100$. The leading order pressure is uniform, $p_0 = -2\bar{\gamma}/h(a_0)$. Note that the radial lengths have been rescaled so that the equilibrium position has $r = 1$ in these images; the corresponding equilibrium radii are $a_0/\sqrt{Rh_0} = 0.30$ and 9.5, respectively. The deviation in meniscus position is not illustrated for simplicity.

The shear force F can be found as a function of the volume V, though in practice it is simpler to use the equilibrium bridge radius a_0 as a parameter and compute the appropriate V given by (2.28) (as discussed before). From this shear force, $F[V(a_0)]$, for a single bridge of volume V the total shear force due to n such bridges can be calculated since $F_{\text{tot}}(V_{\text{tot}}) = nF(V_{\text{tot}}/n)$ with $V_{\text{tot}} = nV$.

The contributions to the required horizontal force from both the resulting Couette flow and the counter flow due to the leading order pressure gradient are both linear in the shear velocity $\mathbf{U} = U\hat{\mathbf{x}}$, and so the shear force is linear in U. The goal is to find the prefactor for this linear relationship as the bridge volume and geometry are varied and, in particular, to determine the role of the splitting described in §2.2.4.

The resistance to shear must be equal and opposite on each of the solids [Batchelor, 1967]. To corroborate the calculation of the resistance to shear on the planar surface, the force applied on the rough surface has also been calculated in Appendix 2.C, taking careful account of the fact that, in this case, the pressure has a horizontal component when it acts on a curved or sloping surface. The difference in the resistance to shear on each surface is found to be less than 0.1% over the range presented here, supporting the accuracy of the calculations. Results are therefore presented for the resistance to shearing of the planar surface, but it is equivalent to consider the shearing of the rough surface.

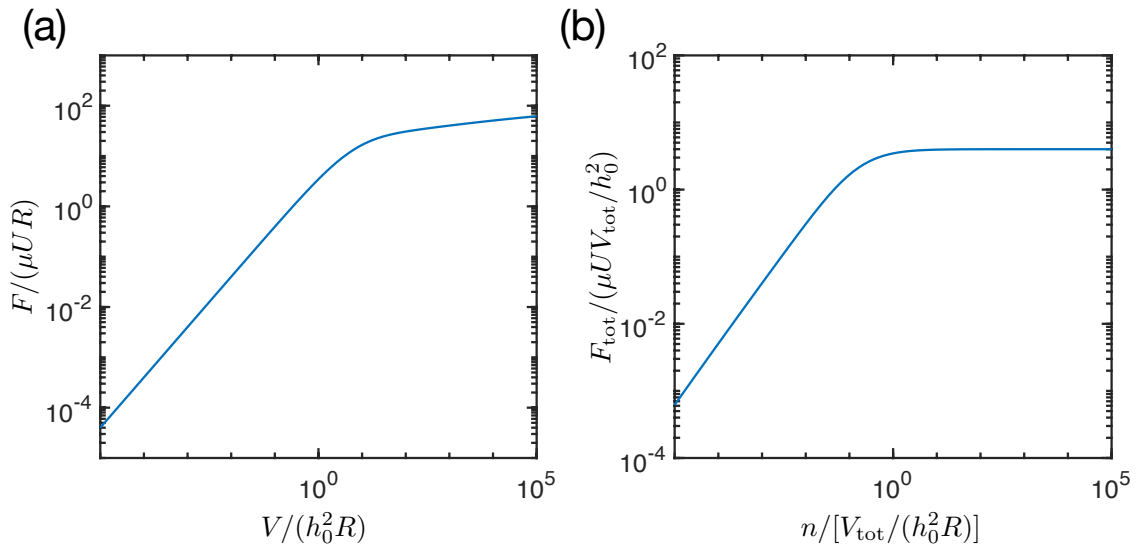

Figure 2.10: (a) The magnitude of the dimensionless shear force for a single bridge as a function of the bridge volume. (b) The magnitude of the total shear force when splitting into n bridges. In both cases, results are presented for the shear force applied on the flat plate only; when the results for the rough surface are plotted as well, they are indistinguishable at the scale of the plot.

The shear force applied on the flat plate by a single bridge depends on which of the two types of pressure fields shown in fig. 2.9 are observed: these lead to different behaviours of $F(V)$, as can be seen in fig. 2.10. Figure 2.10a shows the dimensionless applied shear force for a single bridge; in this case, the force increases more rapidly with dimensionless volume when the volumes are small, $V/(h_0^2R) < O(10)$, than when they are larger, $V/(h_0^2R) \geq O(10)$. For smaller volumes, the shear force increases linearly with volume according to $F/(\mu UR) \approx 4V/(h_0^2R)$ (see Appendix 2.C for a derivation of this relation). For larger bridge volumes, the shear force increases extremely slowly: the dimensionless force $F/(\mu UR)$ increases by approximately 10 for each additional factor of 10 increase in the dimensionless volume $V/(h_0^2R)$ (i.e. it appears to be approximately logarithmic). In the remainder of this chapter, the dimensionless shear force in this large bridge volume scenario will be approximated as constant for simplicity, with a value $F/(\mu UR) \approx 100$.

Having considered the force required to shear a plate past a single bridge, it is important to consider the effect of bridge splitting on the total shear force that is generated. For n such bridges with a fixed total liquid volume, V_{tot}, the total shear force due to this effect is calculated and is plotted in fig. 2.10b. Again there are two distinct behaviours, transitioning when the number of bridges is in the region of $n \approx 0.1[V_{\mathrm{tot}}/(h_0^2R)]$. Below this, the total force increases almost linearly; above the transition, the dimensionless total

force remains approximately constant as more splitting occurs, taking a value $F_{\text{tot}} \approx 4\mu U V_{\text{tot}}/h_0^2$ (again, see Appendix 2.C). For a smaller number of bridges (i.e. larger bridge volumes), the total shear force is approximately independent of the gap width and liquid volume: $F_{\text{tot}} \approx 100\ \mu U R\ n$.

2.3.3 Comparison with measured shear forces

As mentioned earlier, the linear dependence of the shear force on the shear velocity is similar to that observed by Federle et al. [2004] for Asian Weaver ants on a rotating turntable. These experiments suggest a linear relationship with a gradient close to $c = F/U \approx 20\ \mathrm{N\,s/m}$, as shown in fig. 2.7. The question is then to explain the order of magnitude of the friction constant c — can it be explained as being the result of the splitting of capillary bridges on a rough surface?

To make the comparison between the predictions of the model presented here and the experimental observations of Federle et al. [2004], published values of parameters for Asian Weaver ants are taken from Dirks and Federle [2011b], Federle et al. [2004], Federle et al. [2002] and Dirks et al. [2010]. Since the mechanism for generating a shear resistance discussed here would work equally well for a single curved object (i.e. the whole foot pad, or a single asperity,) as many smaller ones, it is not immediately clear whether the relevant scale here is the whole oil secretion (volume $V \approx 10^3\ \mu\mathrm{m}^3$ [Dirks and Federle, 2011b] with radius of curvature $R \approx 100\ \mu\mathrm{m}$ of the whole footpad [Federle et al., 2004]) or the emulsion droplets (smaller volume and a radius of curvature from local asperities). In either case, the experimental capillary number is small, $\mathrm{Ca} \lesssim 0.1$ (based on a shearing rate $U \approx 1\ \mathrm{mm/s}$, viscosity $\mu \approx 0.1\ \mathrm{Pa\,s}$ [Federle et al., 2002], and assuming a similar surface tension to other insect species $\gamma \approx 20$–$30\ \mathrm{mN/m}$ [Dirks, 2014, Gernay et al., 2016]), provided that the separation $h_0 > 100\ \mathrm{nm}$. Hence the small capillary number theory developed here is expected to be valid for these experiments.

At the scale of the whole foot, a single bridge consisting of the entire oily secretion may be considered, and results applied from fig. 2.10a. If the ant's foot is reasonably far from the surface, $h_0 > \sqrt{V/10R} \approx 1\mu\mathrm{m}$, then the force would be expected to be in the linear regime with friction constant $c = F/U \approx 4\mu V/h_0^2$. Using the previously mentioned values, the friction coefficient is found to be $c < 10^{-4}\ \mathrm{N\,s/m}$. This is around five orders of magnitude smaller than the observed value. If the separation were much smaller than this, $h_0 < 1\ \mu\mathrm{m}$, then instead the force-velocity relationship would be expected to saturate, so that $c \approx 100\mu R \approx 10^{-3}\ \mathrm{N\,s/m}$ — again, much smaller than observed experimentally.

Alternatively, it is possible to estimate the shear force from bridges on the scale of the watery droplets within the emulsion, using results from fig. 2.10b. Suppose that

the secretion consists of 10% watery droplets by volume, of typical extent $a_0 \approx 1\ \mu\mathrm{m}$ (estimated from images of the insect secretion [Dirks et al., 2010]), and that these all form bridges on a substrate roughness of a similar scale, $R \approx 1\mu\mathrm{m}$. Then, since the radial lengthscale is $1/100$th of the whole foot and the volume is $1/10$th of the whole secretion, approximately $n \approx 1000$ bridges would be expected for the same separation h_0. At the scale of the individual bridges, the insect foot will look flat compared to the substrate roughness. It is then reasonable to consider a shear being applied on the flat surface, whilst measuring the resulting resistance to shear. If the surface separation is large enough $h_0 > \sqrt{0.1V_{\mathsf{tot}}/nR} \approx 0.1\ \mu\mathrm{m}$, then the shear friction is bounded above by $c \approx 4\mu V_{\mathsf{tot}}/h_0^2 < 10^{-3}\ \mathrm{N\,s/m}$; if h_0 is smaller than this then the friction will be $c \approx 100\mu Rn \approx 10^{-2}\ \mathrm{N\,s/m}$. Again, this remains significantly smaller than the value measured experimentally.

It can therefore be concluded that the shear resistance provided by the migration of capillary bridges is not sufficient to generate the shear forces observed in insects. Nevertheless, this does give an example of a mechanism that would yield a linear relationship between shear force and velocity. Additionally, this bridge migration may help to retain liquid during shear, when in other scenarios the bridges may be sheared away or end up coating the surfaces.

2.4 Conclusions

In this chapter, we have considered theoretically the effects of bridge splitting on both normal adhesion and tangential shear forces between rough and flat surfaces. In particular, it has been shown that the tendency of capillary bridges to spontaneously migrate to regions in which the gap separation is locally minimal acts to enhance the normal capillary adhesion force, as well as leading to a mechanism through which the shear force is linear in the imposed shearing velocity.

By solving for the shape of capillary bridges numerically, the total adhesive capillary force was calculated as the number of bridges or surface roughness is varied. For perfectly wetting liquids, splitting bridges generally results in an increase in the adhesion force — an intermediate maximum in the adhesion force is found in this case, corresponding to optimal capillary adhesion away from the very smallest bridges that are stable. For larger contact angles, the optimal adhesion force is larger and found much closer to rupture, similar to the case of smooth flat surfaces studied previously [De Souza et al., 2008] (see Appendix 2.B). Fixing the number of capillary bridges, the adhesion is found to increase

with the amplitude of the surface roughness, with the maximum capillary adhesion force increasing by orders of magnitude in some cases.

In the case of a small applied shear, steady solutions to the lubrication equations were found, and the tangential force on the base plate required to maintain a steady state was calculated. This shear force is linear in the imposed velocity and initially increases as the liquid is split into more bridges. Whilst the linearity of the force is similar to the findings of experiments on insects [Federle et al., 2004], the magnitude of the force does not appear to be large enough to explain insects' strong resistance to shear. While this hydrodynamic mechanism does not seem to be that behind the resistance to shear seen in these experiments, it is important to emphasize that experiments do suggest a hydrodynamic mechanism of unknown origin.

One physical aspect that has been omitted in the models presented in this chapter is the possibility of contact line pinning, which could be caused by the presence of small-scale roughness or impurities. Pinning would act to hinder the mechanism for the capillary-induced bridge motion used throughout this chapter. It is expected that in scenarios where pinning is important, the bridges may not manage to reach the local minima in gap width and so the observed adhesion force would be lower than the values presented here. However, pinning and contact angle hysteresis could contribute additional resistive forces in the steady shear problem (although the combined force from this and the mechanism of this chapter is unlikely to account for the ant's strong shear resistance).

The analysis in this chapter highlights the possible importance of bridge splitting as a means of exploiting surface roughness to enhance capillary adhesion and resistance to shear. In reality, surfaces will not be as idealized as the identical parabolic asperities studied here, but will vary in both wavelength and amplitude. Indeed, the shape of capillary bridges can be affected by the presence of smaller-scale roughness [Wang et al., 2009], and it will also be important to understand how the results differ for two surfaces that conform closely to one another. Provided that such a roughness can be characterized well by averages of these properties, the predictions of this chapter should carry across qualitatively in these more realistic scenarios. It is hoped that these possible benefits to bridge splitting might inspire more detailed experiments with controlled roughness scales that can test these theoretical predictions quantitatively.

Appendices

2.A Splitting perfectly wetting liquid between plates

The increase in adhesion force with splitting (and intermediate maxima) seen in fig. 2.3 can largely be explained by a competition between the tension force increasing with n and the decreasing pressure force. However, an increase in adhesion force is also initially seen for perfectly wetting liquid, $\theta = 0$, even though in this case there is no tension force, $F_T = 0$.

Heuristically, this is because of changes in shape of the bridge as the liquid is divided more: when splitting, liquid is initially lost preferentially from the centre, or 'neck', of the bridge. This means that the wetted area does not decrease in magnitude as much as might have been expected when splitting perfectly cylindrical bridges (in which the wetted area of a single bridge $A_{\text{wet}} \propto V_1 \propto 1/n$). Despite this 'necking' also causing the curvature to become more positive (i.e. a more repulsive pressure), the pressure force-per-bridge (the product of curvature and wetted area) decreases slowly enough with number of bridges that having more bridges still results in a larger total adhesion force.

As the bridges are further split, the wetted area begins to decrease (and curvature to increase) more rapidly with n, causing an eventual decrease in the pressure force, and hence total force.

This increase in the pressure force is only seen when the liquid is very wetting; for contact angles as small as $\theta = 30^\circ$ the pressure force decreases with increasing number of bridges and the increase in adhesion with splitting is simply due to the tension force only.

2.B Rough capillary adhesion with other wettabilities and roughness geometries

Here, we consider modifications to the results for the adhesion force presented in the main text when taking account of different liquid wettabilities and roughness geometries.

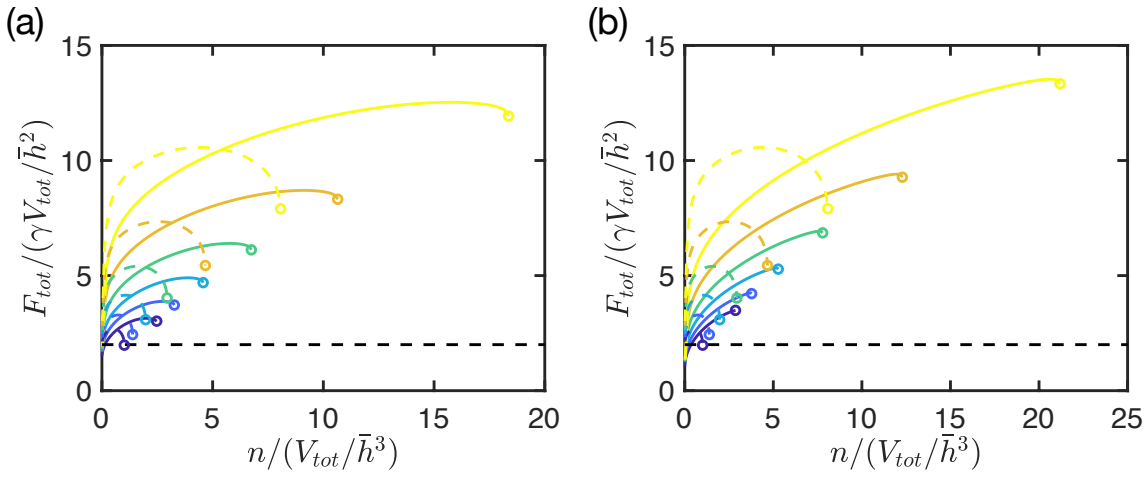

Figure 2.11: Varying θ: the total adhesion force F_{tot} as a function of the number of bridges n for the roughness amplitudes $\Delta h/\bar{h} = \{0, 0.1, 0.2, 0.3, 0.4, 0.5\}$ when (a) $\theta = 45°$, and (b) $\theta = 60°$. In both cases, the dashed curves indicate the results for a perfectly wetting bridge, $\theta = 0$, for comparison with the results in the main text. In both (a) and (b), the direction of increasing $\Delta h/\bar{h}$ and colour code are the same as in fig. 2.5a.

2.B.1 Variation with contact angle

Results in the main text are all for perfectly wetting liquid bridges with contact angle $\theta = 0$. If the contact angle, θ, is varied, then the results remain qualitatively similar (see fig. 2.11). Similarly to the perfectly wetting bridges, rupture is found to occur later and the adhesion force is seen to increase as the roughness amplitude is increased. In fact, splitting is even more beneficial at these contact angles than for perfect wetting: a similar magnitude (or larger) force can be obtained by splitting, but this can be many times more than the large single bridge case of eqn. (2.1), due to the factor $\cos\theta$ there. Additionally, it is possible to get many more bridges before rupture occurs. However, it must be noted that as the contact angle increases, the maximum moves closer to rupture and is not as broad — a more accurate choice of n may be required to maximize the force whilst avoiding rupture.

2.B.2 Variation with aspect ratio

To investigate how the results change as the roughness aspect ratio is altered, α (given by eqn. (2.10)), the force at fixed roughness amplitude is plotted when $\alpha = 100$ and compared to the values obtained at $\alpha = 10$ (the value used for results in the main text). This is shown in fig. 2.12a. If the average height, $\bar{h}$, is held constant and the same roughness amplitudes, Δh, are compared then increasing α corresponds to increasing the

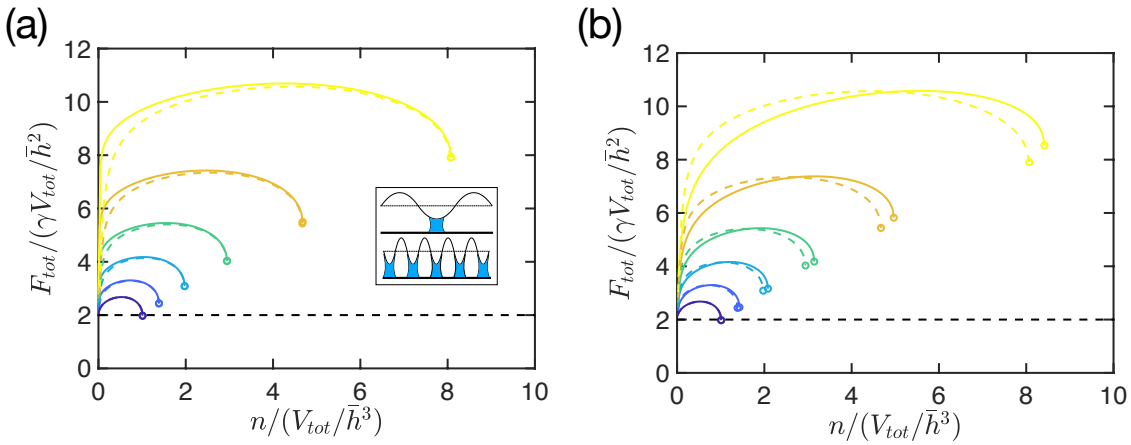

Figure 2.12: The total adhesion force, F_{tot}, as the number of bridges n are varied for various fixed roughness amplitudes $\Delta h/\bar{h} = \{0, 0.1, 0.2, 0.3, 0.4, 0.5\}$ when $\theta = 0$. (a) Varying α: solid curves show numerical results with $\alpha = 100$, while dashed curves reproduce the results of fig. 2.5a (for $\alpha = 10$). Inset: representative profiles showing rough surfaces with aspect ratios of $\alpha = 10$ (lower) and $\alpha = 100$ (upper). (b) The conical case: results for the conical aspect ratio $\beta = \sqrt{20}$ are compared to the parabolic case with $\alpha = 10$ (dashed). In both (a) and (b) the direction of increasing $\Delta h/\bar{h}$ and colour code are the same as in fig. 2.5a.

radius of curvature of the asperity, R, i.e. making the roughness flatter. At the larger aspect ratio, the force initially increases more rapidly with n, but otherwise the behaviour is qualitatively the same: there is an intermediate maximum in the force when varying n and the force increases with the roughness amplitude. There is minimal change in both the force and the value of n at which the bridge ruptures, varying by only a few percent at most.

From this comparison, it seems that changing the value of α does not change the results a great deal, however it should be noted that larger α may mean a sparser density of asperities (since the radius of curvature R is larger, see inset to fig. 2.12a), and so a larger adhesive area may be needed to generate the same strength of adhesion force.

2.B.3 Geometric variation: the conical case

Here, we investigate the effect of changing the local geometry of the roughness. If the roughness is not sufficiently smooth then locally it may look more conical in nature.

Consider a roughness that is locally conical, i.e. $h(r) = h_0 + Br$, for some slope B. The aspect ratio $\beta = \Delta h/B\bar{h}$ is fixed in the same manner that in the parabolic case α was fixed. The eqns. (2.4) are the same as for the parabolic case, but the boundary conditions (2.11) are altered appropriately.

An example of the total adhesion force is given in fig. 2.12b for the case $\beta = \sqrt{20}$. This value of β is used because then the radius at which $\xi(1) = 1$ is the same as for the parabolic case $\alpha = 10$, presented in the main text.

Again, the results are qualitatively similar to the main text: there is an intermediate maximum and the force increases with roughness amplitude. It can be concluded that, regardless of whether the roughness looks locally parabolic or conical, splitting can give a significant increase in adhesion force.

2.C Calculation of the resistance to shear

2.C.1 Shear force on the rough surface

In §2.3 results were presented for the shear force applied by the liquid on the flat surface. Here, the shear force on the rough surface is calculated. In this case, it is important to account for the fact that (in addition to the usual viscous shear $\mu\,\partial\mathbf{u}/\partial z$) the pressure can have a horizontal component that modifies the resistance to shear: the rough surface is sloped and so its normal action leads to a small horizontal component. In terms of the small Ca expansion, this pressure contribution to the shear comes in two main parts, both of which give a leading order correction to the shear that is not seen in the flat case: (i) the uniform leading order pressure $-2/\hat{h}(\hat{a}_0)$ acting over its perturbed radius, and (ii) the asymmetric pressure correction δp acting over the equilibrium footprint $\hat{a}_0$.

The leading order dimensionless shear force that the liquid applies on the rough surface in the x-direction is found to be

$$\frac{F}{\mu U R} = 2\pi \log[\hat{h}(\hat{a}_0)] + \frac{2\pi\hat{a}_0^2}{\hat{h}(\hat{a}_0)}A - \frac{\pi}{2}\int_0^{\hat{a}_0} \hat{r}\hat{h}P' + \hat{h}P + 2\hat{r}^2 P \,\mathrm{d}\hat{r} \tag{2.30}$$

which can be compared to the shear force on the plane (2.29). The second term here is the contribution caused by the moving edge of the liquid bridge; the final term in the integral is the part from the asymmetric pressure correction.

In fig. 2.13, the percentage difference in the calculated shear force on the rough and planar surfaces is plotted. The shear forces differ by less than 0.1% over the range considered — this difference is indistinguishable at the scale of fig. 2.10; default tolerances were used when implementing `bvp4c` (relative and absolute tolerances were 10^{-3} and 10^{-6}, respectively). The difference between shear forces observed here may therefore be attributed to numerical error since the maximum error is within the requested error tolerance. It is therefore suggested that the shear force on each surface is the same, and focus in the main text only on the shear force on the planar surface for simplicity.

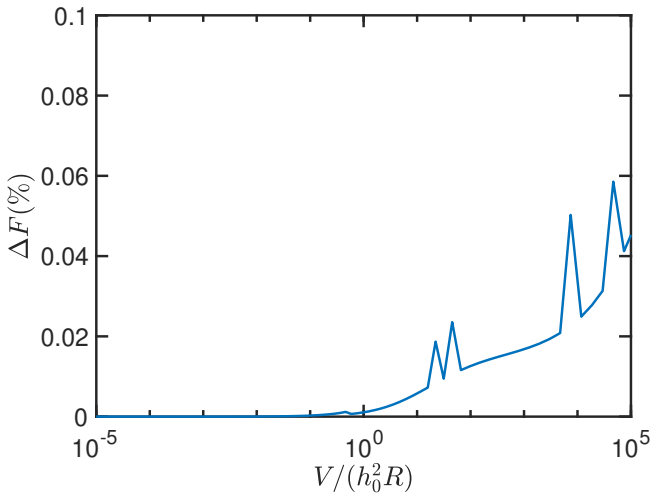

Figure 2.13: The percentage difference in the calculated shear forces on the rough and planar surfaces, $\Delta F = (F_{\text{planar}} - F_{\text{rough}})/F_{\text{planar}}$, is less than 0.1%. The absolute error in $F/(\mu U R)$ is at most 0.04; the relative and absolute tolerances used in these calculations was 10^{-3} and 10^{-6}, respectively. An error of 0.1% corresponds to 10^{-3} relative error, so the maximum observed error here is consistent with the error tolerance.

2.C.2 Behaviour for small bridges

If the bridges are small (but still remain in the lubrication limit), $\hat{a}_0 \ll 1$, then the rough surface will look flat on the scale of the bridge with $\hat{h} \approx 1$ (and also $\log[\hat{h}(\hat{a}_0)] \approx \hat{a}_0^2/2$). The solution of (2.24) is then

$$P(\hat{r}) \approx 6\hat{r}, \tag{2.31}$$

because the condition (2.27) enforces that the pressure behaves linearly at small radii, and the no flux boundary condition at the edge, (2.26), gives a pressure gradient of 6. This linearity in P can be seen in fig. 2.9a. The shear force on the flat surface can then be approximated by

$$\frac{F}{\mu U R} \approx -\pi \hat{a}_0^2 - \frac{\pi}{2} \int_0^{\hat{a}_0} 12\hat{r}\ \mathrm{d}\hat{r} \approx -4\pi \hat{a}_0^2. \tag{2.32}$$

Furthermore, in this small bridge case, the dimensionless bridge volume is $\hat{V} \approx \pi \hat{a}_0^2$ so that the predicted shear force behaviour is

$$\frac{F}{\mu U R} \approx -4\frac{V}{h_0^2 R}, \qquad \text{or} \qquad \frac{F_{\text{tot}}}{\mu U V_{\text{tot}}/h_0^2} \approx -4 \tag{2.33}$$

which is observed in the results of fig. 2.10 for small V or large n.

Chapter 3

Contact adhesion of a deformable sphere

In this chapter, the adhesion of a deformable sphere to a rigid planar substrate is investigated. We consider the cases of an impermeable solid sphere and a poroelastic sphere. The first case reproduces the prior results of Fogden and White [1990] and Goryacheva and Makhovskaya [1999]. The porous sphere is assumed to be saturated with liquid and deformable; therefore, once it makes contact with the plane, the liquid present in the pore space can be drawn out of the sphere by the capillary pressure in the liquid bridge. In equilibrium, this liquid bridge adheres the poroelastic sphere to the substrate. When no external force is applied, the wetting and contact radii are found as functions of the initial sphere size, and are compared to experiments using hydrogel beads. Relationships are then found between the force, contact radius and distance that the sphere has indented into the plate when the applied force is small, and these results are compared to the classic contact adhesion of Hertz [1882] and Johnson, Kendall, and Roberts [1971].

3.1 Introduction

Simple models of rigid spheres adhering to plates (or other spheres) through the surface tension of a liquid bridge suggest that the adhesion force is independent of the amount of liquid within the bridge when close to contact, as discussed in Chapter 1 (see, in particular, eqn. (1.13)). Consistent with this observation, Chapter 2 showed that the adhesion force can be substantially increased by dividing a given amount of adhering liquid into many smaller bridges between a collection of many spherical asperities on a rough surface and a plane — if the adhesion force-per-bridge is independent of volume then removing liquid to supply additional bridges will always result in an increase in the adhesion force. Here,

Figure 3.1: A hydrogel bead rests on a rigid planar substrate. Water may be expelled from the bead as it deforms, forming a liquid bridge around the contact that can adhere the bead to the substrate. (The bead depicted has a diameter of approximately $3\ \mathrm{cm}$.)

we return to investigate the adhesion of a single sphere to a rigid plate, but allow the sphere to deform, focusing on the case where it is in contact with the rigid substrate.

The study of elastic contact between spheres that can deform has a long history, dating back as far as work by Hertz [1882], who found relations between the applied force, size of the contact area and distance of approach of the spheres. This was expanded to include adhesive contact by Johnson, Kendall, and Roberts [1971] — which is often referred to as JKR adhesion — where it was shown that a finite pull-off force is needed to detach contacting surfaces. Similar results have since been found for capillary adhesion of deformable spheres, both in condensation [Fogden and White, 1990] and for a constant liquid volume [Goryacheva and Makhovskaya, 2001].

As mentioned in Chapter 2, in many capillary adhesion scenarios it is not desirable to require condensation of the liquid for adhesion to be achieved. If condensation is not the source of the capillary adhesion then a natural question that follows is: where does the adhering liquid come from? In this chapter, we present a new solution to this problem by considering the adhesion of a saturated poroelastic sphere to a rigid, planar substrate (such as the hydrogel bead shown in fig. 3.1). If this permeable sphere is saturated with a liquid that wets the substrate then, once it is pressed into contact with the substrate, the liquid will naturally form a bridge between the sphere and substrate, with the resulting (negative) capillary pressure drawing more liquid out from the pore space. The presence of this liquid between the poroelastic sphere and substrate will then act to adhere the sphere there. However, the elastic deformation of the sphere will also act to limit the

'leakage' of liquid onto the substrate. In equilibrium, there will therefore be a balance between the applied force, elastic deformation and capillary adhesion.

In recent years, there has been significant interest in a variety of problems related to the interaction between deformable surfaces and surface tension, with so-called elasto-capillary systems exhibiting many interesting and counter-intuitive phenomena [Roman and Bico, 2010, Style et al., 2017, Bico et al., 2018]. In general, capillary forces are able to deform a solid on a scale where they balance the elastic forces — in many scenarios this scale is the elasto-capillary length, $\ell_{ec} = \gamma/E$, where E is the Young's modulus of the solid. The features of elasto-capillarity are typically found on a lengthscale of ℓ_{ec}, which is usually relatively small: for extremely soft systems it can be as large as millimetres, but is usually less than this.

Previous studies of deformable porous solids have shown that leakage of liquid can cause the bouncing of hydrogel beads on a hot surface, called the elastic Leidenfrost effect [Waitukaitis et al., 2017], and we expect that a similar leakage here could lead to capillary forces that may enhance contact adhesion. This adhesion has been previously investigated for hydrogel spheres by Sokoloff [2016], who used a simple model to show that swollen hydrogel could de-swell if the capillary pressure exceeds the osmotic pressure. However, the capillary adhesion forces on the sphere were never fully addressed.

The aim of this chapter is to find equilibrium solutions for the capillary adhesion of a poroelastic sphere to a flat impermeable surface. As part of this, we shall (re-)derive the capillary contact adhesion solutions of Fogden and White [1990] and Goryacheva and Makhovskaya [2001] that will be used as a starting point for attacking the porous problem, as well as being useful for comparison with later results. We begin, however, by reviewing the classic solid-solid contact adhesion of Hertz and JKR.

Hertz contact

When two elastic solids are brought into contact, the force pressing the solids together must balance the resulting elastic deformation within the solids themselves. To understand this balance, we first consider a scaling analysis of two spheres pushed together a distance δ by an applied force F. Assuming a small circular contact region of radius a forms between the two spheres of radius R, the locally parabolic geometry gives $a \propto \sqrt{\delta R}$. The elastic displacements in a sphere of radius R have size δ, resulting in a strain δ/a; the corresponding typical elastic stress is then $\propto E\delta/a$ where E is the Young's modulus. This induced stress acts over a contact area πa^2 and so, in equilibrium, the balance between the force and contact area would therefore be expected to behave like $F \propto Ea\delta \propto Ea^3/R$.

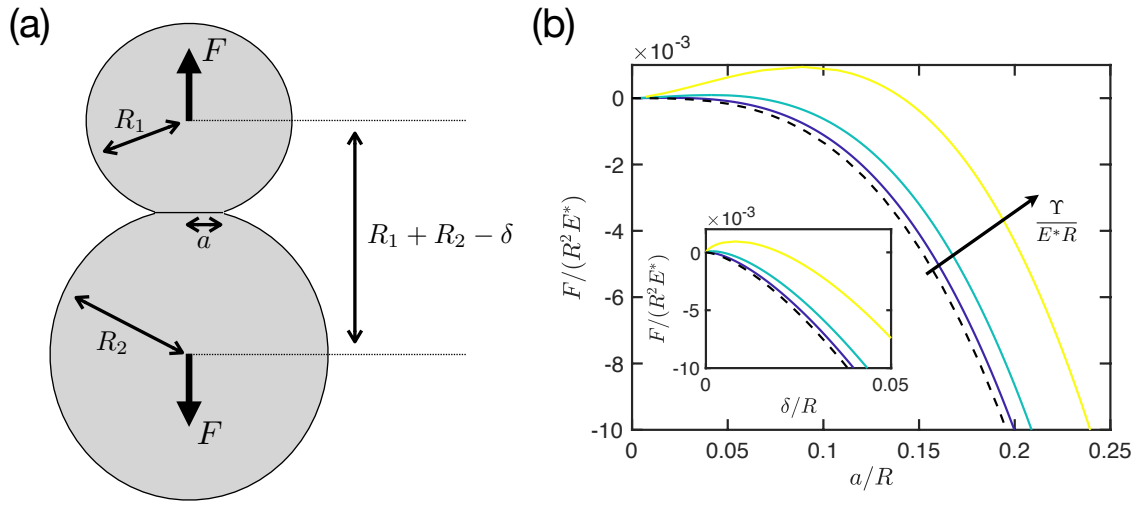

Figure 3.2: (a) Two spheres of radii R_1 and R_2 are in contact under an applied force F. The spheres have approached each other by a distance δ and the contact between them has a radius a. (b) Relationship between the force F and the contact radius a for the JKR solution (3.3) (solid curves) with adhesion strength $\Upsilon/(E^*R) = 10^{-6}, 10^{-5}, 10^{-4}$, compared to the Hertz solution (3.1) (black dashed curve). Here, Υ is the solid-solid surface energy. Inset: Relationship between the force F and the distance of approach of the spheres δ for JKR and Hertz solutions.

A more thorough analysis of the elastic contact between two spheres of radii R_1 and R_2 (illustrated in fig. 3.2a) was conducted by Hertz [1882]. The force F_H and distance of approach of the two spheres δ_H are found in terms of the contact radius to be [Johnson, 1987]

$$F_H = -\frac{4E^* a^3}{3R}, \qquad \delta_H = \frac{a^2}{R}, \tag{3.1}$$

where E^* is defined in terms of each sphere's Young's modulus $E_{1,2}$ and Poisson's ratio $\nu_{1,2}$, and R is defined from the sphere radii $R_{1,2}$, by

$$\frac{1}{E^*} = \frac{1-\nu_1^2}{E_1} + \frac{1-\nu_2^2}{E_2}, \qquad \text{and} \qquad \frac{1}{R} = \frac{1}{R_1} + \frac{1}{R_2}, \tag{3.2}$$

respectively. Note that we choose the sign convention for the force, F, such that $F > 0$ whenever there is adhesion; the force can therefore be thought as being applied to pull the solids apart (as shown in fig. 3.2a). This is different to the usual presentation in the literature: the Hertz force is usually positive in (3.1). Our sign convention is used throughout the rest of this chapter for consistency with the rest of the thesis.

JKR theory

Contacting solids often have a mutual attraction, resulting in solid-solid adhesion. The influence of this on equilibrium solutions was studied by Johnson, Kendall, and Roberts [1971], with this solid-solid adhesion of elastic bodies often called JKR adhesion. Johnson, Kendall, and Roberts [1971] found that, for a solid-solid surface energy Υ, the force F_{JKR} and distance of approach of the spheres δ_{JKR} satisfy the relations

$$F_{JKR} - 6\pi\Upsilon R - \sqrt{12\pi\Upsilon R(3\pi\Upsilon R - F_{JKR})} = -\frac{4E^*a^3}{3R}, \qquad \delta_{JKR} = \frac{a^2}{R}, \qquad (3.3)$$

where R and E^* are as defined in (3.2). Note that (3.3) reduces to (3.1) when there is no solid-solid adhesion, $\Upsilon = 0$.

Some typical solutions for the force-contact radius relationship are shown in fig. 3.2b, for a few different values of the strength of the adhesion compared to the sphere stiffness, $\Upsilon/(E^*R)$. We note that for a given force F, the contact radius a is larger for JKR adhesion than Hertz contact, as might be expected when allowing solid-solid adhesion.

Another important difference between JKR adhesion and Hertz contact is that there is a (positive) maximum in the force: a pull-off force $F_{\text{pulloff}} = 3\pi\Upsilon R$ must be exceeded to detach the two surfaces. When no force is applied there is a non-zero contact radius: the adhesion between the surfaces means that once the force is removed, the surfaces still remain attached. The contact radius and distance of approach of the spheres when there is no applied force, $F = 0$, are

$$a = \left(\frac{9\pi\Upsilon}{E^*}\right)^{1/3} R^{2/3}, \qquad \delta = \left(\frac{9\pi\Upsilon}{E^*}\right)^{2/3} R^{1/3} \qquad (3.4)$$

so that larger spheres have a larger contact radius and are compressed together more.

3.2 Capillary adhesion of an elastic sphere

To understand the adhesion of a poroelastic sphere to a surface, we first need to consider how one of these permeable spheres will deform in contact with a planar surface when subject to capillary stresses and an applied force. A starting point for this is the problem of an impermeable elastic sphere of radius R that is contacting a rigid, planar substrate with an intervening capillary liquid bridge that provides an adhesion force, as illustrated in fig. 3.3.

Similar problems have been previous studied by Fogden and White [1990] for the case of capillary condensation between two elastic spheres, and Goryacheva and Makhovskaya [2001] for a fixed volume of liquid between two axisymmetric elastic bodies with local

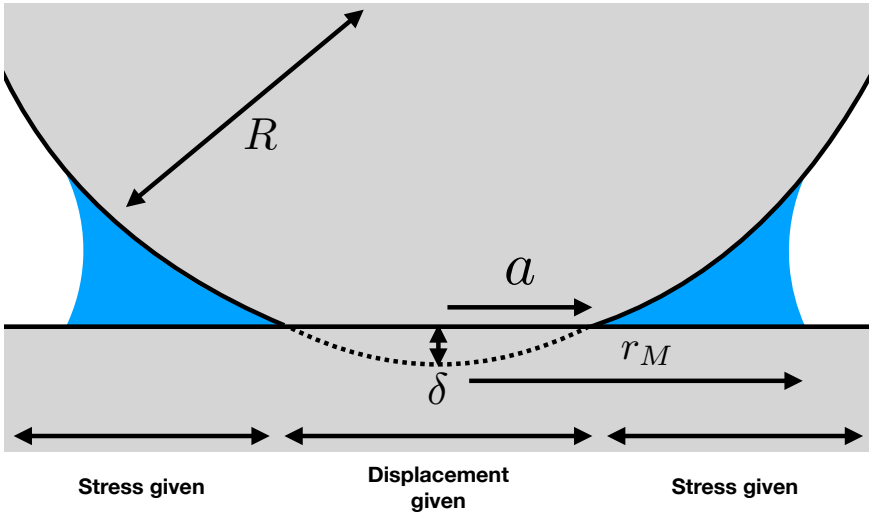

Figure 3.3: An impermeable sphere of radius R contacts a rigid plane, indenting a distance δ with a contact region of radius a. A liquid bridge adheres the sphere to the plane through its surface tension, and wets a radius r_M. The sphere is in equilibrium, with an applied force F directed away from the planar substrate. Within the contact region, $0 \leq r \leq a$, the displacement is known; for $r > a$, the stress on the sphere is known. This diagram is not to scale: the sphere radius, R, is assumed to be much larger than both the contact and wetting radii, a and r_M.

power law shape (i.e. with surfaces that when undeformed have separation $h = Ar^{2n}$). We shall derive the solution for the deformation and stress in an impermeable elastic sphere contacting a rigid plate in the presence of a capillary bridge[1], reproducing some of their results, before adapting this capillary contact solution to solve the related problem of the capillary adhesion of a poroelastic sphere.

3.2.1 Problem set-up

A force F is applied to an elastic sphere of radius R, that is in contact with a rigid planar surface, as shown in fig. 3.3. Once the sphere touches the plane, it deforms and is in contact with this flat substrate over a circular region of radius a. The indent, δ, is the maximum distance that the undeformed sphere would have intersected the plane, or, alternatively, the distance that the centre of the sphere has approached the plane (with $\delta = 0$ defined when the undeformed sphere contacts the plane at a single point). We wish to find equilibrium solutions for the indent and contact radius as functions of the applied force, similar to those already presented for the Hertz and JKR problems.

[1]The solutions here are the same as those of Fogden and White [1990], who did not provide any derivation or reference. Goryacheva and Makhovskaya [2001] solved a similar problem in a different manner, using elliptic integrals.

Our focus is on small deformations; linear elasticity is used to model the deformations of the sphere, which has Young's modulus, E, and Poisson's ratio, ν. Consistent with the assumption of small displacements, the contact area is expected to be small, $a \ll R$, with the strain decaying away from the contact (since the equations of elasticity are elliptic, solutions decay over the same scale as imposed by boundary conditions). Close to the contact, shown in fig. 3.3, both surfaces are sufficiently flat that the deformation of the sphere may be modelled by considering the sphere locally as an elastic half-space and using cylindrical polar coordinates (r, z), with the origin at the centre of the contact on the surface of the plate. Any imposed displacements and stresses on the surface of the sphere can be well approximated by the displacement and stress in the z-direction — $w(r)$ and $\sigma(r)$, respectively — since the normal to the surface is predominantly in the z-direction.

In terms of the adhesion forces on the sphere, we focus on stresses that are applied to the sphere outside the contact and neglect any solid-solid adhesion within the contact area. In particular, we seek solutions for a constant (adhering) capillary pressure over a finite annulus (i.e. the region wetted by the liquid bridge). Then, inside the contact region, $r < a$, the sphere displacement is determined because the shape of the deformed sphere is that of the plane; outside this region, $r > a$, the stress is given, with the wetted region $r < r_M$ subject to the capillary pressure while the non-wetted surface is stress-free (see fig. 3.3).

For now, however, we consider the problem in as general a form as possible: an axisymmetric elastic body contacts a rigid surface, with contact over a region of radius a. There is an arbitrary given displacement inside the contact region and an arbitrary stress outside. This is an example of a mixed boundary value problem.

3.2.2 An elastic mixed boundary value problem

Consider an elastic half-space, $z \geq 0$, with boundary conditions on its surface, $z = 0$, imposing a given displacement, $w = W(r)$, inside the contact radius, $r < a$, and a given (compressive) stress, $\sigma = \Sigma(r)$, outside the contact radius, $r > a$. (Note the sign in the stress here is such that a positive applied stress $\Sigma > 0$ leads to a compressive elastic stress on the sphere, $\sigma > 0$, and similarly a negative applied stress leads to a tensile elastic stress on the sphere; this unusual convention is chosen so that $p = \Sigma(r)$ in the wetted region.)

We solve for the elastic deformation in the half-space using the method outlined in Chapter 10 of Sneddon [1995]. The elastic stresses and displacements in the half-space can be encapsulated by a single function, $\varphi(r, z)$, which is called the Love stress function. The components of the displacement and stress tensor are given in terms of φ in Appendix 3.A.

With these definitions, the elastic stress tensor, τ, satisfies the equilibrium force balance, $\nabla \cdot \tau = 0$, provided that φ obeys the biharmonic equation

$$\nabla^4 \varphi = 0. \tag{3.5}$$

(Note that the compressive stress on the boundary is $\sigma = -\tau_{zz}$ evaluated at $z = 0$.)

To solve for φ in $z \geq 0$, $r \geq 0$, we follow the method of Sneddon [1995] by defining a Hankel transform $\varphi(r, z) \to \tilde{\varphi}(k, z)$ by

$$\tilde{\varphi}(k, z) = \int_0^\infty r\varphi(r, z) J_0(kr)\ \mathrm{d}r, \tag{3.6}$$

where $J_0(x)$ is the zeroth order Bessel function of the first kind. (Note that the Hankel transform is equivalent to a two-dimensional Fourier transform for axisymmetric functions.) Since

$$\widetilde{\nabla^2 \varphi} = \tilde{\varphi}_{zz} - k^2 \tilde{\varphi}, \tag{3.7}$$

we may take a Hankel transform of eqn. (3.5). Enforcing that deformations decay as $z \to \infty$ and that there is no tangential stress at the surface $z = 0$ (using Appendix 3.A), we find the Love stress function must have the form

$$\tilde{\varphi}(k, z) = \frac{A(k)}{k} \left(\frac{\lambda}{\lambda + G} + kz \right) e^{-kz}, \tag{3.8}$$

where λ, G are the Lamé coefficients for the elastic body, and $A(k)$ is an as yet unknown function. Finding the displacements and stresses in the elastic body therefore reduces to solving for this unknown $A(k)$.

From (3.8), the boundary conditions giving the displacement and stress on the boundary ($z = 0$) can be rewritten as two integral equations

$$\begin{aligned} -\frac{\lambda + 2G}{G} \int_0^\infty k^2 A(k) J_0(kr) \mathrm{d}k &= W(r) \qquad r < a, \\ 2(\lambda + G) \int_0^\infty k^3 A(k) J_0(kr) \mathrm{d}k &= -\Sigma(r) \qquad r > a. \end{aligned} \tag{3.9}$$

We rescale the terms in these integral equations as follows: $\zeta = ak$, $\rho = r/a$, $\psi(\zeta) = \zeta^2 A(\zeta/a)$, $f(\rho) = -[Ga^3/(\lambda + 2G)] \times W(a\rho)$, $g(\rho) = -[a^4/2(\lambda + G)] \times \Sigma(a\rho)$. With this rescaling, the dual integral equations (3.9) become

$$\begin{aligned} \int_0^\infty \psi(\zeta) J_0(\rho\zeta) \mathrm{d}\zeta &= f(\rho) \qquad \rho < 1, \\ \int_0^\infty \zeta\psi(\zeta) J_0(\rho\zeta) \mathrm{d}\zeta &= g(\rho) \qquad \rho > 1, \end{aligned} \tag{3.10}$$

where f, g are known functions (from the given stresses and displacements) and ψ is unknown. Once ψ is determined from these equations, then $\tilde{\varphi}$, and hence φ, are also determined; the stresses and displacements in the elastic body may then be readily calculated.

3.2.3 Solution of dual integral equations

Dual integral equations of the form of eqn. (3.10) are common when Hankel transforms are applied to mixed boundary value problems, such as in elastic indentation or electrostatics [Duffy, 2008]. Often in these problems there is no external applied stress, $\Sigma = 0$, so that $g = 0$; solutions can then be found by, for example, using an ansatz $\psi(\zeta) = \int_0^1 \Theta(t)\cos(\zeta t)\mathrm{d}t$ [Sneddon, 1960], which automatically satisfies the second integral equation in (3.10) for $g = 0$.

The analytical solution to (3.10) was found by Noble [1963], which we rewrite as

$$\psi(\zeta) = \frac{2}{\pi}\int_0^1 I_f(t)\cos(\zeta t)\mathrm{d}t + \frac{2}{\pi}\int_1^\infty I_g(t)\cos(\zeta t)\mathrm{d}t, \tag{3.11}$$

where the functions I_f and I_g are determined in terms of integrals of f and g by

$$I_f(t) = \frac{\mathrm{d}}{\mathrm{d}t}\int_0^t \frac{sf(s)}{\sqrt{t^2 - s^2}}\mathrm{d}s, \tag{3.12}$$

$$I_g(t) = \int_t^\infty \frac{sg(s)}{\sqrt{s^2 - t^2}}\mathrm{d}s. \tag{3.13}$$

Noble [1963] also gave expressions for the values of the displacement w outside the contact region, $\rho > 1$, and the (compressive) stress σ inside the contact region, $\rho < 1$. These are

$$-\frac{Ga^3}{\lambda + 2G}w(a\rho) = \frac{2}{\pi}\left[\int_0^1 \frac{I_f(t)}{\sqrt{\rho^2 - t^2}}\mathrm{d}t + \int_1^\rho \frac{I_g(v)}{\sqrt{\rho^2 - v^2}}\mathrm{d}v\right] \qquad \rho > 1, \tag{3.14}$$

$$\frac{a^4}{2(\lambda + G)}\sigma(a\rho) = \frac{2}{\pi\rho}\left[\frac{\mathrm{d}}{\mathrm{d}\rho}\int_\rho^1 \frac{tI_f(t)}{\sqrt{t^2 - \rho^2}}\mathrm{d}t + \frac{\mathrm{d}}{\mathrm{d}\rho}\int_1^\infty \frac{vI_g(v)}{\sqrt{v^2 - \rho^2}}\mathrm{d}v\right] \quad \rho < 1. \tag{3.15}$$

For our sphere-plate geometry, the imposed displacement inside the contact region is

$$W(r) = \delta - \frac{r^2}{2R}, \tag{3.16}$$

where δ is the distance that the sphere has approached, or indented, the plate. Keeping an arbitrary stress profile $\Sigma(r)$ outside the contact region, we find that

$$I_f(t) = -\frac{Ga^3}{\lambda + 2G}\left(\delta - \frac{a^2}{R}t^2\right), \tag{3.17}$$

$$I_g(t) = -\frac{a^4}{2(\lambda + G)}\int_t^\infty \frac{s\Sigma(s)}{\sqrt{s^2 - t^2}}\mathrm{d}s \tag{3.18}$$

which allows for the separation of the two surfaces, $h(r) = w(r) - \delta + r^2/2R$, to be determined outside the contact region ($\rho > 1$)

$$h(a\rho) = \frac{a^2}{\pi R}\left[\sqrt{\rho^2-1} + (\rho^2-2)\arctan\sqrt{\rho^2-1}\right] - \frac{2a}{\pi}\left(\frac{\delta}{a} - \frac{a}{R}\right)\arctan\sqrt{\rho^2-1} + \frac{4a}{\pi E^*}\int_1^\rho \frac{\mathrm{d}v}{\sqrt{\rho^2-v^2}}\int_v^\infty \frac{s\Sigma(s)}{\sqrt{s^2-v^2}}\mathrm{d}s \quad (3.19)$$

and the stress profile inside the contact region ($\rho < 1$)

$$\sigma(a\rho) = \frac{2E^*a}{\pi R}\sqrt{1-\rho^2} + \frac{E^*}{\pi}\left(\frac{\delta}{a} - \frac{a}{R} - \frac{2}{E^*}\int_1^\infty \frac{s\Sigma(s)}{\sqrt{s^2-1}}\,\mathrm{d}s\right)\frac{1}{\sqrt{1-\rho^2}} + \frac{2}{\pi}\int_1^\infty \frac{s\Sigma(s)}{\sqrt{s^2-1}}\frac{\sqrt{1-\rho^2}}{(s^2-\rho^2)}\,\mathrm{d}s. \quad (3.20)$$

The elastic properties of the sphere are encapsulated by the parameter $E^* = E/(1-\nu^2)$, which can be written in terms of the Lamé coefficients as $E^* = 4G(\lambda+G)/(\lambda+2G)$.

Integrating the stress over the contact area gives the force $F = -\int_0^\infty 2\pi r\sigma(r)\mathrm{d}r$ (recalling the sign convention that $F > 0$ corresponds to adhesion)

$$F = -\frac{4E^*a^3}{3R} - 2E^*a^2\left(\frac{\delta}{a} - \frac{a}{R} - \frac{2}{E^*}\int_1^\infty \frac{s\Sigma(s)}{\sqrt{s^2-1}}\,\mathrm{d}s\right) - 4a^2\int_1^\infty s\Sigma(s)\left(\arctan\sqrt{s^2-1} + \frac{1}{\sqrt{s^2-1}}\right)\,\mathrm{d}s. \quad (3.21)$$

The results (3.19)–(3.21) for the separation, compressive stress and force are precisely those derived by Fogden and White [1990], with their parameter $\mathcal{D} = 3/4E^*$. (Although their solution is for two elastic spheres, it is the same as the one presented here if the radius and Young's modulus of one of the spheres are both taken to be infinite, corresponding to a rigid plane — replacing R and E^* here using eqn. (3.2) recovers the two sphere case.) Note that the first term in each of eqns. (3.19)–(3.21) correspond to the Hertz solution, given in eqn. (3.1).

3.2.4 Capillary adhesion

Our focus now moves to capillary adhesion, where we specify the imposed stress Σ: consider a capillary bridge applying an adhering pressure $P < 0$ in an annulus outside the contact region and up to the meniscus position, i.e. $a < r < r_M$. Then, outside the contact region, the imposed stress is

$$\Sigma(\rho) = \begin{cases} P & 1 < \rho < \rho_M \\ 0 & \rho > \rho_M, \end{cases} \quad (3.22)$$

where $\rho_M = r_M/a$ is the rescaled bridge radius. (Note that we neglect the effect of the tension force on the contact line, which is valid if the bridge is wide compared to its height.)

In this capillary adhesion case, the eqns. (3.19)–(3.21) for the separation outside the contact region ($\rho > 1$), the stress inside the contact region ($\rho < 1$) and the force become

$$h(a\rho) = \frac{a^2}{\pi R}\left[\sqrt{\rho^2-1} + (\rho^2-2)\arctan\sqrt{\rho^2-1}\right] - \frac{2a}{\pi}\left(\frac{\delta}{a} - \frac{a}{R}\right)\arctan\sqrt{\rho^2-1} + \frac{4aP}{\pi E^*}\int_1^{\min\{\rho,\rho_M\}} \sqrt{\frac{\rho_M^2-u^2}{\rho^2-u^2}}\mathrm{d}u, \quad (3.23)$$

$$\sigma(a\rho) = \frac{2E^*a}{\pi R}\sqrt{1-\rho^2} + \frac{E^*}{\pi}\left(\frac{\delta}{a} - \frac{a}{R} - \frac{2P}{E^*}\sqrt{\rho_M^2-1}\right)\frac{1}{\sqrt{1-\rho^2}} + \frac{2P}{\pi}\arctan\sqrt{\frac{\rho_M^2-1}{1-\rho^2}}, \quad (3.24)$$

$$F = -\frac{4E^*a^3}{3R} - 2E^*a^2\left(\frac{\delta}{a} - \frac{a}{R} - \frac{2P}{E^*}\sqrt{\rho_M^2-1}\right) - 2a^2P\left[\rho_M^2\arctan\sqrt{\rho_M^2-1} + \sqrt{\rho_M^2-1}\right]. \quad (3.25)$$

Since the stress matches the liquid pressure in the wet region, it cannot be singular at the contact line $r = a$ (i.e. $\rho = 1$); the term proportional to $(1-\rho^2)^{-1/2}$ in (3.24) must therefore vanish, giving a relationship between the indentation δ and the contact radius a

$$\delta = \frac{a^2}{R} + \frac{2aP}{E^*}\sqrt{\rho_M^2-1}. \quad (3.26)$$

In general, the capillary pressure P is related to the shape of the liquid bridge through the Young-Laplace equation (1.2): $P = \gamma\kappa$. The problem of determining the bridge shape is simplified by assuming a thin and wide bridge, which is expected to be reasonable when the contact region is small. This means that, instead of solving in detail for the bridge's shape as in Chapter 2, the bridge's free surface can be approximated by a circular arc. In addition, the effect of the slope of the sphere on the contact angle may be neglected (since slopes are small for small contacts). The capillary pressure P then satisfies the relation

$$P = \frac{-2\bar{\gamma}}{h(a\rho_M)}. \quad (3.27)$$

With a fixed volume of liquid, V, present (e.g. by intentionally applying a droplet of known volume to adhere the surfaces), eqn. (3.23) must be integrated to find the amount of liquid between the two surfaces in the annulus $a < r < r_M$, giving a volume constraint

$$V = \frac{a^4}{2R}\left[(\rho_M^4 - 4\rho_M^2)\arctan\sqrt{\rho_M^2-1} + (2+\rho_M^2)\sqrt{\rho_M^2-1}\right] + 2a^3\left(\frac{\delta}{a} - \frac{a}{R}\right)\left(\sqrt{\rho_M^2-1} - \rho_M^2\arctan\sqrt{\rho_M^2-1}\right) + \frac{8a^3P}{3E^*}(\rho_M-1)^2(2\rho_M+1). \quad (3.28)$$

Non-dimensionalization

This system can be non-dimensionalized by rescaling lengths by R, pressures by E^*, forces by R^2E^* and volumes by R^3 to get the dimensionless variables

$$\hat{a} = \frac{a}{R}, \quad \hat{P} = \frac{P}{E^*}, \quad \hat{F} = \frac{F}{R^2E^*}, \quad \hat{V} = \frac{V}{R^3}. \quad (3.29)$$

This non-dimensionalization introduces an elasto-capillary number

$$\Lambda = \frac{\bar{\gamma}}{RE^*} \quad (3.30)$$

which approximately measures the size of the elasto-capillary length, γ/E, compared to the radius of the sphere: large spheres correspond to weak surface tension and so may be expected to have a small contact region. We therefore consider small values of this elasto-capillary number, Λ. The dimensionless equations are further simplified by defining

$$y = \sqrt{\rho_M^2 - 1}. \quad (3.31)$$

After this rescaling, there are three equations relating $\hat{a}, \hat{P}, \hat{F}, y, \hat{V}, \Lambda$ — namely the force, capillary pressure and volume conditions — which are given by

$$\hat{F} = -\frac{4\hat{a}^3}{3} - 2\hat{a}^2\hat{P}\left[y + (y^2+1)\arctan y\right] \quad (3.32)$$

$$-\frac{2\Lambda}{\hat{P}} = \frac{\hat{a}^2}{\pi}\left[y + (y^2-1)\arctan y\right] - \frac{4\hat{a}\hat{P}}{\pi}\left[y\arctan y - \sqrt{y^2+1} + 1\right] \quad (3.33)$$

$$\hat{V} = \frac{\hat{a}^4}{2}\left[(y^2+1)(y^2-3)\arctan y + (3+y^2)y\right] + 4\hat{a}^3\hat{P}\left[\frac{4}{3}(y^2+1)^{3/2} - y(y^2+1)\arctan y - y^2 - \frac{4}{3}\right]. \quad (3.34)$$

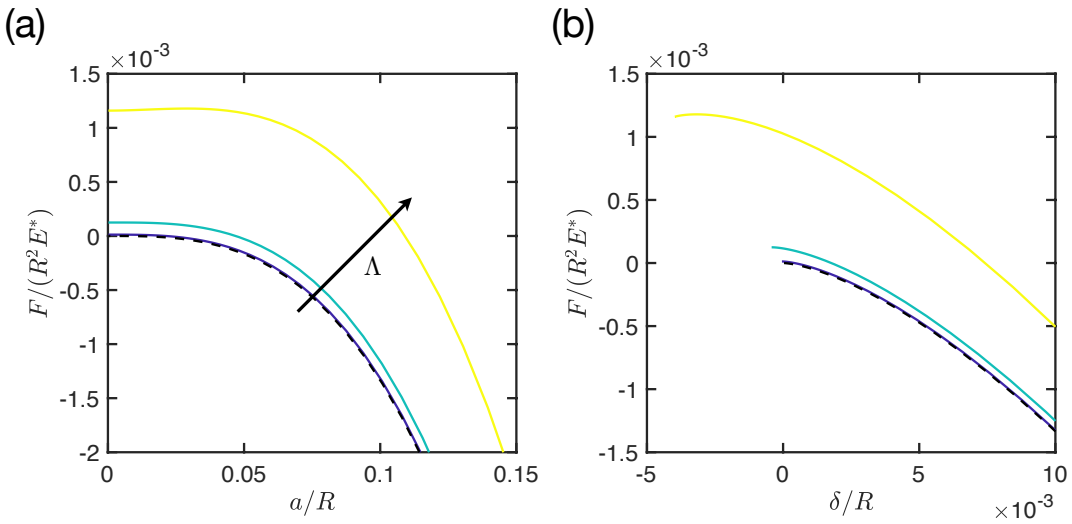

Figure 3.4: Solutions for an impermeable elastic sphere contacting a rigid plate with a liquid bridge of fixed volume. In all cases the liquid volume is $V/R^3 = 10^{-3}$ and there are a range of elasto-capillary numbers $\Lambda = \bar{\gamma}/(E^*R) = 10^{-6}, 10^{-5}, 10^{-4}$ (dark blue, blue-green and yellow respectively). (a) The applied force F as a function of the contact radius a. (b) The force F as a function of the indent δ. The results in both (a) and (b) are compared with the Hertz solution (3.1) (black dashed curve). Note that the curves in (b) terminate when $a = 0$.

These equations are consistent with those derived by Goryacheva and Makhovskaya [2001] for the adhesion of two elastic bodies with parabolic shape[2]. The dimensionless indent, $\hat{\delta} = \delta/R$, can be found from (3.26) in terms of the contact radius and pressure

$$\hat{\delta} = \hat{a}^2 + 2\hat{a}\hat{P}y\,. \tag{3.35}$$

Results

The eqns. (3.32)–(3.34) can be solved after picking values for the liquid volume $\hat{V}$, elasto-capillary number Λ and rescaled meniscus radius y. Sweeping out a range of values for $y > 0$ gives curves of solutions at fixed liquid volume and elasto-capillary numbers; results for $\hat{V} = 10^{-3}$ and $\Lambda = 10^{-6}, 10^{-5}, 10^{-4}$ are plotted in fig. 3.4 and compared to the Hertz solution (3.1).

When Λ is extremely small, the solutions behave much like the Hertz solution — the surface tension has a small effect on the overall behaviour, and there is largely a balance between elastic deformation and applied force. As the elasto-capillary number Λ

[2]The force, pressure and volume conditions here are eqns. (2.7), (2.9) & (2.10) in Goryacheva and Makhovskaya [2001] with $n = 1$. We note, however, that their eqn. (2.9) has a sign error after the φ in the first term (the correct expression is given in eqn. (2.19) of Goryacheva and Makhovskaya [1999] for indenting an elastic half-space, but note the different definition of φ between the two papers).

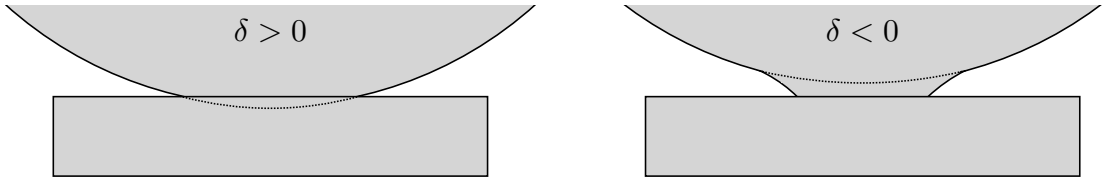

Figure 3.5: Example profiles of sphere indents that are positive, $\delta > 0$, and negative, $\delta < 0$. The sphere with negative indent (on the right) would not contact the substrate if the sphere were undeformed and must have a force applied to pull the sphere away ($F > 0$, adhesion). The sphere with positive indent could have either a force applied towards or away from the substrate (or no force).

is increased, both the contact radius and indent increase for a given applied force because the capillary adhesion increases in strength (relative to the material stiffness), resulting in greater deformation of the sphere. For small indents, the applied force is positive (so that the force applied on the sphere to maintain equilibrium is directed away from the rigid plane) suggesting capillary adhesion. These behaviours are qualitatively similar to the JKR adhesion given by (3.3) and shown in fig. 3.2. Another similarity with JKR adhesion is that there is a finite pull-off force (a maximum in the force), which occurs at a finite non-zero contact radius and indent.

There are some noticeable differences with the JKR solution, however. Firstly the drop-off in force as $a \to 0$ is much less pronounced than that seen in JKR, making the maxima in fig. 3.4 not easily apparent. Additionally, contact is maintained even after the undeformed surfaces would be expected to have separated (see fig. 3.5 for a sketch of how this may look) — maximum adhesion may occur when $\delta < 0$, whereas in JKR the solutions always have $\delta \geq 0$.

Figure 3.4a suggests that the pull-off force, F_{pulloff}, increases in magnitude with the surface tension γ, but how does it depend on the elasticity and liquid volume? For a rigid sphere close to contact, the adhesion force is independent of the liquid volume, $F \approx 4\pi\bar{\gamma}R$ (see eqn. (1.13) in §1.3.2). In fig. 3.6a, the difference between the adhesion force for a rigid sphere and the pull-off force for an impermeable elastic sphere is plotted as a function of liquid volume for fixed elasto-capillary numbers. Little variation is found in the pull-off force as the liquid volume varies, except for a decrease towards very small volumes[3]; the pull-off force deviates only a few percent from the adhesion force for a rigid sphere and plate, $F/(\bar{\gamma}R) = 4\pi \approx 12.6$. This discrepancy is larger for larger Λ, suggesting that adhesion decreases for softer spheres. We conclude from this figure that the pull-off force can be well-approximated by the adhesion of a rigid sphere $F_{\text{pulloff}} \approx 4\pi\bar{\gamma}R$.

[3]As $V \to 0$, the pull-off force is bounded below by zero, $F_{\text{pulloff}} > 0$. In fig. 3.6a, this corresponds to the solutions shown being bounded above by 1.

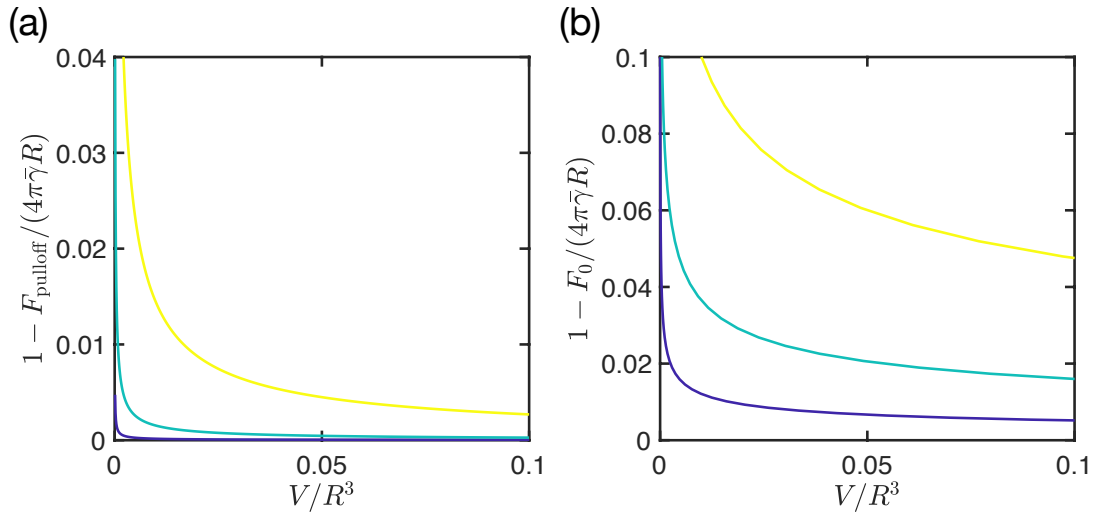

Figure 3.6: (a) The pull-off force, F_{pulloff}, and (b) the force when there is zero indent, F_0, each as a function of the liquid volume V for fixed elasto-capillary numbers $\Lambda = 10^{-6}, 10^{-5}, 10^{-4}$. (The pull-off force is the maximum force F.) In both (a) and (b) the relative difference with the adhesion force for rigid sphere, $F = 4\pi\bar{\gamma}R$, is plotted. In all plots the curves correspond to the same elasto-capillary numbers as in fig. 3.4.

Similarly, plotted in fig. 3.6b is the force when there is no indent, $\delta = 0$, i.e. when an undeformed sphere would touch the planar substrate at a single point. Interestingly, there is a finite adhesion force in this case (which, as previously noted, is not the case for JKR). Again the force behaves much like the rigid sphere, $F \approx 4\pi\bar{\gamma}R$, with only a few percent variation, but here there is a more noticeable drop-off at small volumes — the force here is less than the maximum force, which is obtained when $\delta < 0$.

The results here are in qualitative agreement with those presented in fig. 3b of Goryacheva and Makhovskaya [2001], who looked at adhesion of two elastic bodies with more general power-law shapes, and also considered the solutions after contact was lost. We do not consider this here, but expect our elastic sphere and rigid plate to behave similarly once solid-solid contact is lost (for example by exceeding the pull-off force): the two surfaces are joined only by a capillary bridge, with an adhesion ($F > 0$) that decays to zero as the sphere gets further from the plate — perhaps qualitatively similar to the decay in adhesion for rigid plates or spheres presented in Chapter 1.

3.3 Capillary adhesion of a poroelastic sphere

Having seen how the presence of a liquid bridge around the contact region modifies the adhesion of an impermeable elastic sphere to a rigid plate through surface tension effects,

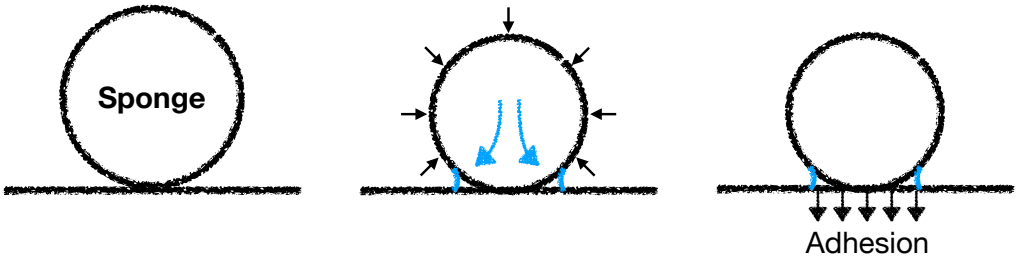

Figure 3.7: A saturated poroelastic sphere contacts a flat, rigid substrate. For a wetting liquid, the capillary pressure in the meniscus draws more liquid out of the pore space. In equilibrium, the liquid pressure in the sphere compresses the solid matrix with capillary forces resisted by elastic deformation in the contact region.

we now turn to consider the scenario of a saturated, porous, deformable sphere contacting a rigid plate. We refer to this as a poroelastic sphere, and have in mind a contact scenario similar to the hydrogel bead shown in fig. 3.1. A key difference from the impermeable case is that the poroelastic sphere can secrete its own adhering liquid: the volume of liquid in the bridge is not known *a priori* since the capillary pressure in the liquid bridge draws more liquid out of the pores, causing compression of the sphere, as illustrated in fig. 3.7.

Consider a poroelastic sphere that when undeformed has a radius R_0. The porous sphere has a Young's modulus E and a drained Poisson's ratio ν_d (both measured when it is dry) — note that the solid matrix may have different microscopic elastic properties. This sphere is saturated by a liquid that has a surface tension γ, before contacting a rigid planar substrate. Upon contact a liquid bridge forms around the contact region. We seek equilibrium solutions for the poroelastic sphere and liquid bridge when a force F is applied to pull the sphere away from the substrate.

The liquid volume secreted cannot be imposed *a priori*, but is determined by the amount of deformation of the pore spaces of the sphere. As well as deformation local to the contact region detailed in §3.2.4, there is also a global contribution: once the poroelastic sphere has equilibrated then the liquid pressure in the pores must match that in the liquid bridge, which is negative, causing a uniform compression across the whole sphere. The total deformation is a combination of this uniform compression and the contact solution of §3.2.4; using linear elasticity, the sphere deforms due to the sum of these contributions.

3.3.1 How much liquid is secreted?

There are two different mechanisms that can cause liquid to be expelled from the pore space of the sphere, both due to the compression of the pore space caused by deformation. Firstly, the (negative) capillary pressure in a wetting liquid bridge formed between the sphere and substrate can draw more liquid out, resulting in a net uniform compression across the whole sphere (once equilibrium is reached). Secondly, the local deformation close to the contact region, similar to that studied in §3.2, can result in compression of the pore space that expels liquid into the meniscus. The overall deformation of the poroelastic sphere, and so also the total liquid secreted into the meniscus region, is a combination of these two effects. We will consider each of these two mechanisms in turn, starting with the uniform compression.

Uniform compression

In equilibrium, the pressure within the pore space of the sphere must be uniform, and equal to that in the liquid bridge. Since the bridge will have a negative capillary pressure, the sphere will be subject to a uniform internal negative pressure $P < 0$ and will be uniformly compressed. Equivalently, by adding on a uniform pressure $-P$ everywhere, the same sphere can be thought of as deforming under a normal compressive stress $|P| > 0$ applied on its surface.

From the equations of linear elasticity, we find that the radial displacement u_r in the interior of the sphere is linear in the distance from the centre, $u_r \propto r$. At the sphere's surface, the stress must match the applied uniform pressure so that $u_r = (P/3K)r$ where K is the bulk modulus of the drained sphere given by $K = E/[3(1-2\nu_d)]$. The radius of a sphere, which has undeformed radius R_0, after compression is then

$$R = \frac{R_0}{1 - P/(3K)} \approx R_0 \left(1 + \frac{P}{3K}\right), \tag{3.36}$$

where a linear approximation has been used since linear elasticity is being applied, and so it is expected that $|P| \ll K$. The compressed volume of the sphere is then

$$V \approx V_0 \left(1 + \frac{P}{K}\right). \tag{3.37}$$

Note that the sphere radius and volume decrease for a negative capillary pressure, $P < 0$. This is exactly what should have been expected, because the bulk modulus, K, can be defined as the ratio of the infinitesimal pressure increase to the resulting relative decrease in volume [Kittel, 2005].

We consider a poroelastic sphere that has been compressed due to a uniform negative internal pressure P. This results in a decrease in volume of the sphere

$$\Delta V = -\frac{4\pi R_0^3}{3}\frac{P}{K}, \tag{3.38}$$

which is positive when $P < 0$. The amount of liquid secreted from the porous sphere is the change in volume of the pore spaces caused by this compression. For simplicity, we will consider a poroelastic sphere where the solid matrix and liquid are both incompressible: all of the volume change therefore occurs from changes in the pore space, and the volume of liquid secreted is given by (3.38). Note that here the bulk modulus K, is that of the drained sphere (i.e. with no liquid inside) [Kümpel, 1991]. K can be finite, even when the solid matrix is incompressible, because of changes to the pore space. (Similarly, the solid matrix can have a microscopic Poisson's ratio $\nu = 1/2$, whilst the drained Poisson's ratio of the sphere $\nu_d \neq 1/2$.)

Local deformation due to contact

As well as the uniform compression of the sphere, there is also deformation caused by the contact with the rigid plane. This deformation behaves precisely like the elastic sphere with capillary adhesion presented in §3.2, but, to combine the effect of both, we mathematically consider the effects of the compression before introducing the contact with the substrate, so that now the solution from §3.2 can be reused with a contracted sphere radius $R < R_0$ due to the effect of the uniform compression. (We could instead consider contracting the sphere after the contact, but care would be needed to account for the changing contact region as the sphere contracted — the calculation presented here is much more straightforward.)

The change in volume of the sphere (and hence the liquid expelled for an incompressible solid matrix) due to contact can be found by integrating the surface deformation $w(r)$ over the surface of the sphere: $\int 2\pi r w(r)\mathrm{d}r$. Noting that $w(r) = h(r) + \delta - r^2/2R$ and substituting for $h(r)$ using (3.23), the integration can be performed in $\rho = r/a$ up to a large distance $\rho = \rho_\infty$, giving a decrease in volume of the deformed sphere due to the local deformation

$$\Delta V = -\frac{2aF}{E^*}\rho_\infty + O(\rho_\infty^{-1}). \tag{3.39}$$

(Note that adhesion, $F > 0$, leads to an increase in volume as the negative capillary pressure pulls down on the sphere and opens the pore spaces.)

The integration was performed to a large ρ_∞ to calculate (3.39), but this extends beyond the domain of validity of the solution (close to the contact where the surfaces

look locally flat). It is not immediately clear what the appropriate cutoff ρ_∞ should be, but since the sphere is finite in size it is certainly at most of size R_0/a. Finding the appropriate value for ρ_∞ requires a solution for the deformation of the sphere over a larger domain (such as a global solution for the indentation of a sphere — a Boussinesq problem).

However, we shall focus on the case where the secreted liquid volume is dominated by the global, uniform compression of the sphere rather than the local contact; this is expected to be valid provided that the force F is small compared to the capillary pressure P (compare eqns. (3.38) and (3.39)). In the worst case scenario, where $\rho_\infty = R_0/a$, this condition requires $|F|/(R_0^2 E^*) \ll |P|/K$. The small force solutions presented in the rest of this chapter may be valid for a larger range of forces than this, but the determination of this limit requires further work.

3.3.2 Governing equations

We non-dimensionalize our problem in a similar manner to (3.29), but scale lengths by the initial sphere radius R_0 rather than the final sphere radius R, defining the dimensionless variables

$$\hat{a} = \frac{a}{R_0}, \quad \hat{P} = \frac{P}{E^*}, \quad \hat{F} = \frac{F}{R_0^2 E^*}, \quad \hat{V} = \frac{V}{R_0^3} \tag{3.40}$$

with the elasto-capillary number

$$\Lambda = \frac{\bar{\gamma}}{R_0 E^*}. \tag{3.41}$$

In addition, we also define the dimensionless sphere radius $\hat{R}$ and the incompressibility parameter $\hat{K}$ by

$$\hat{R} = \frac{R}{R_0}, \quad \hat{K} = \frac{K}{E^*}. \tag{3.42}$$

Note that $\hat{K} = (1 - \nu_d^2)/3(1 - 2\nu_d)$.

Just as in the calculation for the impermeable elastic sphere in §3.2.4, there are conditions that relate the applied force, capillary pressure and volume of liquid. These equations are identical to eqns. (3.32)–(3.34), except that the sphere radius and volume within the liquid bridge are determined by the uniform compression caused by capillary suction, (3.36) and (3.38). In dimensionless form, these are

$$\hat{F} = -\frac{4\hat{a}^3}{3\hat{R}} - 2\hat{a}^2\hat{P}\left[y + (y^2+1)\arctan y\right] \tag{3.43}$$

$$2\Lambda = -\frac{\hat{a}^2\hat{P}}{\pi\hat{R}}\left[y + (y^2-1)\arctan y\right] + \frac{4\hat{a}\hat{P}^2}{\pi}\left[y\arctan y - \sqrt{y^2+1} + 1\right] \tag{3.44}$$

$$-\frac{4\pi}{3}\frac{\hat{P}}{\hat{K}} = \frac{\hat{a}^4}{2\hat{R}}\left[2y^3 + (y^2+1)(y^2-3)\arctan y + (3-y^2)y\right] + 4\hat{a}^3\hat{P}\left[\frac{4}{3}(y^2+1)^{3/2} - y(y^2+1)\arctan y - y^2 - \frac{4}{3}\right], \quad (3.45)$$

where the compressed sphere radius $\hat{R}$ is

$$\hat{R} = 1 + \frac{\hat{P}}{3\hat{K}}, \quad (3.46)$$

and $\hat{P} < 0$. Again, we have imposed that there is no singularity in the elastic stress at the edge of the contact region, meaning that the dimensionless indent is simply

$$\hat{\delta} = \frac{\hat{a}^2}{\hat{R}} + 2\hat{a}\hat{P}y. \quad (3.47)$$

The eqns. (3.43)–(3.47) are five relations for eight variables: $\hat{a}, \hat{P}, y, \hat{F}, \Lambda, \hat{R}, \hat{K}, \hat{\delta}$. If the values of three of these parameters are given then the problem is closed. In general, we expect Λ and $\hat{K}$ to be material parameters, and hence be given. Whether $\hat{F}$ or $\hat{\delta}$ is given depends on whether an experiment is force- or height-controlled.

In section §3.5, we will determine the relationship between $\hat{F}$ and $\hat{\delta}$ (and also the contact radius $\hat{a}$) for different elasto-capillary numbers Λ and elastic constants $\hat{K}$ (or, more precisely, the drained Poisson's ratio, ν_d). First, however, we consider the case of no applied force, $\hat{F} = 0$, and compare these results qualitatively to preliminary results from experiments on hydrogel beads.

3.4 No load: Freely adhered poroelastic spheres

Consider the case of a poroelastic sphere contacting a rigid plane and being adhered by the surface tension of a self-secreted liquid when there is no externally imposed force — the capillary adhesion precisely balances the elastic deformation in the sphere. We would like to quantify how the meniscus radius or indent depth vary as functions of the size of the sphere, since these quantities may be measured experimentally.

When there is no applied force, $\hat{F} = 0$, eqn. (3.43) gives a simple relation for the contact radius in terms of the pressure, $\hat{P}$, and meniscus position, $y = \sqrt{\rho_M^2 - 1}$,

$$\hat{a} = -\frac{3}{2}\hat{R}\hat{P}\left[(y^2+1)\arctan y + y\right]. \quad (3.48)$$

Given a value for the compressibility $\hat{K}$ (or equivalently a drained Poisson's ratio ν_d) it is convenient to use y as a parameter since (3.45) is a relatively simple algebraic equation

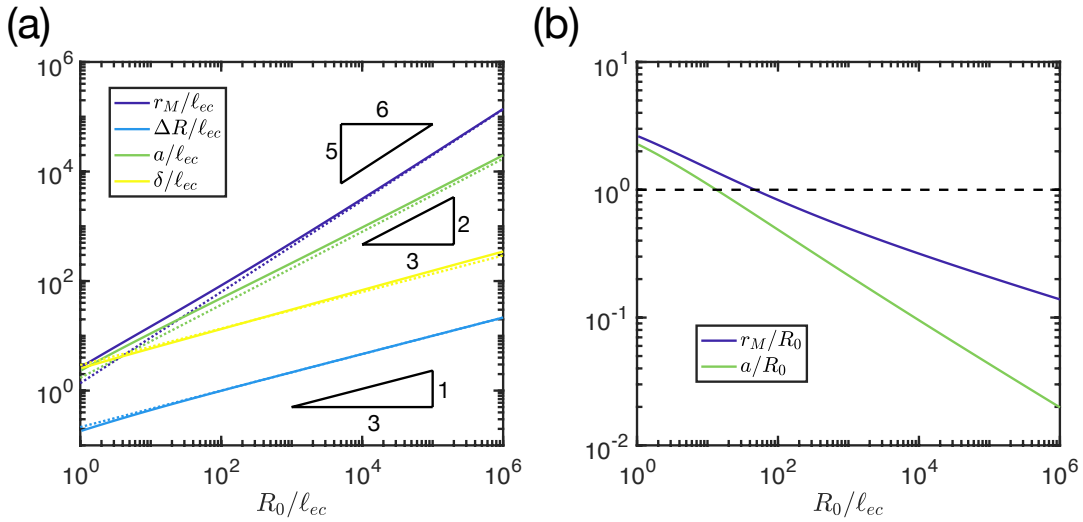

Figure 3.8: Results for the capillary contact of an unloaded poroelastic sphere ($F = 0$) with drained Poisson's ratio $\nu_d = 0.45$. (a) The meniscus radius, r_M; change in sphere radius, $\Delta R = R_0 - R$; indent, δ; and contact radius, a, are each plotted as functions of the initial sphere radius R_0 (solid curves). These are compared to the large R_0/ℓ_{ec} asymptotics derived in §3.4.2 (dotted lines). (b) The size of the meniscus radius, r_M, and contact radius, a, relative to the initial sphere radius R_0. Note that for our analysis, R_0/ℓ_{ec} must be sufficiently large that the contact and meniscus radii are smaller than the sphere size, $r_M \ll R_0$ and $a \ll R_0$ (equality is illustrated by the black dashed line).

for $\hat{P}$, after substituting for $\hat{a}$ and $\hat{R}$ using eqns. (3.48) and (3.46). This determines the sphere radius $\hat{R}$ and the contact radius $\hat{a}$ from (3.46) & (3.48), respectively. The elasto-capillary number Λ is then immediately given by (3.44).

3.4.1 Results

Results for a drained Poisson's ratio $\nu_d = 0.45$ are shown in fig. 3.8. In fig. 3.8a the meniscus radius, r_M; contact radius, a; change in sphere size, $\Delta R = R_0 - R$; and indent, δ, are plotted as functions of the undeformed sphere radius $R_0/\ell_{ec} = (1-\nu_d^2)\Lambda^{-1}$, where the elasto-capillary length is here defined by $\ell_{ec} = \bar{\gamma}/E$ (different from the usual γ/E by a factor $\overline{\cos\theta}$). For large R_0/ℓ_{ec} (or small Λ) these results suggest power-law relations, specifically

$$r_M \sim \ell_{ec}^{1/6} R_0^{5/6}, \quad a \sim \ell_{ec}^{1/3} R_0^{2/3}, \quad \delta \sim \ell_{ec}^{2/3} R_0^{1/3}, \quad \Delta R = R_0 - R \sim \ell_{ec}^{2/3} R_0^{1/3}. \quad (3.49)$$

Larger spheres therefore have a larger contact and size change than smaller spheres composed of the same material. However, these quantities decrease relative to the sphere size as the sphere size increases (see fig. 3.8b): our analysis is valid for large spheres where deformations are small on the scale of the sphere.

It remains to explain the power-law behaviour that is observed in fig. 3.8a; we turn to investigate this now.

3.4.2 Scaling laws for no applied force

When the radius of the undeformed sphere is large compared to the elasto-capillary length, $R_0 \gg \ell_{ec} = \bar{\gamma}/E$, then the deformation of the sphere due to surface tension should be small. It may then be expected to look relatively undeformed, with the separation between the plate and sphere $h(r) \approx r^2/2R$ and a very small contact region. The liquid volume in the capillary bridge can then be approximated by

$$V_{\text{bridge}} = \int_a^{r_M} 2\pi r h(r)\, \mathrm{d}r \approx \frac{\pi r_M^4}{4R} \tag{3.50}$$

and the capillary pressure by

$$P = -\frac{2\bar{\gamma}}{h(r_M)} \approx -\frac{4\bar{\gamma}R}{r_M^2}. \tag{3.51}$$

Meanwhile, the liquid volume that is squeezed out of the pore space of the sphere is dominated by the uniform capillary compression, since there is no external force applied. This liquid volume is therefore (see eqn. (3.38))

$$V_{\text{squeeze}} = -\frac{4\pi R_0^3}{3}\frac{P}{K}. \tag{3.52}$$

All of the expelled liquid ends up in the capillary bridge so that $V_{\text{bridge}} = V_{\text{squeeze}}$, approximated by (3.50) and (3.52), respectively. Substituting the capillary pressure (3.51), and assuming small sphere deformations, $R \approx R_0$, gives a scaling relation for the wetted radius

$$\frac{r_M}{\ell_{ec}} \approx 2(1-2\nu_d)^{1/6}\left(\frac{R_0}{\ell_{ec}}\right)^{5/6}, \tag{3.53}$$

where the bulk modulus K has been replaced by the drained Poisson's ratio ν_d through the relation $K = E/3(1-2\nu_d)$. The liquid pressure can then be determined from (3.51) as

$$\frac{P}{E} \approx -(1-2\nu_d)^{-1/3}\left(\frac{R_0}{\ell_{ec}}\right)^{-2/3}. \tag{3.54}$$

This allows for the determination of the change in sphere radius, since $\Delta R = R_0 - R \propto P$ from (3.36), so that

$$\frac{R_0 - R}{\ell_{ec}} \approx (1-2\nu_d)^{2/3}\left(\frac{R_0}{\ell_{ec}}\right)^{1/3}. \tag{3.55}$$

The contact radius and indent occur at a smaller scale than the capillary bridge; a reasonable assumption is therefore that the contact radius is much smaller than the

meniscus radius, $a \ll r_M$ so that $y \gg 1$. The dimensionless contact radius is related to the meniscus radius and capillary pressure through (3.48), which simplifies for large y to $\hat{a} \approx -\pi \hat{P} y^2/2$. The contact radius can therefore be approximated by

$$\frac{a}{\ell_{ec}} \approx [2\pi(1-\nu_d^2)]^{1/3} \left(\frac{R_0}{\ell_{ec}}\right)^{2/3}. \tag{3.56}$$

The power law for the indent can then similarly be found from expanding (3.47) with large y, which gives

$$\frac{\delta}{\ell_{ec}} \approx [2\pi(1-\nu_d^2)]^{2/3} \left(\frac{R_0}{\ell_{ec}}\right)^{1/3}. \tag{3.57}$$

Note that the contact radius and indent here obey the same power-law scaling with sphere radius as that found for JKR adhesion with no force, (3.4), but with a different prefactor.

The approximations (3.53) and (3.55)–(3.57) are plotted in fig. 3.8a as dotted lines; these power-law relations are found to agree closely with the calculated numerical solution. For a large range of sphere sizes, an unloaded poroelastic sphere can be well-approximated by a uniformly compressed sphere with a small contact, and the scaling laws (3.53) and (3.55)–(3.57). We now turn to see whether one of these scaling laws can be seen in practice, using preliminary experiments on the contact of swollen hydrogel beads.

3.4.3 Comparison with hydrogel bead experiments

To test the applicability of the theoretical results for a poroelastic sphere under no applied force, experiments on hydrogel beads were conducted by Lucie Domino (University of Oxford) in the Maths Observatory. These experiments were performed on a pair of contacting beads, rather than a single bead and plate, to get clearer images of the contact region (and hence more reliable results).

The hydrogel beads were left in de-ionised water to swell for 24 hours and, after removal, their outer surface was dried with a low lint precision wipe to remove excess water. A pair of similar-sized beads were then brought into contact and left to equilibrate. Two photographs were taken from the side, one containing both beads and another that was a magnification of the contact region (see fig. 3.9); images were taken within 30 minutes of contact to reduce the effect of evaporation. From these images, the bead radii and wetting radius were measured using ImageJ (NIH). (Since the change in sphere radius is expected to be small, the undeformed sphere radius, R_0, is approximated by the measured bead radius in contact, R.)

Results for a range of bead sizes are shown in fig. 3.9c. Note that by changing from a single sphere and plate to two contacting spheres, it is expected that the scaling relations

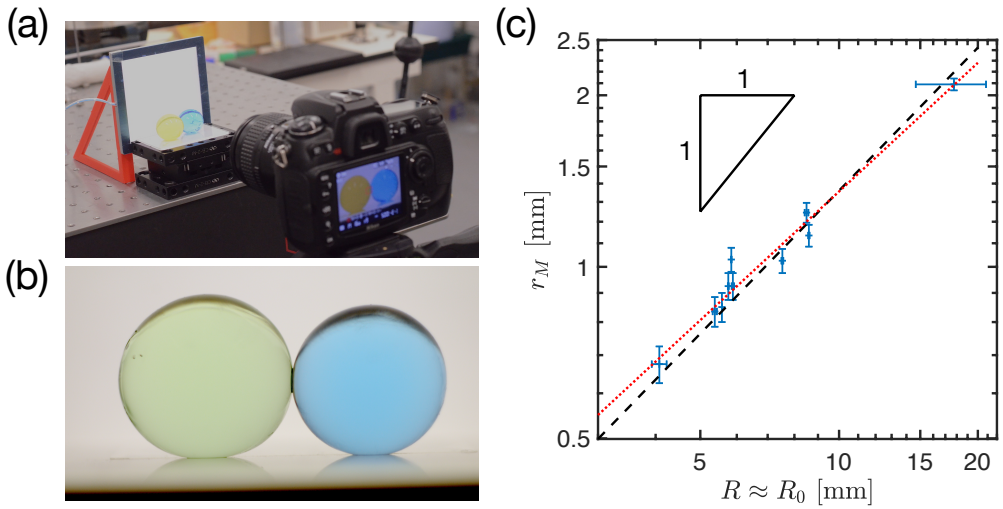

Figure 3.9: Two saturated hydrogel beads of similar size are contacted, with the radius of wetting around the contact area measured as a function of the bead radius. (a) The beads are photographed from the side at two different magnifications, with measurements recorded from these images. (b) An example image of the contacting hydrogel beads. (c) Preliminary experimental results of the wetting radius as a function of the bead size for a range of hydrogel beads. These are plotted on a doubly logarithmic scale and are compared to a best-fit 5/6 power law (dashed line), as well as a best-fit 3/4 power law (red dotted line) and a slope of gradient 1. Images and data courtesy of Lucie Domino.

from §3.4.2 still hold but with the single poroelastic sphere radius R_0 and elastic constant E^* replaced using (3.2); for two identical spheres of radius R_0 and Young's modulus E, the R_0 and E for a single sphere in the equations of §3.4.2 are replaced by $R_0/2$ and $E/2$, respectively.

The data presented in fig. 3.9c are consistent with the $r_M \propto R_0^{5/6}$ power-law derived in §3.4.2. A least-squares fitting of the experimental data to a 5/6 power suggests a relation $r_M \approx 0.2 R_0^{5/6}$ (all lengths measured in mm). From the theoretical scaling (3.53) (with R_0 replaced by $R_0/2$), it is expected that $r_M \approx [4(1-2\nu_d)\ell_{ec}]^{1/6} R_0^{5/6}$. Since hydrogel beads swell when wetted, it is not clear what the appropriate values for the drained Poisson's ratio should be (but the dependence on ν_d should be weak unless it is very close to incompressible because of the factor $(1-2\nu_d)$); we take a value $\nu_d = 0.45$. Matching the theoretical scaling with the fitted slope of fig. 3.9c then suggests an elasto-capillary length $\ell_{ec} \approx 2 \times 10^{-7}$ m; using a value of $\bar{\gamma} = 70$ mN/m for (perfectly wetting) water leads to an estimation for the Young's modulus of $E \approx 4 \times 10^5$ Pa. A typical hydrogel may have a Young's modulus in the range of $E = 0.01$–1 MPa [Zhu et al., 2017, Waitukaitis et al., 2017], suggesting this estimated Young's modulus is reasonable. In future work, we aim to determine the various elastic parameters for the hydrogel beads used in these

preliminary experiments.

It should be noted that while these preliminary results are promising, they do not conclusively demonstrate the theory presented in this chapter. For example, if the adhering liquid is instead provided by a thin film of water on the surface of the beads then a simple balance of volumes (so that eqn. (3.50) is proportional to bead surface area, $r_M^4/R \propto R^2$) suggests an alternative relation: $r_M \propto R_0^{3/4}$. Drying the beads should have reduced this effect, but a best-fit 3/4 power also appears a good fit to the data (dotted line in fig. 3.9c). However, the data do appear to be distinct from a linear relationship, $r_M \propto R_0$.

There are some further caveats when interpreting this data: the Young's moduli may not be the same across different bead sizes and the swelling of the hydrogel beads may lead to markedly different behaviour compared to the idealized poroelastic spheres of this chapter. In particular, there may be additional elastic stresses not accounted for here and a strong capillary pressure could result in de-swelling of the hydrogel [Sokoloff, 2016]. Further experimentation is required to resolve these issues.

3.5 Poroelastic sphere under a small applied force

Having considered the equilibria of unloaded poroelastic spheres, we now consider the equilibrium of a poroelastic sphere in contact with a rigid planar substrate and subject to a small applied force, $|\hat{F}| \ll 1$. In particular, the force is sufficiently small that the volume change of the sphere caused by the deformation close to the contact region is negligible compared to the global uniform compression of the sphere caused by the capillary pressure. Recall that this requires that (at worst) forces are small compared to the pressure, $|F|/(R_0^2 E^*) \ll |P|/K$; in the dimensionless variables this is $|\hat{F}| \ll |\hat{P}|$.

Equations (3.43)–(3.45) are solved for the force, $\hat{F}$, pressure, $\hat{P}$, and contact radius, $\hat{a}$, for given values of the elasto-capillary number, Λ, and incompressibility, $\hat{K}$, again using the (rescaled) meniscus radius y, as a parameter.

In fig. 3.10, solutions are plotted for a poroelastic sphere with drained Poisson's ratio $\nu_d = 0.45$ and elasto-capillary numbers $\Lambda = 10^{-6}, 10^{-5}, 10^{-4}$. Solutions are only presented for $|\hat{F}| < |\hat{P}|$ (and so the curves terminate as $|\hat{F}|$ increases).

There are many similarities between the results here for the poroelastic sphere and the impermeable elastic sphere with a given liquid volume in §3.2.4. Firstly, the force-contact radius and force-indent relations behave much like the Hertz solution for very small Λ, and a region of adhesion is found for small contact radii or indents. As Λ increases, adhesion is present for a larger range of a and δ. Additionally, there is a finite maximum in F — a pull-off force — that occurs at non-zero contact radius a, and with a negative indent

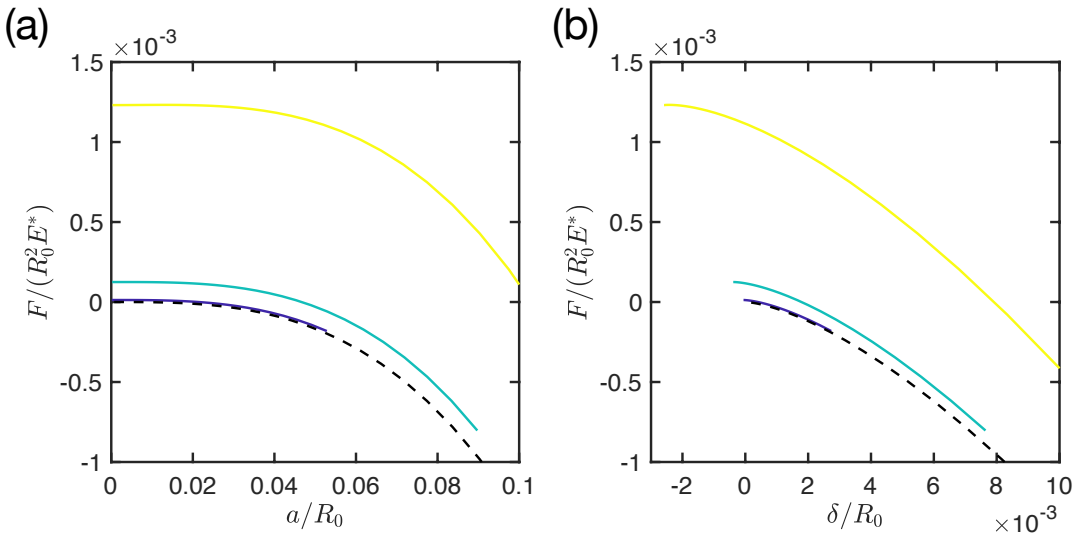

Figure 3.10: Solutions for equilibrium of a saturated poroelastic sphere contacting a rigid plate, adhered by surface tension of secreted liquid when the applied force is small. In all cases the drained Poisson's ratio is $\nu_d = 0.45$ and there are a range of elasto-capillary numbers $\Lambda = \bar{\gamma}/(E^* R_0) = 10^{-6}, 10^{-5}, 10^{-4}$ (dark blue, blue-green and yellow respectively). (a) The applied force F as a function of the contact radius a. (b) The force F as a function of the indent δ. Solutions are compared to the Hertz solutions (3.1) (black dashed curve).

$\delta < 0$. (Again the drop-off in the force towards $a = 0$ is small and so it may be hard to distinguish the maximum at the scale of the plots.)

The pull-off force, F_{pulloff}, is plotted in fig. 3.11 as a function of the elasto-capillary number, Λ, and the dimensionless undeformed sphere radius, R_0/ℓ_{ec}, for a range of drained Poisson's ratios, ν_d. The pull-off force is again found to be close to the equivalent force for a capillary-adhered rigid sphere, $4\pi\bar{\gamma}R_0$. The combination of figs. 3.10 and 3.11 show that the pull-off force increases with strength of surface tension γ but decreases with the (modified) Young's modulus $E^* = E/(1-\nu_d^2)$ — softer spheres are easier to detach.

To explore the dependence of the pull-off force on the drained Poisson's ratio, ν_d, in fig. 3.11b we plot the pull-off force as a function of R_0/ℓ_{ec} (since $\Lambda = \bar{\gamma}/R_0 E^*$ is ν_d-dependent but $R_0/\ell_{ec} = R_0 E/\bar{\gamma}$ is not). The pull-off force changes very little over a large range of ν_d, except for when the porous sphere is close to being incompressible; as the Poisson's ratio approaches $\nu_d = 1/2$, the pull-off force has a noticeable decrease from $F_{\text{pulloff}}/(\bar{\gamma}R_0) \approx 4\pi \approx 12.6$. This suggests that poroelastic spheres that are difficult to compress do not adhere as well as more compressible spheres; less compressible spheres secrete less liquid into the contact zone, so these results are consistent with the decrease in pull-off force seen for impermeable spheres at small liquid volumes (fig. 3.6).

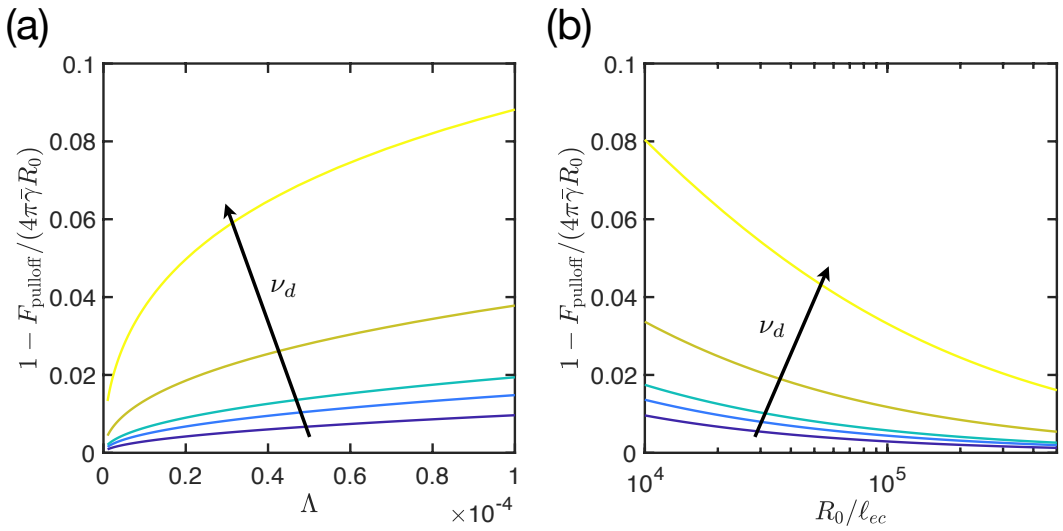

Figure 3.11: The difference between the pull-off force for a poroelastic sphere, F_{pulloff}, and the rigid sphere adhesion force, $4\pi\bar{\gamma}R_0$, as a function of (a) the elasto-capillary number $\Lambda = \bar{\gamma}/(R_0E^*)$, and (b) the undeformed sphere radius $R_0/\ell_{ec} = (1-\nu_d^2)/\Lambda$ where the elasto-capillary length $\ell_{ec} = \bar{\gamma}/E$. Solutions are plotted for a range of drained Poisson's ratios $\nu_d = 0.1, 0.4, 0.45, 0.49, 0.499$.

3.6 Conclusions

In this chapter, we have considered the equilibrium capillary adhesion of a deformable elastic sphere in contact with a rigid planar substrate. The theory of Fogden and White [1990] for capillary adhesion of an impermeable elastic sphere was re-derived, and results presented for this capillary adhesion when there is a constant liquid volume, analogous to those of Goryacheva and Makhovskaya [2001]. These results for an impermeable sphere were adapted to study the capillary adhesion of a saturated poroelastic sphere. The interesting feature of this problem is that the sphere provides its own adhering liquid, which is extracted by a combination of the capillary pressure and the deformation of the sphere.

The behaviour of the capillary adhesion of both impermeable and permeable elastic spheres to rigid plates is found to be qualitatively similar to the JKR adhesion of dry elastic spheres with solid-solid contact adhesion [Johnson, Kendall, and Roberts, 1971], although some differences were noted. In particular, in this contact capillary adhesion the maximal force occurs at a negative indent, which is not seen in JKR; experimental observations may therefore be able to differentiate JKR and capillary adhesion depending on whether adhesion is maintained when withdrawing (quasi-statically) beyond the sphere position at initial contact.

In the absence of an applied force, theoretical solutions were found for the amount of deformation in the poroelastic sphere and the amount of liquid expelled as a function of the sphere size. Over a wide range of sphere radii, power law scalings were observed that could be explained by an asymptotic analysis for small contact regions. In particular, the prediction that the capillary bridge radius should scale with the $5/6$ power of the sphere radius is supported by preliminary experiments involving pairs of contacting hydrogel beads.

A finite pull-off force was discovered in both the impermeable and poroelastic sphere adhesion. For the impermeable elastic sphere, this was investigated as a function of the liquid volume; a weak dependence on the volume was found, with a decrease in the pull-off force at small volumes, but otherwise the maximum adhesion force was found to be quantitively close to what would be expected from a contacting rigid sphere, $F = 4\pi\bar{\gamma}R$. Similarly, the pull-off force was investigated for the poroelastic sphere, which was also often found to be close to the rigid result. In both cases, the maximum adhesion force increases with the surface tension but, perhaps surprisingly, decreases slightly as the spheres are made softer.

Solutions for the poroelastic sphere were found for small applied forces, where the volume of liquid secreted as the sphere deforms is dominated by the uniform compression due to the capillary pressure. It would be interesting to extend these results by removing this restriction to small forces and also including the liquid volume in the bridge due to the local deformation of contact. In particular, when the force is positive ($F > 0$, adhesion), the pulling of the capillary pressure on the sphere boundary may open up the pore space and reduce the amount of liquid in the meniscus (note the sign of the volume change in eqn. (3.39)). A global understanding of the elastic deformation in the sphere is required to tackle these problems at larger forces, since the finite size of the sphere impacts on the calculation of the volume change.

The results presented in this chapter for poroelastic spheres were also focused on an incompressible solid matrix. An interesting extension would be to see how the results change for more general elastic properties; allowing the solid volume to change would introduce the explicit importance of the porosity ϕ (here the proportion of pore space to solid matrix is only implicit within the equations, affecting the elastic properties of the poroelastic sphere such as the bulk modulus K, or equivalently the drained Poisson's ratio ν_d).

Finally, if using a poroelastic sphere as a capillary adhesive, it would be important to know how the liquid is secreted dynamically to determine how fast the sphere equilibrates, as well as finding the evolution of the adhesion force in time.

Appendices

3.A Stresses and displacements from the Love stress function

For axisymmetric deformations, the components of the elastic stress tensor, τ, are given in terms of the Love stress function φ by [see Chapter 10 of Sneddon, 1995]

$$\begin{aligned}
\tau_{rr} =& \lambda\nabla^2\frac{\partial\varphi}{\partial z} - 2(\lambda+G)\frac{\partial^3\varphi}{\partial r^2\partial z},\\
\tau_{zz} =& (3\lambda+4G)\nabla^2\frac{\partial\varphi}{\partial z} - 2(\lambda+G)\frac{\partial^3\varphi}{\partial z^3},\\
\tau_{\vartheta\vartheta} =& \lambda\nabla^2\frac{\partial\varphi}{\partial z} - 2(\lambda+G)\frac{1}{r}\frac{\partial^2\varphi}{\partial r\partial z},\\
\tau_{rz} =& (\lambda+2G)\frac{\partial}{\partial r}\nabla^2\varphi - 2(\lambda+G)\frac{\partial^3\varphi}{\partial r\partial z^2},
\end{aligned} \tag{3.58}$$

where ϑ is the azimuthal angular coordinate and λ, G are the Lamé coefficients for the elastic body. The corresponding elastic displacements in the radial and vertical directions are

$$u_r = -\frac{\lambda+G}{G}\frac{\partial^2\varphi}{\partial r\partial z}, \qquad u_z = \frac{\lambda+2G}{G}\nabla^2\varphi - \frac{\lambda+G}{G}\frac{\partial^2\varphi}{\partial z^2}. \tag{3.59}$$

The stresses (3.58) for an elastic body in equilibrium must obey the equilibrium force balance, $\nabla\cdot\tau = 0$. When decomposed into radial and vertical directions, this becomes

$$\frac{\partial\tau_{rr}}{\partial r} + \frac{\partial\tau_{rz}}{\partial z} + \frac{\tau_{rr}-\tau_{\vartheta\vartheta}}{r} = 0, \tag{3.60}$$

$$\frac{\partial\tau_{rz}}{\partial r} + \frac{\partial\tau_{zz}}{\partial z} + \frac{\tau_{rz}}{r} = 0. \tag{3.61}$$

The definitions (3.58) are such that they automatically satisfy the radial stress equation (3.60). Upon substituting the stresses into (3.61), we find that φ must satisfy the biharmonic equation

$$\nabla^4\varphi = 0. \tag{3.62}$$

This also ensures that compatibility of strains is satisfied.

Chapter 4

Controlling elasto-capillary adhesion via deformability

In this chapter, we study the interaction between capillary forces and deformation in the context of a deformable capillary adhesive: a clamped membrane under tension is adhered to a rigid substrate by the surface tension of a liquid bridge. We find that the equilibrium adhesion force for this elasto-capillary adhesive is significantly enhanced in comparison to the capillary adhesion between rigid plates. In particular, the equilibrium adhesion force is orders of magnitude larger when the membrane is sufficiently deformed to contact the substrate. From a dynamic perspective, however, the formation of a liquid-filled dimple slows this approach to contact and means that stable attachment is only achieved if adhesion is maintained for a minimum time. The inclusion of a variable membrane tension (as a means of modifying the deformability) gives additional control over the system, allowing new detachment strategies to be explored.

4.1 Introduction

Simple models of capillary adhesion are often based on adhering rigid surfaces. However, when designing adhesives, there is often choice over one of the surfaces which we wish to stick to a particular substrate. Indeed, detailed observations of the adhesive organs of insects show that the smooth footpads of some insect species are in fact soft and deformable [Gorb et al., 2000]. The question then arises of why this is the case and, further, what effect the deformation has on adhesion — perhaps having a foot that deforms under a capillary force can lead to an improvement in adhesion? In Chapter 3, we saw that the addition of capillary adhesion can modify the adhesion and deformation during contact between elastic bodies, and moreover that this deformation due to surface tension can be substantial (even global in the case of the poroelastic sphere). The coupling

of deformability and adhesion may allow surfaces to come into closer contact, thereby increasing the maximum adhesion force. Moreover, if this deformation can be controlled then it may also allow for new mechanisms of detachment. In this chapter, we turn to investigate the effect of deformation on capillary adhesion in detail using a mathematical model of an elasto-capillary adhesive.

A common theme in elasto-capillary settings is the occurrence of hysteresis and rapid transitions between markedly different states, for example, the zipping and unzipping of fibres by a droplet as the fibre tension or separation is varied [Duprat et al., 2012, Duprat and Protiere, 2015]. Furthermore, theory and experiments suggest that liquid bridges are capable of significant deformation of surfaces: beams clamped at one end can be bent into contact [Taroni and Vella, 2012, Kwon et al., 2008] and two soft elastic half-spaces can be pulled together by the forces of a single liquid bridge [Wexler et al., 2014]. In some scenarios, this capillary deformation may be unwanted, but recent advances show that there are possibilities to make good use of elasto-capillarity: for example in the creation of patterned nanostructures [Pokroy et al., 2009, de Volder and Hart, 2013], or in generating passive motion of droplets [Bradley et al., 2019].

The ideas of elasto-capillarity have recently been turned towards investigating adhesion. In particular, the adhesive hairs that are found on several insect species (including flies and beetles) have been modelled as flexible beams that are clamped at one end [Gilet et al., 2019], whilst the smooth pads of other species (such as stick insects and ants) have been approximated by a soft elastic layer [Li and Cai, 2014, Wexler et al., 2014]. Gilet et al. [2019] divided their beam model into three scenarios (depending on whether solid-solid contact occurs between the beam and substrate, and whether that contact is only at the beam's tip or over a finite length), allowing them to consider the effects of foot-substrate contact on adhesion. The calculated adhesion force increases when in close contact and exhibits hysteresis; moreover the theoretically calculated value agrees well with a comparative simple experimental system after fitting. Both Li and Cai [2014] and Wexler et al. [2014] considered a capillary bridge between two soft layers, finding the resulting deformation as their separation was varied until solid-solid contact occurs. The results of Li and Cai [2014] suggest that the adhesion force increases with decreasing separation distance, and is stronger for substrates that are more deformable. However, the adhesion force is not controllable in these systems, but is fixed by the material properties of the system. More recently, elasticity has been explored as a means to control adhesion, such as using the fibre tension in the work of Duprat et al. [2020]; we investigate a similar mechanism for control of adhesion here.

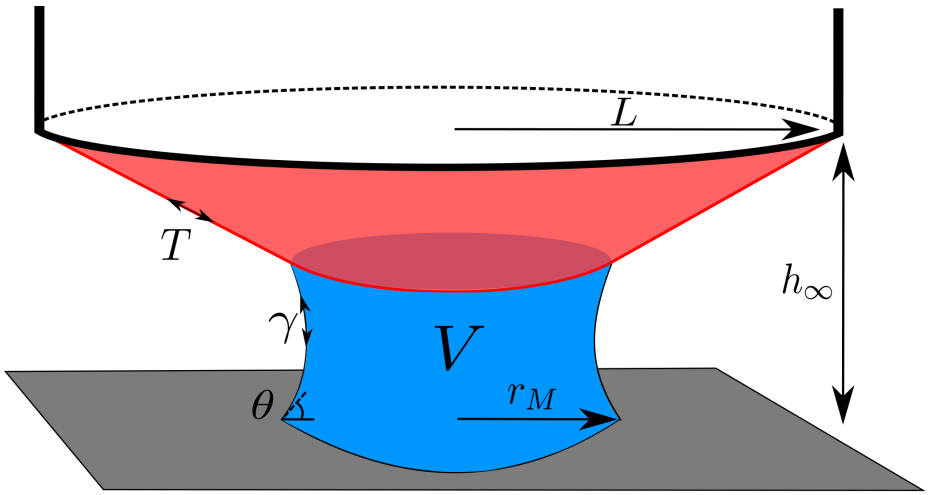

Figure 4.1: A liquid bridge (blue) of volume V joins a rigid plate (grey) and a deformable membrane (red). The membrane (of thickness τ) is clamped around a circle of radius L with an applied tension T and at a height h_∞ above the plate. The free surface of the liquid has a surface tension γ and makes a contact angle θ with each surface.

In this chapter, we consider a model of a deformable capillary adhesive: a tensed membrane is adhered to a rigid, planar substrate by the surface tension of a liquid bridge. We will outline a mathematical model of this system, and determine the governing equations from a local force balance and highlight the key parameters. We study the equilibria, focusing on the adhesion force, taking care to include solutions in which the membrane is deformed sufficiently to contact the substrate. These results are compared to experimental data that supports the equilibrium picture but also hints at the importance of dynamics, which we then further study using lubrication theory. Finally, we consider adhesive detachment, focusing on finding a strategy that minimizes the work required to release the membrane from the substrate, and demonstrate that this system gives us a controllable adhesion. (The work in this chapter has been published, see Butler et al. [2019].)

4.2 Mathematical model

To investigate the possible role of elasticity in capillary adhesion, we consider perhaps the simplest deformable surface possible: a circular membrane of thickness τ and Young's modulus E. We shall consider only small axisymmetric deformations of the membrane, which is subject to a constant imposed tension, T, and clamped at the radial position $r = L$. Adhesion to a flat and rigid substrate (which lies a distance h_∞ below the clamped edge of the membrane) is achieved by introducing a liquid bridge between the two surfaces, as shown in fig. 4.1.

The surface tension of the liquid deforms the membrane because of the forces it exerts on the membrane. This deformation in turn modifies the surface tension force leading to novel feedbacks in this system; our aim is to understand how the interaction between capillarity and deformability affect the adhesive properties of the system, particularly in comparison to capillary adhesion of rigid surfaces described in Chapter 1.

4.2.1 Modelling assumptions

We anticipate that the two surfaces will generally be 'close to contact' and hence that the aspect ratio is large, $L/h_\infty \gg 1$, though for clarity the figures will exaggerate the vertical scale; furthermore the effect of gravity on the liquid bridge and membrane is neglected.

For simplicity, the tension T in the membrane shall be taken to be uniform and T is treated as a control parameter: we neglect any modification of the uniform tension due to additional stretching of the membrane during vertical deformation. To understand when this approximation is valid, note that simple geometry gives the deformation-induced strain $\varepsilon \lesssim (h_\infty/L)^2$. The thickness-integrated stress in the membrane is then $\sigma \sim T + E\tau h_\infty^2/L^2$: in scaling terms, the effect of deformation-induced stretching is negligible provided that $T \gg E\tau(h_\infty/L)^2$.[1] Crucially, it is possible for the applied tension to dominate the geometry-induced tension even while the membrane remains Hookean, which requires that the tension-induced strain remains sufficiently small, $T/(E\tau) \ll 1$. This therefore requires: $(h_\infty/L)^2 \ll T/(E\tau) \ll 1$. The bending stiffness of the membrane shall also be neglected, which is valid when $T \gg E\tau^3/L^2$.

As described previously in this thesis, a liquid bridge applies a capillary force to each adjoining surface in two distinct ways: (i) a Laplace pressure force acting over the liquid-solid contact area, and (ii) a tension force pulling on the contact line. Similarly to the pancake solution (1.6) for bridge between rigid plates, we consider a wetting liquid that is confined to a very narrow gap. With this simplification, the pressure force dominates because the area-scaling of the pressure force 'beats' the length-scaling of the line force. Additionally, at this contact line it may be expected that the surface tension contributes to a discontinuity in the membrane tension, $[T]^+_- \propto \gamma$, but this is neglected because of the high tensions considered, $T \gg \gamma$. These assumptions shall be made throughout the rest of this chapter.

[1] Note that this is a different condition from that for the pre-existing tension in a membrane to dominate that induced by a spherical cap droplet, $T \gg \gamma^{2/3}(E\tau)^{1/3}$ [Davidovitch and Vella, 2018]. The reason for this difference is that in Davidovitch and Vella [2018], the unknown pressure must be solved for, whereas here it is set by the meniscus height.

To quantify the adhesion force, the interfacial curvature must be determined. Consistent with the assumption of a thin gap (and just like the pancake solution of §1.3.1), the main curvature contribution is assumed to be from the component between the solids and the meniscus is approximated as a circular arc of radius $h_M/(2\cos\theta)$. Here, h_M is the height of the membrane above the substrate where the meniscus meets the membrane (or 'meniscus height') and θ is the equilibrium contact angle of the liquid-solid-vapour system, taken for simplicity to be the same on both surfaces.[2] The pressure at the meniscus (relative to the ambient pressure) is then given by

$$p_{\text{meniscus}} = -\frac{2\bar{\gamma}}{h_M}, \tag{4.1}$$

recalling that $\bar{\gamma} = \gamma\cos\theta$.

4.2.2 Deformation

The liquid bridge is assumed to be axisymmetric and positioned at the centre of the membrane — bridges that start off-centre will move to the centre because of a capillary pressure gradient (similar to the mechanism described in §1.2.2). The vertical position of the membrane may then be written $z = h(r,t)$ with r the radial coordinate and t time.

A local force-balance on the membrane requires that the membrane shape $h(r,t)$ satisfies a membrane Young–Laplace equation

$$T\nabla_r^2 h = -p, \tag{4.2}$$

where ∇_r^2 denotes the axisymmetric Laplacian operator $\nabla_r^2 f = \frac{1}{r}\frac{\partial}{\partial r}(r\frac{\partial f}{\partial r})$ for any function $f(r,t)$, and $p(r,t)$ is the pressure field within the liquid. In static scenarios p is uniform but may vary spatially when considering the dynamic scenarios in §4.5. Here it has been assumed that the membrane slope remains small throughout (consistent with the large aspect ratio of the bridge itself) and, further, the inertia of the membrane has been neglected.

Finally, a fixed liquid volume, V, is imposed through

$$V = 2\pi\int_0^{r_M} rh\ \mathrm{d}r, \tag{4.3}$$

where r_M is the radial position of the meniscus. Note that it has again been assumed the meniscus shape has negligible impact on the volume because of the large aspect ratio of the liquid bridge.

[2] Any variations in the contact angle from the value given by the Young-Dupré law (1.3) are neglected, because the applied tension $T \gg \gamma$ [Davidovitch and Vella, 2018]. The effect of the membrane slope at the contact line on the contact angle is also ignored as the slopes are taken to be small, $h_r \ll 1$.

4.2.3 Non-dimensionalization

The problem is rendered dimensionless using the extrinsic radial lengthscale L and by rescaling the liquid volume to unity, introducing the vertical length scale V/L^2 in the process. Pressures, p, are rescaled by the typical Laplace pressure $\bar{\gamma}L^2/V$, and forces, f, are non-dimensionalized by $\bar{\gamma}L^4/V$. To begin with, we shall only consider equilibria and so do not need to define a timescale for now — this will be defined when studying dynamics in §4.5. We therefore define dimensionless variables

$$R = \frac{r}{L}, \quad H(R) = \frac{h(r)}{V/L^2}, \quad P = \frac{p}{\bar{\gamma}L^2/V}, \quad F = \frac{f}{\bar{\gamma}L^4/V}. \tag{4.4}$$

With this non-dimensionalization, the static membrane shape is controlled by two dimensionless parameters

$$\Gamma = \frac{\bar{\gamma}L^6}{TV^2}, \qquad H_\infty = \frac{L^2 h_\infty}{V}. \tag{4.5}$$

Physically, the parameter H_∞ represents the rescaled gap width and influences the system via the boundary condition that the membrane edge is at a fixed height $H(1) = H_\infty$; varying H_∞ corresponds to changing the separation of the membrane from the substrate. The parameter Γ represents the competition between a typical capillary pressure force pulling down on the membrane, $pr^2 \sim \gamma L^2/h \sim \gamma L^4/V$, and a restoring membrane tension force, $Tr\ \mathrm{d}h/\mathrm{d}r \sim TV/L^2$. A tension $T \gg \gamma$ is imposed; nevertheless Γ may remain an $O(1)$ quantity because of the amplifying effect of the ratio L^6/V^2 in (4.5).

The parameter Γ can be considered a measure of the extent to which capillarity is able to deform the membrane: for $\Gamma \ll 1$, the membrane is relatively rigid and little deformation occurs while for $\Gamma \gg 1$ the membrane is highly deformed by the liquid's capillarity. We therefore refer to Γ as the 'deformability' of the membrane.

In the relatively undeformable case, $\Gamma \ll 1$, we expect to recover the rigid result (1.6), which can be written in dimensionless terms as

$$F_{\text{rigid}} = \frac{f_{\text{pancake}}}{\bar{\gamma}L^4/V} = \frac{2}{H_\infty^2}, \tag{4.6}$$

where f_{pancake} is the (dimensional) pancake solution (1.6) and F_{rigid} is dimensionless. Note that in this rigid scenario the force is controlled solely by the gap width, H_∞. To understand how the adhesion force deviates from this result as the deformability Γ increases, we turn to study the equilibrium problem. A key aim is to understand how the adhesion force $F(\Gamma, H_\infty)$ behaves.

4.3 Equilibria

In equilibrium there is no fluid flow and so the internal liquid pressure must be uniform, and equal to the value at the meniscus, i.e. $P = -2/H(R_M)$ where R_M denotes the radial position of the meniscus. The problem of determining the equilibrium membrane shape, $H(R; \Gamma, H_\infty)$, therefore reduces to solving Poisson's equation (4.2) with forcing pressure

$$P(R) = \begin{cases} -\frac{2}{H(R_M)}, & 0 \leq R < R_M \\ 0, & R_M \leq R \leq 1. \end{cases} \tag{4.7}$$

The relevant boundary conditions are due to the imposed clamping (at $R = 1$) and symmetry/regularity at the origin, i.e. $H(1) = H_\infty$ and $H'(0) = 0$. At the meniscus, the membrane height is continuous; the slope may be discontinuous there because of the action of the surface tension force at the contact line. A horizontal force balance at the contact line between membrane, liquid and gas shows that this discontinuity in slope is proportional to $\gamma \sin\theta$; this can be neglected provided that the bridge aspect ratio $r_M/h_M \gg \tan\theta$.

4.3.1 Problem statement

In dimensionless terms, the equilibria of the system satisfy

$$\nabla_R^2 H = \begin{cases} 2\Gamma/H_M, & 0 < R < R_M, \\ 0, & R_M < R < 1. \end{cases} \tag{4.8}$$

The solution of (4.8) is to be found subject to the boundary conditions

$$[H]_-^+ = \left[\frac{\mathrm{d}H}{\mathrm{d}R}\right]_-^+ = 0, \qquad \text{at } R = R_M, \tag{4.9}$$

$$\frac{\mathrm{d}H}{\mathrm{d}R} = 0, \qquad \text{at } R = 0, \tag{4.10}$$

$$H = H_\infty, \qquad \text{at } R = 1. \tag{4.11}$$

Note that the radial position of the meniscus, R_M, and its height, H_M, are not known *a priori* and must be determined as part of the solution. Two additional relations are therefore required. The first of these is simply that $H(R_M) = H_M$. The second, and final, condition is the imposed volume constraint, namely

$$1 = 2\pi \int_0^{R_M} RH \, \mathrm{d}R. \tag{4.12}$$

For given values of H_∞ and Γ, the system (4.8)–(4.12) may be solved analytically to give a single transcendental equation for R_M:

$$(\pi H_\infty R_M^2 - 1)^2 + (1 - 4\log R_M)(\pi H_\infty R_M^2 - 1) - \frac{\pi^2}{4}\Gamma\,(1 - 4\log R_M)^2 R_M^6 = 0. \quad (4.13)$$

This equation could be rearranged to give H_∞ for given R_M, but we prefer to solve (4.13) numerically to find the (unknown) radius R_M for given Γ and H_∞, subject to the constraint that the liquid must remain within the domain, i.e. $R_M < 1$.

Numerical solutions of eqn. (4.13) suggest that, for some parameter values, the membrane touches the lower plane, i.e. $H = 0$ at some radial position R, which is generally $R = 0$ (since the membrane is most deformable in the centre). When this happens, the nature of the solution changes (since the membrane cannot penetrate the base, $H(R) \geq 0$ for all $0 \leq R \leq 1$); we therefore consider contacting solutions separately now.

4.3.2 Contacting solutions

When the membrane is in contact with the rigid surface in some region $R < C$, it is no longer solely subject to the capillary pressure but also to an unknown reaction force provided by the base. In this contacting region, the shape of the membrane is therefore no longer governed by (4.2) but rather by the requirement that the membrane conforms to the base, i.e. $H = 0$. At the boundary between contacting and non-contacting regions, a local force balance reveals that the membrane height and gradient should be continuous (assuming that contact does not give rise to additional adhesion or repulsion). It is therefore required that at the edge of the solid–solid contact region (i.e. $R = C$): $H = \mathrm{d}H/\mathrm{d}R = 0$. (Note that with this condition, it is not possible to have an equilibrium with an annular contact containing trapped liquid.)

The contacting problem is therefore largely the same as the non-contacting problem, except that $H = 0$ for $R < C$. The most significant change is that the wet region is now $C < R < R_M$ with C an additional unknown to be found. The additional constraint required to find C comes from the two continuity conditions at the edge of the solid–solid contact region

$$H = \frac{\mathrm{d}H}{\mathrm{d}R} = 0, \qquad \text{at } R = C, \quad (4.14)$$

which replace the symmetry boundary condition of (4.10), $H'(0) = 0$.

More concretely, the contact problem reduces to solving the following three non-linear

simultaneous equations for R_M, H_M and C

$$H_M = \frac{\Gamma}{2H_M}\left[R_M^2 - C^2 + 2C^2\log\left(C/R_M\right)\right], \tag{4.15}$$

$$H_\infty = H_M - \frac{\Gamma}{H_M}(R_M^2 - C^2)\log R_M, \tag{4.16}$$

$$1 = \frac{\pi\Gamma}{H_M}\left[\frac{1}{4}(R_M^4 - C^4) + C^2R_M^2\log\left(C/R_M\right)\right]. \tag{4.17}$$

4.3.3 Adhesion force and multiple solutions

The adhesion force in equilibrium, i.e. the force acting normal to the rigid surface (or equivalently the force that must be applied at the clamps to maintain the equilibrium), is readily determined to be:

$$F = \begin{cases} 2\pi\ \frac{R_M^2}{H_M} & \text{non-contacting,} \\ \\ 2\pi\ \frac{R_M^2 - C^2}{H_M} & \text{contacting.} \end{cases} \tag{4.18}$$

Therefore, to calculate the adhesion force, all that is required is a solution of the transcendental equations for the equilibrium meniscus position R_M and height H_M (as well as the edge of the solid–solid contact region, C, if it exists), which may readily be found numerically. Substituting these values into (4.18), the dimensionless adhesion force, F, is found as a function of the gap separation H_∞ when Γ is fixed (fig. 4.2a); alternatively F may be plotted as a function of the deformability Γ when H_∞ is fixed (fig. 4.2b).

In fig. 4.2a, the edge height is varied at several (fixed) values of the deformability Γ and the resulting adhesion force is plotted alongside the force in the rigid case (4.6). At each value of the edge height the adhesion force is larger for a deformable membrane (regardless of the applied tension Γ) than for the rigid case $\Gamma = 0$. The deformable adhesion force can be as much as two orders of magnitude larger than the corresponding rigid adhesion force. Similarly the more deformable membranes are able to achieve a given adhesion force (for example to support a given load) at a larger gap separation. This suggests that the addition of deformability into a capillary adhesive may improve its adhesive capabilities significantly.

The behaviour of the solution, and in particular its adhesion force, is strongly characterized by whether contact occurs or not: when contact occurs, the bridge spreads further (fig. 4.3a) and the meniscus height is significantly smaller (see fig. 4.3b, as well as the two profiles that contrast the contacting and non-contacting states shown in the inset to fig. 4.3a). Although the width of the wetted region, $R_M - C$, appears to be approximately

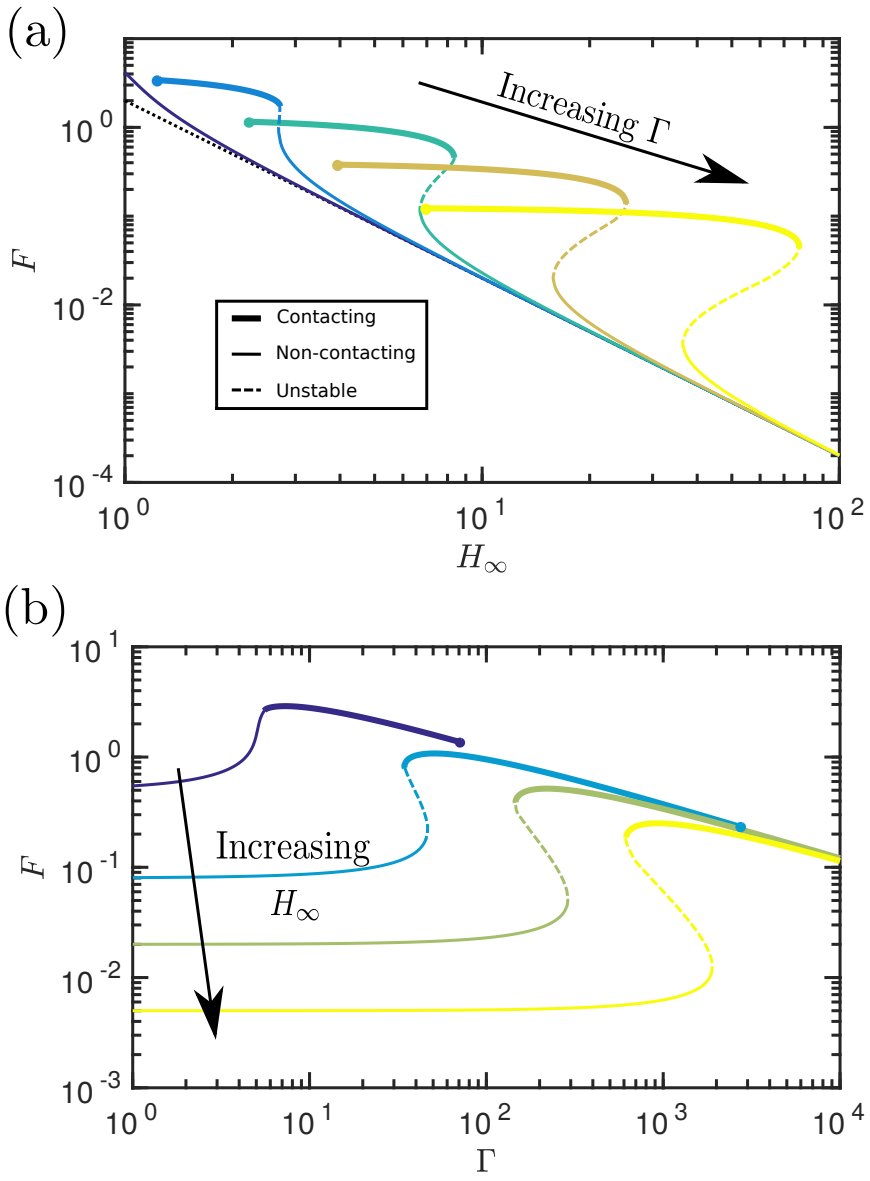

Figure 4.2: The dimensionless adhesion force $F(\Gamma, H_\infty)$. Results are shown for: (a) fixed deformability $\Gamma = 1, 10, 10^2, 10^3, 10^4$ and varying edge height H_∞ and (b) fixed edge height $H_\infty = 2, 5, 10, 20$ and varying membrane deformability Γ. The computation stops when the system is flooded, i.e. $R_M = 1$ (solid circles). In (a) the force is compared to a perfectly rigid membrane $\Gamma = 0$ (black dotted line) and in both panels different thickness curves are used to distinguish different states, as described in the legend of (a). Note that the adhesion force is significantly larger when the membrane is in contact with the base (thicker solid curves) but even out of contact (thinner solid curves) the adhesion force remains larger than in the rigid case.

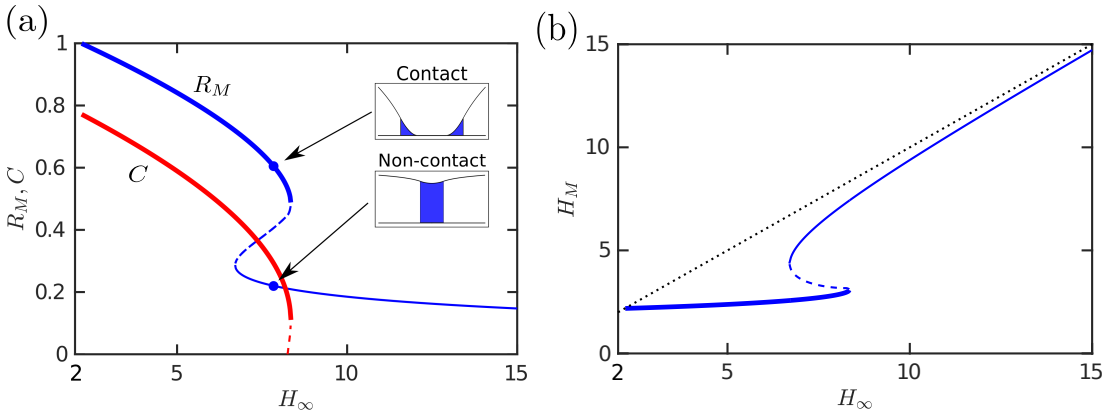

Figure 4.3: (a) The equilibrium meniscus radius R_M (blue) and contact point C (red) vary with gap width H_∞, when Γ is fixed (here $\Gamma = 100$). There is a non-contacting stable solution (thin solid curve), an unstable solution (dashed curve) and a contacting stable solution (thick solid curve). Each of these three states only exists over a specific range of values of H_∞. Inset: Membrane profiles of the contacting and non-contacting stable solutions when $H_\infty = 8$ (blue circles). (b) The variation of the meniscus height H_M with H_∞ (again shown for $\Gamma = 100$). The dotted line denotes $H_M = H_\infty$ for comparison.

constant (see fig. 4.3a) the net result of the spreading in contact is an increase in the bridge footprint area. The dual effects of an increased Laplace pressure and a larger area over which it acts lead to the dramatic increase in the adhesion force in the case of contact and motivate a more detailed study of *when* contact occurs.

Exploring the (Γ, H_∞) parameter space for the number and type of equilibrium solutions, three key regions are found: one in which there is a single non-contacting solution, another with a single contacting solution, and one region where three solutions are possible (of these three, one is contacting, one non-contacting and the third can be either, depending on the parameter choice). Figure 4.4 summarizes which regions of parameter space each behaviour is observed in. A stability analysis using Maddocks' Theorem [Maddocks, 1987] reveals that, in the case of 3 solutions, the intermediate solution is linearly unstable; the remaining two equilibria are linearly stable and consist of one contacting and one non-contacting solution. (Note that when H_∞ becomes sufficiently small then the liquid floods the system and there is no longer any physically relevant solution.)

In this system, a fixed separation H_∞ has been imposed and the resulting force F calculated; alternatively the system could be loaded with a given force F and then the corresponding H_∞ determined (as described in Chapter 1). In such a force-controlled scenario we expect all solutions to be unstable, with a small perturbation to the bridge or membrane resulting in either attachment with $H_\infty \to 0$ or detachment with $H_\infty \to \infty$ (similar to the rigid case detailed in §1.3.3). We investigate the effect of force-control in

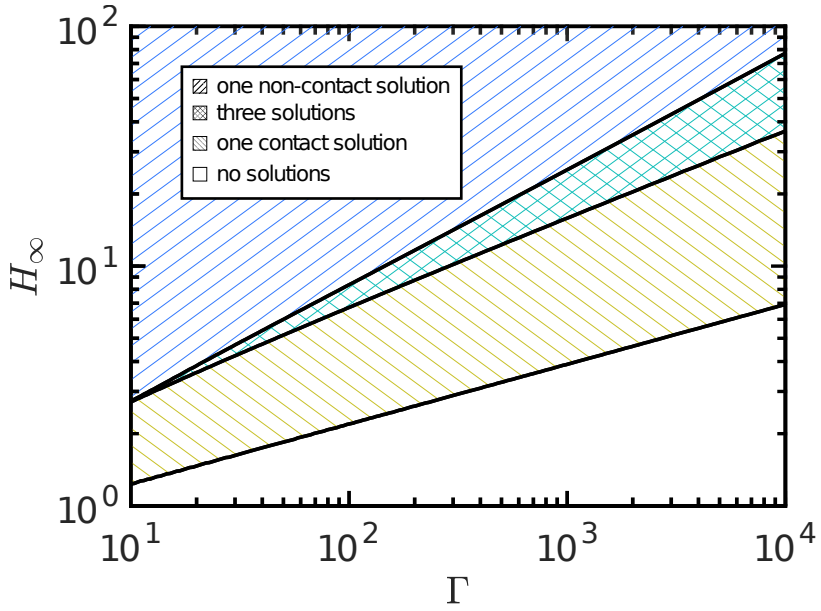

Figure 4.4: The number and type of equilibria varies with the two parameters Γ and H_∞. The hatching in each region denotes the number of contacting or non-contacting solutions, as described in the legend.

capillary adhesion further in Chapter 5.

From fig. 4.2b, it appears that at a given edge separation in the contacting regime, the force decreases as the strength of surface tension (γ) increases. However, because the force has been non-dimensionalized by the surface tension in (4.4), the *dimensional* force *increases* as the surface tension increases, as expected.

The transition between non-contacting and contacting states (and vice versa) is sharp as the parameters are varied (figs. 4.2, 4.3 & 4.4); this transition is a saddle-node bifurcation and introduces hysteresis into the system. The system can therefore be thought of as being 'switchable': varying the parameters can 'turn on' and 'turn off' contact (and hence strong adhesion) as these transition points are passed. As we shall see shortly, this gives alternative routes to de-adhere from the substrate: one can either increase H_∞ while fixing Γ ('yanking') or reduce Γ while maintaining H_∞ ('peeling'). Before discussing this in more detail, however, we consider an experimental realization of the system discussed so far.

4.4 Comparison with experiments

The study of the equilibrium states of this system reveals two interesting features. Firstly, the system exhibits bi-stability — for the same parameters (namely Γ and H_∞) the system

may be in one of two stable equilibrium states. Secondly, the adhesion force of these two states may differ by more than an order of magnitude. To test whether these two stable equilibrium states are physical, and to confirm the large difference in force between them, an experimental version of this simple adhesive system was developed.

The relevant experiments were conducted by Finn Box (University of Oxford) and Thomas Robert (ENS, Paris) in the Maths Observatory, and details of the experimental set-up are listed in Appendix 4.A. In this section we compare these results to the theory.

4.4.1 Results

By fixing the tension in the sheet and varying the gap width, force-displacement and radius-displacement curves were obtained, and are presented in fig. 4.5 with the corresponding (static) theoretical prediction with no fitting parameters. Note that the experiment exhibits the same phenomenological behaviour as predicted by the theory: there are two different stable states, each with markedly different adhesion force (and liquid extent) and, further, the transition between these two states is sharp as the gap width is varied. This transition occurs at different values of H_∞ depending on the current state, i.e. the system exhibits hysteresis. The critical parameter values at which the transition occurs, as well as the magnitude of the force and radius jump are predicted well by the equilibrium theory. This transition is noticeably much slower when the force is increasing towards contact than when the strong adhesion solution is lost (note that in fig. 4.5 data points are shown at constant intervals of $2.5\ \mathrm{s}$, with many more points plotted during the motion into contact than the motion out of contact). We show in §4.5 that the slowness of approach to contact may be explained by liquid being trapped beneath the membrane as contact is approached.

There are, however, some discrepancies between the theory and experiment which could be explained by factors including: a misalignment of $H_\infty = 0$ (calibrated before the liquid is added), dynamic effects, and additional forces not included in the model. As an example of an effect not included in the model, note that at larger gap separations we start to move out of the large aspect ratio regime required by the theory (leading to the bridge necking and eventually rupturing); furthermore, the small bridge radius in these cases also means that the measurements of the radius become more unreliable as small errors in the fitting are more pronounced.

At fixed gap width, experiments also reveal that when starting in the high-adhesion contacting state it is possible to significantly decrease the adhesion force solely through an increase in the tension (decrease in the deformability Γ, example shown in fig. 4.6). This

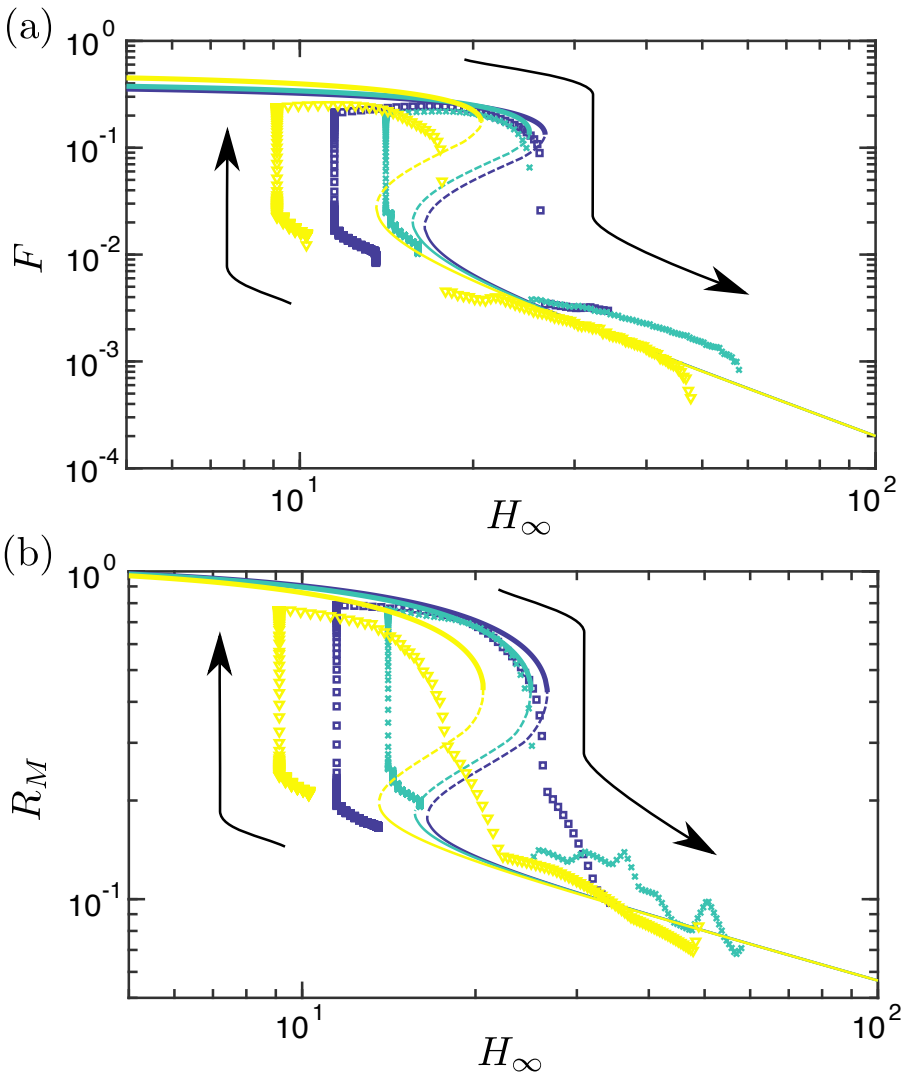

Figure 4.5: The measured dimensionless (a) adhesion force and (b) bridge radius (symbols) compared with the theoretical predictions without any fitting parameter (curves) for three different experiments. The arrows illustrate the progression of the experiment: an initial lowering of the membrane, followed by a period at fixed height and then retraction at constant speed. Dark blue squares: $T = 4.9$ N/m, $V = 7.8$ μL, $\Gamma = 1100$. Blue-green crosses: $T = 5.1$ N/m, $V = 8.2$ μL, $\Gamma = 970$. Yellow triangles: $T = 5.2$ N/m, $V = 9.9$ μL, $\Gamma = 650$. Experimental results obtained by Thomas Robert.

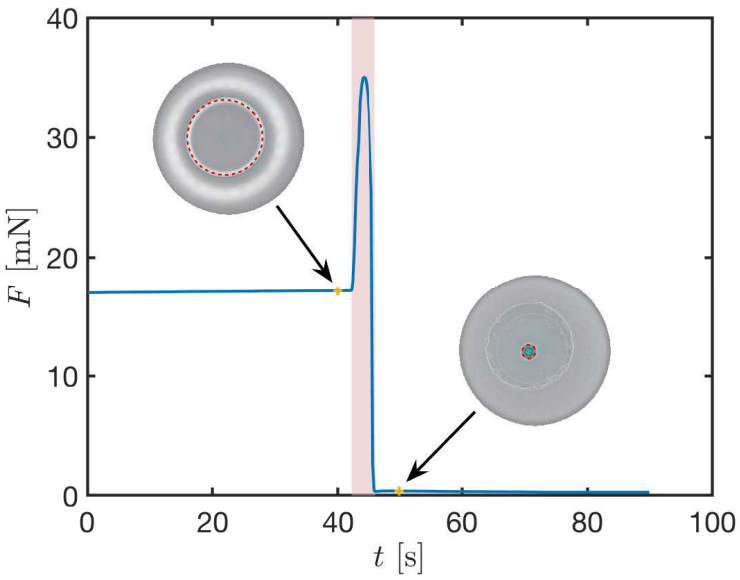

Figure 4.6: Increasing the tension, while maintaining a fixed separation, results in the 'switching off' of strong adhesion. The tension is increased from $T = 2.5\ \mathrm{N/m}$ to $T = 7.1\ \mathrm{N/m}$ over the duration of the highlighted region, and is constant otherwise. Examples of the bridge extent before and after the tension change are shown, with the meniscus position denoted by a red dashed circle. Here the clamp was fixed at a height $h_\infty = 1.1\ \mathrm{mm}$, with a bridge volume $V = 7.8\ \mu\mathrm{L}$. Experiment by Thomas Robert.

confirms that tension variation could be used as a detachment mechanism. We investigate this possibility further later.

4.4.2 Adhesion testing

To test the feasibility of this system as an adhesive, Finn Box tasked it with lifting some small loads attached to a glass slide (fig. 4.7a-c). For the parameters in the tests ($\bar{\gamma} = \gamma\cos\theta = 29\ \mathrm{mN/m}$, $L = 15\ \mathrm{mm}$, $T = 2\ \mathrm{N/m}$, $V = 10\ \mu\mathrm{L}$) the equilibrium theory predicts that a load corresponding to a mass of $2.7\ \mathrm{g}$ can be comfortably supported at a separation $h_\infty = 0.3\ \mathrm{mm}$; moreover, for these parameter values, the equilibrium theory predicts that there should be an equilibrium configuration with the membrane in contact with the glass slide. Note, however, that once a load is lifted then the bridge-membrane system evolves at fixed force, rather than with a given gap separation; it is expected that either the membrane is pulled into close contact and remains stuck, or detaches completely.

On lowering the clamp to a separation $h_\infty = 0.3\ \mathrm{mm}$ and lifting immediately, the load drops off. Holding the sheet at this set distance for a short period of time increases the

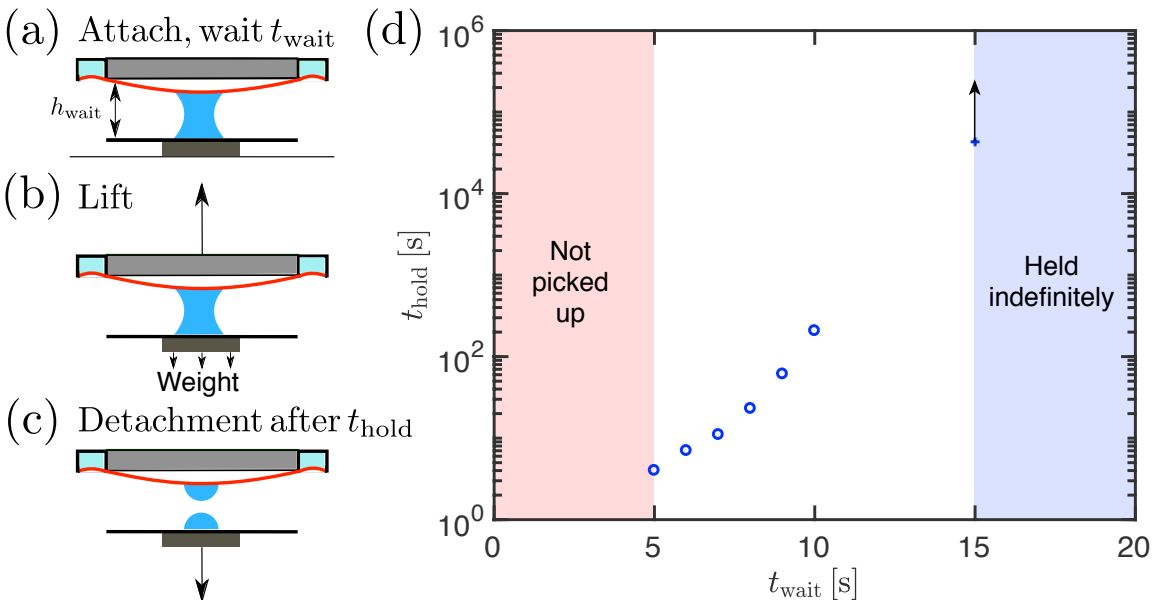

Figure 4.7: Schematic of the dynamic adhesive test performed by Finn Box. (a) The clamp is lowered to a set distance from the glass plate. (b) After a time t_{wait} the clamp is raised at a constant speed, lifting the glass plate and load. (c) After some time t_{hold} detachment may occur and the load falls back. (d) Experimental results showing the relationship between the time the system is left to equilibrate, t_{wait}, and the adhesion time, t_{hold}, for $h_\infty = 0.3$ mm, $T = 2$ N/m, $V = 10$ μL and lifting a mass of 2.7 g. Experiments were performed with $t_{\text{wait}} \leq 4$ s but no noticeable lift-off was observed. When $t_{\text{wait}} \gtrsim 10$ s the load would remain attached on the time scale of hours, making it difficult to obtain an accurate value for t_{hold}, and for $t_{\text{wait}} = 15$ s the load remained attached overnight (over 12 hours).

length of time for which the adhesion is successful (fig. 4.7d). Indeed, if the two surfaces are held at the fixed separation for sufficiently long (on the order of 15 s) then the load is adhered indefinitely (timescale of days). This suggests that the dynamics of adhesion are non-trivial and deserve further study. We therefore turn to study the dynamics of adhesion now.

4.5 Dynamics

To study the dynamics of adhesion, a lubrication-type model is used: we assume that the flow in the thin gap between the membrane and substrate is viscous, consistent with the assumption of large aspect ratio used in studying the equilibrium of the system. Applying the no-slip boundary condition (i.e. zero velocity) at both the membrane and wall, the

Stokes equation for the flow is readily integrated to give the radial fluid flux as

$$q = -\frac{h^3}{12\mu}\frac{\partial p}{\partial r} = \frac{T}{12\mu}h^3\frac{\partial}{\partial r}(\nabla^2 h), \tag{4.19}$$

with μ the dynamic viscosity of the liquid.

Conservation of mass [Leal, 2007] then gives an evolution equation for the membrane height, $h(r,t)$, which is known as Reynolds' equation: $h_t + \nabla \cdot q = 0$. This can be non-dimensionalized in the same manner as the static scenarios, i.e. we again have $H = h/(V/L^2)$ and $R = r/L$, with the natural timescale $t_* = 12\mu L^4/\bar{\gamma}V$ used to non-dimensionalize time (though t is used to denote dimensionless time to avoid confusion with the applied tension T). The dimensionless partial differential equation for the evolution of the membrane is then

$$\frac{\partial H}{\partial t} = \frac{1}{R}\frac{\partial}{\partial R}\left[RH^3\frac{\partial P}{\partial R}\right], \tag{4.20}$$

where the dimensionless pressure $P = p/(\bar{\gamma}L^2/V)$ is

$$P = -\frac{1}{\Gamma}\nabla_R^2 H. \tag{4.21}$$

As boundary conditions at the origin ($R = 0$), we impose zero membrane slope (axisymmetry) and no radial flux, i.e.

$$\frac{\partial H}{\partial R} = 0 \qquad \text{at } R = 0, \tag{4.22}$$

$$\frac{\partial}{\partial R}(\nabla_R^2 H) = 0 \qquad \text{at } R = 0. \tag{4.23}$$

At the meniscus, $R = R_M$, the pressure in the liquid must balance the pressure jump across the meniscus (as discussed in Chapter 1, a local Young-Laplace equation is valid when applying the lubrication approximation to a liquid bridge); this provides a condition on the membrane curvature at $R = R_M$. Also, just as in the static problem, the slope of the membrane and the membrane displacement must both be continuous. Finally, the membrane must reach the clamp, $H(1) = H_\infty$. Since the problem in the dry membrane is quasi-static, the membrane shape may be solved analytically in this region for given values of H_M and R_M; the result is that there are two conditions at the meniscus, namely

$$\nabla_R^2 H = \frac{2\Gamma}{H_M} \qquad \text{at } R = R_M, \tag{4.24}$$

$$\frac{\partial H}{\partial R} = \frac{H_M - H_\infty}{R_M \log R_M} \qquad \text{at } R = R_M. \tag{4.25}$$

An equation for the motion of the meniscus, $R_M(t)$, is determined by requiring it to have the velocity that balances the flux, i.e.

$$\frac{\mathrm{d}R_M}{\mathrm{d}t} = -H_M^2 \left.\frac{\partial P}{\partial R}\right|_{R=R_M} . \tag{4.26}$$

Note that this motion of the meniscus ensures that global conservation of mass, i.e. fixed volume $2\pi \int_0^{R_M} RH \, \mathrm{d}R = 1$, is automatically satisfied throughout.

The partial differential equation (4.20) is solved numerically subject to the boundary conditions (4.22)–(4.26) and the initial condition $H(R,0) = H_\infty$. To determine the numerical solution, space is discretized in a flux-conservative manner and evolved in time using the method of lines, integrated with MATLAB's ODE solvers. (Further details are given in Appendix 4.B.)

4.5.1 Contacting & non-contacting dynamics

Numerical solutions of the dynamic problem qualitatively confirm the results of the static analysis presented in §4.3. In particular, the system appears to have two distinct types of equilibria characterized by whether the membrane and base are in physical contact. Furthermore, it is possible to switch between these states by changing the applied tension, for example. However, the dynamic simulations demonstrate a further key difference between these types of solution: with fixed control parameters (Γ and H_∞) the approach to equilibrium is significantly quicker in the non-contacting case than it is in the contacting case (compare the different time scales in figs. 4.8a and 4.8b). This also agrees qualitatively with the experimental observation in fig. 4.5.

The results of fig. 4.8 are presented with a fixed gap width H_∞ but with various values of the membrane deformability Γ. We see that with lower values of Γ (more tense, hence less deformable, membranes), the adhesion force decays exponentially to the expected equilibrium value. These relatively undeformable membranes have equilibria that are out-of-contact; the membrane approaches these equilibria quickly, and the exponential decay of the adhesion force to the equilibrium value may be understood by a standard linear stability analysis about the equilibrium configuration (see Appendix 4.C). Increasing Γ to values for which the equilibrium analysis suggests a contacting solution exists, we see (fig. 4.8b) that the adhesion force approaches its final value significantly more slowly than might be expected from a linear stability analysis: the decay appears to be power law, rather than exponential.

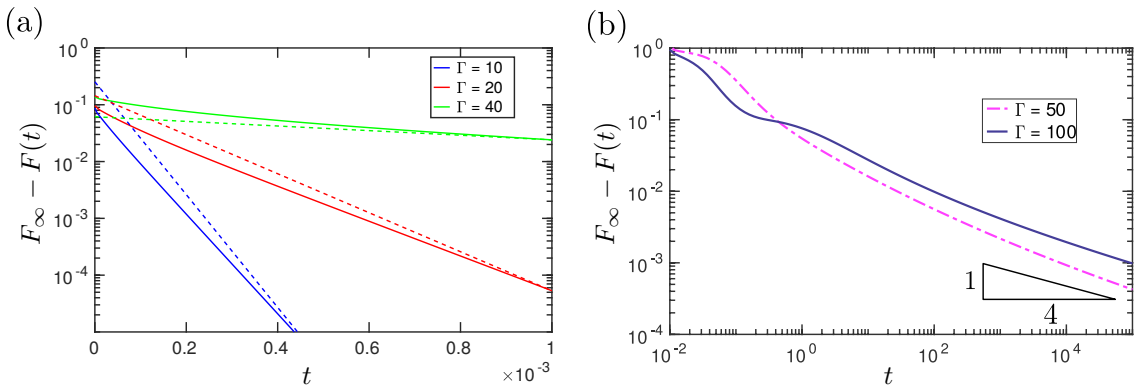

Figure 4.8: The dynamic approach of the dimensionless adhesion force, $F(t)$, to its equilibrium value F_∞ in both (a) non-contacting and (b) contacting cases. (a) In the non-contacting case, the force decays exponentially to its equilibrium value, consistent with a linear stability analysis of the equilibrium (dashed lines show the expected decay rate, i.e. slope, only). (b) In the contacting case, the force instead appears to decay according to a power law. In each case, the equilibrium force, F_∞, is calculated from the static theory, and $H_\infty = 5$.

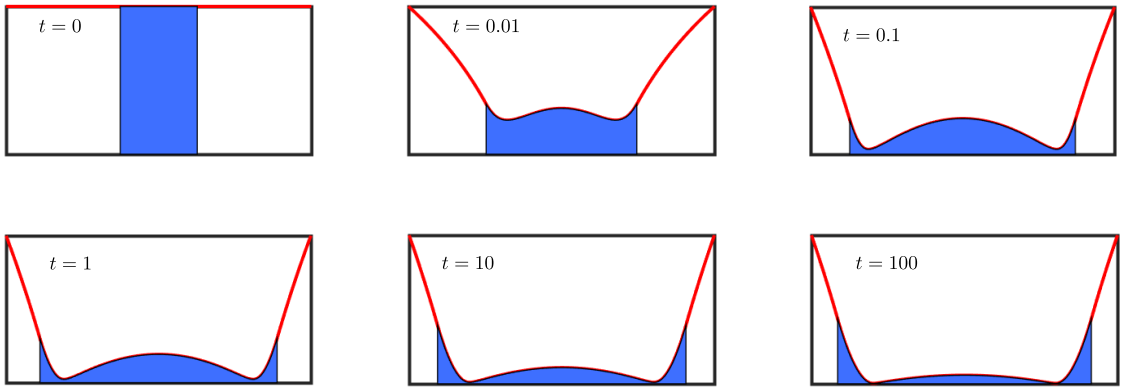

Figure 4.9: Snapshots of the cross-sectional profile of the membrane and liquid bridge during the approach to contact of a highly deformable membrane (here $\Gamma = 100, H_\infty = 5$). Note that some of the liquid is trapped in a dimple beneath the membrane and drains very slowly. The initial condition is shown in the top-left panel with the behaviour at five subsequent times also shown. Note that the vertical scale is exaggerated here (by the different scales used to non-dimensionalize horizontal and vertical lengths) — in reality the bridge is thin and wide.

4.5.2 Trapped liquid slows contact

The different dynamic behaviour in the approach to contact (compared to that out-of-contact) can be explained by the formation of a liquid dimple under the membrane (see snapshots of the membrane shape from simulations in fig. 4.9). Here the membrane is pulled towards contact by the capillary forces of the liquid bridge, and to accommodate this motion the liquid must be squeezed radially outwards towards the meniscus. However, this flow is sufficiently resisted by viscosity that some of the liquid becomes trapped beneath the membrane and only drains slowly; we shall see that this slow drainage controls the dynamics at late times.

The dimple formation shown in fig. 4.9 is reminiscent of previous work on a bubble approaching an interface or rigid wall through a viscous liquid [e.g. Jones and Wilson, 1978, Yiantsios and Davis, 1990, Lister et al., 2006a], as well as the formation of collars and lobes during capillary drainage of an annular film on/inside a cylinder [e.g. Hammond, 1983, Lister et al., 2006b]. The methods of these studies are used as templates with which to study the dynamics of the system presented in this chapter. At sufficiently late times the bulk of the liquid inside the dimple is at uniform pressure, and likewise for the liquid outside. Crucially, however, the two regions have different pressures and are joined by a narrow region at the dimple edge, in which the shape of the membrane controls the leakage flux; the structure of the problem is shown in fig. 4.10.

In fig. 4.10, we see that the portion of the membrane that separates the regions of approximately constant pressure is narrow. It is expected that, once the dimple has formed, this narrow gap will be located close to the equilibrium contact point, C_∞, calculated from the equilibrium theory and so its location is taken to be at C_∞, to leading order. The height there, $H_{\mathsf{min}} = H(C_\infty)$, is assumed negligible in comparison to the height away from $R = C_\infty$. With this assumption, we see from Reynolds' equation for the dimensionless flux, $Q = -H^3 \partial P/\partial R$, that the pressure gradient is largest where the gap width H is small, justifying taking the pressure to be uniform away from $R = C_\infty$.

Inside the dimple the uniform pressure is positive and dictates the membrane shape via a Poisson equation. The profile of the dimple may therefore be written in the form $H(R) \approx H_0(1 - R^2/C_\infty^2)$ where H_0 is the height at the centre, $R = 0$. Integrating, the volume trapped within the dimple is found to be $V_{\mathsf{dimple}} \approx \pi C_\infty^2 H_0/2$.

Outside the dimple the constant liquid pressure must be negative (since it must match the pressure at the meniscus); this pressure is therefore written as $P = -\Pi$ with $\Pi > 0$. As with the dimple region, the flow here is negligible, so that the membrane shape evolves quasi-statically (though for simplicity the shape of the membrane in this region is not given explicitly here).

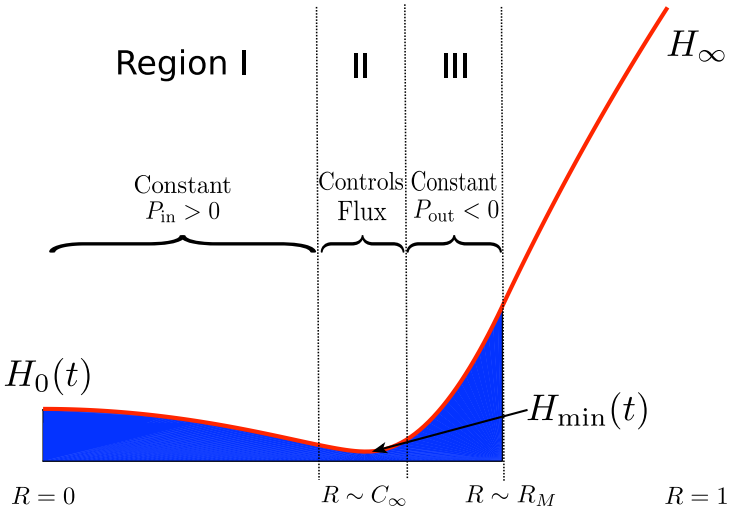

Figure 4.10: When approaching contact, a dimple forms beneath the membrane. To understand the evolution of the dimple, the wet region of the membrane is split into 3 distinct regions: region I is the dimple at uniform positive pressure with dimple height $H_0(t)$, region III is the meniscus region at uniform negative pressure, and region II is a small annular region surrounding the narrow gap, H_{min}, that controls the fluid flux, and is at a radial position close to the edge of the equilibrium contact region, C_∞.

In the small gap at the edge of the dimple (which shall be called the 'neck', illustrated by region II in fig. 4.10) the volumetric flux of fluid, Q, is controlled by the local membrane geometry via a lubrication flow. A local coordinate $X = R - C_\infty$ is introduced in the neck region (i.e. $|X| \ll C_\infty$) so that

$$Q \approx \Gamma^{-1} H^3 \frac{\partial^3 H}{\partial X^3} \tag{4.27}$$

there.

Equation (4.27) can be solved to give the shape of the membrane in the neck region, but requires matching conditions as $X \to \pm\infty$, as well as a value for the flux Q. In these local coordinates the curvature due to the pressure in the meniscus requires $\partial^2 H/\partial X^2 \to \Gamma\Pi$ as $X \to \infty$; similarly, the membrane gradient at the interior edge of the neck region requires $\partial H/\partial X \to -2H_0/C_\infty$ as $X \to -\infty$. Finally, the integrated flux through the neck region, $2\pi C_\infty Q$, must balance the rate at which the volume of the dimple decreases, $\dot{V}_{\text{dimple}}$. Combining these three relations with (4.27), scaling relations are obtained

$$\frac{H_{\text{min}}}{X_*^2} \sim \Gamma\Pi, \qquad \frac{H_{\text{min}}}{X_*} \sim \frac{H_0}{C_\infty}, \qquad \frac{C_\infty^2 H_0}{t} \sim \frac{C_\infty H_{\text{min}}^4}{\Gamma X_*^3}, \tag{4.28}$$

where X_* is the typical horizontal scale in the neck region. Balancing these equations gives leading order scalings for the dimple height H_0, as well as the height H_{min} and width X_* of the narrow gap region, in terms of Γ, Π, C_∞, t as follows:

$$\begin{aligned} H_0 &\sim \Gamma^{1/2}\Pi^{1/4}\, C_\infty^{3/2}\, t^{-1/4}, \\ X_* &\sim \Gamma^{-1/2}\Pi^{-3/4}\, C_\infty^{1/2}\, t^{-1/4}, \\ H_{\mathsf{min}} &\sim \Pi^{-1/2}\, C_\infty\, t^{-1/2}. \end{aligned} \tag{4.29}$$

This scaling analysis reveals that the dimple height evolves like $H_0 \sim t^{-1/4}$, and the membrane height in the narrow gap like $H_{\mathsf{min}} \sim t^{-1/2}$, similar to the scalings obtained by Jones and Wilson [1978] in drop coalescence. Thus contact between the membrane and base will not occur in finite time (unless another shorter-range force, such as van der Waals, takes over).

The similarity solution for the membrane shape in this transition region is found to be the same as that calculated by Jones and Wilson [1978] (see Appendix 4.D.1). However, the pre-factors in the scaling relations (4.29) differ because in this problem the outer curvature is set by the pressure at the meniscus (i.e. the meniscus height) rather than, for example, a bubble radius or volume. These pre-factors may be found in terms of the membrane deformability Γ and the equilibrium contact point C_∞ (which is itself a function of Γ and H_∞); the pre-factors also depend on the meniscus pressure Π (at late times, it is expected that $\Pi \sim 2/H_M^\infty$, with H_M^∞ the equilibrium meniscus height, since the pressure is set by the meniscus curvature).

Our main focus here is on the evolution of the key properties of the system at late times, especially the adhesion force (but also the meniscus position and height). To progress, the membrane is assumed to behave quasi-statically outside the dimple, evolving due to the volume increase as liquid leaks through the neck region. The meniscus position, R_M, its height, H_M, and the (effective) contact position, C, therefore obey (4.15)–(4.17), but with the left hand side of (4.17) modified to $1 - V_{\mathsf{dimple}}$ to account for the (decreasing) amount of liquid trapped within the dimple. We note that (see Appendix 4.D.1)

$$V_{\mathsf{dimple}} \sim \frac{\pi}{2} A \Gamma^{1/2}\Pi^{1/4} C_\infty^{7/2} t^{-1/4} \tag{4.30}$$

for a constant $A \approx 0.20$ that is found numerically. (The radial flux is then given by $Q \sim \dot{V}_{\mathsf{dimple}}/2\pi C_\infty \sim t^{-5/4}$.)

Expanding R_M, H_M and C about their equilibrium values, and using the leading order expression for the dimple volume, (4.30), the three conditions (4.15)–(4.17) are linearized to calculate the first order corrections to the radius, height and apparent contact radius

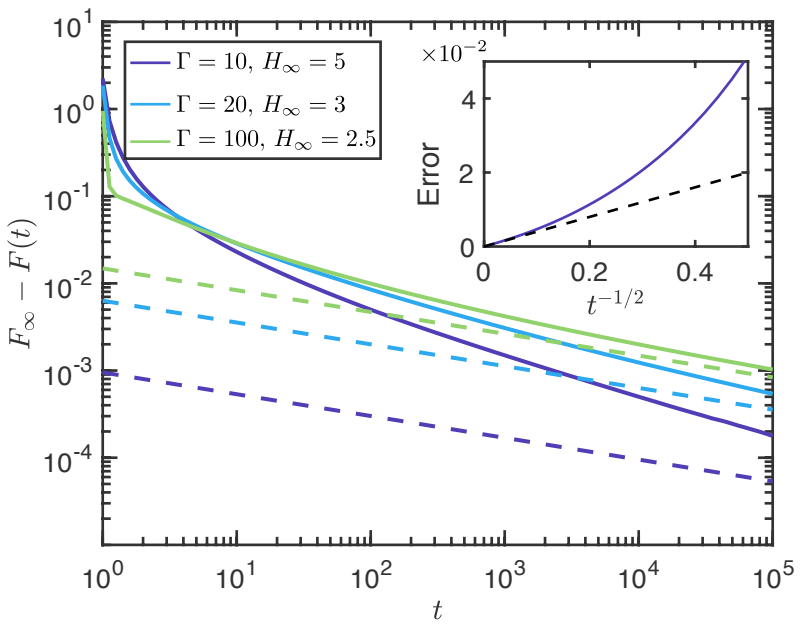

Figure 4.11: The adhesion force decaying to its equilibrium value, F_∞ (calculated from the analysis of §4.3), in the contacting regime. The numerics (solid curves) approach the asymptotic dimple theory (dashed lines) at late times. Inset: the absolute error (solid curve) between the numerically calculated force $F(t)$ and the first two terms of the asymptotic expansion is approximately linear (black line for comparison) in $t^{-1/2}$ at late times (here $\Gamma = 10, H_\infty = 2.5$).

(Appendix 4.D.2). The correction to the adhesion force is then determined from linearizing the relation

$$F = -2\pi \int_C^{R_M} RP(R,t)\ \mathrm{d}R = \frac{2\pi}{\Gamma}\frac{H_M - H_\infty}{\log R_M} \tag{4.31}$$

which leads to

$$F \sim F_\infty - F_1\ t^{-1/4} \tag{4.32}$$

for a constant F_1 that can be computed numerically (see Appendix 4.D.2). Note that here F_∞ is the force calculated from the static theory; although the pressure within the dimple is positive (and hence slightly reduces the adhesion force), at late times this correction is small and the adhesion force is dominated by the suction pressure outside the dimple.

Figure 4.11 shows the numerically-determined decay of the adhesion force to its equilibrium value, together with the full prediction of the asymptotic theory (including prefactors). Qualitatively we see a reasonable match between the two quantities at late times, suggesting that the expected algebraic decay of (4.32) is indeed that observed numerically. The inset of fig. 4.11 shows the absolute error in (4.32) and confirms that the error does indeed occur at higher order (i.e. at $O(t^{-1/2})$).

While the leading-order asymptotic results are in good agreement with numerical simulations for very late times, the convergence is relatively slow: the results suggest an expansion in powers of $t^{-1/4}$ so that to obtain an error of less than 10% requires waiting for a time $t = O(10^4)$ or greater. Indeed, the numerical results shown in fig. 4.11 confirm that the $t^{-1/4}$ scaling is only observed for dimensionless times $t \gtrsim 10^4$. In the experiments of §4.4, the dimensional timescale is $t_* = 12\mu L^4/\bar{\gamma}V \approx 400$ s; the time needed to observe this dynamic scaling with the experimental parameters here would therefore be on the order of weeks, and effectively not observable.

4.6 Detachment

The equilibrium theory of §4.3 has shown that, from the perspective of maximizing the adhesion force, it is beneficial to be in the contacting regime. Contact can be achieved either by decreasing the gap width (decreasing H_∞) until the membrane snaps to contact, or by decreasing the tension sufficiently (increasing Γ). As shown in the last section, the larger forces associated with contact are moderated by the caveat that the force approaches its higher contacting value relatively slowly, $F_\infty - F(t) \sim t^{-1/4}$. Nevertheless, the order of magnitude increase in adhesion force seen as contact is approached, as well as the reasonable waiting times for significant attachment that were observed in §4.4.2, suggest that operating in the (Γ, H_∞) parameter regime corresponding to contacting equilibria is still beneficial.

Having investigated adhesion to a substrate, and seen the importance of being close to contact, it is natural to then ask how can one detach from the surface efficiently? In particular, if one begins close to contact, is there a 'best' way to unstick? The key quantity of interest is the effective work of separation, which is defined to be the work done to separate the surfaces,

$$W_{\text{sep}} = \int_{H_\infty^0}^{\infty} F \, \mathrm{d}H_\infty + \Delta U_{\text{elast}}, \tag{4.33}$$

where $H_\infty^0 = H_\infty(t = 0)$ is the initial gap between clamp and substrate and ΔU_{elast} is the change in elastic energy due to stretching of the sheet. Note that the upper limit of integration in (4.33) is $H_\infty = \infty$, since we want to completely separate the surfaces.[3]

[3] In reality, the liquid bridge would be expected to rupture at a finite separation, similarly to that in Chapter 2. Here, we are assuming that the liquid is in the thin film (lubrication) limit so that the rupture occurs at a very large dimensionless separation $H_\infty = H_{rup}$ that may effectively be taken as infinite. In addition, we may expect the majority of the work of separation to be done when the adhesion force is strongest, and so the effect of ignoring the rupture point would be expected to be small.

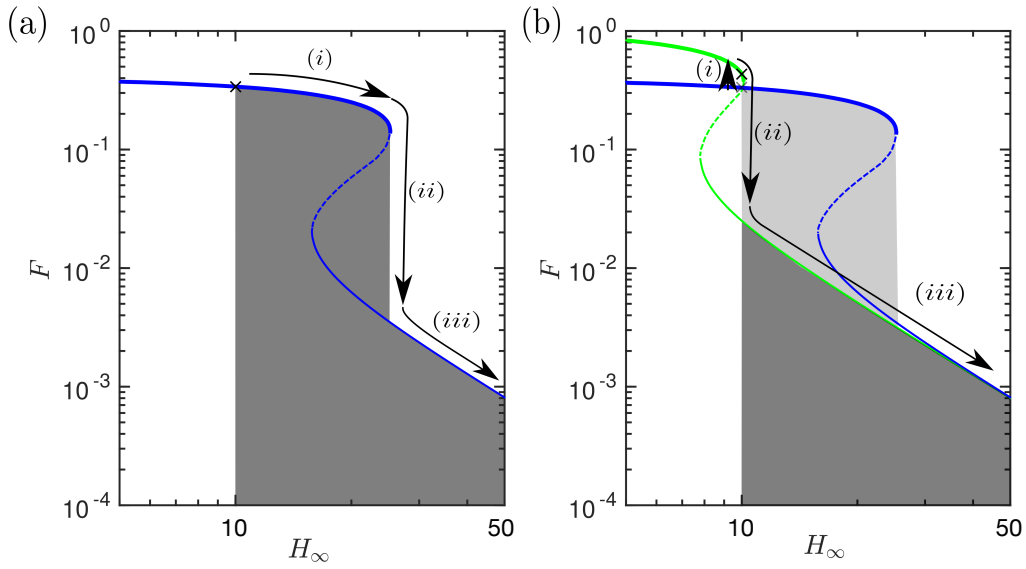

Figure 4.12: The quasi-static work of separation from different methods of detachment. (a) Pull directly away ('yanking'), $H_\infty \to \infty$ with Γ fixed. As H_∞ increases, the solution takes the equilibrium value (blue solid curves), and jumps from contact to non-contact at the fold (ii). The work of separation is the integral $\int F \, \mathrm{d}H_\infty$, and is illustrated by the shaded dark grey area. (b) If, instead, the tension is first increased (decrease the deformability Γ) at fixed H_∞ before yanking, the work of separation may be significantly reduced. The different stages are: (i) Initially decrease Γ (to green solution) before (ii) increasing H_∞ to pull away through the snap-off transition. The total work is the sum of dark grey area and the work done to increase the tension in stage (i) and will be preferable to yanking provided that the energy needed to stretch the membrane in (b)(i) is less than the yanking energy saving compared to (a), illustrated by the light grey region.

In practice, the work of separation in the quasi-static case that follows is calculated from the increase in the total equilibrium energy of the sheet. Here the energy input will be stored in two different ways: elastic energy in the stretched sheet and surface energy at the interfaces. Ignoring small terms, the dimensionless energy, U, can be written as

$$\Gamma U = \pi \int_0^1 R \left(\frac{\mathrm{d}H}{\mathrm{d}R} \right)^2 \mathrm{d}R - 2\pi\Gamma R_M^2. \tag{4.34}$$

In dynamic scenarios, we focus on the case where the tension in the sheet is constant and $\Delta U_{\text{elast}} = 0$, and so a thorough definition of this term is omitted here.

4.6.1 Quasi-static detachment

The problem of detachment is approached by considering an initial condition corresponding to a contacting equilibrium state (i.e. strong adhesion). The detachment problem is then to choose a path in (Γ, H_∞)-space that minimizes the work of separation, W_{sep}.

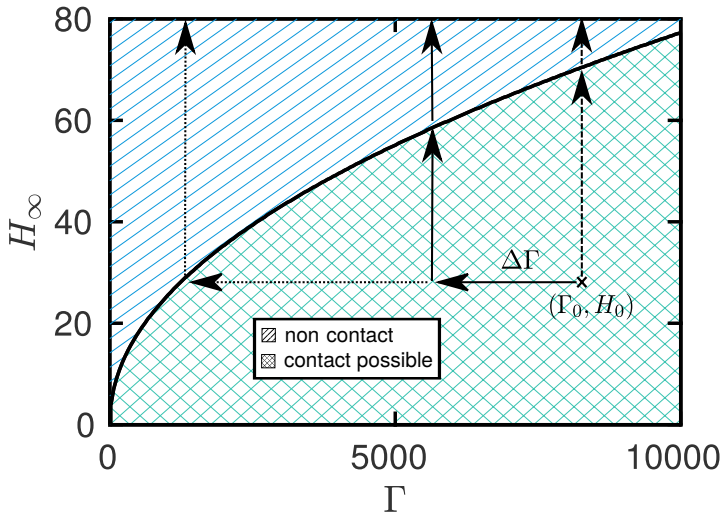

Figure 4.13: Starting from an initial contacting state (Γ_0, H_0), there are many possible paths in parameter space that result in detachment. The simplest of these is a direct pull off at constant tension ('yanking', dashed path). We investigate various quasi-static paths that involve decreasing Γ by $\Delta\Gamma$ before taking $H_\infty \to \infty$ (solid path); the optimal (smallest work of separation) path is to decrease Γ until contact is lost before pulling away (dotted path). Note that here the area labelled 'contact possible' contains the three solution region seen in fig. 4.4, and the region with no solutions has been omitted for simplicity.

A simple option is to pull directly away from the substrate at fixed tension: this is termed 'yanking', and this path is illustrated, together with the associated work of separation, in fig. 4.12a. Yanking requires working directly against the strong adhesion force of contact. However, the tension in the membrane may also be varied and so another possibility is to increase the tension (decrease Γ) whilst keeping H_∞ fixed (at least initially). We have already seen experimentally that decreasing Γ sufficiently results in the membrane 'peeling' off the base (fig. 4.6) and losing contact at a smaller gap separation H_∞, i.e. without first pulling the membrane up. Once out of contact, the adhesion force is smaller and so we might expect to then be able to increase H_∞ with significantly less resistance than if yanking without a tension change. This alternative mode of detachment is shown in fig. 4.12b, together with a cartoon of how much energy might be saved in this way. Of course, decreasing Γ itself has an energetic cost, ΔU_{elast}, and so we must consider the trade-off between the work required to increase the tension and the subsequent reduction in work done against adhesion due to this tension change.

From a quasi-static perspective, the key piece of information is where in the parameter space the path crosses the discontinuous jump from contact to non-contact. As this

discontinuity is passed, the system will lose energy that cannot be regained. We therefore need to consider separately the energy change, calculated using (4.34), both before and after this jump to determine the energy required to detach.

Paths are considered where Γ is initially decreased (the tension is increased) by an amount $\Delta\Gamma$, before pulling away ($H_\infty \to \infty$) as illustrated in fig. 4.13. W_{sep} is calculated from the change in surface and stretching energy of the sheet. We find that increasing the tension results in an overall energy saving. In fact, the best strategy is to increase the tension until contact is lost (at which point the adhesion force is substantially lower) before pulling away (increasing H_∞). Surprisingly, however, the benefit of this change is relatively modest: in simulations the reduction in W_{sep} made by increasing the tension first was typically in the region of 5–10%. While this is surprising, we must also consider the effect of the *rate* of yanking on the work of separation; we saw that the dynamics of adhesion significantly modifies the equilibrium picture, and so it is natural to wonder whether the same might be true of dynamic detachment.

4.6.2 Dynamic detachment

Numerical simulations were performed in which the edge height H_∞ is increased at a constant pulling rate, $\dot{H}_\infty$, while Γ is maintained at a constant value. This shows that the instantaneous adhesion force at a given edge height has a significant rate dependence (fig. 4.14a): at high rates, viscous forces become important and resist the separation of the membrane from the substrate — a mechanism that is often called 'Stefan adhesion' [Labonte and Federle, 2015, Bikerman, 1968, Brau et al., 2016]. The peak adhesion force is increased, and the force remains high over a larger range of gap widths H_∞. It is therefore expected that the work of separation in this case, $W_{\text{sep}} = \int F \, \mathrm{d}H_\infty$, will be significantly increased. An illustration of how the work of separation increases with the rate of detachment is shown in fig. 4.14b for a particular choice of Γ and $H_\infty(t = 0)$. Details of the numerical calculation of W_{sep} are given in Appendix 4.E. In this example, the work done against the adhesion increases markedly when $\dot{H}_\infty \gtrsim 10$ and by more than a factor of two between $\dot{H}_\infty = 1$ and $\dot{H}_\infty = 100$.

Note that the dynamic yanking is compared with the optimal quasi-static strategy (changing the tension in the membrane); this quasi-static model does not include dynamic effects for several reasons. Firstly, the stretching sheet always has a uniform tension, and this tension therefore cannot do any work against the viscous shear force, and there is no rate-dependence in the varying tension model.[4] Secondly, although one might expect

[4] However, note that in this scenario, the dynamics of detachment may be non-trivial, as suggested by detailed studies of 'peeling by pulling' [McEwan and Taylor, 1966, Lister et al., 2013].

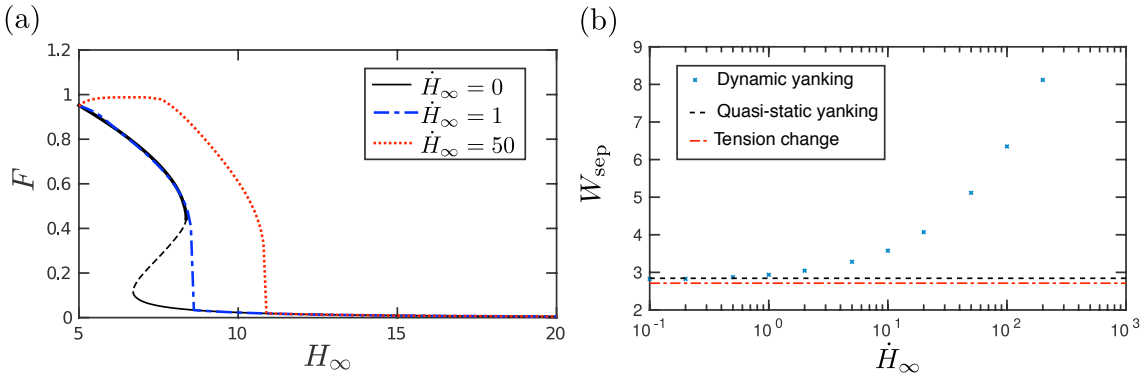

Figure 4.14: (a) Pulling the membrane off at a faster rate results in a larger adhesion force over a wider range of gap widths, H_∞. (b) The energy required to detach ($H_\infty \to \infty$) when retracting at constant speed increases with the retraction speed, $\dot{H}_\infty$. Dynamic simulations (blue 'x') are performed at different constant retraction rates and compared to the quasi-static change in energy at fixed Γ (black dashed) and the optimal quasi-static strategy (red dash-dotted) in which Γ is decreased until contact is lost before pulling away at fixed Γ. In both figures the initial condition for dynamic simulations is close to the contacting equilibrium with parameters $\Gamma = 100, H_\infty = 5$.

rate to have an effect once contact between the membrane and base is lost and we switch to yanking, the rapid exponential decay towards equilibrium and the small adhesion force suggests that this contribution is negligible in determining the work of separation.

We conclude that it is energetically favourable to detach at a slow speed when only 'yanking'. However, in applications for which detachment is required to occur within a shorter time scale, slow pulling rates are impractical: in the experiments presented in this chapter, the relevant time scale is $400\ \mathrm{s}$. In such scenarios, detachment within seconds would require a significant $\dot{H}_\infty$ and hence a non-negligible increase in the adhesion force (and work of separation) compared to the quasi-static case. This means that the optimal strategy of first increasing the tension would then have a substantial benefit over 'yanking' in scenarios such as the laboratory experiments of §4.4; it may also be that this is a preferential method for detaching quickly in other scenarios.

4.7 Conclusions

Using a theoretical model of a membrane under tension attached to a rigid substrate by a liquid bridge, we have studied some key features of elasto-capillary adhesion. This model system highlights that deformability can improve adhesive capabilities, with the coupling between the surface tension and elasticity resulting in an increase in the adhesion force over the comparable rigid case. As in other similar scenarios [Duprat and Protiere, 2015,

Wexler et al., 2014], the capillary forces can deform surfaces sufficiently that they form solid-solid contact. This contact can result in stronger adhesion forces [as has also been observed in capillary adhesion of fibres by Duprat et al., 2020], even without accounting for additional adhesion between the two solid surfaces.

Two key parameters determine the equilibrium behaviour of the system: the dimensionless gap separation, H_∞, and the membrane deformability, Γ. These can be actively (and separately) controlled via the clamp height, $h_\infty \propto H_\infty$, and the imposed membrane tension, $T \propto \Gamma^{-1}$, respectively. Crucially, it is shown that by a careful choice of these parameters it is possible to switch the strong adhesion of contact on or off. However, the dynamic approach to contact is found to be relatively slow: the adhesion force obeys a scaling law $F(t) - F_\infty \sim t^{-1/4}$ at late times because liquid is trapped in a dimple and must be squeezed outwards through a narrow gap to allow contact. This slow squeezing out of liquid complicates the use of this adhesive to lift loads: adhesion is not maintained if the surfaces are not left together long enough that this dimple significantly drains. However, a quantitative understanding of this effect is still lacking since, in practice, the adhesion fails via peeling from one edge, which is a feature that cannot be reproduced by the axisymmetric theory presented here. We shall investigate this further with a simple model system in Chapter 5.

Active control of the two parameters H_∞ and Γ allows for the development of different strategies for effective adhesion and detachment from the substrate, and it is suggested that, from an energetic perspective, it is better to 'peel' off the base by increasing the tension than to 'yank' by pulling directly against the strong adhesion.

The relatively simple framework of this theory has allowed the exploration of some of the key features of adhesion in elasto-capillary systems. However, this analysis neglects some important aspects of surface deformation. For example, it has been required that the membrane is in close proximity to the substrate so that membrane slopes are small and the bridge is sufficiently wide and short that the effects of the circumferential meniscus curvature and the capillary line force may be neglected. It was also assumed for simplicity that the tension in the membrane dominates bending, additional stretching in the membrane, and the surface tension acting at the meniscus. In addition to these simplifications to the modelling of the solid deformation (and consistent with the rest of this thesis) contact line pinning has been ignored in this chapter; the impact this may have is unclear, but it may act to reduce the observed adhesion force in some scenarios, and also slow the formation and drainage of the dimple. As well as understanding the effect of lifting these restrictions, it would be interesting to see how adding other extra effects, such as solid-solid adhesion or surface roughness, would modify the results of this chapter.

Appendices

4.A Experiments

4.A.1 Set-up

A thin (thickness $\tau \sim 100\ \mu\mathrm{m}$), soft (Young's modulus $E = 200\ \mathrm{kPa}$) circular sheet of Poly-vinyl siloxane (PVS) was fabricated by spin-coating. The sheet was clamped onto an annular chamber with radius $L = 15\ \mathrm{mm}$; the sheet tension was varied by withdrawing air from the chamber using a syringe, this created a pressure difference that sucked the outer edge of the membrane into the chamber, pulling the entire sheet taut across the clamp (see fig. 4.15). The value of the tension was inferred by an indentation technique [Vella and Davidovitch, 2017] prior to each experiment; when the tension was varied during the experiment, its value was also measured after the experiment. To ensure that the surface properties of the substrate were the same as that of the membrane (and, in particular, that the contact angles were the same), a rigid glass plate was coated with a layer of PVS with thickness $\sim 100\ \mu\mathrm{m}$ to form the substrate. A dyed droplet of oil (Mineral Oil light, Sigma-Aldrich, UK; volume $1\ \mu\mathrm{L} \lesssim V \lesssim 10\ \mu\mathrm{L}$) was confined between the clamped sheet and the PVS-covered glass, which itself rested on a mass balance accurate to 0.1mg (Pioneer PA64C Analytic Balance, Ohaus, Switzerland) which measured the effective weight of the substrate; this arrangement allowed the adhesion force to be determined to $1\ \mu\mathrm{N}$ precision. Mineral oil was chosen to reduce the effects of evaporation and the effect of impurities. The height of the clamped membrane was varied using a linear stage (M228.10S, Physik Instrumente, Germany) driven by a stepper motor (Mercury Step C663.11, Physik Instrumente, Germany), with a combined accuracy of $\pm 2\ \mu\mathrm{m}$. The force f and plate separation h_∞ were both recorded digitally in MATLAB; typical measurements were in the range 0.1–50 mN and 0.4–2 mm, respectively.

A camera positioned above the experiment recorded the bridge's shape in plan view (viewed through the elastic sheet, which is relatively translucent because of its thinness). The bridge radius was determined by least-squares fitting of a circular profile to the liquid's edge. The surface tension of the mineral oil was measured to be $\gamma = 32.1 \pm 0.2\ \mathrm{mN/m}$

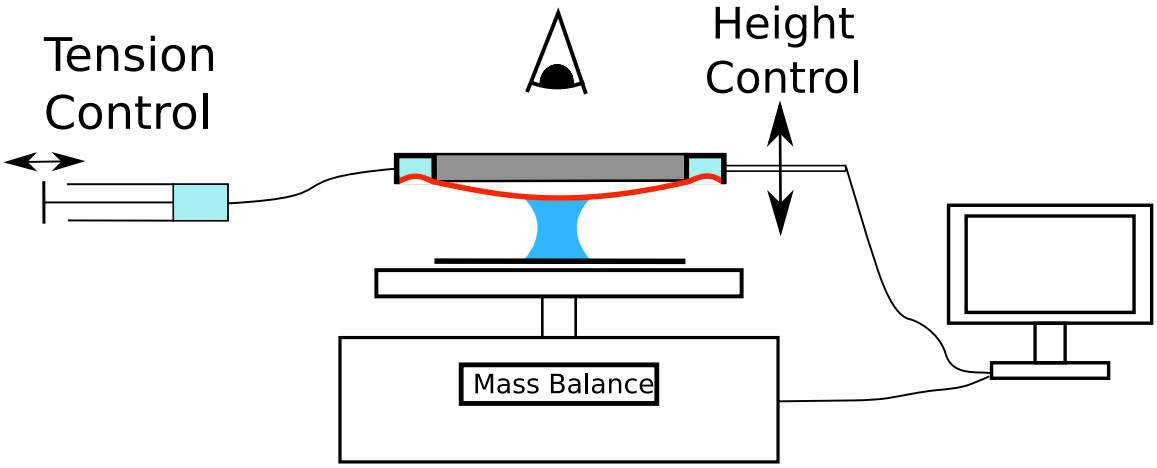

Figure 4.15: Schematic of the experimental set-up. A dyed droplet of mineral oil (blue) was confined between a PVS-coated glass plate and a clamped PVS sheet (red). This system rested on a mass balance that recorded the adhesion force. The height of the clamp (grey) was varied using a computer-controlled linear actuator, and the tension in the sheet could be increased by withdrawing air from an annular chamber (light blue) in the clamp, which sucked the outer edge of the sheet into the chamber, pulling the whole membrane taut. A camera imaged the experiment from above.

via the Wilhelmy plate method, while the contact angle on PVS was measured to be $\theta = 23.5 \pm 2.5°$.

With these parameter values, the tension-dominated regime of interest occurs when $T \gg T_c \equiv E\tau h_\infty^2/L^2$; here $T_c \leq O(0.1)\ \mathrm{N/m}$. These experiments were conducted with the aspect ratio $L/h_\infty \geq O(10)$ and membrane tensions that were in the range of $1\ \mathrm{N\,m^{-1}} \lesssim T \lesssim 10\ \mathrm{N\,m^{-1}}$ so that $\gamma/T \lesssim 3 \times 10^{-2}$. Therefore these experiments do indeed satisfy the various assumptions made to simplify the theoretical analysis (i.e. $h_\infty \ll L$, $\gamma \ll T$, $T \gg E\tau(h_\infty/L)^2$ and $T \gg E\tau^3/L^2$).

4.A.2 Loading protocol

Experiments were initially performed at fixed sheet tension, varying the gap width. A droplet of the mineral oil was placed on the PVS-covered glass. The clamped membrane was then lowered towards the droplet, with liquid contact detected by a sudden jump in the weight of the system (since the glass plate was partially lifted by the adhesion force of the liquid bridge as soon as it formed).

Once it was detected that the liquid had bridged the membrane-substrate gap, there were three key stages to the experiment: (i) the clamp was lowered in steps of a few $\mu\mathrm{m}$, being left to settle on a timescale of $100\ \mathrm{s}$ between steps, until the force began to evolve dynamically (when an inflection point was seen in the real-time measured force

as a function of time), at which point (ii) the separation (h_∞) was kept constant for approximately 10 minutes to allow the system time to equilibrate, before (iii) retracting at a constant speed ($5\ \mu\mathrm{m/s}$) until the capillary bridge ruptured. The force was recorded throughout this process via changes in the weight recorded by the mass balance, and the radius inferred from processing of images taken from above. The separation distance was determined from readings of the height of the clamp relative to the position at which dry surfaces contacted (measured prior to introduction of the liquid).

Further experiments were performed to understand the effect of changing tension. For these, the procedure was followed as above but once strong adhesion was achieved at the end of stage (ii), the sheet tension was increased over a period of $O(10\ \mathrm{s})$, instead of retracting the clamp.

4.B Numerical scheme

The free boundary problem (4.20)–(4.26) is transformed to a fixed domain problem using the change of variables $\xi = R/R_M$. Defining $\Lambda(\xi) = R_M^2 H$ then allows us to re-write the governing PDE in the form of a conservation equation $\partial\Lambda/\partial t + \nabla_\xi \cdot \hat{\mathbf{Q}} = 0$, where the flux $\hat{\mathbf{Q}} = \hat{Q}\mathbf{e}_\xi$ (with ξ a radial coordinate) is given by

$$\hat{Q} = -\frac{\Lambda^3}{R_M^6}\frac{\partial \hat{P}}{\partial \xi} - \frac{\xi \Lambda \dot{R}_M}{R_M}, \qquad \hat{P} = -\frac{1}{\Gamma R_M^4}\nabla_\xi^2 \Lambda, \tag{4.35}$$

and the meniscus position evolves according to the equation

$$\dot{R}_M = -\frac{\Lambda(1)^2}{R_M^5}\left.\frac{\partial \hat{P}}{\partial \xi}\right|_{\xi=1}. \tag{4.36}$$

This system is solved numerically using the method of lines: the domain $\xi \in [0,1]$ is split into concentric annuli $\xi_{i-1/2} < \xi < \xi_{i+1/2}$ — within each annulus both the height Λ_i and the pressure $\hat{P}_i$ are uniform. For this problem, n equal-width annuli were used, each having a median radius $\xi_j = j/n$ for $j = 1, 2, \ldots n$. At the centre of the system there is a circle of radius $\xi_{1/2} = 1/2n$ about the origin, which has height Λ_0 and pressure $\hat{P}_0$. In the simulations presented, a typical discretization used $n = 800$, with second-order central finite differences applied to discretize the derivative terms.

The annuli heights change due to the flux at the edges, $\hat{Q}_{i\pm1/2}$, giving evolution

equations for the Λ_i in terms of R_M and the neighbouring Λ_i and $\hat{P}_i$:

$$\frac{\mathrm{d}\Lambda_j}{\mathrm{d}t} \approx \frac{2}{\xi_{j+1/2}+\xi_{j-1/2}}\frac{1}{\Delta\xi}\left[\frac{1}{R_M^6}\frac{A_{j+1/2}\hat{P}_{j+1}-(A_{j+1/2}+A_{j-1/2})\hat{P}_j+A_{j-1/2}\hat{P}_{j-1}}{\Delta\xi} + \frac{\dot{R}_M}{R_M}(\xi_{j+1/2}^2\Lambda_{j+1/2}-\xi_{j-1/2}^2\Lambda_{j-1/2})\right] \quad (4.37)$$

for $j = 1, 2, \ldots n-1$, where $A_i = \xi_i\Lambda_i^3$ and $\Delta\xi = 1/n$. Note that Λ takes the mean value of the neighbouring annulus heights when evaluated at an edge $\Lambda_{i+1/2} = (\Lambda_{i+1}+\Lambda_i)/2$. The pressures $\hat{P}_j$ on each annulus are determined by

$$\hat{P}_j \approx -\frac{1}{R_M^4}\frac{2}{\xi_{j+1/2}+\xi_{j-1/2}}\frac{\xi_{j+1/2}\Lambda_{j+1}-(\xi_{j+1/2}+\xi_{j-1/2})\Lambda_j+\xi_{j-1/2}\Lambda_{j-1}}{(\Delta\xi)^2}. \quad (4.38)$$

Similarly, the central circle evolves due to the flux coming in at the edge

$$\frac{\mathrm{d}\Lambda_0}{\mathrm{d}t} \approx 4\frac{\Lambda_{1/2}^3}{R_M^6}\frac{\hat{P}_1-\hat{P}_0}{(\Delta\xi)^2}+2\frac{\dot{R}_M}{R_M}\Lambda_{1/2} \qquad \text{where } \hat{P}_0 \approx -\frac{4}{R_M^4}\frac{\Lambda_1-\Lambda_0}{(\Delta\xi)^2}. \quad (4.39)$$

The boundary conditions at $\xi = 0$ are accounted for by the discretization at the centre, so it is only necessary to consider the boundary conditions at $\xi = 1$, equivalent to (4.24) and (4.25). Applying these conditions fixes the value of Λ_n, which is calculated by adding an additional 'ghost' annulus outside the meniscus with height Λ_{n+1} and using central differences to discretize the two boundary conditions at each time step. The value for the annulus height by the meniscus is found to be

$$\Lambda_n = \frac{\Delta\xi(2+\Delta\xi)R_M^2H_\infty - 2\Lambda_{n-1}\log R_M + \sqrt{\Omega}}{2[\Delta\xi(2+\Delta\xi)-2\log R_M]}, \quad (4.40)$$

where the term $\Omega(\Lambda_{n-1}; R_M, \Delta\xi, H_\infty, \Gamma)$ in the square root is given by

$$\Omega = [\Delta\xi(2+\Delta\xi)R_M^2H_\infty - 2\Lambda_{n-1}\log R_M]^2 + 8\Gamma R_M^6\log R_M(\Delta\xi)^2[\Delta\xi(2+\Delta\xi)-2\log R_M]. \quad (4.41)$$

Additionally, we note that the pressure at the edge is known

$$\hat{P}_n = -\frac{2\Gamma R_M^2}{\Lambda_n}. \quad (4.42)$$

The meniscus position evolves due to the (discretized) pressure gradient there:

$$\dot{R}_M \approx -\frac{\Lambda_n^2}{R_M^5}\frac{\frac{3}{2}\hat{P}_n-\hat{P}_{n-1}+\frac{1}{2}\hat{P}_{n-2}}{\Delta\xi}. \quad (4.43)$$

The solution to the ODEs (4.37) & (4.39), including the evolution of R_M (4.43), is found numerically from a given initial condition using MATLAB's inbuilt solver `ode15s`.

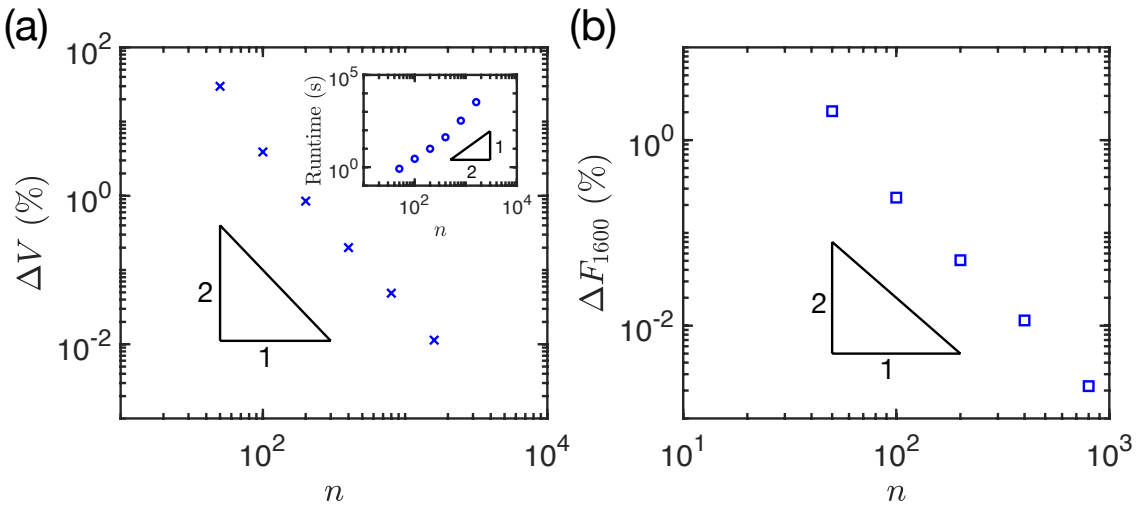

Figure 4.16: Simulations of the sheet relaxing from an initially flat state, $H(r,0) = H_\infty$, up to a dimensionless time $t = 100$ with parameters $\Gamma = 100$ and $H_\infty = 5$ for various numbers of grid points $n = \{50, 100, 200, 400, 800, 1600\}$. (a) The maximum percentage change in liquid volume decreases like n^{-2}. Inset: the time taken for the computation increases like n^2. (b) The maximum percentage difference in force, compared to the $n = 1600$ case, decreases like n^{-2}.

4.B.1 Accuracy of the numerical scheme

To test the accuracy of the numerical scheme, several simulations with different number of grid points n were run on a test case: an initially flat membrane with tension $\Gamma = 100$ at a clamped height $H_\infty = 5$ relaxes towards its contacting equilibrium from time $t = 0$ to time $t = 100$, with results recorded at each integer time.

The total volume of liquid should be conserved during the simulations, and so this can be used as a test for accuracy of the numerical scheme. The maximum percentage change in the dimensionless volume from $V = 1$ is shown in fig. 4.16a, with an inset showing the time taken to compute each solution. As n increases, the volume change appears to decrease like n^{-2}, while the runtime for each solution increases quadratically. The decrease in the error in V is consistent with the use of second-order discretization.

We are most interested in how the adhesion force behaves as time progresses, and so for completeness plot the maximum variation in the adhesion force over the same simulations in fig. 4.16b. In this case, there is not an exact solution for what the force should be at each time-step, and so the numerical solution is compared with the most refined discretization: $n = 1600$. Again, we find that the results (this time the adhesion force) appear to converge like an inverse square law with the number of spatial points: $\Delta F \sim n^{-2}$. This inverse square law is also in agreement with the fact that a second-order

finite difference method was used to approximate the spatial derivatives.

In the simulations presented throughout the chapter, the discretization had $n = 800$. Looking at fig. 4.16, we can see that this choice has a good combination of both accuracy (volume error of less than 0.1%) and runtime (the given simulation finished in less than 6 minutes).

4.C Linear stability analysis (of non-contacting equilibria)

Small perturbations to a given non-contacting equilibrium membrane shape, $\bar{H}(R)$, and corresponding meniscus radius, $\bar{R}$, are considered at fixed values of (Γ, H_∞). Solutions are calculated by taking a standard ansatz of the form

$$\begin{aligned} H(R,t) &= \bar{H}(R) + \varepsilon f(R) e^{\sigma t} \\ R_M(t) &= \bar{R} + \varepsilon e^{\sigma t}, \end{aligned} \tag{4.44}$$

where $\varepsilon \ll 1$ and σ is the growth rate of the perturbation.

The function $f(R)$ and the growth rate σ are determined by linearizing (with respect to ε) the evolution equation (4.20) and boundary conditions (4.22)–(4.26), as well as volume conservation (4.12). An ODE is obtained for $f(R)$

$$\frac{1}{R}\frac{\mathrm{d}}{\mathrm{d}R}\left[R\bar{H}^3\frac{\mathrm{d}}{\mathrm{d}R}\left(\frac{1}{R}\frac{\mathrm{d}}{\mathrm{d}R}\left[R\frac{\mathrm{d}f}{\mathrm{d}R}\right]\right)\right] + \sigma\Gamma f = 0, \tag{4.45}$$

together with the boundary conditions

$$\begin{aligned} f'(0) = 0, \qquad f'''(0) &= 0, \\ f'(\bar{R}) - \frac{f(\bar{R})}{\bar{R}\log\bar{R}} &= \frac{-2\Gamma}{\bar{H}(\bar{R})}, \\ f''(\bar{R}) + \frac{f'(\bar{R})}{\bar{R}} + \frac{2\Gamma f(\bar{R})}{[\bar{H}(\bar{R})]^2} &= \frac{-2\Gamma[\bar{H}(\bar{R}) - H_\infty]}{[\bar{H}(\bar{R})]^2\bar{R}\log\bar{R}}. \end{aligned} \tag{4.46}$$

These boundary conditions emerge from, respectively: symmetry at the origin, no radial flux at the origin, fixed position at the clamp/gradient matching at the meniscus, and the curvature-imposed meniscus pressure. There is also a global volume conservation condition

$$\int_0^{\bar{R}} z f(z)\mathrm{d}z = -\bar{R}\bar{H}(\bar{R}). \tag{4.47}$$

When solving this system numerically, it is convenient to define a function that measures the change in liquid volume within $r < R$: $I(R) = \int_0^R z f(z)\mathrm{d}z$. Then the volume

integral condition (4.47) can be replaced by an extra ODE that couples to (4.45)

$$\frac{\mathrm{d}I}{\mathrm{d}R} = Rf \tag{4.48}$$

subject to the two boundary conditions

$$I(0) = 0, \qquad I(\bar{R}) = -\bar{R}\bar{H}(\bar{R}). \tag{4.49}$$

The ODEs (4.45) & (4.48) are solved numerically subject to the boundary conditions (4.46) & (4.49) using MATLAB's in-built boundary value problem solver `bvp4c` to find the growth rate σ, for given parameter values (Γ, H_∞) and the appropriate equilibrium solution $\bar{H}(R)$. The dashed lines plotted in fig. 4.8a have slope corresponding to the growth rate determined in this way.

4.D Dimple drainage calculation

4.D.1 Similarity solution

The pre-factors in the scaling relations (4.29) are determined by first finding a similarity solution for the membrane shape in the neck region (region II in fig. 4.10). Note that the decrease in volume of the dimple controls the flux through this drainage region $2\pi C_\infty Q = -\dot{V}_{\text{dimple}}$, and so from (4.27) the shape in this region must obey

$$H^3 \frac{\partial^3 H}{\partial X^3} = -\frac{\Gamma}{4} C_\infty \dot{H}_0, \tag{4.50}$$

where we recall that $X = R - C_\infty$ is a local coordinate in the neck region.

Far from this region the solution is matched to the curvature outside the dimple and the membrane slope immediately inside the dimple, i.e.

$$\begin{aligned} \frac{\partial^2 H}{\partial X^2} &\to \Gamma\Pi && \text{as } X \to +\infty \\ \frac{\partial H}{\partial X} &\to -\frac{2H_0}{C_\infty} && \text{as } X \to -\infty. \end{aligned} \tag{4.51}$$

A similarity solution is sought in terms of a similarity variable

$$\eta = \frac{\Gamma^{1/2}\Pi^{3/4}}{C_\infty^{1/2}} t^{1/4}(R - C_\infty), \tag{4.52}$$

which is motivated by the scaling results (4.29). The similarity solution, $f(\eta)$, is defined by

$$H = \frac{C_\infty}{\Pi^{1/2}}\, t^{-1/2} f(\eta) \tag{4.53}$$

and $H_0 = A\ \Gamma^{1/2}\Pi^{1/4}C_\infty^{3/2}\ t^{-1/4}$ where A is a constant. Both A and $f(\eta)$ are to be determined from the solution of the boundary value problem

$$\begin{aligned} f^3 f''' &= \frac{A}{16}, \\ f' \to -2A \qquad &(\eta \to -\infty), \\ f'' \to 1 \qquad &(\eta \to \infty). \end{aligned} \tag{4.54}$$

Note that it is already known [Jones and Wilson, 1978] that there is a unique solution $g(z)$ to the problem $g^3 g''' = 1$ with boundary condition $g' \to -1$ as $z \to -\infty$ and $g'' \to k$ as $z \to \infty$ for some k. The constant k is found numerically to be $k \approx 1.21$. We therefore seek to rescale the problem (4.54) onto this classical problem by looking for a solution of the form $f(\eta) = ag(\eta/b)$. We find that

$$\begin{aligned} A &= (2^9 k)^{-1/4} \approx 0.20, \\ a = \frac{1}{2^7 A^2}, \qquad & b = \frac{1}{2^8 A^3} \end{aligned} \tag{4.55}$$

and thus have found a similarity solution for the profile at the dimple edge. See Jones and Wilson [1978] for a plot of the similarity solution $g(z)$.

4.D.2 Adhesion force evolution

To find the time-dependence of the adhesion force arising from this similarity solution, we must first determine how the meniscus position and radius evolve. At leading order the membrane shape outside the dimple will behave quasi-statically, changing due to a small influx in volume as the liquid dimple drains. Similarly to the equilibrium contact solutions (4.15)–(4.17), there are three conditions relating the meniscus radius, height and the contact point but (4.17) is replaced by

$$1 - V_{\text{dimple}} = \frac{\pi\Gamma}{H_M}\left[\frac{R_M^4 - C^4}{4} + C^2 R_M^2 \log\frac{C}{R_M}\right]. \tag{4.56}$$

From the dimple scaling analysis (4.30), it is known that at a given time t the volume of the dimple is approximately $V_{\text{dimple}} \approx \frac{\pi}{2} A\Gamma^{1/2}\Pi^{1/4}C_\infty^{7/2}t^{-1/4}$ where $A \approx 0.20$.

The eqns. (4.15), (4.16) & (4.56) are expanded as follows:

$$\begin{aligned} R_M &= R_M^\infty + \delta R_M(t), \\ H_M &= H_M^\infty + \delta H_M(t), \\ C &= C_\infty + \delta C(t) \end{aligned} \tag{4.57}$$

with the leading terms (denoted with a super- or sub-script ∞) obeying the equilibria equations (4.15)–(4.17) and the corrections (denoted by δ) being small. Linearizing, the

resulting three linear equations for the first order corrections can be written in the form $M\mathbf{x} = \mathbf{v}$ where the matrix M has components

$$\begin{aligned}
M_{11} &= \Gamma({R_M^\infty}^2 - C_\infty^2), \\
M_{12} &= -2R_M^\infty H_M^\infty, \\
M_{13} &= -2\Gamma R_M^\infty C_\infty \log(R_M^\infty/C_\infty), \\
M_{21} &= \Gamma({R_M^\infty}^2 - C_\infty^2 + 2{R_M^\infty}^2 \log R_M^\infty), \\
M_{22} &= R_M^\infty(H_\infty - 2H_M^\infty), \\
M_{23} &= -2\Gamma R_M^\infty C_\infty \log R_M^\infty, \\
M_{31} &= 2\pi R_M^\infty {H_M^\infty}^2, \\
M_{32} &= -1, \\
M_{33} &= \pi\Gamma C_\infty[{R_M^\infty}^2 - C_\infty^2 - 2{R_M^\infty}^2 \log(R_M^\infty/C_\infty)]
\end{aligned} \tag{4.58}$$

and the vectors $\mathbf{x}$ and $\mathbf{v}$ are

$$\mathbf{x} = \begin{pmatrix} \delta R_M \\ \delta H_M \\ \delta C \end{pmatrix}, \tag{4.59}$$

$$\mathbf{v} = -\frac{\pi}{2} A\Gamma^{1/2}\Pi^{1/4} C_\infty^{7/2} H_M^\infty \; t^{-1/4} \begin{pmatrix} 0 \\ 0 \\ 1 \end{pmatrix}. \tag{4.60}$$

From this formulation, we see that if the equilibrium solutions are known then we can find the late-time leading order corrections to the radius and height of the meniscus, as well as the correction to the position of the apparent contact point. From linearity, we also see that $\mathbf{x} \propto t^{-1/4}$.

The correction to the adhesion force can then be calculated from the expression

$$F = \frac{2\pi}{\Gamma} \frac{H_M - H_\infty}{\log R_M} \tag{4.61}$$

which, when linearized, gives the first order force correction

$$\delta F = F_\infty - F = \frac{2\pi(H_\infty - H_M^\infty)}{\Gamma R_M^\infty (\log R_M^\infty)^2} \delta R_M + \frac{2\pi}{\Gamma \log R_M^\infty} \delta H_M, \tag{4.62}$$

where F_∞ is the equilibrium value of the force. Hence, we find that the leading order correction to the adhesion force is of size $t^{-1/4}$. More precisely, the pre-factor to this scaling can be calculated, with results for some given parameters plotted as the gradients of the dashed lines in fig. 4.11.

4.E Calculation of the dynamic work of separation

The numerical scheme described in Appendix 4.B is used to calculate the dynamic work of separation numerically. These simulations begin with the membrane close to its equilibrium shape (the initial condition used for fig. 4.14 was found by evolving the system from the flat state $H = H_\infty$ for a dimensionless time $t = 10^3$ with $H_\infty = 5$ and $\Gamma = 100$ both fixed). The value of the edge height H_∞ is then increased at a given constant rate, $\dot{H}_\infty$.

The integral that defines the work of separation W_{sep}, (4.33), involves integrating until $H_\infty = \infty$; in practice, the dynamic numerics is terminated at a separation H^*, which is chosen to satisfy two requirements: (i) the adhesion force at H^* should be within 1% of the corresponding equilibrium value and (ii) the work of separation in moving from $H^*/5$ to H^* is within 1% of the corresponding quasi-static work of separation. For $H_\infty \geq H^*$ it is therefore expected that the adhesion force remains very close to the quasi-static value and the work of separation in moving from H^* to ∞ is accounted for as the value of the equilibrium work of separation from H^* to ∞. For the results presented in fig. 4.14b, a typical value was found to be $H^* = 100$.

Chapter 5

Detachment of a capillary load

In this chapter, the dynamics of detachment in two-dimensional capillary adhesion is studied by considering a plate under an applied load that is attached to a flat, rigid substrate via the surface tension of a liquid bridge. In particular, the focus is on the effect of allowing the plate to tilt freely during its subsequent motion. A linear stability analysis shows that small perturbations from equilibrium decouple into two modes: one in which the plate separates from the substrate, remaining parallel, and another in which it tilts, simultaneously causing the bridge to migrate. If the initial tilt perturbation is of a similar magnitude to (or bigger than) the separation perturbation, then the presence of this second, tilting mode can significantly alter the dynamics. Indeed, this tilting mechanism changes the ultimate fate of the plate: depending on the size of the plate and the initial perturbation, the plate may anomalously detach. This observation is discussed in relation to previous experiments on a three-dimensional system that showed a qualitatively similar anomalous detachment.

5.1 Introduction

In Chapter 4, experimental evidence was presented that showed that the deformable capillary adhesive was able to pick up and release loads in a similar manner to the expectation from the theory (see §4.4). However, comparisons between the load supported and the various control parameters showed that loads often detached, even when the equilibrium theory suggested strong adhesion should be achieved. It was suggested that this is partly due to the long time taken for the deformable surface to approach contact with the rigid surface — a delay caused by the formation of a liquid dimple beneath the membrane that drains slowly, meaning that lasting adhesion may realistically only be achieved if the two surfaces are left to adhere for some time. This explanation is consistent with the observation that loads adhere indefinitely if left in contact for sufficiently long times.

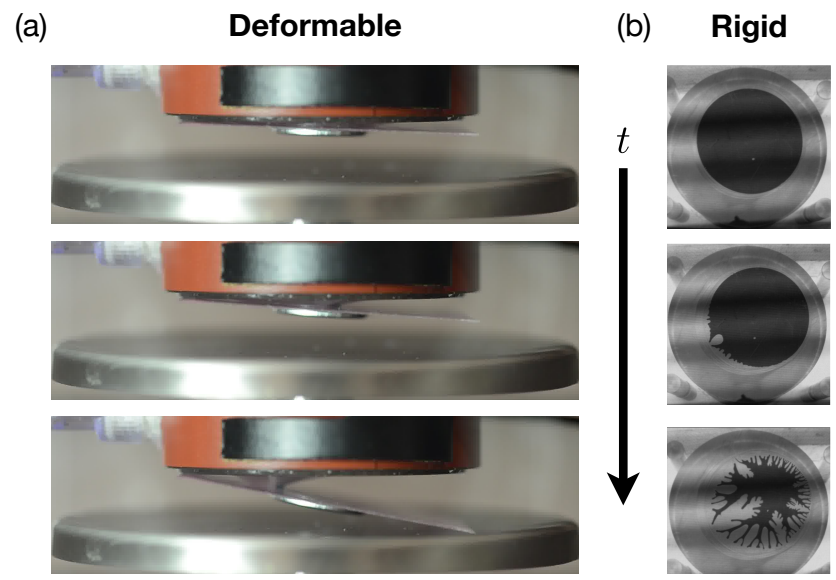

Figure 5.1: Evidence for asymmetric detachment in previous experiments. (a) In the deformable adhesive of Chapter 4, after a transient adhesion, the load detaches by tilting. Images courtesy of Finn Box. (b) Plan view of the liquid bridge when a rigid capillary adhesive detaches. In the second image, there is evidence of detachment beginning towards the bottom left corner of the liquid. Images in (b) reprinted from Ward [2011], with permission from Elsevier.

However, observations of *how* the load detaches in the unsuccessful adhesion experiments reveal that this detachment propagates from one edge and the load tilts, as shown in the snapshots in fig. 5.1a. The axisymmetric theory of Chapter 4 is unable to reproduce this scenario and so, when trying to predict the detachment time, it is likely to overestimate the length of time that the load would stay attached. In this chapter, we aim to understand this asymmetric detachment mechanism by modelling the dynamics of a related capillary system and determining how any relative tilting of the surfaces affects how, and when, detachment occurs.

We begin by again returning to the basic plate-plate adhesion scenario considered in §1.3.1, with the capillary bridge sufficiently short and wide that the inverse square law of the pancake solution (1.6) holds. For a given applied load, F, and given properties of the liquid bridge (i.e. given V and $\bar{\gamma}$), eqn. (1.6) gives a condition for the equilibrium displacement of the rigid plates that would provide sufficient force to support that load. The question then arises of whether this equilibrium is stable.

The stability of an axisymmetric bridge supporting a given planar load was studied previously by Ward [2011]. In particular, by modelling the motion of the liquid within the bridge using lubrication theory, Ward [2011] derived an ordinary differential equation

(ODE) for the evolution of the plate–substrate separation and found that the equilibrium (1.6) is linearly unstable to small perturbations at fixed load. The analysis of Ward [2011] showed that perturbations that act to decrease the plate–substrate separation (relative to the equilibrium value) ultimately lead to contact between the two planar surfaces; perturbations that increase this separation ultimately lead to further separation (though the ultimate dynamics of rupture of the liquid bridge were not considered). These results were largely supported by experimental observations.

However, a similar tilting asymmetry to that observed in the deformable adhesion in fig. 5.1a is also visible in snapshots of the experiments of Ward [2011]: fig. 5.1b shows evidence that at least some experiments initially detach from one edge. This suggests that tilting may be an important component of detachment beyond the deformable case in Chapter 4, and hence warrants further study. We emphasise that this tilting is distinct from 'peeling' studied by McEwan and Taylor [1966]: peeling can only occur with a flexible substrate, but tilting is possible for rigid surfaces too. In the experiments of Chapter 4, both tilting and peeling are likely to be important.

In addition, Ward [2011] also found that, in some cases, small inward perturbations in the plate–substrate separation (which would be expected to lead to contact between plate and substrate) ultimately led to complete separation (see fig. 5.4a). Ward [2011] suggests that this discrepancy could be attributed to some experimental inaccuracies or the assumption of perfect wettability. Here we suggest, and then investigate, the possibility that relative tilting of the plate compared to the substrate [which was neglected by Ward, 2011] might in fact lead to a similar behaviour: we shall consider a two-dimensional model of the dynamics of a loaded plate attached to a substrate by the capillary force of a liquid bridge, including the effects of tilting and translation on the plate, as well as allowing the bridge to move. (The work presented in this chapter has been published, see Butler and Vella [2020].)

5.2 Detachment of a loaded plate in two dimensions

To understand the possible importance of tilting in detachment, rather than simply detaching by separating, we consider a simplified model of detachment in capillary adhesion: a two-dimensional bridge of volume V (per unit depth into the page) is confined between a rigid substrate and a rigid plate of length 2ℓ, with the liquid meeting each surface at a constant angle θ (the same on each surface for simplicity). This scenario is illustrated in fig. 5.2. The substrate is flat and fixed in place, whilst the plate has a load (per unit length) F applied at its centre of mass. (This load could be the weight of the plate, for

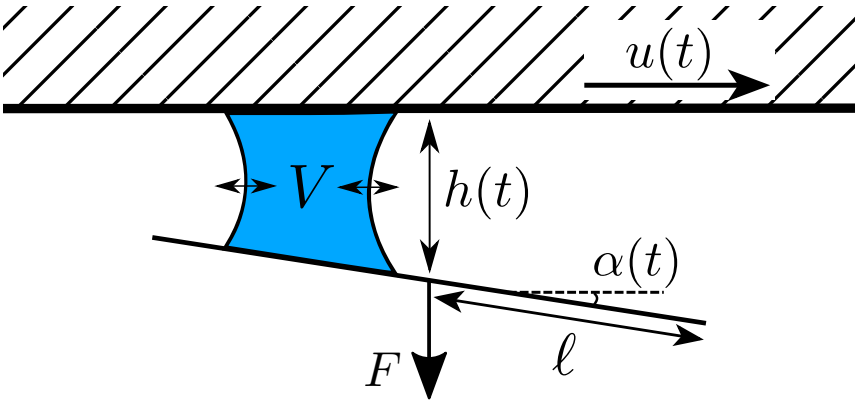

Figure 5.2: The surface tension of a two-dimensional capillary bridge of volume V adheres a mobile plate of length 2ℓ subject to an applied load (per unit depth) F to a fixed planar substrate. The mobile plate makes an angle $\alpha(t)$ to the substrate and its centre of mass lies a vertical distance $h(t)$ below the substrate. The model is presented in the frame of reference of the (mobile) plate, so that the top surface may move relative to the plate at a speed $u(t)$.

example.) In general, it shall be assumed that the plate is free to separate from the substrate, tilt relative to it, and translate parallel to the substrate. These motions are defined by the separation h between the centre of mass of the loaded plate and the substrate, the angle α between them, and the horizontal speed u of the plate relative to the substrate.

As the plate separates from the substrate and tilts, the change in geometry that the bridge experiences alters the capillary pressure at the meniscus, and the flow of the liquid gives an additional viscous forcing. Ignoring the effect of gravity on the liquid (since the Bond number of such bridges is typically small), the combination of these two forces determines the motion of the plate and bridge together.

The possibility that the plate may tilt is important since the geometry of tilting, together with the pressure jump across a meniscus caused by surface tension, means that as soon as the plate tilts the capillary pressure 'at' the two menisci must differ. For the wetting liquids considered here, such a tapering-induced pressure difference will tend to drive the bridge towards the narrower end (as described in Chapter 1). A key effect of allowing the plate and substrate to tilt relative to one another is, therefore, that any tilting motion may be accompanied by bridge migration. Moreover, the asymmetry induced by a capillary pressure difference across the bridge, together with the induced motion of the bridge away from the centre of the plate, will, in general, apply a torque that acts to tilt the loaded plate even further — the horizontal state of the plate is expected to be unstable to tilting.

In addition, once the plate is tilted, the flow of liquid towards the narrower end due to the capillary pressure gradient will exert a viscous shear force on the plate, and a component of the adhering capillary pressure will act horizontally on the angled plate. The combination of these forces may lead to the plate drifting horizontally. Previous studies of rigid plates supported by thin fluid layers have found that an angled plate can migrate horizontally when sedimenting in a viscous bath towards a wall [Argentina et al., 2007], while Trinh et al. [2014] and Moriarty and Terrill [1996] explored the steady state translation of a plate on the surface of a thin fluid film. It is possible that similar horizontal drift may be observed in the adhesion problem here that will affect the evolution of the plate-bridge system, and so the possibility of this is included in the model as well.

To quantify our intuition about the tilting instability, we consider a liquid bridge that is substantially wider than the plate separation. This means that the effect of the capillary tension force from the pull of the meniscus on the plate at the liquid's edge can be ignored, since it is approximately a bridge aspect ratio smaller in size. Instead, the force is calculated solely from the capillary pressure acting over the wetted footprint of the bridge.

We shall begin by considering the equilibrium of this system, before moving on to consider two simplified models: the first reprises the model of Ward [2011] (albeit in 2D) with no tilting of the plate (the angle $\alpha = 0$ is fixed). In the second simplified model, the plate is considered to be fixed about a central hinge (*i.e.* constant h with no horizontal translation) and able to tilt freely. This 'see-saw' motion isolates the effect of bridge migration and the concomitant torque. These two motions are then combined with the added effect of plate shearing in §5.3 into a full model in which the plate may slide parallel to, separate from, and tilt relative to, the substrate — the resulting model equations are solved numerically, but can also be understood using a linear stability analysis and by referring back to the simpler models considered in this section.

5.2.1 Equilibrium

When the system is in equilibrium, the plate and the liquid in the bridge are stationary and the menisci lie at $x = \pm x_0$; furthermore there is no pressure gradient. For this to be true, the curvature of the two free surfaces must be constant and equal, and so take the shape of arcs of circles with $\alpha = 0$. Matching the contact angle θ on each side, these circular arcs have radius $h_0/(2\cos\theta)$ with $h = h_0$ the equilibrium plate separation. The pressure inside the bridge is then $p = -2\bar{\gamma}/h_0$ with $\bar{\gamma} = \gamma\cos\theta$, and this capillary pressure force must balance the load, i.e.

$$F = \int_{-x_0}^{x_0} -p \, \mathrm{d}x = \frac{4\bar{\gamma}x_0}{h_0}. \tag{5.1}$$

Hence, given a load F and bridge volume $V = 2x_0h_0$, there is a unique equilibrium plate separation

$$h_0 = \sqrt{\frac{2\bar{\gamma}V}{F}}. \tag{5.2}$$

Note that a simple relationship between the load applied and the aspect ratio of the liquid bridge emerges naturally from this analysis, namely

$$\frac{2x_0}{h_0} = \frac{F}{2\bar{\gamma}}. \tag{5.3}$$

5.2.2 Modelling the fluid dynamics

We now consider the motion of the plate, which is coupled closely to the dynamics of the liquid in the capillary bridge. Because the bridge is assumed to be much wider than the plate separation, $x_0/h_0 \gg 1$, the lubrication approximation is used, in which the liquid motion is mostly tangential to the substrate and viscosity dominates over the inertia of the liquid. As a result, many of the equations and results presented in the rest of this chapter will be reminiscent of related classical lubrication problems, such as the squeeze film [e.g. Acheson, 1990], slider bearing [e.g. Batchelor, 1967] or rocker bearing [e.g. Raimondi and Boyd, 1955a,b].

Consistent with the lubrication approximation, the plate angle (and hence the slope) must remain small, $\alpha \ll 1$, and the approximation $\tan\alpha \approx \alpha$ is taken so that the separation of the plate from the substrate is given by $h(t) + \alpha(t)x$ along its length. Additionally, since the inertia of the liquid is negligible, it is possible to choose in which Galilean frame of reference to view the fluid flow problem. We shall consider the evolution of the system in the frame of motion of the plate; the substrate shears at a speed $u(t)$ in the x-direction with $h(t)$ being the separation at the plate's centre of mass at each point in time, as shown in fig. 5.2. The horizontal distances x are measured with respect to the centre of mass, so that the plate has its ends at $x = \pm\ell\cos\alpha \approx \pm\ell$.

Using the no-slip boundary condition on the two surfaces together with conservation of mass in the standard manner [see Chapter 5 of Leal, 2007, for example] shows that the pressure $p(x,t)$ must obey Reynolds' equation

$$\frac{\partial(h+\alpha x)}{\partial t} + \frac{\partial q}{\partial x} = 0, \qquad q = -\frac{(h+\alpha x)^3}{12\mu}\frac{\partial p}{\partial x} + \frac{h+\alpha x}{2}u, \tag{5.4}$$

where q is the depth-integrated volumetric flux and μ is the dynamic viscosity of the liquid.

Integrating Reynolds' equation, (5.4), once with respect to x, and introducing an (unknown) integration constant $c = c(t)$, gives the pressure gradient

$$\frac{\partial p}{\partial x} = 6\mu\frac{\dot{\alpha}x^2 + 2\dot{h}x + c}{(h+\alpha x)^3} + \frac{6\mu u}{(h+\alpha x)^2}, \tag{5.5}$$

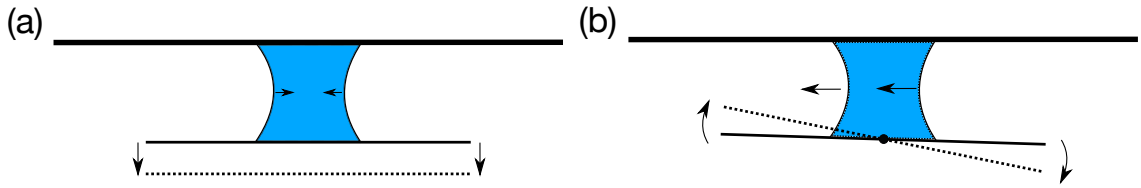

Figure 5.3: The dominant two modes through which the plate may move in relation to the substrate: (a) pure separation from the substrate (no tilting) and (b) pure tilting about a central hinge (the 'see-saw' mode). Note that the tilting mode induces a pressure gradient within the liquid bridge, which leads to the bridge itself migrating into the taper that is created by tilting.

where dots are used to denote derivatives with respect to time. Note that $c = -2q_0$ is related to the volumetric flux across the midpoint of the plate, $q_0 = q(x = 0)$.

At the meniscus, the action of surface tension causes a jump in the normal stress proportional to the curvature of the interface. As previously mentioned in Chapter 1, the pressure dominates the fluid stress in the lubrication approximation, and so the liquid pressure must obey the Young-Laplace equation

$$p(x_\pm) = \frac{-2\bar{\gamma}}{h + \alpha x_\pm}, \tag{5.6}$$

where the external atmospheric pressure has been taken as the pressure datum, $p = 0$.

To close the system, global relations for the motion of the plate are required, such as force and torque balances. Which relations are needed depends on the set-up of the problem; we will now consider the two distinct motions shown in fig. 5.3, and the relevant global relations will be introduced as they arise. (We shall see ultimately that the horizontal translation is only a small effect and so do not include this in our discussion of the dominant modes of the plate motion.)

5.2.3 Parallel plate: No tilting

Consider the case where the plate does not tilt and remains parallel to the substrate, moving either directly towards or away from the substrate (without sliding by symmetry), as depicted in fig. 5.3a. In this case the plate position is given by $h = h(t)$ only, and the pressure gradient (5.5) can be simplified (eliminating the integration constant through the symmetry of the problem) to give

$$\frac{\partial p}{\partial x} = 12\mu\frac{\dot{h}x}{h^3}. \tag{5.7}$$

A vertical force balance is imposed between the load and capillary force acting on the loaded plate

$$F = \int_{x_-}^{x_+} -p \, \mathrm{d}x = -[xp]_{\text{bridge}} + \int_{x_-}^{x_+} x \frac{\partial p}{\partial x} \, \mathrm{d}x, \tag{5.8}$$

where $[f(x)]_{\text{bridge}} = f(x_+) - f(x_-)$ denotes the difference in the function $f(x)$ across the bridge. The pressure at each end is determined by the pressure jump due to capillary effects (5.6).

If the position of the bridge menisci are given by $x_\pm = \pm x_M$ then volume conservation immediately gives $V = 2x_M h$. Substituting (5.7) into (5.8), and using this volume conservation to eliminate x_M, gives the evolution equation for the plate separation

$$\dot{h} = \frac{F}{\mu V^3}(h^2 - h_0^2)h^4. \tag{5.9}$$

As expected, $h = h_0$ is an equilibrium of (5.9); moreover, (5.9) is similar to the form of the dimensionless equation found by Ward for the axisymmetric system [eqn. 3 of Ward, 2011].[1] It is easy to see from the non-linear ODE (5.9) that $\dot{h} < 0$ whenever $0 < h < h_0$ while $\dot{h} > 0$ whenever $h > h_0$: as discussed in the introduction the equilibrium $h = h_0$ is an unstable equilibrium and the plate will tend to approach the substrate for an initial perturbation with $h(0) < h_0$ or to separate from it for an initial perturbation with $h(0) > h_0$.

Considering a small perturbation from equilibrium $h(t) = h_0 + \Delta h(t)$ with $\Delta h \ll h_0$ and linearizing, confirms that the equilibrium is linearly unstable and that the perturbation grows exponentially:

$$\Delta h(t) = \Delta h(0) \; e^{t/t_*}, \tag{5.10}$$

over a time scale

$$t_* = \frac{\mu V^3}{2F h_0^5} = \frac{\mu x_0^2}{\bar{\gamma} h_0}. \tag{5.11}$$

Note that by assuming that viscous forces precisely balance the load F, as expressed in (5.8), the inertia of the plate itself has been neglected. This assumption is valid provided that the plate inertia, $m\ddot{h}$ (with m the plate mass per unit length), is small compared to the pressure force and the applied load F. This means the plate inertia is unimportant over times t such that $F \gg m h_0/t^2$; for inertia to be negligible over time scales comparable with t_* in (5.11), the load must, surprisingly, be sufficiently large and, in particular, satisfy $F/\bar{\gamma} \gg [m^2\bar{\gamma}^2/(\mu^4 V)]^{1/9}$. In general, the load is independent of the weight of the plate, but in cases where the load is provided by the weight of

[1] In the axisymmetric case, the pre-factor and equilibrium solution are different, as well as there being one power fewer of h than here.

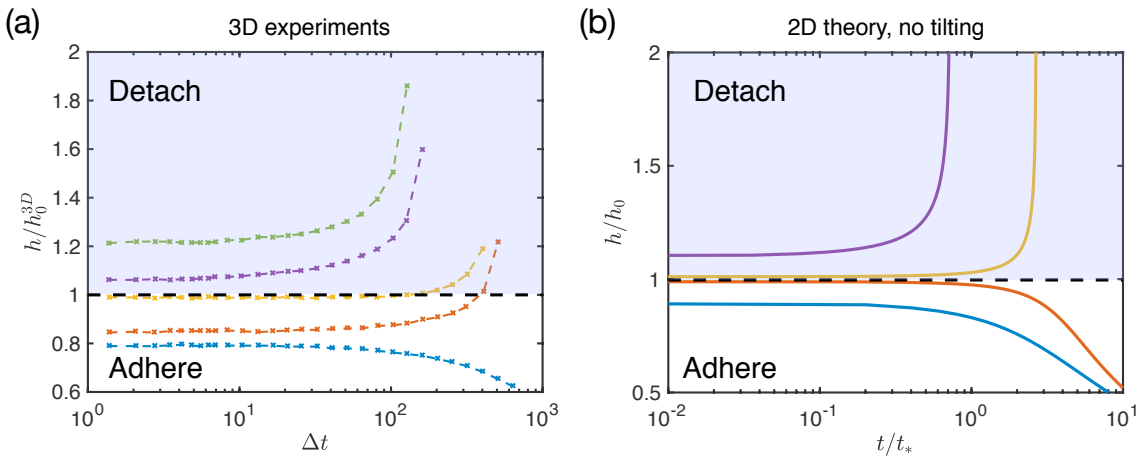

Figure 5.4: Qualitative comparison of the evolution of the gap separation, $h(t)$, between three-dimensional experiments [Ward, 2011] and the simplest two-dimensional model in which the plate remains parallel to the substrate throughout the motion. (a) Experimental measurements of the separation of an acrylic mass from a fixed (acrylic) substrate resisted by a bridge of silicone oil over time, Δt, measured in seconds. [Data digitally captured from fig. 6a of Ward, 2011]. The horizontal dashed line denotes the unstable equilibrium predicted within the axisymmetric theory, with h_0^{3D} given by the pancake solution, eqn. (1.6). (b) Numerical solutions of (5.9), which describes the separation of the two-dimensional system with no tilting of the plate. In both plots the lightly shaded region corresponds to that in which a linear stability analysis of parallel plates suggests detachment should occur, while the unshaded region shows that in which the two surfaces should move towards contact — adhesion. Note that in (a) two experimental trajectories begin within the 'adhere' region but ultimately detach — anomalous detachment.

the plate, $F = mg$ with g the acceleration due to gravity, then this condition can be rewritten as $F/\bar{\gamma} \gg [\bar{\gamma}^4/(\mu^4 g^2 V)]^{1/7}$. From (5.3), these conditions for neglect of plate inertia correspond to sufficiently thin bridges in equilibrium, consistent with the use of lubrication theory to model the flow of the liquid. (Note that for very early times, a temporal boundary layer is expected; for the large aspect ratio bridges of interest here, this phase is expected to be very brief and, hence, to have negligible effect on the subsequent dynamics considered here.)

In fig. 5.4b is the evolution of the plate separation, as determined from equation (5.9), when starting from small perturbations to the equilibrium solution (denoted by the horizontal dashed line). As predicted by the linear stability analysis, any perturbation grows. Experiments on the three-dimensional system, however, appear to have a more complex behaviour (see fig. 5.4a): some loads detach when they would be expected to stick, i.e. they ultimately detach even when $h(0) < h_0^{3D} = \sqrt{2\bar{\gamma} V_{3D}/F_{3D}}$ where h_0^{3D} is the unstable equilibrium solution for the three-dimensional system with an applied load

F_{3D} and bridge volume V_{3D} (see eqn. (1.6), the pancake solution). We refer to this as 'anomalous detachment'. One aspect that may be present in the experimental system, but has not been taken into account in the modelling thus far, is any possible perturbation to the orientation of the plate. We turn to consider first the effect of this tilting in isolation.

5.2.4 A hinged plate: Only tilting

Now, instead, consider a plate that is hinged at its centre $x = 0$ and is free to tilt (but not translate), as shown in fig. 5.3b. For simplicity, the hinge is taken to be at the equilibrium distance h_0 from the substrate. In this case, the plate separation is $h_0 + \alpha x$ and (5.5) becomes

$$\frac{\partial p}{\partial x} = 6\mu \frac{\dot{\alpha} x^2 + c}{(h_0 + \alpha x)^3}. \tag{5.12}$$

Since the position of the hinge here is fixed, there is no need to consider force balance on the tilting plate. Instead, note that the pressure gradient integrated across the bridge must match the capillary-enforced pressure at the edges, and consider the torque balance (taken about the hinge) to determine how the angle α changes. Together these conditions can be written as

$$[p]_{\mathsf{bridge}} = \int_{x_-}^{x_+} \frac{\partial p}{\partial x} \, \mathrm{d}x, \tag{5.13}$$

$$0 = \int_{x_-}^{x_+} xp \, \mathrm{d}x = \frac{1}{2}[x^2 p]_{\mathsf{bridge}} - \frac{1}{2}\int_{x_-}^{x_+} x^2 \frac{\partial p}{\partial x} \, \mathrm{d}x, \tag{5.14}$$

recalling from (5.6) that $p(x_\pm) = -2\bar{\gamma}/(h_0 + \alpha x_\pm)$. Performing the integrals in (5.13) and (5.14) using (5.12) gives equations of the form

$$\begin{aligned} f_\alpha(\alpha, x_+, x_-)\dot{\alpha} + f_c(\alpha, x_+, x_-)c &= f(\alpha, x_+, x_-) \\ g_\alpha(\alpha, x_+, x_-)\dot{\alpha} + g_c(\alpha, x_+, x_-)c &= g(\alpha, x_+, x_-), \end{aligned} \tag{5.15}$$

where the functions f_α, g_α etc. are determined by performing the integration (the precise form of these equations are omitted since the focus here is on linear stability).

Similarly to the no tilting case, in writing down the torque balance (5.14) the rotational inertia of the plate, $I\ddot{\alpha}$, has been neglected, where $I = m\ell^2/3$ is the moment of inertia for a plate of uniform density, width 2ℓ and mass per unit length m. To understand when this neglect of rotational inertia is appropriate, note that a bridge centred on the pivot will induce a torque on the plate because the pressure at its menisci becomes unequal immediately following a tilt α. The magnitude of this capillary torque, $\tau_{\mathsf{cap}} \propto x_0^2 \Delta p$ where the pressure difference $\Delta p \propto \bar{\gamma}\alpha x_0/h_0^2$ [Bradley et al., 2019]; therefore $\tau_{\mathsf{cap}} \propto \bar{\gamma}\alpha x_0^3/h_0^2$ dominates the rotational inertia for times $t \gg [mh_0^2\ell^2/(\bar{\gamma}x_0^3)]^{1/2}$. This holds in particular

for times on the capillary time scale t_* provided that $F/\bar{\gamma} \gg [m^2\bar{\gamma}^2\ell^4/(\mu^4 V^3)]^{1/11}$ or, if $F = mg$, then when $F/\bar{\gamma} \gg [\bar{\gamma}^4\ell^4/(\mu^4 g^2 V^3)]^{1/9}$. Again, this is satisfied for sufficiently large loads (or bridge aspect ratios).

Finally, since the bridge is free to migrate, the motion of the mensici in response to tapering must also be considered. To conserve bridge volume, it is assumed that the menisci move with the speed given by the local fluid flux, i.e.

$$\dot{x}_\pm = -\frac{(h_0 + \alpha x_\pm)^2}{12\mu} \left.\frac{\partial p}{\partial x}\right|_{x_\pm}. \tag{5.16}$$

This choice ensures that global mass conservation is inherited from local mass conservation [see Taroni and Vella, 2012, for example].

Consider a small perturbation in angle and bridge position from the equilibrium: $x_\pm = \pm x_0 + \delta x_\pm$ with $\delta x_\pm \ll x_0$ and $\alpha \ll 1$. Eliminating c from the linearizations of (5.15)–(5.16) gives the system of linear equations

$$\dot{\mathbf{y}} = \frac{1}{t_*}\begin{pmatrix} \frac{5}{2} & -15 \times \frac{h_0}{2x_0} \\ -\frac{1}{2} \times \frac{2x_0}{h_0} & \frac{5}{2} \end{pmatrix}\mathbf{y}, \qquad \text{where } \mathbf{y} = \begin{pmatrix} \alpha \\ \frac{\delta x_+ + \delta x_-}{2x_0} \end{pmatrix}. \tag{5.17}$$

Note that there are only two linear equations, after eliminating c from the four equations given in (5.13), (5.14) & (5.16) — volume conservation enforces that the bridge width, $x_+ - x_-$, remains constant to linear order in the small perturbations and so this is omitted from the linear system of equations.

The matrix in (5.17) has eigenvalues $\sigma = (5 \pm \sqrt{30})/2$ with corresponding eigenvectors $\mathbf{y} = (\sqrt{30}h_0, \mp 2x_0)$. The larger of these eigenvalues is $\sigma_{\circlearrowleft} = (5 + \sqrt{30})/2 > 0$, which corresponds to the plate tilting and the bridge moving towards the narrower end; this is the motion that will generally be seen for small perturbations since the other eigenvalue is negative and so its amplitude will decay with time. (While an anti-clockwise arrow is used here, the sign of the tilt is determined by that of the initial perturbation.)

Note that the growth rate of the tilting perturbation, $\sigma_{\circlearrowleft} = (5 + \sqrt{30})/2 \approx 5.24\ldots$ is larger than the growth rate of the separating perturbation, $\sigma_{\updownarrow} = 1$ (by choice of the time scale t_*).

5.3 Full system: Separating and tilting

Having seen how the modes of plate separation and plate tilting behave in isolation, these two modes are combined with the added effect of horizontal shear to obtain a system describing a mobile plate under the action of an applied load supported by the capillary force of a liquid bridge. We seek to understand how the tilting and separating modes interact.

5.3.1 Theoretical formulation

The full model uses the same theory presented in §5.2: Reynolds' equation is used to describe the flow of the liquid with the width of the gap described by $h(t) + \alpha(t)x$ (again assuming small angles, $\alpha \ll 1$). The resulting pressure gradient within the bridge is (5.5), which contains four unknowns: $\alpha(t)$, $h(t)$, $u(t)$ and $c(t)$. These unknowns are related through the constraints of vertical force balance, (5.8), a known pressure drop, (5.13), and torque balance (5.14). However, since these constraints also involve the *a priori* unknown meniscus positions, $x_\pm$, these must also be solved for from conservation of mass while including the effect of shear: (5.16) is modified to become

$$\dot{x}_\pm = -\frac{(h + \alpha x_\pm)^2}{12\mu} \left.\frac{\partial p}{\partial x}\right|_{x_\pm} + \frac{u}{2}. \tag{5.18}$$

To complete this system of equations, one more relation is required, namely a horizontal force balance on the plate. The horizontal forces acting on the plate are an aspect ratio smaller in size than the normal forces [see eqn. 4.8.18 of Batchelor, 1967, for example], and so it is relatively easy to slide the plate sideways; with no forcing imposed in this direction, it is not clear *a priori* whether this horizontal motion will be significant compared to the vertical motion. There are two mechanisms through which the liquid bridge provides a sideways force on the plate: viscous shear as the liquid drags on the plate as it flows past, and the pressure acting normally on the plate having a horizontal component because of the plate's slope. Summing these contributions, the horizontal force balance is found to be

$$0 = \int_{x_-}^{x_+} -\frac{h + \alpha x}{2}\frac{\partial p}{\partial x} + \frac{\mu u}{h + \alpha x} - \alpha p \, \mathrm{d}x = \int_{x_-}^{x_+} -\frac{\alpha}{2}p + \frac{\mu u}{h + \alpha x} \, \mathrm{d}x, \tag{5.19}$$

where the pressure gradient term has been integrated by parts.

Note that the plate inertia in the horizontal direction, $m\dot{u}$, has been ignored when taking a horizontal force balance, (5.19), despite the shear forces on the plate being an aspect ratio smaller in size than the normal forces. Using a typical horizontal velocity scale x_0/t, this inertia is found to be negligible for times $t \gg [mx_0/\bar{\gamma}]^{1/2}$; for times on the capillary timescale t_*, this holds when the load is sufficiently large: $F/\bar{\gamma} \gg [m^2\bar{\gamma}^2/(\mu^4 V)]^{1/5}$. Note that if the load is the weight of the plate, $F = mg$, then this becomes $F/\bar{\gamma} \gg [\bar{\gamma}^4/(\mu^4 g^2 V)]^{1/3}$.

The integral condition (5.19) can be evaluated, using the vertical force balance (5.8) to find the integral of the pressure, to give a solution for the shear velocity $u(t)$ in terms of the plate and bridge positions

$$u = \frac{-F\alpha^2}{2\mu \left[\log(h + \alpha x)\right]_{\text{bridge}}}. \tag{5.20}$$

In words, this means that, to balance the horizontal forces on the plate, the substrate must shear to the left when the plate is tilted so that α is positive (in the sense of fig. 5.2); in the lab frame, where the substrate is fixed, the plate moves to the right as the capillary pressure pulls on the angled plate, with the bridge moving towards the left end of the plate.

5.3.2 Non-dimensionalization

For simplicity, the problem is non-dimensionalized using the equilibrium separation h_0, the associated bridge width $2x_0$, and the time scale t_* from (5.10); in other words, new variables are defined as

$$H = \frac{h}{h_0}, \quad X = \frac{x}{2x_0}, \quad \beta = \frac{2x_0}{h_0}\alpha, \quad P = \frac{p}{2\bar{\gamma}/h_0}, \quad T = \frac{t}{t_*}, \quad U = \frac{u}{2x_0/t_*}. \tag{5.21}$$

In these dimensionless variables, the unstable equilibrium solution is now $H = 1$ with menisci at $X_\pm = \pm 1/2$ and angle $\beta = 0$, and the bridge has unit volume. The new rescaled angle, β, may be thought of as the dimensionless height difference over the bridge's initial width that is caused by tilting. Note that, since the pressure is rescaled by a factor $\cos\theta$ (recalling $\bar{\gamma} = \gamma\cos\theta$), this analysis is not valid as $\theta \to \pi/2$. This is consistent with the neglect of the tension force applied at the edges ($\propto \gamma\sin\theta$) in comparison to the force generated by the capillary suction within the bridge ($\propto x_0 \times \gamma\cos\theta/h_0$), which requires $\tan\theta \ll x_0/h_0$.

The dimensionless lubrication pressure gradient is

$$\frac{\partial P}{\partial X} = 12\frac{\dot{\beta}X^2 + 2\dot{H}X + C}{(H+\beta X)^3} + \frac{12U}{(H+\beta X)^2}, \tag{5.22}$$

where $C = C(T)$ is an (as yet unknown) function of time T and dots now denote differentiation with respect to T.

Since the pressure at each end is constrained by the capillary pressure, which is $P(X_\pm) = -1/(H + \beta X_\pm)$, the integral of the pressure gradient must match the difference in capillary pressure across the bridge

$$\int_{X_-}^{X_+} \frac{\partial P}{\partial X}\,\mathrm{d}X = [P]_{\text{bridge}} = -[(H+\beta X)^{-1}]_{\text{bridge}}, \tag{5.23}$$

which is the dimensionless version of (5.13). Furthermore, vertical force and torque balances are imposed on the loaded plate, (5.8) and (5.14), which can be written in

dimensionless terms as

$$1 = \int_{X_-}^{X_+} -P \, \mathrm{d}X = -[XP]_{\text{bridge}} + \int_{X_-}^{X_+} X \frac{\partial P}{\partial X} \, \mathrm{d}X \tag{5.24}$$

$$0 = \int_{X_-}^{X_+} XP \, \mathrm{d}X = \frac{1}{2}[X^2 P]_{\text{bridge}} - \frac{1}{2} \int_{X_-}^{X_+} X^2 \frac{\partial P}{\partial X} \, \mathrm{d}X, \tag{5.25}$$

respectively. Surprisingly, this non-dimensionalization does not leave any further parameter in the problem — the load F might be expected to feature, but in effect disappears because the equilibrium gap width and bridge width (h_0 and $2x_0$, respectively) are used to non-dimensionalize the vertical and horizontal length scales separately, whilst being related through the equilibrium condition (5.3). As a result, the capillary pressure scale $p_* = 2\bar{\gamma}/h_0$ can also be written $p_* = F/(2x_0)$, and the term representing the applied vertical load becomes unity.

The edges of the bridge move because of the fluxes of liquid there (5.18), which in dimensionless form becomes

$$\dot{X}_\pm = -\frac{(H + \beta X_\pm)^2}{24} \left. \frac{\partial P}{\partial X} \right|_{X_\pm} + \frac{U}{2} = -\frac{\dot{\beta} X_\pm^2 + 2\dot{H} X_\pm + C}{2(H + \beta X_\pm)}. \tag{5.26}$$

From the horizontal force balance, (5.19), the dimensionless shear velocity, $U(T)$, is found to be

$$U = \frac{-\beta^2}{4 \left[\log(H + \beta X) \right]_{\text{bridge}}}. \tag{5.27}$$

5.3.3 Equations of motion for the plate and liquid bridge

After substituting for the dimensionless pressure gradient (5.22) and integrating, the eqns. (5.23)–(5.25) can be written in the form

$$12 I_2 \dot{\beta} + 24 I_1 \dot{H} + 12 I_0 C + 12(H I_0 + \beta I_1) U = -\left[\frac{1}{H + \beta X} \right]_{\text{bridge}} \tag{5.28}$$

$$12 I_3 \dot{\beta} + 24 I_2 \dot{H} + 12 I_1 C + 12(H I_1 + \beta I_2) U = 1 - \left[\frac{X}{H + \beta X} \right]_{\text{bridge}} \tag{5.29}$$

$$12 I_4 \dot{\beta} + 24 I_3 \dot{H} + 12 I_2 C + 12(H I_2 + \beta I_3) U = -\left[\frac{X^2}{H + \beta X} \right]_{\text{bridge}}, \tag{5.30}$$

respectively, where the integrals $I_n = I_n(H, \beta, X_+, X_-)$ are defined by

$$I_n = \int_{X_-}^{X_+} \frac{X^n}{(H + \beta X)^3} \, \mathrm{d}X. \tag{5.31}$$

Upon substitution for the value of U using (5.27), the system (5.28)–(5.30) with (5.26) gives five equations involving $\beta(T), H(T), X_\pm(T)$ and $C(T)$ and the derivatives of

β, H & $X_\pm$, i.e. a system of differential-algebraic equations. Note that this system of five equations can be reduced to four ODEs in four unknowns by eliminating C; using (5.28), the value of C can be found to be

$$C = \frac{-[(H+\beta X)^{-1}]_{\text{bridge}} - 12I_2\dot{\beta} - 12I_1(2\dot{H}+\beta U)}{12I_0} - HU. \tag{5.32}$$

To simplify further, the integrals I_n, defined in (5.31), must be evaluated in the cases $n = 0, 1, 2, 3$ and 4; to facilitate this the following functions of time only are defined as

$$\psi_n(T) = \begin{cases} [(H+\beta X)^n]_{\text{bridge}} & n \neq 0 \\ [\log(H+\beta X)]_{\text{bridge}} & n = 0 \end{cases}. \tag{5.33}$$

Straightforward calculations give

$$\begin{gathered} I_0 = \frac{-\psi_{-2}}{2\beta}, \quad I_1 = \frac{-2\psi_{-1}+H\psi_{-2}}{2\beta^2}, \quad I_2 = \frac{2\psi_0+4H\psi_{-1}-H^2\psi_{-2}}{2\beta^3}, \\ I_3 = \frac{2\psi_1-6H\psi_0-6H^2\psi_{-1}+H^3\psi_{-2}}{2\beta^4}, \\ I_4 = \frac{\psi_2-8H\psi_1+12H^2\psi_0+8H^3\psi_{-1}-H^4\psi_{-2}}{2\beta^5}, \end{gathered} \tag{5.34}$$

which may then be substituted, along with the value of the shear velocity $U = -\beta^2/4\psi_0$, into the ODEs for the vertical force- and torque-balance to give

$$\begin{aligned} \frac{12}{\beta^4}\left(\psi_1 - 2H\psi_0 - 2\frac{\psi_0\psi_{-1}}{\psi_{-2}} - 4H\frac{\psi_{-1}^2}{\psi_{-2}}\right)\dot{\beta} + \frac{12}{\beta^3}\left(2\psi_0 + 4\frac{\psi_{-1}^2}{\psi_{-2}}\right)\dot{H} \\ = 4 + 2\frac{\psi_{-1}^2}{\beta\psi_{-2}} + 6\frac{\psi_{-1}^2}{\psi_{-2}\psi_0} \end{aligned} \tag{5.35}$$

and

$$\begin{aligned} \frac{12}{\beta^5}\left(\psi_2 - 8H\psi_1 + 8H^2\psi_0 + 4\frac{\psi_0^2}{\psi_{-2}} + 16H\frac{\psi_0\psi_{-1}}{\psi_{-2}} + 16H^2\frac{\psi_{-1}^2}{\psi_{-2}}\right)\dot{\beta} \\ + \frac{12}{\beta^4}\left(4\psi_1 - 8H\psi_0 - 8\frac{\psi_0\psi_{-1}}{\psi_{-2}} - 16H\frac{\psi_{-1}^2}{\psi_{-2}}\right)\dot{H} \\ = -2\frac{\psi_1}{\beta^2} - 4\frac{\psi_0\psi_{-1}}{\beta^2\psi_{-2}} - 8H\frac{\psi_{-1}^2}{\beta^2\psi_{-2}} \\ + \frac{3}{\beta\psi_0}\left(2\psi_1 - 4H\psi_0 - 4\frac{\psi_0\psi_{-1}}{\psi_{-2}} - 8H\frac{\psi_{-1}^2}{\psi_{-2}}\right). \end{aligned} \tag{5.36}$$

Additionally, from (5.26), there are also two equations which describe the motion of each of the menisci

$$\begin{aligned} \dot{X}_\pm = -\frac{1}{2(H+\beta X_\pm)}\left\{\left(\frac{2\psi_0+4H\psi_{-1}-H^2\psi_{-2}}{\beta^2\psi_{-2}} + X_\pm^2\right)\dot{\beta}\right. \\ \left. + \left(\frac{-4\psi_{-1}+2H\psi_{-2}}{\beta\psi_{-2}} + 2X_\pm\right)\dot{H} + \frac{\beta^2\psi_{-1}}{2\psi_{-2}\psi_0} + \frac{\beta\psi_{-1}}{6\psi_{-2}}\right\}. \end{aligned} \tag{5.37}$$

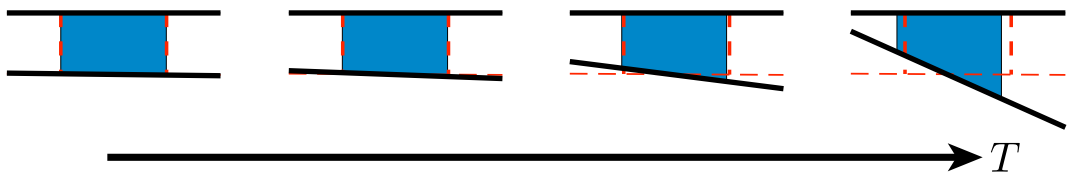

Figure 5.5: Snapshots generated from the numerical solution at early times showing the initial tilting of the plate when $\delta H(0) = \beta(0) = 10^{-2}$ and the bridge begins centrally, $X_+(0) + X_-(0) = 0$. The substrate is at the top of each plot, while the lower plate is free to tilt and separate. The snapshots are presented in the frame of reference of the plate (here, the substrate shears to the left since $U < 0$). Solutions are evaluated at dimensionless times $T = 0.2, 0.4, 0.6, 0.8$ with the initial position overlaid as red dashed lines.

5.3.4 Numerical solutions

The dimensionless system of ODEs (5.35), (5.36) & (5.37) has no parameters, and is solved numerically from given initial conditions using MATLAB's stiff ODE solver `ode15s`.

Figure 5.5 shows an example of the evolution of the system at various early times when starting with a small perturbation from the unstable equilibrium solution in both the tilt and separation, namely $\delta H(0) = \beta(0) = 10^{-2}$. From this solution, it would appear that the predominant motion of the plate is to tilt rather than separate. This raises the question of why this is what is seen at early times — a question that we turn to investigate using linear stability analysis.

5.3.5 Linear stability analysis

Considering small perturbations about the (unstable) equilibrium solution $H = 1 + \delta H$, $X_\pm = \pm 1/2 + \delta X_\pm$, with $\delta H, \delta X_\pm, \beta, C, U \ll 1$, and, ignoring higher order terms, the linearized pressure gradient is found to be

$$\frac{\partial P}{\partial X} = 12\ \dot{\beta}\ X^2 + 24\ \delta\dot{H}\ X + 12C + 12U. \tag{5.38}$$

Substituting this into (5.23)–(5.26) gives the linear system of equations

$$\begin{aligned}
\dot{\beta} &= \beta - 12(C+U) \\
2\delta\dot{H} &= \delta H - (\delta X_+ - \delta X_-) \\
\frac{3}{10}\dot{\beta} &= \frac{1}{2}\beta - 2(C+U) - 2(\delta X_+ + \delta X_-) \\
\delta\dot{X}_+ + \delta\dot{X}_- + \frac{1}{4}\dot{\beta} &= -C \\
\delta\dot{X}_+ - \delta\dot{X}_- + \delta\dot{H} &= 0.
\end{aligned} \tag{5.39}$$

Note that volume conservation

$$1 = (X_+ - X_-)\left[H + \frac{\beta}{2}(X_+ + X_-)\right] \tag{5.40}$$

becomes $\delta X_+ - \delta X_- + \delta H = 0$ upon linearization, and so the last equation in (5.39) is simply the time derivative of the linearized volume conservation. This means that the order of the linearized system can be reduced by 1: $\delta X_+ - \delta X_-$ can be replaced in favour of δH, and the evolution of bridge position can be considered using only $\delta X_+ + \delta X_-$ and δH — the individual values of δX_+ and δX_- can be reconstructed if desired from volume conservation.

Eliminating C and $\delta X_+ - \delta X_-$ from (5.39), and rearranging, the system simplifies to

$$\dot{\mathbf{Y}} = \begin{pmatrix} 1 & 0 & 0 \\ 0 & \frac{5}{2} & -15 \\ 0 & -\frac{1}{2} & \frac{5}{2} \end{pmatrix} \mathbf{Y} + \begin{pmatrix} 0 \\ 0 \\ U \end{pmatrix}, \tag{5.41}$$

where $\mathbf{Y} = (\delta H, \beta, \delta X_+ + \delta X_-)$.

If the plate is constrained so that it cannot migrate horizontally, $U = 0$, the linear system decouples into precisely the separating and tilting modes that were discussed in §5.2 and are illustrated in fig. 5.3. One mode has eigenvalue $\sigma_{\updownarrow} = 1$ and corresponds to the load falling or rising with no tilting. The fastest growing mode is $\sigma_{\circlearrowleft} \approx 5.24$, which involves the plate tilting and the bridge migrating towards the narrower end.

For an unconstrained free plate, the effect of shearing must also be included and so it is important to consider the horizontal force balance on the plate, (5.19). The dimensionless shear speed U in (5.27) can be linearized to give

$$U = -\frac{\beta}{4}. \tag{5.42}$$

This modifies the evolution of the plate so that now

$$\dot{\mathbf{Y}} = \begin{pmatrix} 1 & 0 & 0 \\ 0 & \frac{5}{2} & -15 \\ 0 & -\frac{3}{4} & \frac{5}{2} \end{pmatrix} \mathbf{Y}. \tag{5.43}$$

The motion again decouples into the two separate modes shown in fig. 5.3. However, the tilting mode now has eigenvalues $\sigma_\pm = (5 \pm 3\sqrt{5})/2$ with $\sigma_- < 0 < \sigma_+$, and the linearized system has solutions of the form

$$\begin{aligned} \delta H(T) &= \delta H(0) e^T \\ \beta(T) &= A e^{\sigma_+ T} + B e^{\sigma_- T} \\ \delta X_+(T) + \delta X_-(T) &= \frac{1}{2\sqrt{5}}\left(-A e^{\sigma_+ T} + B e^{\sigma_- T}\right) \end{aligned} \tag{5.44}$$

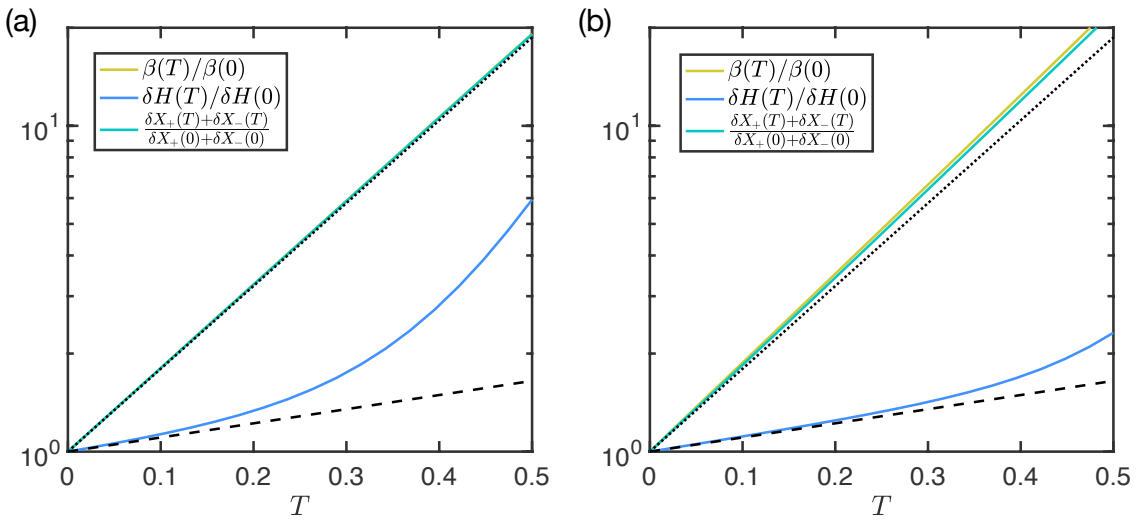

Figure 5.6: The evolution of the perturbations to the height, angle and bridge position at early times for small perturbations to the equilibrium solution, compared to the predictions of a linear stability analysis (dashed line for height, dotted line for angle and position of bridge centre). Here the initial perturbation is chosen to excite just the growing mode, $B = 0$ in (5.44). Each plot has an initial angular perturbation of $\beta(0) = 10^{-2}$, with the value of the initial height perturbation varied: (a) $\delta H(0) = 10^{-3}$ and (b) $\delta H(0) = 10^{-2}$. (Note the logarithmic y-scale to highlight the exponential growth.)

Including the shear has the effect of amplifying the growth rate of the tilting mode, which now grows with $\sigma_+ \approx 5.85 > \sigma_{\circlearrowleft}$.

In fig. 5.6, a numerical solution to the full equations, (5.35)–(5.37), is plotted at early times compared to the predictions of the linear stability analysis for different perturbation sizes. Here, initial conditions are chosen such that the σ_- mode is not present, i.e. the initial angle is $\beta(0) = -2\sqrt{5}[\delta X_+(0) + \delta X_-(0)]$ so that the coefficient B vanishes, $B = 0$ in (5.44). From this, it can be seen that when the perturbations are both small and of similar size, the evolution agrees well with the linear stability analysis. However, when the angular perturbation is significantly larger than the height perturbation (fig. 5.6a) then the evolution of δH deviates from the expected value much sooner — the tilt and migrate mode dominates and affects the evolution of the separation.

Figure 5.7 shows the evolution of the height, angle and bridge centre's position when the bridge centre is initially aligned with the centre of mass of the plate, $X_-(0) = -X_+(0)$ (i.e. the system is no longer forced solely into the growing mode, since $B \neq 0$). For this case the numerical solutions also follow the predictions of the linear stability analysis well at early times: the influence of the constant $B \neq 0$ decays quickly so that the numerical results are well approximated by the later time behaviour of the linear stability analysis,

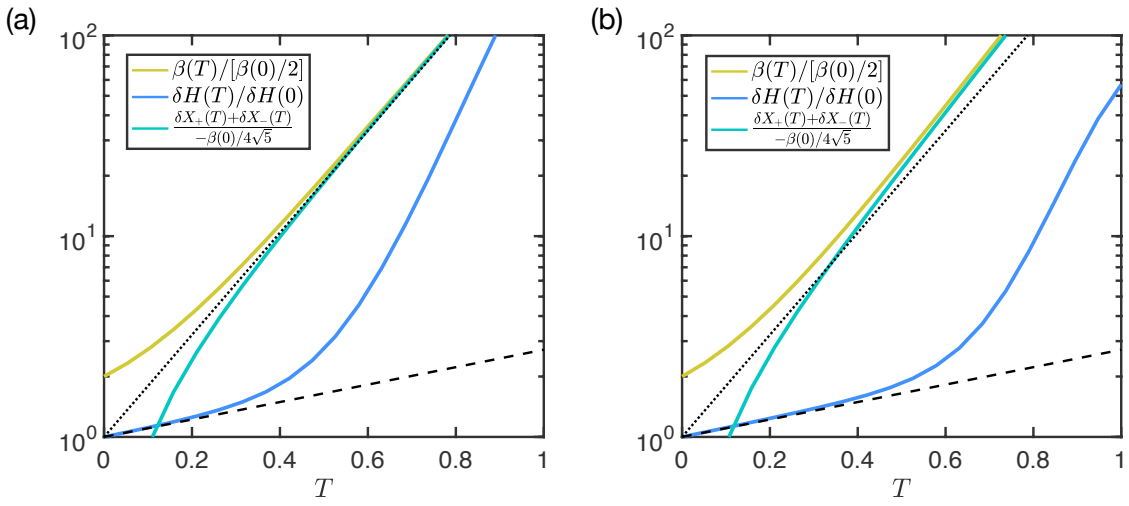

Figure 5.7: Comparison between the prediction of the linear stability analysis (dashed and dotted lines) and numerical solutions of the full problem (coloured curves). The parameter values are precisely as in fig. 5.6, so that $\beta(0) = 10^{-2}$ with (a) $\delta H(0) = 10^{-3}$ and (b) $\delta H(0) = 10^{-2}$. However, here the bridge starts at the centre of the plate, $X_-(0) = -X_+(0)$, thereby also exciting the exponentially decaying mode, σ_-, so that $B \neq 0$ in (5.44). Note that the angle and bridge centre position have been normalized by the pre-factor for the growing mode, $A = \beta(0)/2$, so that perfect agreement with the unstable mode of the linear stability analysis at late times would be $\exp(\sigma_+ t)$ with $\sigma_+ \approx 5.85$, which is shown by the dotted line on this logarithmic y-scale. The dashed line shows the corresponding prediction of linear stability analysis for $H(T)$.

i.e. $\beta \approx A\exp(\sigma_+ t)$. This agreement for a generic initial condition further suggests that the linear stability analysis is a good predictor of the initial motion and emphasizes the dominance of the tilting mode in the plate's dynamics. For simplicity, from here onwards the calculations shown will be for an initially centred liquid bridge, as in this figure.

5.4 Dynamics after contact at an edge

The linear stability analysis shows that any tilt initially present in the system grows more rapidly than a comparable perturbation to the separation of the centre. This tilting may lead to contact between the rigid substrate and the load at one edge, depending on the perturbations and the half-width of the plate ℓ. In this section, we investigate the dynamics once this contact has occurred.

If contact occurs between the plate and substrate at one edge, then the physics determining the motion are modified due to the presence of a reaction force at the corner. This means that it is no longer appropriate to consider a vertical force balance on the load as a whole (which would simply determine the size of the reaction force) and, further,

that it is more natural to consider a torque balance about the contact point. In addition, it is assumed that there is sufficient friction between the plate and substrate that the point of contact remains fixed; there is no longer any shearing of the plate relative to the substrate, $U = 0$, and so the horizontal force balance is also omitted. For simplicity, our focus is on the case where contact occurs at the left edge, $X = -L$ for a dimensionless plate half-width $L = \ell/(2x_0)$; the same equations hold at the right edge once the change $L \to -L$ is made.

5.4.1 Equations of motion after edge contact

Once contact has occurred, the wedge angle and separation at the centre are coupled through the geometric condition $H = \beta L$; as a result, the problem remains well-defined, despite the loss of the vertical force balance condition. Using this simplification, the lubrication pressure gradient (5.22) is found to be

$$\frac{\partial P}{\partial X} = \frac{12}{\beta^3}\frac{(X^2 + 2LX)\dot{\beta} + C}{(L+X)^3} = \frac{12}{\beta^3}\frac{(L+X)^2\dot{\beta} + D}{(L+X)^3}, \tag{5.45}$$

where a new function of time $D(T) = C(T) - L^2\dot{\beta}(T)$ has been defined to simplify the ensuing calculations. Integrating over the width of the bridge, gives a condition on the pressure equivalent to (5.23)

$$\frac{12}{\beta^3}\left(J_{-1}\dot{\beta} + J_{-3}D\right) = -\frac{[(L+X)^{-1}]_{\text{bridge}}}{\beta}, \tag{5.46}$$

where $J_n(X_+, X_-; L) = \int_{X_-}^{X_+}(L+X)^n \, \mathrm{d}X$.

The torque balance (taken about the contacting edge for simplicity to avoid the unnecessary calculation of the reaction force) can be written in dimensionless terms as

$$L = \int_{X_-}^{X_+} -(L+X)P \, \mathrm{d}X = \left[-\frac{(L+X)^2}{2}P\right]_{\text{bridge}} + \int_{X_-}^{X_+}\frac{(L+X)^2}{2}\frac{\partial P}{\partial X} \, \mathrm{d}X. \tag{5.47}$$

which can alternatively be written as

$$\frac{6}{\beta^3}\left(J_1\dot{\beta} + J_{-1}D\right) = L - \frac{[L+X]_{\text{bridge}}}{2\beta} \tag{5.48}$$

and the bridge menisci move according to the two equations (5.26), which may now be written as

$$\dot{X}_\pm = -\frac{(L+X_\pm)^2\dot{\beta} + D}{2\beta(L+X_\pm)}. \tag{5.49}$$

Again, this is a set of differential-algebraic equations for the plate and liquid bridge evolution: (5.46), (5.48) and (5.49). These equations can be reduced to a system of ODEs by eliminating D; similarly to (5.33), the functions $\phi_n(T)$ are defined as

$$\phi_n(T) = \begin{cases} [(L+X)^n]_{\text{bridge}} & n \neq 0 \\ [\log(L+X)]_{\text{bridge}} & n = 0. \end{cases} \tag{5.50}$$

Evaluating the integrals in (5.46) allows for the evaluation of D, just like the calculation for C in (5.32),

$$D = \frac{2\phi_0}{\phi_{-2}}\dot{\beta} + \frac{\beta^2\phi_{-1}}{6\phi_{-2}}. \tag{5.51}$$

Substituting for D using (5.51) in the torque balance (5.48) and meniscus motion equations (5.49), ODEs for $\beta(T)$ and $X_\pm(T)$ are obtained

$$\frac{12}{\beta^3}\left(\frac{\phi_2}{2} + \frac{2\phi_0^2}{\phi_{-2}}\right)\dot{\beta} = 2L - \frac{1}{\beta}\left(\phi_1 + \frac{2\phi_0\phi_{-1}}{\phi_{-2}}\right) \tag{5.52}$$

$$\dot{X}_\pm + \frac{1}{2\beta(L+X_\pm)}\left((L+X_\pm)^2 + \frac{2\phi_0}{\phi_{-2}}\right)\dot{\beta} = -\frac{\phi_{-1}\beta}{12\phi_{-2}(L+X_\pm)} \tag{5.53}$$

which are again solved using MATLAB's `ode15s` with the values of β and $X_\pm$ immediately prior to contact used as initial conditions.

5.4.2 The liquid bridge reaches the corner in finite time

After the plate has made contact with the substrate, numerical solutions suggest that the liquid bridge may migrate sufficiently that the meniscus gets close to the corner at $X = -L$. The equations of motion (5.52) & (5.53) appear to become singular as $X_- \to -L$ (or $X_+ \to +L$ if the plate has tilted anticlockwise). A natural question to ask is then: does the bridge reach the corner of the resulting wedge in a finite time and, if so, how long does it take? With a wedge angle that is constant in time, previous work [Reyssat, 2014, Gorce et al., 2016] showed that the leading meniscus does reach the wedge corner in a finite time. Moreover, these studies showed that the leading meniscus propagates at a constant speed as the corner is approached, though this speed is proportional to the wedge angle. In the present problem, the wedge angle β is *not* constant, and so the question then becomes whether its time-dependence modifies the propagation of the bridge significantly?

To facilitate an analysis that will address this question, new variables are introduced corresponding to the position of the bridge's midpoint (measured with respect to the corner), $\bar{X}$, and the width, ω, of the bridge:

$$\bar{X} = \frac{X_+ + X_-}{2} + L, \qquad \omega = X_+ - X_-. \tag{5.54}$$

Note that $2\bar{X} > \omega$ and the left hand meniscus reaches the corner when $2\bar{X} = \omega$. The functions ϕ_i, given by (5.50), can be written in terms of $\bar{X}$ and ω by

$$\begin{aligned} \phi_2 &= 2\bar{X}\omega, \qquad \phi_1 = \omega, \qquad \phi_0 = \log\left(\frac{2\bar{X}+\omega}{2\bar{X}-\omega}\right), \\ \phi_{-1} &= -\frac{4\omega}{4\bar{X}^2-\omega^2}, \qquad \phi_{-2} = -\frac{32\bar{X}\omega}{(4\bar{X}^2-\omega^2)^2}. \end{aligned} \tag{5.55}$$

Using these expressions, and taking the sum and difference of the two equations defined in (5.53), the eqns. (5.52) & (5.53) can be rewritten as

$$\frac{12}{\beta^3}\omega\bar{X}\left[1-\frac{\phi_0}{4}\frac{4\bar{X}^2-\omega^2}{\bar{X}\omega}\right]\left[1+\frac{\phi_0}{4}\frac{4\bar{X}^2-\omega^2}{\bar{X}\omega}\right]\dot{\beta} = 2L - \frac{\omega}{\beta}\left[1+\frac{\phi_0}{4}\frac{4\bar{X}^2-\omega^2}{\bar{X}\omega}\right] \tag{5.56}$$

$$\dot{\bar{X}} + \frac{\bar{X}}{2\beta}\left[1-\frac{\phi_0}{4}\frac{4\bar{X}^2-\omega^2}{\bar{X}\omega}\right]\dot{\beta} = -\frac{\beta}{24} \tag{5.57}$$

$$\dot{\omega} + \frac{\omega}{2\beta}\left[1+\frac{\phi_0}{4}\frac{4\bar{X}^2-\omega^2}{\bar{X}\omega}\right]\dot{\beta} = \frac{\beta\omega}{24\bar{X}}. \tag{5.58}$$

Note that if a constant angle were enforced so that $\dot{\beta} = 0$ then (5.57) gives $\dot{\bar{X}} = -\beta/24$; in dimensional terms this is $\dot{\bar{x}} = -\bar{\gamma}\alpha/6\mu$ which is precisely the result found by Reyssat [2014] for a bridge migrating into a wedge of constant angle α.

Numerical solutions of (5.52) & (5.53) suggest that the bridge width and plate angle follow scaling laws at late times (see fig. 5.8a for an example). In particular, the results suggest that $\beta \sim T^{-1/3}$ and $\omega \sim T^{+1/3}$ with $\bar{X}$ approximately constant (in fig. 5.8a the variation in $\bar{X}$ is less than 1%). If such scalings do indeed hold, then the meniscus will reach the corner in finite time (since $2\bar{X} - \omega \to 0$ at a finite T). The question therefore becomes one of understanding the origin of these scaling laws.

The meniscus may approach the corner in two distinct ways: migration of the whole liquid bridge towards the corner, or squeezing of the bridge as the plate angle decreases. In both scenarios, the capillary component of the torque increases. This is because the capillary pressure at each meniscus is inversely proportional to its distance from the corner, $P = -1/[\beta(X+L)]$, so that the capillary torque provided by the bridge $\int(X+L)(-P)\,\mathrm{d}X$ is ω/β; whether migrating at constant angle or squeezing, the bridge width ω increases as it experiences a narrower gap between the plate and substrate (in the squeezing case the angle β also decreases). If this increase in the capillary torque is sufficiently large, it is expected that the load torque (which remains constant) becomes comparatively negligible, and from then on a balance is maintained in eqn. (5.56) between capillary and viscous terms. This observation allows for considerable simplification of (5.56) to

$$\frac{12}{\beta^2}\bar{X}\left[1-\frac{\phi_0}{4}\frac{4\bar{X}^2-\omega^2}{\bar{X}\omega}\right]\dot{\beta} \approx -1. \tag{5.59}$$

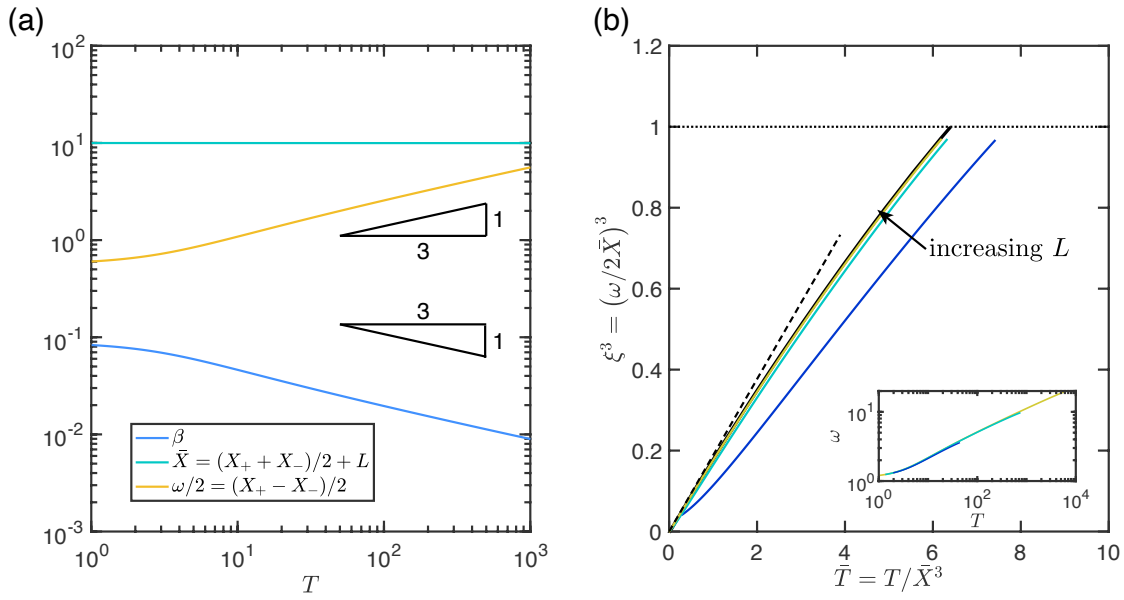

Figure 5.8: (a) Evolution of $\beta, \bar{X}, \omega$ in time T after a plate of half-width $L = 10$ has made contact with the substrate. At late times, the bridge width ω and the plate angle β appear to follow scaling laws (as indicated), with $\bar{X}$ constant. (These scaling laws are confirmed by the analysis in the main text.) The initial perturbations used were $\beta(0) = 10^{-2}, \delta H(0) = -10^{-2}$. (b) Numerical solutions for the bridge width $\omega(T)$ for various plate half-widths L (solid curves) have ω^3 increasing approximately linearly in time T. These results are compared with the solution to the ODE (5.61) (solid black curve) and the scaling $\omega \sim (3T/2)^{1/3}$ (dashed line). The liquid bridge reaches the corner when $\xi = \omega/2\bar{X} = 1$ (dotted line). The solutions shown are for plates of half-width $L = 2$ (dark blue), $L = 5$ (light green), and $L = 10$ (gold). In all cases the initial perturbations were $\beta(0) = 10^{-2}, \delta H(0) = -10^{-1}$. Inset: the raw results for $\omega(T)$ from numerical simulations.

since the term $[1 + \phi_0(4\bar{X}^2 - \omega^2)/(4\bar{X}\omega)] > 0$ and so can be cancelled. The relationship (5.59) can then be substituted into the bridge motion equations (5.57) & (5.58), and significantly simplifies the relations for $\bar{X}$ and ω to:

$$\dot{\bar{X}} \approx 0, \qquad \dot{\omega} + \frac{\omega}{\beta}\dot{\beta} \approx 0. \tag{5.60}$$

The bridge midpoint is fixed, $\bar{X} =$ constant, and the width and angle are inversely related $\omega \propto \beta^{-1}$. More concretely, the bridge volume is fixed, $\beta\bar{X}\omega = 1$, and so the bridge width and plate angle are related through $\omega(T) = 1/[\bar{X}\beta(T)]$ with $\bar{X}$ constant. It remains to determine β, or equivalently ω, as a function of time T.

Eliminating β from (5.59) in favour of ω, and defining $\xi(T) = \omega(T)/2\bar{X} \leq 1$, the ODE for ξ is obtained as

$$\dot{\xi}\left[1 - \frac{1-\xi^2}{2\xi}\log\left(\frac{1+\xi}{1-\xi}\right)\right] = \frac{1}{24\bar{X}^3}. \tag{5.61}$$

For further insight, note that when the meniscus is far from the corner, $\xi \ll 1$, then $\log[(1+\xi)/(1-\xi)] \sim 2\xi + 2\xi^3/3$ and (5.61) can be simplified to

$$\xi^2\dot{\xi} \sim \frac{1}{16\bar{X}^3} \quad \Longrightarrow \quad \omega \sim \left(\omega_0^3 + \frac{3}{2}T\right)^{1/3}, \qquad \beta \sim \frac{1}{\bar{X}}\left(\omega_0^3 + \frac{3}{2}T\right)^{-1/3} \tag{5.62}$$

for some constant ω_0, which corresponds to an effective initial bridge width. At late times, it is therefore expected that $\omega \sim (3T/2)^{1/3}$ and $\beta \sim \bar{X}^{-1}(3T/2)^{-1/3}$.

The numerical solutions of the full system confirm that ω^3 increases approximately linearly with T, as shown in fig. 5.8b. The agreement with the scaling relations is relatively good for wider plates; for very narrow plates there is an offset that is attributed to changes in $\bar{X}$ at early times: in fig. 5.8a, the change in $\bar{X}$ once the plate has contacted the substrate is less than 1%, but can be as much as 10% for the narrowest plate shown in fig. 5.8b ($L = 2$). This in turn happens because the plate angle is steeper for narrow plates, causing a stronger capillary pressure gradient and so the bridge drifts more off-centre before the viscous-capillary balance described by eqn. (5.59) kicks in. Additionally, the faster migration speeds and narrower distance to travel to the corner may mean that, with narrower plates, it is not possible to reach sufficiently late times for the load torque to be neglected; in these cases, the meniscus still reaches the corner in finite time (the load torque eventually becomes negligible as in other cases) but perhaps not following the scaling as closely as the wider plates.

Note also that the solution of (5.61) is universal, once time is rescaled according to $\bar{T} = T/\bar{X}^3$; the numerical solution of this equation is therefore also plotted in fig. 5.8b. From this solution, it is determined that $\xi \to 1$ as $\bar{T} \to \bar{T}_c \approx 6.4$ which is not far from the estimate made by extrapolating the power-law scaling (valid only for small ξ): $\omega \to 2\bar{X}$ as $T \to 16\bar{X}^3/3$. Further, note that the initial contact often occurs on small timescales in which the bridge will not have moved far, and so it may be expected that $\bar{X} \approx L$ (especially for wider plates). We conclude that the liquid bridge reaches the corner in a finite time, with an estimate for the time taken given by $T \approx 6.4 \times L^3$ (although this appears to be an underestimate for narrow plates). As a point of comparison, the corresponding time for a bridge to migrate a distance L in a wedge of fixed angle β is $T = 24L/\beta$ [Reyssat, 2014]; here, the typical wedge angle is $\beta \sim 1/L$, which suggests a migration time $T \propto L^2$ — for wide plates, the evolving wedge angle in this problem slows the bridge's motion into the corner compared to the constant wedge angle case.

Finally, note that the capillary-viscosity balance is valid provided that the torque applied by the load is much smaller than the other terms in eqn. (5.56). From the scaling relations when $\xi = \omega/2\bar{X} \ll 1$, it is expected that the final term on the right-hand side of (5.56)

looks like $\bar{X}T^{2/3}$ at late times; if $\bar{X} \approx L$ then the load is negligible for sufficiently late times $T \gg 1$.

5.4.3 Dynamics with a wet corner

Once the bridge has migrated far enough to reach the edge of the plate (now the corner of the wedge), there is no fluid flux in the corner and the remainder of the motion can be determined: assuming without loss of generality that the bridge reaches the left-most corner, a torque balance (5.47) gives that the evolution of the angle satisfies

$$L = \frac{X_+ + L}{2\beta} + \frac{3(X_+ + L)^2}{\beta^3}\dot{\beta}. \tag{5.63}$$

Note that this is simply (5.48) with $D = 0$ and $X_- = -L$.

5.5 Does the load fall or stick?

We have seen that a linear stability analysis suggests that there can be two distinct initial motions of the plate for small perturbations, depending on the relative sizes of perturbations to the separation and angle of the plate. However, this does not tell us the response of the system at later times: is the loaded plate ultimately pulled in to stick to the fixed substrate indefinitely, or does it instead detach? We turn to investigate this now, combining the numerical solutions of the systems presented in §5.3 & §5.4.

If there is little or no tilt, then the motion of the plate is expected to largely follow that considered by Ward [2011], with detachment occurring for any outward perturbations and adhesion maintained if the load is perturbed inwards — the boundary criterion dividing whether a load attaches or detaches is then an initial separation perturbation $\delta H(0) = 0$.

However, based on the analysis so far, any tilt that is initially present in the system grows more rapidly than a comparable perturbation to the separation of the centre. This tilting would lead to contact between the rigid substrate and the load at one edge. In this case, the ultimate fate of the attached load is expected to depend a great deal on when this contact occurs, and what happens beyond it. In addition to how the plate is initially perturbed, the (dimensionless) plate half-width L will be important in determining these outcomes.

5.5.1 Determining whether the load sticks or falls

The motion of the loaded plate is simulated for a variety of different plate half-widths L and perturbations from equilibrium. The eqns. (5.35)–(5.37) are solved numerically,

given appropriate initial conditions, using MATLAB's `ode15s`. Event detection is used to determine whether either edge of the plate touches the substrate; after this, the plate transitions from these free-plate equations to the equations with solid contact at one edge, (5.52) & (5.53). Details of the conditions used to determine whether the load ultimately adheres or detaches are given in Appendix 5.A.

If the liquid reaches the plate-substrate corner (after a finite time, as shown in §5.4.2) then the remainder of the motion can be found analytically from (5.63). In fact, it is not necessary to calculate the resulting motion since the sign of $\dot{\beta}$ in (5.63) is determined by whether the capillary torque $(X_+ + L)/2\beta$ is greater or less than the load torque L: if

$$X_+ + L - 2L\beta > 0 \tag{5.64}$$

at the instant the bridge meniscus reaches the corner, then $\dot{\beta} < 0$ and β decreases with further increases in time. Decreasing β ensures that the inequality in (5.64) holds for all subsequent times if it holds initially, and so it can be concluded that the plate ultimately sticks if the inequality (5.64) holds at the instant that the left hand meniscus reaches the corner, $X_- = -L$. (A similar condition holds if the bridge first reaches the right hand edge, albeit with L replaced by $-L$ and X_+ replaced by X_-, since $\beta < 0$ in this case.)

5.5.2 Results for stick or fall

Since there is no material parameter remaining after this non-dimensionalization, it is expected that the fate of a particular load will be determined by the plate half-width, L, and the initial conditions alone. To explore this relationship, the initial angle $\beta(0)$ is fixed, with the separation perturbation $\delta H(0)$ and plate half-width L both varied. Figure 5.9 shows regime diagrams of the regions of the $[L, \delta H(0)]$ parameter space for which the plate ultimately sticks or detaches when $\beta(0) = 10^{-2}, 10^{-1}$. (Here, the plotted boundary was calculated using interval bisection.)

Qualitatively, when the plate half-width L is smaller, the load detaches even for some inward perturbations, $\delta H(0) < 0$ — there is anomalous detachment. For wider plates, this effect is reduced, and the boundary between the load sticking or detaching is much closer to what would be expected from the linear stability analysis of parallel plates presented in §5.2; specifically, the boundary between sticking and detaching is very close to $\delta H(0) = 0$. Additionally (comparing fig. 5.9b to fig. 5.9a), when the angle perturbation is larger, a greater inward perturbation is needed to stick at small L and there is a larger region in which anomalous detachment occurs. These results show that the presence of even small amounts of tilting can fundamentally change the ultimate fate of a load adhered via surface tension and is a possible cause of the anomalous detachment seen in fig 5.1.

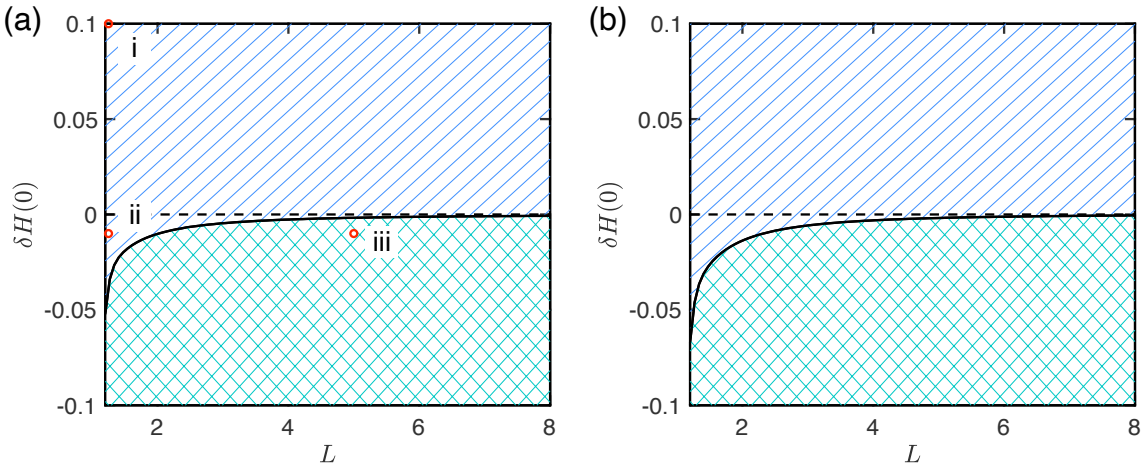

Figure 5.9: Plot showing results of whether the load ultimately adheres to the substrate (cross hatched region) or ultimately detaches (striped region) for different values of the plate half-width L and perturbation size $\delta H(0)$ when the bridge begins at the plate centre, $X_+(0) + X_-(0) = 0$. Results are shown with initial angular perturbations: (a) $\beta(0) = 10^{-2}$, and (b) $\beta(0) = 10^{-1}$. The horizontal dashed line indicates no initial separation perturbation, $\delta H(0) = 0$; linear stability analysis with a parallel plate predicts that above this line the plate detaches, while below it adhesion persists; the region between the solid curve and dashed line therefore corresponds to anomalous detachment. The red circles in (a) denote the parameter values for the snapshots presented in fig. 5.10.

Looking in more detail at the evolution of the numerical solutions in these different regions (see, for example, fig. 5.10), the tilting of the plate is found to cause contact at the plate edge on relatively short timescales. Once this has occurred, the subsequent evolution is determined by the competition between load and capillary torques about the corner. In some cases, the bridge reaches the corner and the condition (5.64) must be applied.

Smaller-sized plates have a relatively large angle and the capillary torque may be beaten by the load torque, resulting in detachment, even for some inward perturbations (see fig. 5.10ii). Plots of the plate midpoint separation $H(T)$ with time for a plate of half-width $L = 1.25$ are shown in fig. 5.11a. In particular, two cases are shown where the initial perturbation was inwards and yet the separation increases and the plate detaches, qualitatively similar to the experimental trajectories of anomalous detachment highlighted in fig. 5.4a.

For wider plates, contact at the edge occurs sooner and the plate angle is smaller. For some perturbations where narrower plates would detach, the capillary torque levers the plate upwards (see fig. 5.10iii). Figure 5.11b shows the midpoint separation $H(T)$ for a plate of half-width $L = 5$. The initial contact occurs earlier than in fig. 5.11a (the plate is

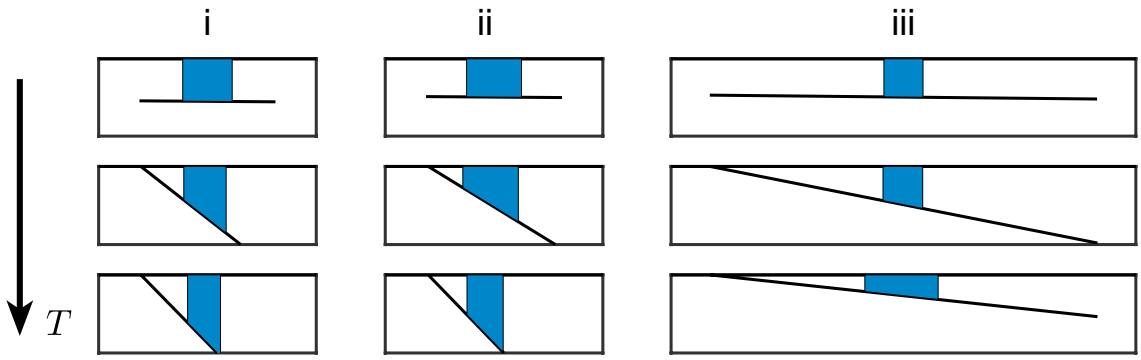

Figure 5.10: Plots of plate and liquid bridge positions (in the lab frame) at different time intervals, showing the role of plate size. The initial conditions used and times plotted are: (i) $\delta H(0) = +10^{-1}, L = 1.25$, at times $T = 0, 0.5, 0.65$, (ii) $\delta H(0) = -10^{-2}, L = 1.25$, at times $T = 0, 1, 2.75$, (iii) $\delta H(0) = -10^{-2}, L = 5$, at times $T = 0, 1, 10$. In all cases $\beta(0) = 10^{-2}$. Note that the evolution of the mean separation, $H(T)$, in each case is shown in fig. 5.11.

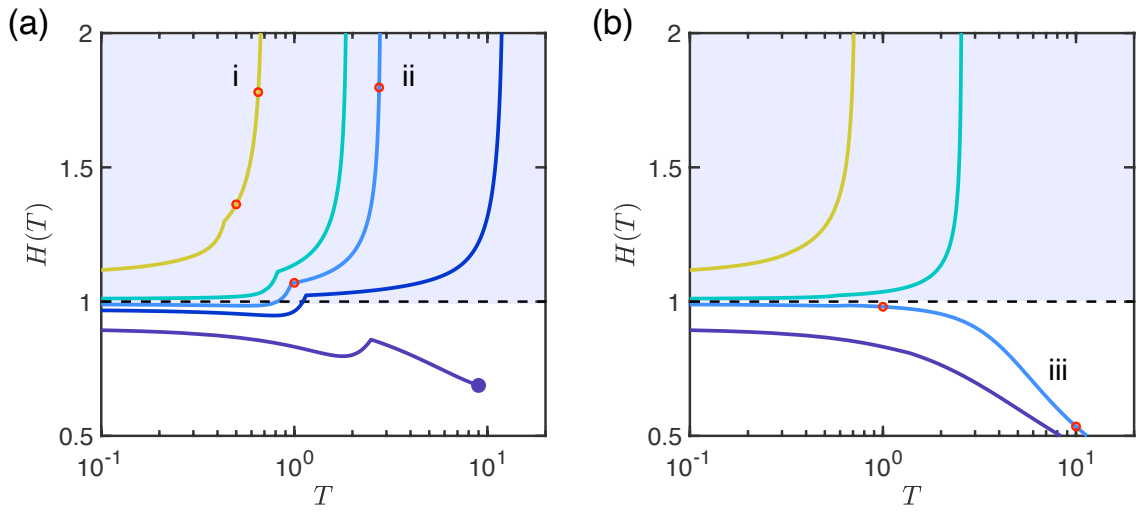

Figure 5.11: The evolution of the dimensionless separation of the plate centre of mass, $H(T)$, for various values of the perturbation from equilibrium, $\delta H(0)$, and two different plate half-widths (a) $L = 1.25$, and (b) $L = 5$. Each plot shows trajectories with initial separation perturbations of $\delta H(0) = \pm 10^{-2}, \pm 10^{-1}$; in (a) an additional trajectory with $\delta H(0) = -0.03$ is also shown. In all cases the angle perturbation is $\beta(0) = 10^{-2}$. Filled circles show when the numerical integration terminates due to the bridge nearing the corner (see Appendix 5.A). The three solutions labelled with roman numerals are the trajectories corresponding to the snapshots shown in fig. 5.10, with the red circles indicating the corresponding time points for plots with $T > 0$. The shaded region in each plot is the region in which the usual parallel stability analysis would predict detachment; note that in (a) some trajectories that begin in the lower (adhering) region ultimately detach — they detach anomalously.

wider and so does not need to tilt as much to touch the substrate) and the perturbation $\delta H(0) = -10^{-2}$ does not anomalously detach for this wider plate case, even though it does when $L = 1.25$. Moreover, the overall stick/detach behaviour is similar to what would be expected from the parallel plate's linear stability (compare to fig. 5.4b) — for wider plates, the tilting does not appear to have a significant effect on whether the loaded plate sticks or detaches.

5.5.3 Horizontal plate motion and the ultimate fate of the plate

A linear stability analysis showed that the shearing of the liquid, and hence horizontal migration of the plate in the lab frame, amplifies the initial growth rate of the tilting motion. It is natural, therefore, to wonder whether the total horizontal migration (prior to contact) is significant in comparison to the plate width. In fig. 5.12a, the horizontal displacement of a plate (relative to its initial position) is shown as a function of time, $X_{\text{plate}}(T) = -\int_0^T U(\tau)\mathrm{d}\tau$, for a plate of half-width $L = 1.25$ when subject to different initial vertical perturbations at the centre of mass, $\delta H(0)$. The migration of the plates speeds up over time, but contact with the substrate is made on an $O(1)$ timescale; hence the horizontal motion is limited to a small fraction of the plate width (the horizontal motion of the plate ends is indiscernible between the snapshots of fig. 5.10). For wider plates, the same trajectories are followed but the plates contact the substrate sooner, and so the horizontal deviation of the plate is reduced even further. In fig. 5.12b, the total distance moved by the plate up to the point of contact is shown as a function of the plate half-width, L. The overall sideways drift decreases with increasing plate width, appearing to follow a scaling $X_{\text{plate}} \sim L^{-1}$; this can be rationalized by remembering that at early times the plate moves at a speed $U \propto \beta$ from (5.42) and the angle β grows exponentially until it has reached a size $1/L$. In conclusion, the plate's sideways drift is small (in comparison to the plate width), despite having a noticeable effect on the growth rate of instability.

Finally, it remains to address the expected final state of the plate and liquid bridge in this system. The theory presented here is a lubrication model — assuming a thin film of liquid — and so is not able to account for rupture of the bridge as the plate separation increases; in the situations where it has been concluded that the plate 'detaches' or 'falls', it is expected that the liquid bridge will eventually rupture as it elongates. In the cases where the plate 'sticks' or 'adheres', the bridge will eventually be squeezed between the two surfaces sufficiently that the menisci reach both edges of the plate. Once this has occurred, the plate may lose contact with the substrate and the menisci become pinned at the plate edges (the contact angle is no longer fixed). The bridge can then reach a stable

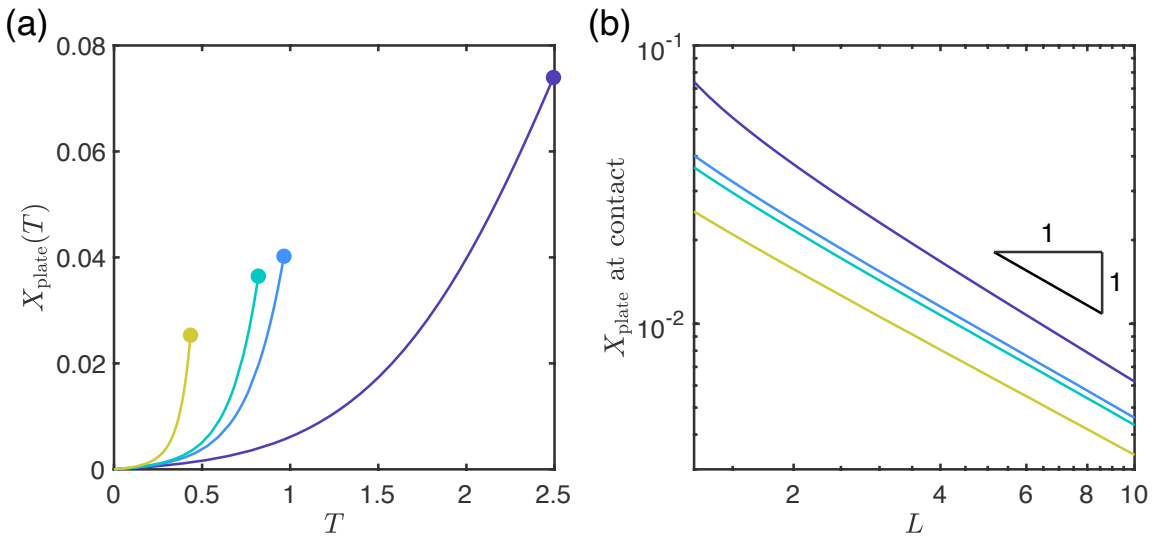

Figure 5.12: (a) The horizontal position of the centre of mass of the plate, $X_{\text{plate}}(T)$, in the lab frame as a function of time T for various perturbations $\delta H = \pm 10^{-2}, \pm 10^{-1}$ (colours correspond to those shown in fig. 5.11a). The angle perturbation is $\beta(0) = 10^{-2}$ and the plate has half-width $L = 1.25$. The filled circles denote when the plate contacts the substrate at an edge and the shearing motion ends. (b) The total distance the plate has moved before contacting the substrate as a function of the plate half-width, L, for the same perturbations as in (a).

equilibrium state close to the substrate — when the edges of the bridge are pinned, there is an equilibrium solution that is stable to both constant force and constant displacement perturbations [see Slater et al., 2014, for example].

5.6 Conclusions

In this chapter, we have considered the motion of a loaded plate that is joined to a flat substrate by the surface tension of a capillary bridge. Allowing the plate to tilt freely and the liquid bridge to migrate in response to the resulting tapered geometry allows for a variety of different dynamical processes to be explored.

For a given volume of liquid and applied load, a single equilibrium solution is found and a linear stability analysis shows that this is unstable to perturbations at fixed load. The linear stability decouples into two distinct modes: (i) motion perpendicular to the substrate (either towards or away) or (ii) tilting of the plate and migration of the bridge into the narrower gap. The tilting mode grows fastest, and its growth is amplified by the sideways shearing of the plate, but which mode is seen will depend on the size of the initial perturbation from equilibrium — if perturbations to the angle β and separation H

are orders of magnitude different then one may dominate over the other.

Studying the evolution at later times numerically, it was determined whether the load is pulled in to stick closely to the substrate or ultimately detaches. In exploring this motion, there was allowance for situations in which there was sufficient tilt for the plate to contact the substrate and then pivot around its contacting edge, as well as consideration of what happens when the liquid reaches this corner (which was shown to occur in finite time). The final state of the plate depends sensitively on the plate size (beyond the initial bridge size) as well as the relative sizes of the perturbation. This suggests that it is important to take the tilt into account in such a capillary system. Moreover, it is possible that the presence of even a relatively small amount of this tilting motion may help to explain why the boundary between sticking and detaching was not found at $H = 1$ in the experiments of Ward [2011] — these experiments were performed with relatively large liquid bridges (or small plates), so that $L \sim 1$. As such, they are expected to be in the regime where sufficiently small negative perturbations cause detachment, rather than adhesion, just as is observed experimentally (see fig. 5.4a). It would be interesting to see whether further experiments agree with the dependence of adhesion on the plate half-width L found here.

The model and analysis presented in this chapter is limited to a relatively simple two-dimensional system. Nevertheless, it produces some interesting results that may carry over (at least qualitatively) into more realistic three-dimensional systems. It would be interesting to see how the added components of an additional direction of curvature, as well as the possibility of fluid flow in other directions and plate twisting, would affect the bridge-plate motion. A key complication here is the evolution of the shape of the bridge's footprint as it migrates into the wedge; experiments by Reyssat [2014] for a liquid bridge migrating into a wedge with fixed angle suggested that the bridge's contact line may remain approximately circular. This previous work also suggests that the difference between two-dimensional and three-dimensional bridges is quantitative, rather than qualitative [Reyssat, 2014, Gorce et al., 2016]: in both cases the leading meniscus reaches the corner in finite time and at a constant speed. Nevertheless, whether this qualitative similarity between the 2D and 3D cases, together with the simple contact line shape of the bridge, remain when the wedge angle evolves dynamically, as described here, remains an open question. In particular, the three-dimensional problem would require consideration of the stability of the liquid interface — during detachment, air would displace the more viscous liquid in the bridge, and the interface should generally be expected to be unstable to a Saffman–Taylor instability, forming liquid fingers as the plate separates from the substrate, as studied in bridges between accelerating surfaces by Brulin et al. [2020] and observed in the experiments of Ward [2011] (fig. 5.1b).

A number of other physical effects have been neglected in the analysis presented here. For example, only undeformable surfaces were considered, while the experiments presented in Chapter 4 involved a flexible membrane subject to a load. Including the deformation of the loaded surface would allow for peeling [as studied by McEwan and Taylor, 1966, for example] to occur in addition to the tilting and separation considered here — conversely, peeling with a time-dependent peeling angle, as would occur in this case, would provide an interesting extension of the classic McEwan and Taylor [1966] problem. Contact angle hysteresis may also play an important role in limiting the motion of a liquid bridge in a rigid system, which would likely eventually force the system into the separating mode over tilt and migrate. Indeed, Ataei et al. [2017] found that in the presence of contact angle hysteresis, the tilt must exceed a critical angle for the bridge to begin migrating, which may limit the effect of tilting mentioned here. These extensions would each be worth further work; which of them is most pressing should perhaps be guided by the results of further experiments.

Appendices

5.A Numerical details

5.A.1 Fall or stick criteria

To decide whether the loaded plate ultimately sticks or detaches, conditions are required to terminate the simulations. To this end, it is concluded that the plate sticks to the substrate if the separation at the centre of the plate reaches $H = 0.2$ and similarly it detaches if the separation gets as high as $H = 5$. These values were chosen as they require a significant deviation from the initial plate positions near $H = 1$ so it is reasonable to assume the plate motion is consistent from then on. At the same time, these are not too far that the calculations run unnecessarily long or so close to $H = 0$ that the liquid bridge is squashed enough to entirely coat the plate. Varying these termination bounds independently does not noticeably affect the results of fig. 5.9.

5.A.2 Detecting a meniscus reaching a plate edge

In practice, the governing equations become singular when the gap width at the bridge meniscus vanishes completely, which can only happen in the contacting regime; this compromises the ability to reach $X_- = -L$ in simulations. However, note from the analysis in §5.4.2 that, despite this, the bridge reaches the corner in finite time. Moreover, when the capillary-viscous balance of §5.4.2 holds, the bridge centre does not migrate sideways and $\beta\omega = \beta(X_+ - X_-)$ remains constant by mass conservation. Therefore a small error in X_- will only result in a small error in the numerical estimates for X_+ and β that are then substituted as the initial conditions for (5.64) that determines the fate of the plate.

The numerical solutions are therefore terminated when one of the menisci, $X_\pm$, reaches within a short distance of the corner, in particular when $X_- = -0.99L$ or $X_+ = 0.99L$. Once this has occurred then the condition (5.64) is checked to decide whether the loaded plate ultimately sticks or falls. This should be a reasonable approximation — the values of β and $X_+ + L$ are expected to change by only a small amount when running the solution all the way to the corner.

5.A.3 Sensitivity to initial bridge position

In calculating fig. 5.9, simulations were started with the liquid bridge located centrally on the plate, i.e. with $X_- = -X_+$ so that $\delta X_+ + \delta X_- = 0$. If, instead, the bridge is initially in the position associated with the growing mode $\sigma_{\circlearrowleft}$ so that the coefficient $B = 0$ in (5.44), then the boundaries in fig. 5.9 do alter a small amount (for example in fig. 5.9a the stick/fall boundary is further from $\delta H(0) = 0$, increasing in magnitude by approximately $10 - 20\%$ everywhere). This is perhaps expected, since forcing the initial fastest growing mode should cause the bridge to migrate and the plate to tilt faster, accentuating the importance of the tilt mechanism when compared to the centred bridge case.

Note that the main conclusions of this study remain the same regardless, but it seems more natural to present results in which the liquid bridge begins at the centre.

5.A.4 Results at small angles and plate widths

The results presented in this chapter all have initial angles $\beta \geq 10^{-2}$, with no result presented where the magnitude of the angle is $\beta = 10^{-3}$ or smaller. When the angle is sufficiently small, the presence of high powers of β in the ODEs (5.35) and (5.36) (in particular the β^{-5} term) mean that the numerical solver cannot meet integration tolerances. One way to avoid this may be to take the small angle approximation further, linearizing all terms $H + \beta X$ with respect to β to get simplified ODEs. Since the effect of the tilting perturbation decreases with $\beta(0)$, this is not pursued here.

Additionally, any cases where the bridge meniscus reached the plate edge ($X_\pm = \pm L$) before any contact occurred were not investigated. In this case, it is expected that the contact line becomes pinned at the plate edge and the contact angle varies instead, with extra physics required to decide how to couple the change in interface curvature at the pinned edge to the flux of incoming liquid from lubrication theory. This scenario seems to occur often when the plate widths are not much larger than the initial bridge width (the bridges do not have far to migrate to the edge). To avoid the complication of this situation, results with plate half-width $1/2 < L < 1$ are not presented.

Chapter 6

Conclusions

6.1 Summary of the thesis

In this thesis, we have studied how the surface tension of a liquid bridge confined between two solid surfaces applies forces to those surfaces. We have considered various models of this capillary adhesion, looking at both the statics and dynamics, and compared their predictions to available experimental results of comparable real world systems.

In Chapter 2, we considered whether splitting a finite volume of liquid into many smaller bridges could increase the capillary force exerted on the adjoining solids. Simplified models of wide and thin bridges did not accurately predict the increase in the adhesion force observed when splitting, and so it was important to carefully calculate the equilibrium shape of liquid bridges. Expanding on previous work by De Souza et al. [2008] that showed a small increase in adhesion by splitting between parallel plates, we investigated the increase in adhesion force observed by splitting if one surface were rough. Modelling an asperity locally as a parabola, it was shown that a significant increase in adhesion was possible for splitting bridges on rough surfaces. This mechanism is particularly effective because it is aided by a geometry-induced capillary migration that causes bridges to equilibrate at local minima in the gap width, simultaneously maximizing the wetted area and the suction pressure. This migration can also resist shearing of the surfaces; this effect was quantified using a dynamic lubrication model. Steady state solutions were found for small capillary numbers, with the resulting resistance to shear calculated as a function of bridge volume, as well as the total shear resistance caused by many such bridges. By comparing the theoretical shear force to experiments on insects, however, it appeared that the resistance to shear generated by this mechanism alone is unlikely to be large enough to explain insects' strong resistance to shear.

Chapter 3 considered contact adhesion between impermeable or poroelastic spheres and a rigid plane in the presence of a capillary bridge. The elastic deformation in the

sphere was modelled close to the contact region by a mixed boundary value problem, and was reduced to solving a dual integral equation. Specifying the displacement and stress along the boundary led to simultaneous equations that related the force on the sphere, liquid volume, capillary pressure, meniscus radius and contact radius. For an impermeable sphere, once the elastic properties and liquid volume were specified, solution curves were found that behaved qualitatively like JKR adhesion, as had been found in previous similar studies [Fogden and White, 1990, Goryacheva and Makhovskaya, 1999]. For a poroelastic sphere, the sphere is able to naturally secrete its own adhering capillary liquid as it deforms. Solutions were found with no external force applied. In this case, we found power law relations when the sphere radius is large in comparison to the elasto-capillary length. These scaling laws were derived by considering a simplified problem with a small contact region and little deformation, and the predicted relationship between the secreted bridge size and sphere radius was observed in preliminary experiments on contacting hydrogel beads. The results for poroelastic spheres was then extended to small applied forces, where the secreted liquid volume is dominated by the deformation due to a uniform compression of the sphere, and the pull-off force was calculated for a range of adhesion strengths and elastic properties.

The effect of deformation on capillary adhesion was investigated in more detail in Chapter 4 using a model of a thin membrane under tension adhered to a rigid, planar substrate by a capillary bridge. The equilibria of this system depend on two key parameters that are related to the clamp separation from the substrate and the tension in the membrane. For sufficiently low tensions, the membrane may contact the surface, substantially increasing the adhesion force, often by an order of magnitude or more compared to a comparable rigid case. These equilibrium results were generally supported by experiments on a real world version of the model system. However, adhesion appeared to not always be achieved when expected by the equilibrium theory. A dynamic lubrication model suggested that this may be due to the formation of a liquid dimple as the membrane is pulled towards contact: drainage of the dimple delays contact. The asymptotic behaviour of the dimple drainage was found at long times, and agrees well with numerical simulations of the dynamic problem. We then discussed how the two parameters that characterize the equilibrium can best be chosen to ensure detachment; it was suggested that increasing the tension (rather than simply yanking) would minimize the work done to detach.

Finally, in Chapter 5 the dynamic detachment of a capillary load was investigated through a two-dimensional model of a mobile loaded plate attached to a rigid substrate by a wetting liquid bridge. Under a fixed load, the plate's equilibrium is linearly unstable: perturbations towards the stationary substrate should lead to contact while those

away from it should lead to detachment. A linear stability analysis showed that motion away from this unstable equilibrium decouples into two modes: one in which the plate purely separates from (or approaches) the substrate, and another in which it tilts and the bridge migrates towards the narrow end (with shear causing a small horizontal migration of the plate). The tilting mode has the largest eigenvalue and so is expected to grow fastest. Sufficient tilting of the plate relative to the substrate can lead to contact at one edge, depending on the width of the plate. The physics of motion after this contact were considered separately, and the bridge was shown to reach the corner in finite time. An investigation of the ultimate fate of the plate, depending on the initial perturbation and plate width, showed that if the plate is relatively narrow and the initial tilt is sufficiently large then the plate could detach even when perturbed inwards at its centre. This anomalous detachment is qualitatively similar to that observed in the experiments of Ward [2011], though 3D effects may play an important role experimentally.

6.2 Avenues for future work

This thesis has covered numerous aspects of capillary adhesion, but there remain many opportunities for further work. Here, we shall discuss a few ideas that could be investigated in the future, including some developments on the work presented in this thesis.

There are many possible extensions to the work presented in Chapter 3 of capillary adhesion of a poroelastic sphere. One obvious extension would be to find a more complete understanding of the equilibria by considering solutions for larger forces. Since the elastic displacement near the contact region decays sufficiently slowly at large distances (like $1/r$), the volume change in the sphere caused by the contact (found by integrating the displacements over the surface) must depend on the larger-scale displacements in the sphere; the model presented in this thesis is not valid at large distances from the contact region, and so it is necessary to couple this solution to the global elastic deformation in an indented sphere. A search of the literature has so far failed to find related elastic indentation problems that account for the finite sphere size (the spherical Boussinesq problem) and so there seems to be a range of related novel problems to be considered. In addition, the study in Chapter 3 was entirely static; it would be interesting to consider the dynamic behaviour of this system, e.g. the timescale to reach equilibrium.

Insects are observed to leave barely any fluid behind when walking about on surfaces, and an outstanding problem in insect adhesion is to explain this. There are a range of dynamic rupture problems that could be studied; one related directly to this thesis would be to investigate how the liquid bridge behaves as the poroelastic sphere of Chapter

3 is withdrawn from the substrate — could the porous sphere, for example, passively suck the adhering liquid back into its pore space as it is retracted? This problem may also be pertinent to inkjet printing and dip-pen lithography where it is desired that the amount of liquid deposited on a surface is carefully controlled [such as the rupture study of Eichelsdoerfer et al., 2014].

A simple two-dimensional detachment model was presented in Chapter 5, and it would be interesting to see how capillary detachment occurs using more complex models. For example, aspects of Chapters 4 and 5 could be combined to understand more fully the detachment of loads by peeling from one edge observed in the loading experiments of the elasto-capillary adhesive. As discussed in the conclusions to Chapter 5, this could be approached using a model similar to the McEwan and Taylor [1966] peeling, but with a time-dependent peeling angle.

Finally, one aspect of capillary adhesion that remains to be addressed is how to provide a resistance to lateral forces and shears. Ideally an adhesive should be able to adhere to horizontal and vertical surfaces equally well, and so must be able to withstand normal and tangential forces. Lubrication models of Newtonian fluids (as have often been considered in this thesis) give a large discrepancy between normal and tangential forces, and so some other mechanism is needed to increase the resistance to shear. Nevertheless, experiments on insects show a clear linear relationship between shear force and velocity — usually this is associated with a hydrodynamic mechanism. In Chapter 2, one such mechanism for resisting shear was proposed, but did not appear to explain the large shear resistance observed in insects. Many other suggestions have been made for how insects are able to achieve a strong resistance to shear, but if insects do adhere predominantly using surface tension then a quantifiable explanation for this strong shear resistance involving capillary effects, as well as an explanation for the linearity with velocity, still remain to be found.

References

D. J. Acheson. *Elementary fluid dynamics*. Oxford University Press, 1990.

M. Argentina, J. Skotheim, and L. Mahadevan. Settling and swimming of flexible fluid-lubricated foils. *Phys. Rev. Lett.*, 99(22):224503, 2007.

E. Arzt, S. Gorb, and R. Spolenak. From micro to nano contacts in biological attachment devices. *Proc. Natl. Acad. Sci. U.S.A*, 100(19):10603–10606, 2003.

M. Ataei, H. Chen, T. Tang, and A. Amirfazli. Stability of a liquid bridge between nonparallel hydrophilic surfaces. *J. Colloid Interface Sci.*, 492:207–217, 2017.

K. Autumn, M. Sitti, Y. A. Liang, A. M. Peattie, W. R. Hansen, S. Sponberg, T. W. Kenny, R. Fearing, J. N. Israelachvili, and R. J. Full. Evidence for van der Waals adhesion in gecko setae. *Proc. Natl. Acad. Sci. U.S.A*, 99:12252–12256, 2002.

S. Baik, D. W. Kim, Y. Park, T.-J. Lee, S. H. Bhang, and C. Pang. A wet-tolerant adhesive patch inspired by protuberances in suction cups of octopi. *Nature*, 546:396–400, 2017.

W. J. P. Barnes, P. J. P. Goodwyn, M. Nokhbatolfoghahai, and S. N. Gorb. Elastic modulus of tree frog adhesive toe pads. *J. Comp. Physiol. A*, 197:969–978, 2011.

H. Barrio-Zhang, É. Ruiz-Gutiérrez, S. Armstrong, G. McHale, G. G. Wells, and R. Ledesma-Aguilar. Contact-angle hysteresis and contact-line friction on slippery liquid-like surfaces. *Langmuir*, 36:15094–15101, 2020.

G. Batchelor. *An Introduction to Fluid Mechanics*. Cambridge University Press, Cambridge, 1st edition, 1967.

R. G. Beutel and S. N. Gorb. Ultrastructure of attachment specializations of hexapods (arthropoda): evolutionary patterns inferred from a revised ordinal phylogeny. *J. Zool. Syst. Evol. Res.*, 39(4):177–207, 2001.

J. Bico, E. Reyssat, and B. Roman. Elastocapillarity: When surface tension deforms elastic solids. *Annu. Rev. Fluid Mech.*, 50:629–659, 2018.

J. J. Bikerman. *The Science of Adhesive Joints*. Academic Press, 1968.

J. B. Bostwick and P. H. Steen. Stability of constrained capillary surfaces. *Annu. Rev. Fluid Mech.*, 47:539–568, 2015.

A. T. Bradley, F. Box, I. J. Hewitt, and D. Vella. Wettability-independent droplet transport by bendotaxis. *Phys. Rev. Lett.*, 122(7):074503, 2019.

F. Brau, D. Lanterbecq, L.-N. Zghikh, V. Bels, and P. Damman. Dynamics of prey prehension by chameleons through viscous adhesion. *Nat. Phys.*, 12:1–8, 2016.

S. Brulin, I. V. Roisman, and C. Tropea. Fingering instability of a viscous liquid bridge stretched by an accelerating substrate. *J. Fluid Mech.*, 899, 2020.

J. M. R. Bullock, P. Drechsler, and W. Federle. Comparison of smooth and hairy attachment pads in insects: friction, adhesion and mechanisms for direction-dependence. *J. Exp. Biol.*, 211(20):3333–3343, 2008.

J. W. M. Bush. Surface tension. In A. Goriely, M. M. Müller, and L. Cugliandolo, editors, *New Trends in the Physics and Mechanics of Biological Systems: Lecture Notes of the Les Houches Summer School*, volume 92, chapter 2, pages 27–64. Oxford University Press, 2011.

M. Butler, F. Box, T. Robert, and D. Vella. Elasto-capillary adhesion: Effect of deformability on adhesion strength and detachment. *Phys. Rev. Fluids*, 4(3):033601, 2019.

M. D. Butler and D. Vella. Detachment in capillary adhesion: the relative roles of tilting and separation. *IMA J. Appl. Math.*, 85(5):673–702, 2020.

H.-J. Butt and M. Kappl. Normal capillary forces. *Adv. Colloid Interface Sci*, 146:48–60, 2009.

S. Cai and B. Bhushan. Meniscus and viscous forces during separation of hydrophilic and hydrophobic surfaces with liquid-mediated contacts. *Mater. Sci. Eng. R*, 61(1-6): 78–106, 2008.

W. C. Carter. The forces and behavior of fluids constrained by solids. *Acta Metall.*, 36 (8):2283–2292, 1988.

N. Chakrapani, B. Wei, A. Carrillo, P. M. Ajayan, and R. S. Kane. Capillarity-driven assembly of two-dimensional cellular carbon nanotube foams. *Proc. Natl. Acad. Sci. U.S.A*, 101(12):4009–4012, 2004.

T. S. Chan, F. Yang, and A. Carlson. Directional spreading of a viscous droplet on a conical fibre. *J. Fluid Mech.*, 894:A26, 2020.

T. S. Chan, C. Pedersen, J. Koplik, and A. Carlson. Film deposition and dynamics of a self-propelled wetting droplet on a conical fibre. *J. Fluid Mech.*, 907:A29, 2021.

H. Cho, G. Wu, J. C. Jolly, N. Fortoul, Z. He, Y. Gao, A. Jagota, and S. Yang. Intrinsically reversible superglues via shape adaptation inspired by snail epiphragm. *Proc. Natl. Acad. Sci. U.S.A*, 116(28):13774–13779, 2019.

C. J. Clemente, J.-H. Dirks, D. R. Barbero, U. Steiner, and W. Federle. Friction ridges in cockroach climbing pads: Anisotropy of shear stress measured on transparent, microstructured substrates. *J. Comp. Physiol. A*, 195:805–814, 2009.

P. Concus and R. Finn. Discontinuous behavior of liquids between parallel and tilted plates. *Phys. Fluids*, 10:39–43, 1998.

P. Concus, R. Finn, and J. McCuan. Liquid bridges, edge blobs, and Scherk-type capillary surface. *Indiana U. Math. J.*, 50:411–441, 2001.

B. Davidovitch and D. Vella. Partial wetting of thin solid sheets under tension. *Soft Matter*, 14:4913–4934, 2018.

P.-G. de Gennes, F. Brochard-Wyart, and D. Quéré. *Capillarity and Wetting Phenomena: Drops, Bubbles, Pearls, Waves*, volume 336. Springer, 2004.

E. J. De Souza, M. Brinkmann, C. Mohrdieck, and E. Arzt. Enhancement of capillary forces by multiple liquid bridges. *Langmuir*, 24(16):8813–8820, 2008.

M. de Volder and A. J. Hart. Engineering hierarchical nanostructures by elastocapillary self-assembly. *Angew. Chem. Int. Ed.*, 52:2412–2425, 2013.

F. W. DelRio, M. L. Dunn, L. M. Phinney, C. J. Bourdon, and M. P. de Boer. Rough surface adhesion in the presence of capillary condensation. *Appl. Phys. Lett.*, 90(16): 163104, 2007.

J.-H. Dirks. Physical principles of fluid-mediated insect attachment - Shouldn't insects slip? *Beilstein J. Nanotechnol.*, 5:1160–1166, 2014.

J.-H. Dirks and W. Federle. Fluid-based adhesion in insects: principles and challenges. *Soft Matter*, 7:11047–11053, 2011a.

J.-H. Dirks and W. Federle. Mechanisms of fluid production in smooth adhesive pads of insects. *J. R. Soc. Interface*, 8(60):952–960, 2011b.

J.-H. Dirks, C. J. Clemente, and W. Federle. Insect tricks: two-phasic foot pad secretion prevents slipping. *J. R. Soc. Interf.*, 7:587–593, 2010.

E. J. Doedel, T. F. Fairgrieve, B. Sandstede, A. R. Champneys, Y. A. Kuznetsov, and X. Wang. AUTO-07P: Continuation and bifurcation software for ordinary differential equations. Technical report, 2007.

P. Drechsler and W. Federle. Biomechanics of smooth adhesive pads in insects: influence of tarsal secretion on attachment performance. *J. Comp. Physiol. A*, 192(11):1213–1222, 2006.

D. G. Duffy. *Mixed boundary value problems*. CRC Press, 2008.

C. Duprat and S. Protiere. Capillary stretching of fibers. *EPL*, 111:56006, 2015.

C. Duprat, S. Protiere, A. Y. Beebe, and H. A. Stone. Wetting of flexible fibre arrays. *Nature*, 482(7386):510, 2012.

C. Duprat, C. Noûs, and S. Protière. Controlling wet adhesion with elasticity. *Soft Matter*, 16(28):6463–6467, 2020.

D. J. Eichelsdoerfer, K. A. Brown, and C. A. Mirkin. Capillary bridge rupture in dip-pen nanolithography. *Soft Matter*, 10(30):5603–5608, 2014.

T. Eisner and D. J. Aneshansley. Defense by foot adhesion in a beetle (hemisphaerota cyanea). *Proc. Natl. Acad. Sci. U.S.A*, 97(12):6568–6573, 2000.

M. W. England, T. Sato, M. Yagihashi, A. Hozumi, S. N. Gorb, and E. V. Gorb. Surface roughness rather than surface chemistry essentially affects insect adhesion. *Beilstein J. Nanotechnol.*, 7(1):1471–1479, 2016.

W. Federle. Why are so many adhesive pads hairy? *J. Exp. Biol.*, 209(14):2611–2621, 2006.

W. Federle and D. Labonte. Dynamic biological adhesion: mechanisms for controlling attachment during locomotion. *Phil. Trans. R. Soc. B*, 374(1784):20190199, 2019.

W. Federle, M. Riehle, A. S. G. Curtis, and R. J. Full. An integrative study of insect adhesion: mechanics and wet adhesion of pretarsal pads in ants. *Integr. Comp. Biol.*, 42(6):1100–1106, 2002.

W. Federle, W. Baumgartner, and B. Hölldobler. Biomechanics of ant adhesive pads: frictional forces are rate-and temperature-dependent. *J. Exp. Biol.*, 207(1):67–74, 2004.

L. R. Fisher and J. N. Israelachvili. Direct measurement of the effect of meniscus forces on adhesion: A study of the applicability of macroscopic thermodynamics to microscopic liquid interfaces. *Colloids Surf.*, 3(4):303–319, 1981.

R. A. Fisher. On the capillary forces in an ideal soil; correction of formulae given by WB Haines. *J. Agr. Sci.*, 16:492–505, 1926.

A. Fogden and L. R. White. Contact elasticity in the presence of capillary condensation. I. The nonadhesive Hertz problem. *J. Colloid Interface Sci.*, 138:414–430, 1990.

C. Gao and B. Bhushan. Tribological performance of magnetic thin-film glass disks: its relation to surface roughness and lubricant structure and its thickness. *Wear*, 190(1): 60–75, 1995.

A. K. Geim, S. V. Dubonos, I. V. Grigorieva, K. S. Novoselov, A. A. Zhukov, and S. Yu. Shapoval. Microfabricated adhesive mimicking gecko foot-hair. *Nat. Mater.*, 2:461–463, 2003.

S. Gernay, W. Federle, P. Lambert, and T. Gilet. Elasto-capillarity in insect fibrillar adhesion. *J. R. Soc. Interface*, 13(121):20160371, 2016.

T. Gilet, L. Heepe, P. Lambert, P. Compère, and S. N. Gorb. Liquid secretion and setal compliance: the beetle's winning combination for a robust and reversible adhesion. *Curr. Opin. Insect. Sci.*, 30:19–25, 2018.

T. Gilet, S.-M. Gernay, L. Aquilante, M. Mastrangeli, and P. Lambert. Adhesive elasto-capillary force on a cantilever beam. *Soft Matter*, 15(19):3999–4007, 2019.

S. Gorb, Y. Jiao, and M. Scherge. Ultrastructural architecture and mechanical properties of attachment pads in tettigonia viridissima (orthoptera tettigoniidae). *J. Comp. Physiol. A*, 186:821–831, 2000.

S. N. Gorb. The design of the fly adhesive pad: distal tenent setae are adapted to the delivery of an adhesive secretion. *Proc. R. Soc. Lond. B*, 265(1398):747–752, 1998.

S. N. Gorb, M. Sinha, A. Peressadko, K. A. Daltorio, and R. D. Quinn. Insects did it first: a micropatterned adhesive tape for robotic applications. *Bioinspir. Biomim.*, 2(4):S117, 2007.

J.-B. Gorce, I. J. Hewitt, and D. Vella. Capillary imbibition into converging tubes: Beating Washburn's law and the optimal imbibition of liquids. *Langmuir*, 32(6):1560–1567, 2016.

I. G. Goryacheva and Y. Y. Makhovskaya. Capillary adhesion in the contact between elastic solids. *J. Appl. Maths Mechs*, 63(1):117–125, 1999.

I. G. Goryacheva and Y. Y. Makhovskaya. Adhesive interaction of elastic bodies. *J. Appl. Maths Mechs*, 65(2):273–282, 2001.

Y. Guo, H.-P. Zhao, X.-Q. Feng, and H. Gao. On the robustness of spider capture silk's adhesion. *Extreme Mech. Lett.*, 29:100477, 2019.

W. B. Haines. Studies in the physical properties of soils: II. A note on the cohesion developed by capillary forces in an ideal soil. *J. Agr. Sci.*, 15(4):529–535, 1925.

T. C. Halsey and A. J. Levine. How sandcastles fall. *Phys. Rev. Lett.*, 80(14):3141, 1998.

P. S. Hammond. Nonlinear adjustment of a thin annular film of viscous fluid surrounding a thread of another within a circular cylindrical pipe. *J. Fluid Mech.*, 137:363–384, 1983.

B. J. Hamrock, S. R. Schmid, and B. O. Jacobson. *Fundamentals of fluid film lubrication*. CRC press, 2004.

G. Hanna, W. Jon, and W. P. J. Barnes. Adhesion and detachment of the toe pads of tree frogs. *J. Exp. Biol.*, 155(1):103–125, 1991.

F. Hauksbee. An account of an experiment touching the direction of a drop of oil of oranges, between two glass planes, towards any side of them that is nearest press'd together. By Mr. Fr. Hauksbee, F. R. S. *Phil. Trans. R. Soc.*, 27:395–396, 1710.

R. B. Heady and J. W. Cahn. An analysis of the capillary forces in liquid-phase sintering of spherical particles. *Metall. Trans.*, 1(1):185–189, 1970.

H. Hertz. Ueber die berührung fester elastischer körper. *J. Reine Angew. Math.*, 1882 (92):156–171, 1882.

R. Hooke. *Micrographia*. The Royal Society, 1665.

S. Ishii. Adhesion of a leaf feeding ladybird epilachna vigintioctomaculta (coleoptera: Coccinellidae) on a virtically smooth surface. *Appl. Entomol. Zool.*, 22(2):222–228, 1987.

H. Jiang, E. W. Hawkes, C. Fuller, M. A. Estrada, S. A. Suresh, N. Abcouwer, A. K. Han, S. Wang, C. J. Ploch, A. Parness, and M. R. Cutkosky. A robotic device using gecko-inspired adhesives can grasp and manipulate large objects in microgravity. *Sci. Robot.*, 2:eaan4545, 2017.

K. L. Johnson. *Contact mechanics*. Cambridge University Press, 1987.

K. L. Johnson, K. Kendall, and A. D. Roberts. Surface energy and the contact of elastic solids. *Proc. R. Soc. Lond. A.*, 324(1558):301–313, 1971.

A. F. Jones and S. D. R. Wilson. The film drainage problem in droplet coalescence. *J. Fluid Mech.*, 87:263–288, 1978.

C. Kittel. *Introduction to solid state physics*, volume 8. Wiley New York, 2005.

A. Kreitschitz, A. Kovalev, and S. N. Gorb. Slipping vs sticking: Water-dependent adhesive and frictional properties of Linum usitatissimum L. seed mucilaginous envelope and its biological significance. *Acta Biomater.*, 17:152–159, 2015.

H.-J. Kümpel. Poroelasticity: parameters reviewed. *Geophys. J. Int.*, 105(3):783–799, 1991.

H.-M. Kwon, H.-Y. Kim, J. Puëll, and L. Mahadevan. Equilibrium of an elastically confined liquid drop. *J. Appl. Phys.*, 103:093519, 2008.

D. Labonte and W. Federle. Scaling and biomechanics of surface attachment in climbing animals. *Phil. Trans. R. Soc. B*, 370:20140027, 2015.

D. Labonte, C. J. Clemente, A. Dittrich, C.-Y. Kuo, A. J. Crosby, D. J. Irschick, and W. Federle. Extreme positive allometry of animal adhesive pads and the size limits of adhesion-based climbing. *Proc. Natl. Acad. Sci. U.S.A*, 113(5):1297–1302, 2016.

P. Lambert. *Surface tension in microsystems*. Springer, 2013.

P. S. Laplace. *Mechanique Celeste, Supplement to Book 10*. 1806.

L. G. Leal. *Advanced Transport Phenomena: Fluid Mechanics and Convective Transport Processes*, volume 7. Cambridge University Press, 2007.

B. Levich and L. Landau. Dragging of a liquid by a moving plate. *Acta Physicochim. URSS*, 17:42, 1942.

K. Li and S. Cai. Wet adhesion between two soft layers. *Soft Matter*, 10:8202–8209, 2014.

J. R. Lister, N. F. Morrison, and J. M. Rallison. Sedimentation of a two-dimensional drop towards a rigid horizontal plane. *J. Fluid Mech.*, 552:345–351, 2006a.

J. R. Lister, J. M. Rallison, A. A. King, L. J. Cummings, and O. E. Jensen. Capillary drainage of an annular film: the dynamics of collars and lobes. *J. Fluid Mech.*, 552: 311–343, 2006b.

J. R. Lister, G. G. Peng, and J. A. Neufeld. Viscous control of peeling an elastic sheet by bending and pulling. *Phys. Rev. Lett.*, 111:154501, 2013.

B. J. Lowry and P. H. Steen. Capillary surfaces: Stability from families of equilibria with application to the liquid bridge. *Proc. R. Soc. A*, 449:411–439, 1995.

C. Lv, C. Chen, Y.-C. Chuang, F.-G. Tseng, Y. Yin, F. Grey, and Q. Zheng. Substrate curvature gradient drives rapid droplet motion. *Phys. Rev. Lett.*, 113(2):026101, 2014.

A. M. Macner and P. H. Steen. Adaptive adhesion by a beetle: Manipulation of liquid bridges and their breaking limits. *Biointerphases*, 9:011001, 2014.

J. H. Maddocks. Stability and folds. *Arch. Ration. Mech. An.*, 99:301–328, 1987.

E. H. Mansfield, H. R. Sepangi, and E. A. Eastwood. Equilibrium and mutual attraction or repulsion of objects supported by surface tension. *Phil. Trans. R. Soc. A*, 355(1726): 869–919, 1997.

G. Mason and W. C. Clark. Liquid bridges between spheres. *Chem. Eng. Sci.*, 20(10): 859–866, 1965.

C. H. Mastrangelo and C. H. Hsu. Mechanical stability and adhesion of microstructures under capillary forces - part 1: Basic theory. *J. MEMS*, 2:33–43, 1993.

C. M. Mate. Application of disjoining and capillary pressure to liquid lubricant films in magnetic recording. *J. Appl. Phys.*, 72(7):3084–3090, 1992.

J. McCarthy, D. Vella, and A. A. Castrejón-Pita. Dynamics of droplets on cones: self-propulsion due to curvature gradients. *Soft Matter*, 15(48):9997–10004, 2019.

A. D. McEwan and G. I. Taylor. The peeling of a flexible strip attached by a viscous adhesive. *J. Fluid Mech.*, 26:1–15, 1966.

J. C. Melrose. Model calculations for capillary condensation. *AIChE J*, 12(5):986–994, 1966.

J. Meseguer. Stability of slender, axisymmetric liquid bridges between unequal disks. *J. Cryst. Growth*, 67(1):141–143, 1984.

M.-H. Meurisse and M. Querry. Squeeze effects in a flat liquid bridge between parallel solid surfaces. *J. Tribol.*, 128:575, 2006.

G. V. Middleton and P. R. Wilcock. *Mechanics in the earth and environmental sciences*. Cambridge University Press, 1994.

J. A. Moriarty and E. L. Terrill. Mathematical modelling of the motion of hard contact lenses. *Eur. J. Appl. Math.*, 7(6):575–594, 1996.

B. Noble. The solution of bessel function dual integral equations by a multiplying-factor method. *Math. Proc. Camb. Philos. Soc.*, 59(2):351–362, 1963.

A. Nyarko, H. Barton, and A. Dhinojwala. Scaling down for a broader understanding of underwater adhesives - a case for the Caulobacter crescentus holdfast. *Soft Matter*, 12: 9132–9141, 2016.

F. M. Orr, L. E. Scriven, and A. P. Rivas. Pendular rings between solids: meniscus properties and capillary force. *J. Fluid Mech.*, 67(4):723–742, 1975.

M. Pakpour, M. Habibi, P. Møller, and D. Bonn. How to construct the perfect sandcastle. *Sci. Rep.*, 2:549, 2012.

B. N. J. Persson. Wet adhesion with application to tree frog adhesive toe pads and tires. *J. Phys. Condens. Matter*, 19(37):376110, 2007.

B. N. J. Persson. Capillary adhesion between elastic solids with randomly rough surfaces. *J. Phys. Condens. Matter*, 20(31):315007, 2008.

B. N. J. Persson and S. Gorb. The effect of surface roughness on the adhesion of elastic plates with application to biological systems. *J. Chem. Phys.*, 119(21):11437–11444, 2003.

O. Pitois, P. Moucheront, and X. Chateau. Liquid bridge between two moving spheres: an experimental study of viscosity effects. *J. Colloid Interface Sci.*, 231(1):26–31, 2000.

B. Pokroy, S. H. Kang, L. Mahadevan, and J. Aizenberg. Self-organization of a mesoscale bristle into ordered, hierarchical helical assemblies. *Science*, 323(5911):237–240, 2009.

H. Power. *Experimental Philosophy*. Martin and Allestry, London, UK, 1664.

J. Qian and H. Gao. Scaling effects of wet adhesion in biological attachment systems. *Acta Biomater.*, 2:51–58, 2006.

Y. I. Rabinovich, J. J. Adler, M. S. Esayanur, A. Ata, R. K. Singh, and B. M. Moudgil. Capillary forces between surfaces with nanoscale roughness. *Adv. Colloid Interface Sci.*, 96(1-3):213–230, 2002.

A. A. Raimondi and J. Boyd. Applying bearing theory to the analysis and design of pad-type bearings. *Trans. ASME*, 77(3):287–309, 1955a.

A. A. Raimondi and J. Boyd. The influence of surface profile on the load capacity of thrust bearings with centrally pivoted pads. *Trans. ASME*, 77(4):321–330, 1955b.

Lord Rayleigh. On the instability of jets. *Proc. London Math. Soc.*, 1(1):4–13, 1878.

P. Renvoisé, J. W. M. Bush, M. Prakash, and D. Quéré. Drop propulsion in tapered tubes. *EPL*, 86(6):64003, 2009.

E. Reyssat. Drops and bubbles in wedges. *J. Fluid Mech.*, 748:641–662, 2014.

E. Reyssat. Capillary bridges between a plane and a cylindrical wall. *J. Fluid Mech.*, 773: R1, 2015.

B. Roman and J. Bico. Elasto-capillarity: deforming an elastic structure with a liquid droplet. *J. Phys. Condens. Mat.*, 22(49):493101, 2010.

É. Ruiz-Gutiérrez and R. Ledesma-Aguilar. Lattice-Boltzmann simulations of the dynamics of liquid barrels. *J. Phys. Condens. Matter*, 32:214007, 2020.

É. Ruiz-Gutiérrez, C. Semprebon, G. McHale, and R. Ledesma-Aguilar. Statics and dynamics of liquid barrels in wedge geometries. *J. Fluid Mech.*, 842:26–57, 2018.

L. E. Scriven and C. V. Sternling. The marangoni effects. *Nature*, 187(4733):186–188, 1960.

Z. Shi, Y. Zhang, M. Liu, D. A. H. Hanaor, and Y. Gan. Dynamic contact angle hysteresis in liquid bridges. *Colloids Surf.*, 555:365–371, 2018.

D. Shin, W. T. Choi, H. Lin, Z. Qu, V. Breedveld, and J. C. Meredith. Humidity-tolerant rate-dependent capillary viscous adhesion of bee-collected pollen fluids. *Nat. Commun.*, 10(1):1379, 2019.

D. M. Slater, M. J. Vogel, A. M. Macner, and P. H. Steen. Beetle-inspired adhesion by capillary-bridge arrays: pull-off detachment. *J. Adhes. Sci. Technol.*, 28:273–289, 2014.

I. N. Sneddon. The elementary solution of dual integral equations. *Glasgow Math. J.*, 4 (3):108–110, 1960.

I. N. Sneddon. *Fourier transforms*. Courier Corporation, 1995.

J. H. Snoeijer and B. Andreotti. Moving contact lines: scales, regimes, and dynamical transitions. *Annu. Rev. Fluid Mech.*, 45:269–92, 2013.

J. B. Sokoloff. Effects of capillary forces on a hydrogel sphere pressed against a surface. *Langmuir*, 32(1):135–139, 2016.

S. Song, D.-M. Drotlef, C. Majidi, and M. Sitti. Controllable load sharing for soft adhesive interfaces on three-dimensional surfaces. *Proc. Natl. Acad. Sci. U.S.A*, 114:1620344, 2017.

R. Spolenak, S. Gorb, and E. Arzt. Adhesion design maps for bio-inspired attachment systems. *Acta Biomater.*, 1(1):5–13, 2005.

N. E. Stork. A comparison of the adhesive setae on the feet of lizards and arthropods. *J. Nat. Hist.*, 17(6):829–835, 1983.

R. W. Style, Y. Che, S. J. Park, B. M. Weon, J. H. Je, C. Hyland, G. K. German, M. P. Power, L. A. Wilen, J. S. Wettlaufer, and E. R. Dufresne. Patterning droplets with durotaxis. *Proc. Natl. Acad. Sci. U.S.A*, 110(31):12541–12544, 2013.

R. W. Style, A. Jagota, C.-Y. Hui, and E. R. Dufresne. Elastocapillarity: Surface tension and the mechanics of soft solids. *Annu. Rev. Condens. Matter Phys.*, 8:99–118, 2017.

T. Tanaka, M. Morigami, and N. Atoda. Mechanism of resist pattern collapse during development process. *Jpn. J. Appl. Phys.*, 32(12S):6059, 1993.

M. Taroni and D. Vella. Multiple equilibria in a simple elastocapillary system. *J. Fluid Mech.*, 712:273–294, 2012.

P. H. Trinh, S. K. Wilson, and H. A. Stone. A pinned or free-floating rigid plate on a thin viscous film. *J. Fluid Mech.*, 760:407–430, 2014.

A. Tulchinsky and A. D. Gat. Viscous-poroelastic interaction as mechanism to create adhesion in frogs' toe pads. *J. Fluid Mech.*, 775:288–303, 2015.

D. Vella and B. Davidovitch. Indentation metrology of clamped, ultra-thin elastic sheets. *Soft Matter*, 13:2264–2278, 2017.

M. J. Vogel and P. H. Steen. Capillarity-based switchable adhesion. *Proc. Natl. Acad. Sci. U.S.A*, 107:3377–3381, 2010.

S. R. Waitukaitis, A. Zuiderwijk, A. Souslov, C. Coulais, and M. Van Hecke. Coupling the leidenfrost effect and elastic deformations to power sustained bouncing. *Nat. Phys.*, 13 (11):1095–1099, 2017.

J. Wang, J. Qian, and H. Gao. Effects of capillary condensation in adhesion between rough surfaces. *Langmuir*, 25(19):11727–11731, 2009.

J.-P. Wang, E. Gallo, B. François, F. Gabrieli, and P. Lambert. Capillary force and rupture of funicular liquid bridges between three spherical bodies. *Powder Technol.*, 305:89–98, 2017.

T. Ward. Capillary-pressure driven adhesion of rigid-planar surfaces. *J. Colloid Interface Sci.*, 354(2):816–824, 2011.

J. S. Wexler, T. M. Heard, and H. A. Stone. Capillary Bridges between soft substrates. *Phys. Rev. Lett.*, 112, 2014.

C. D. Willett, M. J. Adams, S. A. Johnson, and J. P. K. Seville. Capillary bridges between two spherical bodies. *Langmuir*, 16(24):9396–9405, 2000.

S. D. R. Wilson. The drag-out problem in film coating theory. *J. Eng. Math.*, 16(3): 209–221, 1982.

G. Worster. *Understanding Fluid Flow*. AIMS Library of Mathematical Sciences. Cambridge University Press, 2009.

S. G. Yiantsios and R. H. Davis. On the buoyancy-driven motion of a drop towards a rigid surface or a deformable interface. *J. Fluid Mech.*, 217:547–573, 1990.

T. Young. III. An essay on the cohesion of fluids. *Phil. Trans. R. Soc. Lond.*, (95):65–87, 1805.

L. Zhu, J. Qiu, and E. Sakai. A high modulus hydrogel obtained from hydrogen bond reconstruction and its application in vibration damper. *RSC Adv.*, 7(69):43755–43763, 2017.

S. Zilberman and B. N. J. Persson. Adhesion between elastic bodies with rough surfaces. *Solid State Commun.*, 123(3-4):173–177, 2002.